RESOLVING THE MORPHOLOGICAL AND MECHANICAL PROPERTIES OF PALM PETIOLES: SHAPE ANALYSIS METHODS FOR SYMMETRIC SECTIONS OF NATURAL FORM

A thesis submitted for the degree of

Doctor of Philosophy

by

Andrea Windsor-Collins

Department of Mechanical, Aerospace and Civil Engineering

College of Engineering, Design and Physical Sciences

Brunel University London

August 2016

Total Word Count = 61,346

Abstract

Palms support the largest leaves in the world and have evolved on Earth for over 120 million years. They are often reported to be the only structure left standing post-hurricane.

Cross-sectional shapes of cantilevered structures are important design factors affecting torsional and bending performance. Understanding the shape contribution of natural sections such as palm *petioles* (modified leaf stalks) is more difficult than those for simple 2D shapes because conventional methods of calculating section properties are not well suited to these irregular shapes.

The role of internal structure, material properties and external shape of palm *petioles* in cantilever performance has been investigated and three main contributions to knowledge result from this research. Firstly, 3D mapping, i.e., the size, orientation and position, of vascular bundles in the *Trachycarpus fortunei* palm *petiole* reveals the distributions of stress and Young's modulus values, providing a more detailed understanding of *petioles* than previous work. Secondly, bulk elastic material properties along the longitudinal axis of the same *petiole* are then input to a bi-layered model of the same *petiole* establishing the Young's modulus of the two layers without mechanically testing them individually and for determining that the outer layer is not lignified. Thirdly, the largest contribution is the introduction of modified *shape transformers* employing the use of circular envelopes, eliminating error caused by approximating second moment of area with the torsional constant. This leads to a novel Shape Edge Mapping (SEM) technique which deconstructs *petiole* cross section shape elements and enables the structural contribution of these elements to be calculated, improving the understanding of the *petiole* section and how it relates to its mechanical function.

This thesis makes a valuable addition to the knowledge of palm function and presents novel techniques for non-destructive extraction of natural shape data for abstraction and use in preliminary engineering design.

Acknowledgements

A big thank you to my main supervisor, Dr. Mark Atherton for his straightforwardness and patience for what has been a long research project interspersed with multiple life changing events. Thank you also to my other supervisors namely Dr. Guilio Alfano, Professor David Cutler (Royal Botanic Gardens, Kew) and Professor Michael Collins for their input, inspiration and encouragement at various stages during this long project.

Thanks to Professor, Barry Tomlinson for hosting my visit to Fairchild Gardens Florida, for the opportunity to test palms in the lab with him and for sharing his vast knowledge of palms with me. Thanks also to Mr. Keith Withers, the technician in the Strength of Materials lab for helping to test natural materials on machines designed for materials with more regular structure. It has been fun thinking out of the box and being pragmatic.

My parents who have always been there – thank you for listening and for your encouragement. Last but not least, thank you to my family for my time taken away from them which I shall endeavour to make up for by way of encouragement to explore and investigate just as I have had the opportunity to do.

Author's declaration

I hereby declare that I am the sole author of this thesis. I authorise Brunel University London to lend this thesis to other institutions or individuals for the purpose of scholarly research.

Andrea Windsor-Collins

I further authorise Brunel University London to reproduce this thesis by photocopying or by other means, in total or in part, at the request of other institutions or individuals for the purpose of scholarly research

Andrea Windsor-Collins

Publications arising from this research

Windsor-Collins, A. G., Atherton, M. A., Collins, M. W. & Cutler, D. F., 2006. Structural and torsional properties of the Trachycarpus fortunei palm *petiole*. In: C. A. Brebbia, ed. *Design & Nature III: Comparing design in nature with science and engineering.* Southampton: WIT Press, pp. 185 - 194.

Windsor-Collins, A. G., Atherton, M. A., Collins, M. W. & Cutler, D. F., 2007a. Section properties of palm *petioles*, Part 1: The influence of shape on the flexural and torsional properties of selected palm *petioles*. *International Journal of Design & Nature and Ecodynamics,* 2(4), pp. 328-355.

Windsor-Collins, A. G., Cutler, D. F., Atherton, M. A. & Collins, M. W., 2007b. The palm - a model for success?. In: J. A. Bryant, M. A. Atherton & M. W. Collins, eds. *Design and Information in Biology - from Molecules to Systems.* Southampton: WIT Press, pp. 303-324.

Windsor-Collins, A. G., Atherton, M. A., Collins, M. W. & Cutler, D. F., 2008. Section properties of palm *petioles*, Part 2: The relationship of palm histology with the torsional rigidity of the palm Trachycarpus fortunei. *International Journal of Design & Nature and Ecodynamics,* 3(3), pp. 190-202.

Contents

List of figures

List of tables

List of equations

Glossary

Term	**Definition**
Abaxial surface	The lower surface of a bifacial leaf.
Adaxial surface	The surface of a leaf or bud adjacent to the stem.
Boundary layer	The layer of fluid in the immediate vicinity of a bounding surface.
Convergent evolution	When organisms not closely related independently evolve similar traits through adaption to similar environments.
Costapalmate	Shaped like the palm of a hand with part of the leaf stalk extending into the leaf blade.
Dicotyledon	One of the two groups comprising the flowering plants, the dicotyledonous embryo has two cotyledons (seed leaves).
Forced convection	Where the motion of the fluid is imposed externally.
Hastula	Flap of tissue borne at the insertion of the blade on the petiole on the upper, lower, or both leaf blade surfaces.
Insolation	Exposure to the rays of the sun.
Monocotyledon	One of the two groups comprising the flowering plants, the Monocotyledonous embryo has a single cotyledon (seed leaf).
Petiole	The stalk at the base of the leaf blade, attaching and supporting the leaf blade to the stem.
Palmate	Leaf blades on one leaf stem arranged like fingers on the palm of a hand.
Parenchyma	Unspecialised, highly vacuolated cells with typically only a primary wall of uniform thickness; it occurs as extensive regions of tissue in the pith, cortex and mesophyll of the plant body. Secondary thickening of walls may occur.

Phloem	The main food transporting tissue of vascular plants; consisting in palms of conducting sieve elements, companion cells and types of parenchyma and sclerenchyma.
Pinnate	Leaf blades on one leaf stem arranged like the veins of a feather.
Sclerenchyma	A supporting tissue whose cells are commonly dead at maturity and possess thick, lignified secondary walls, as in fibres and sclereids.
Shape factor	A dimensionless quantity used in image analysis to numerically describe shape, independent of its size. It is not normalised.
Shape transformer	A dimensionless quantity used in image analysis to numerically describe shape, independent of its size which is normalised.
Tracheary element	A collective term for the vessels and tracheids of the xylem.
Transpiration	The movement of water from the root to the shoot in the tracheary elements of the xylem and the subsequent loss of the water vapour from the leaf surface via the stomata or leaf surface generally.
Turgor	The state of fullness of a cell or blood Vessel or capillary resulting from pressure of the contents against the wall or membrane.
Vascular bundle (VB)	An isolated unit of the conducting system of vascular plants, consisting of xylem and phloem, frequently with other interspersed cells or a sheath of thick-walled cells
Vessel	A series of Vessel elements joined end to end by their perforated end walls.
Xylem	A complex tissue composed of the water conducting tracheary elements, parenchyma and sclerenchyma.

Nomenclature

SI (Système International d'Unités) units have been used throughout the thesis, but for pragmatic reasons of scale, derivatives of SI units have been used where appropriate, for example millimetres instead of metres.

Name	Definition	Symbol	Units
	Material Properties		
Young's modulus (Elastic constant)	Stress/strain	E	GPa
Rigidity modulus	Shear stress / displacement per unit sample length	G	GPa
Poisson's ratio	Ratio of transverse contraction strain to longitudinal extension strain in the direction of stretching force	ν	Dimensionless
Density	m/V	ρ	mg.m^{-3}
Material performance index for a tie in tension	E/ρ	M_1	N.m.g^{-1}
Material performance index for a beam in flexure	$E^{1/2}/\rho$	M_2	GPa$^{1/2}$(mg.m^{-3})$^{-1}$
Material performance index for plate in flexure	$E^{1/3}/\rho$	M_3	GPa$^{1/3}$(mg.m^{-3})$^{-1}$
	Buckling		
Critical Euler buckling load, applying to straight upright cantilevers of height *h*	$\pi^2 \frac{EI}{4h^2}$	P_c	N

Maximum bending stress for a branch of length L, density $\boldsymbol{\rho}$ and diameter $\boldsymbol{d_b}$ of the root of the branch	$\frac{2L^2\rho}{3d_b}$	σ_b	$N.m^{-2}$
Strength before fracture where A_i^c = is the minimum area required by each member to withstand the internal force F_i^c	$\frac{F_i^c}{A_i^c}$	σ_f	MPa
Strength before fracture of a beam in flexure per unit density	$\sigma_f^{2/3}\rho^{-1}$	M5	$MPa^{2/3}(mg.m^{-3})^{-1}$
Torsion and Flexion			
Deflection (the Euler-Bernoulli beam equation)	$\frac{FL^3}{3EI}$	δ	m
Torque (for shafts of circular cross section)	$\frac{GJ\theta}{L}$	T	N.m
Boundary conditions coefficient		c_1	Dimensionless
Non-linear Elastic Torsion			
Torque on shaft at distance z along axis of torsion member where I_n is the nonlinear 'Wagner' constant	$GJ_T\frac{d\Theta}{dz} - Ew\left(\frac{d^3\Theta}{dz^3}\right) + \left(\frac{1}{2}\right)EI_n\left(\frac{d\Theta}{dz}\right)^3$	T	N.m
Warping section constant	For non-circular cross-sections, there are no exact analytical equations for finding the torsion constant.	w	mm^4
Non-linear Wagner constant		l_n	m^4rad^{-1}
Microstructure			
Density of a solid shaft		ρ_s	kg / m^3
Radius of a solid shaft		r_s	mm
Second moment of area of a solid shaft		I_s	mm^4

Mass		m	kg
Shape transformers			
Cross-sectional area		A	mm^2
Cross-sectional second moment of area		I	mm^4
Cross-sectional polar second moment of area		J	mm^4
Torsional constant (function of warping for non-circular shapes)		J_T	mm^4
Cross-sectional area of circumscribing envelope		A_D	mm^2
Second moment of area of circumscribing envelope		I_D	mm^4
Polar second moment of area of circumscribing envelope		J_D	mm^4
Area (A) *shape transformer*	A/A_D	ψA	Dimensionless
Second moment of area (I) *shape transformer*	I/I_D	ψI	Dimensionless
shape transformer for torsional constant	$\frac{J_T}{J_{TD}}$	ψ_{JT}	Dimensionless
shape transformer for torsional constant where J_C is the polar second moment of area of a circle	J_T/J_C	ψ_{JC}	Dimensionless
Bending stiffness (geometric)	EI	k	GPa.mm^4
Torsional rigidity (geometric)	GJ		GPa.mm^4
Twist-to-bend ratio	EI/GJ		Dimensionless
Performance index for the shape bending stiffness mass-efficiency (uniform and isotropic material)	ψ_I/ψ_A	λ_I	Dimensionless
Performance index for the shape torsional rigidity mass-efficiency (uniform and isotropic material)	$\frac{\psi_{JT}}{\psi_A}$	λ_{JT}	Dimensionless

Performance index for bending stiffness to torsional rigidity ratio (twist-to-bend ratio)	$\frac{\psi_I}{\psi_{JT}}$	λ_{IJT}	Dimensionless
Torsion of Shafts			
Maximum shear stress on a rectangular shaft subjected to torque *T* for a rectangular section of breadth and depth b and d	$\frac{(1.8b + 3d)T}{b^2 d^2}$	τmax	N.m^{-2}
Angle of twist *Θ* on a rectangular section shaft of length *l*, sides of breadth b, depth d and modulus of rigidity *G*	$\frac{7Tl(b^2 + d^2)}{2Gb^3 d^3}$	Θ	Radians
Maximum shear stress on a circular shaft subject to torque T, where r is the radius of circular section	$\frac{Tr}{J}$	τmax	N.m^{-2}
Scale Factors			
Breadth scaling factor where B_0 is the breadth of the rectangular scaling envelope	$\frac{B}{B_0}$	u	Dimensionless
Height scaling factor where H_0 is the height of the rectangular scaling envelope	$\frac{H}{H_0}$	v	Dimensionless
Scaling parameter, when $u \geq v$,	$\frac{\ln(uv)}{\ln(u^{1.55} v^{2.45})}$	q	Dimensionless

1 Introduction

1.1 Botanical background

Palms are plants which are very well known to have outstanding structural performance, supporting the largest leaf blades in the plant kingdom. A specific component of the palms, the ‘*petiole*’, which deforms but rarely breaks is the subject of the research.

The term ‘*petiole*’ (Figure 1) when applied to palms is a convenient way of referring to that part of the plant that connects the leaf blade to the stem. Strictly speaking, the term ‘*petiole*’ is not used in the ‘*Monocotyledons*’ class of plant which palms belong to, but it has been used in this thesis for convenience.

Figure 1 ***Palmate*** **leaves from the palm** ***Trachycarpus wagnerianus*** **(Miniature Chusan wax palm). Photo taken at the Palm Centre, Ham, Richmond, UK (Windsor-Collins, et al., 2007b).**

There are three types of leaf blade in palms: *pinnate*, *palmate* and *costapalmate*. The *pinnate* leaf blade is comprised of separate leaflets adjoining a rachis as shown in Figure 2. The *palmate* leaf blade is directly attached to the *petiole* (Figure 1) and has no rachis. Lastly, the *costapalmate* leaf blade (Figure 3) incorporates a rachis and can be described as being between that of a *palmate* and *pinnate* leaf blade.

Figure 2 *Pinnate* leaves from the palm Dypsis lutescens. Photo taken at The Palm Centre, Ham, Richmond, UK (Windsor-Collins, et al., 2007b)

palmate leaf blades are mainly found in the forest under-storey where the sun is weakly filtered through the canopy and where the wind speed is low. The leaflet equivalents are mainly fused to support the large leaf blade, although, at the distal ends, they are often separated to reduce the turbulent flow of the wind over them. *palmate* leaves are usually found in dark, wet areas and are often very large.

The *costapalmate* type leaf has a corrugated shaped leaf blade incorporating a rachis which can vary in length according to type. These leaves are thought to be the largest of the three types and so this design can support the heaviest load although this has not been verified.

Figure 3 ***Costapalmate*** **palm leaf showing the** ***petiole*** **extending into the leaf blade from the palm** ***Sabal bermudana*** **- photo taken at Royal Botanic Gardens, Kew (Windsor-Collins, et al., 2007b)**

Palms can take many different forms and although they are specialised, their morphology can vary greatly. They hold the world record on many different counts, but most notably, their vascular systems:

1) The longest stem recorded is about 172 metres from a species of *Calamus* (Tomlinson, 2006) although these palms are not self-supporting when adult.
2) *Ceroxylon quinduiense* has the longest, self-supporting, un-branched terrestrial stem in the world, commonly known as the Andean Wax Palm. *Ceroxylon quindiuense* can reach heights of up to 60 metres (Gibbons, 2003). It grows in very large groups as part of the forest and is often left when the forest is cleared because it seems the wood blunts chainsaws almost instantly. Although it has the tallest free-standing trunk in the world, it is not necessarily the most structurally efficient un-branched stem in the world.
3) Raphia, a climbing palm, has the longest *pinnate* leaves recorded at 25.11 metres in length (Halle, 1977).
4) *Corypha umbraculifera* is a species of *palmate* palm that produces the world's largest leaf (Tomlinson, 2006) measuring up to eight metres in diameter with a correspondingly long *petiole* of about five metres.
5) Palms have the oldest metabolically active differentiated cells with age of several centuries (Tomlinson & Hugget, 2012).

6) The double coconut (*Lodoicea*) produces the heaviest seed, which up to 25 kg. A fruit containing three seeds can weigh as much as 45 kg however (Tomlinson, 2006).
7) *Corypha umbraculifera* also hold the record for the largest cluster of flowers and only flowers once in its lifetime. Each flower cluster can contain as many as 23.9 million flowers (Fisher, et al., 1987).

As well as having extreme dimensions, palms are among the least branched terrestrial plants in the world. Their energy goes into extending the trunk and producing fruit, leaves and roots rather than lateral branching growth. However, branching occurs in the inflorescences and roots, and some palms branch basally just below the surface of the soil. Palms have survived for a very long time on the evolutionary tree risking the destruction of the one and only apical bud, a kind of design compromise. Despite their apparently simpler structure, palms have survived as a recognisable group through millions of years (Windsor-Collins, et al., 2007b). In fact, *Monocotyledon*s lost their vascular cambium through evolution (Tomlinson & Hugget, 2012) seemingly to evolve from a complex form to a 'simpler' one. The earliest fossil palm material probably dates from the early to late Cretaceous period (Harley, 2006) 120 million years ago.

The habitat of palms known to survive hurricanes are summarised in Table 1 together with their leaf blade type, height and natural environment (Dransfield & Baker, 2015).

Table 1 Palm hurricane survival list

Palm genus and species	***Leaf blade type***	***Typical height of mature palm***	***Natural Environment***
Washingtonia robusta	*Palmate*	30 m	Solitary in desert mountain valleys and canyons
Sabal palmetto	*Costapalmate*	21 m	Solitary on beaches, forests and swamps
Syagrus romanzoffiana	*Pinnate*	15 m	Solitary, sub-tropical woodlands
Pseudophoenix sargentii	*Pinnate*	8 m	Solitary in coastal habitats

This ties in with Winter who noted that tall, thin palms, among them *Washingtonia robusta,* have a remarkable resilience to bending in strong winds (Winter, 1993). Abbey recommends that the following would survive hurricanes (Abbey, 1998): *Pseudophoenix sargentii* (*pinnate*), *Washingtonia robusta* (*Palmate*), *Arecastrum romanzoffianui* (*pinnate*) and *Sabal palmetto* (*costapalmate*). The only difference with those more recently described in Table 1 being that *Arecastrum romanzoffianui* (*pinnate*) replaces *Syagrus romanzoffiana* (*pinnate*).

According to Tomlinson, the *petioles* of *costapalmate* and *palmate* palms are usually very well developed since they extend the leaf blade away from the crown to minimise leaf blade overlap (Tomlinson, 1990). This is of particular importance in understorey palms which need to maximise their ability to photosynthesise. Physical stresses that an understorey palm leaf blade has to withstand to survive are rain, wind, [snow], falling debris, epiphylls, leaf-hopping insects and vertebrates (Chazdon, 1985). Learning from the remarkable ability of the '*petioles*' of *palmate* and *costapalmate* palms to support large leaf blades is a general aim of this work. *petioles* are therefore the botanical structures of interest in this thesis.

The tallest palms that withstand hurricanes are those with *palmate* and *costapalmate* leaf blades (Dransfield & Baker, 2015). However, precipitation, *forced convection* and falling debris on the leaf blade, generate combined flexural and torsion loads on the *petiole* whether the palm is exposed or located in the forest understorey. Understanding how the section properties of the *petiole* withstand this combined loading is the rationale for exploring the structure of the *palmate* and *costapalmate petioles* in this thesis.

In order to understand how the intrinsic parts of the palm *petiole* functions, insight into its internal structure, material properties as well as external shape is necessary. Internally, the arrangement of vascular bundles within the *parenchyma* matrix will be examined, requiring the destructive testing of a *petiole*. As the *T. fortunei* palm is not endangered and permission has been given for removal of samples, it is identified as the palm to use for histology sectioning and for material property testing.

A comprehensive glossary of botanical terms which may be unfamiliar to the reader is on page xix and xx.

The thesis spans two traditional disciplines; that of botany and structural engineering. The area of study named *Biomimetics* was introduced in the 1950s by Otto Schmitt (Harkness, 2002) in which designs are abstracted from nature. It is hoped that some of the practices developed in this thesis will be useful in Biomimetic research as well as to the design engineer.

1.2 Conventional shape transformer methodology

At the preliminary stage of engineering design, it is efficient to preselect the general type of structure required. This can be achieved with the aid of design charts and performance indices. A brief overview of work previously carried out in the field of *shape factor*s and *shape transformers* is presented in Chapter 2.

During the Second World War, material and shape were co-selected with the aim of reducing the weight to strength ratio of aircraft structures (Shanley, 1960). Cox (Cox, 1965) later looked at the yield stress to density performance of beams under compression and bending. The material dilution factor was defined by Parkhouse (Parkhouse, 1984) comparing different structural concepts to equivalent reference cross sections, and coupled selection research was also carried out by Birmingham (Birmingham, 1994). Extensive work by Ashby (Ashby, 1991) and (Ashby, 1999) concentrated on material selection charts and the case of height and width restrictions on shape and material selection. Weaver and Ashby provide the earliest work on torsion *shape factor*s before the advent of shape envelopes or non-proportional/relative scaling. A *shape factor* is dimensionless quantity used in image analysis to numerically describe shape, independent of its size (but is not normalised). Weaver and Ashby defined function, objective and constraints in structures that bend or twist and produced *shape factor*s to achieve the objective (for example to minimise mass) for tubes, box beams and I-sections, irrespective of size (Weaver & Ashby, 1996). In 2000, Burgess published a paper on *shape factor*s and material indices (relating to structural efficiency) for dimensionally constrained shafts (Burgess, 1999), the transverse section shapes of which were circular, elliptical and box cross sections. The latest paper on torsional *shape factor*s (Mirjalili & Pasini, 2007) describes *shape factor*s with limited torsion stiffness design and minimal mass objectives for cross sections that are scaled differently horizontally and vertically for circular, elliptical and box cross sections in the form of solid, thin walled and open walled sections.

An efficient way to analyse the effect of shape is to use *shape transformers*. *Shape transformers* are dimensionless parameters defined to measure geometric quantities of a shape irrespective of its size. They normalise geometric quantities to enable comparison with other shapes through relative scaling unlike *shape factor*s. Normalisation is achieved by dividing the geometric quantity of the shape by the geometric quantity of its circumscribed envelope, which is conventionally a rectangle (Mirjalili & Pasini, 2007).

The *shape transformer* for a *petiole* of transverse-sectional area A, corresponds to the smallest rectangle, A_D that will enclose its shape (Figure 4).

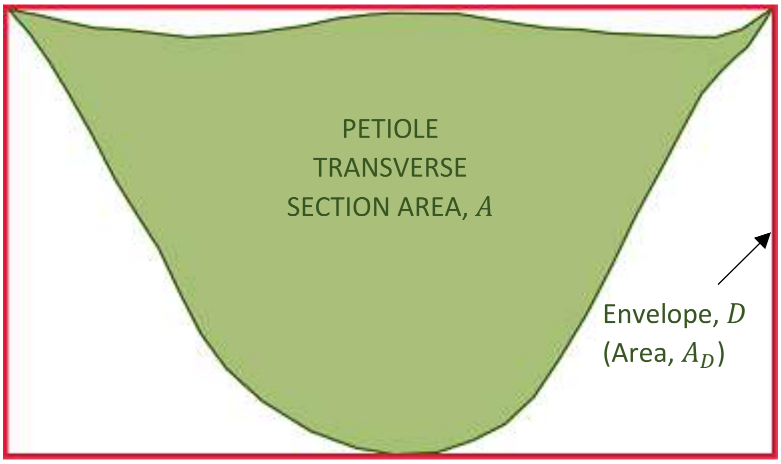

Figure 4 Profile of *petiole* transverse section, S, and circumscribed rectangular envelope, D.

An example of a *shape transformer*, ψ_A, is defined in equation (1) as the ratio of the area of the shape, A, to the area of the circumscribed envelope, A_D:

$$\boldsymbol{\psi_A = A/A_D} \tag{1}$$

Likewise, the *shape transformer*, ψ_I, is defined in equation (2) as the ratio of the second moment of the area of the shape, I, about its x axis to the second moment of area of the circumscribed envelope, I_D, again about its x axis:

$$\boldsymbol{\psi_I = I/I_D} \tag{2}$$

Please refer to the literature review for the explanation of the *shape transformer* for the polar second moment of area, ψ_{JT}, in equation (26).

To date, research on *shape transformers* applied to palm *petioles* has not been carried out, apart from that performed by the author (Windsor-Collins, et al., 2007a) and (Windsor-Collins, et al., 2008) on seven palm genus' using rectangular envelopes. In particular, no work has been done on palm *petiole* shape and its effect on the ability for the *petiole* to flex and twist which is surprising considering the ability of some to withstand hurricanes or to support the world's largest leaf. Palms have evolved over 120 million years, are one of the most diverse tropical families and have attained many firsts. In addition to supporting the world's largest self-supporting leaves, the longest unrooted aerial stem, the largest inflorescence, largest seed and the most easily transplanted living trees, "Palms achieve massive primary stature because of distinctive features of leaf development, stem vasculature and anatomical properties." (Tomlinson, 2006). This makes the likelihood of finding something special in the shape of the *petiole* all the more likely.

Furthermore, *shape transformer* development has been limited to shafts of circular and eccentric ellipses and box section cross sections, with no apparent research done on *shape transformer* development of other shapes, in particular, complex, irregularly shaped natural forms. Problems to address are warping factors and torsional constants both of which add to the in-preciseness in the comparative measurement of shape in relation to how it contributes to torsion and bending resistance.

To determine the direct effect of *petiole* shape on the overall palm *petiole* performance, *shape transformers* will be used. Through the process of normalisation, they enable shapes to be compared while keeping all other variables, such as size and material, constant.

1.3 Performance index methodology

The minimisation of mass is an important objective in the design of structures. *Shape factor*s can be used to assess the structural efficiency of a beam and make comparative analysis with other materials, natural and man-made, in addition to shape analysis. For a given mass, the stiffness of a structure is greatly determined by the shape and material of the structure. So if the dimensions of the object are restrained, then the ideal material is one with a high ratio of Young's modulus to density (Burgess, 2005).

Consider the design of a lightweight beam of length, L, where the objective is to maximise bending stiffness per unit mass. Equation (3) for bending stiffness design is:

$$\frac{F}{\delta} = \frac{c_1 EI}{L^3} \tag{3}$$

The load, F, per unit deflection, δ, which is the stiffness of the beam, equates to the product of the Young's modulus, E, the second moment of area of the transverse section of the beam, I, and the coefficient, c_1, depending on the boundary conditions, divided by the cube of the length, L, of the beam (Pasini, 2007).

The mass of the beam, m, is shown in equation (4) and is the product of density, ρ, area, A, and the length of the beam, L:

$$m = \rho A L \tag{4}$$

Substituting in *shape transformers* for I and A from equations (2) and (1) into equation (3)(3) and (4) respectively, gives equations (5) and (6):

$$\frac{F}{\delta} = \frac{c_1 E \psi_I I_D}{L^3} \tag{5}$$

$$m = \rho \psi_A A_D L \tag{6}$$

The design variables are then isolated and put on the right hand side of equations (5) and (6) to give the functional requirement, F', in equation (7) and the objective function m , the mass per unit length, L, of the beam in equation (8).

The prime symbol in F', is used to generate a variable for something that is similar, so it is used here as it is related to the load, F:

$$F' = \frac{FL^3}{\delta c_1} = E \psi_I I_D \tag{7}$$

$$m = \rho \psi_A A_D \tag{8}$$

However, equations (7) and (8) only apply when comparing shapes that have the same aspect ratio and do not require relative scaling i.e. the geometric quantities of the envelopes are the same.

A performance index, p_S, in equation (14) can be derived which best minimises the mass of the beam. The higher the performance index, the lighter the cross section. Consider the ratio of the functional requirement and the objective function in equation (9):

$$\frac{F'}{m} = \frac{E \psi_I I_D}{\rho \psi_A A_D} \tag{9}$$

The constants are grouped into the design requirement, F'' , the double prime being used because it is related to F' as in equation (10):

$$\boldsymbol{F''=\frac{F'A_D}{I_D}=\frac{FL^3A_D}{\delta c_1 I_D}} \tag{10}$$

By substituting the design requirement F'' into equation (9), equation (11) is obtained whereby $1/F''$ is constant:

$$\boldsymbol{\frac{1}{m}=\frac{E\psi_I}{\rho\psi_A F''}} \tag{11}$$

Equation (11) can now be used to find performance indices for three types of selection. Performance indices are made by keeping certain variables constant so for example, if co-selection of material and shape was required for a given design requirement ($1/F''$), the performance index, p, shown in equation (12) would be:

$$\boldsymbol{p=\frac{E\psi_I}{\rho\psi_A}} \tag{12}$$

If selection of a material was required for a given shape and design requirement, ($1/F''$), the performance index, p_m shown in equation (13) would be:

$$\boldsymbol{p_m=\frac{E}{\rho}} \tag{13}$$

If selection of a shape was required for a given shape and design requirement, ($1/F''$), the performance index, p_s shown in equation (14) would be:

$$\boldsymbol{p_s=\frac{\psi_I}{\psi_A}} \tag{14}$$

The above is true only for non-scaled sections as $1/F''$ would not be constant, which results from a variable ratio of A_D/I_D.

The derivation of the scaling factor to be applied to scaled sections is detailed in Chapter 2.

Shape can therefore be decoupled from the size of the shape through the equations and performance selection charts for which the input are the performance indices.

1.4 Motivation for the research

Shape transformer analysis enables pure shape data from structures to be extracted irrespective of size and compares shapes through normalisation. Comparisons of efficiency with respect to mass (for the 2D case, mass per unit length) between regular shapes and natural shapes for selection purposes in a particular design are made. A deeper understanding of how the individual components of structure work together is attained, the results of which are shown in this thesis. By isolating shape from material properties, size and the function of a structure, it is possible to see how shape alone influences the performance of natural structures. The torsion and bending efficiency of a shape is compared across transverse sections whose envelopes are non-proportionally scaled in the x and y orientations. This eliminates the need for individual scaling parameters to be calculated and applied to each shape. Improving the accuracy of the torsion *shape transformers* by replacing the torsional constant, $J_{T,}$ with the polar second moment of area, J, in a new *shape transformer* design is an integral part of this work. The research applies a modified, improved *shape transformer* method to palm *petiole* structure, the distinct and striking forms of which have fascinated botanists for a long time.

As the dry density, elastic modulus and modulus of rupture of selected arborescent palm stems increases with age (Rich, 1987), the same may be true of palm *petioles*. Following on from what Niklas (Niklas, 1992) says in that it is more easy to change geometry than the constituent materials in plants, shape rather than cell wall structure and chemical composition (to be later explained in section 2.2.1 and 2.2.5 of the Literature Review), may account for the higher strength, stiffness and specific gravity relative to that modelled for cellular solids. Shape as well as material are both significant contributors to the stiffness and rigidity of the palm *petiole*.

Only by researching the findings from internal structure, material properties and external shape, can a true understanding of the processes involved in the survival of the palm *petiole* in reaction to natural environmental forces and self-weight be achieved.

1.5 Aims and objectives

The aim of the thesis is to extend the knowledge of palm *petioles*, in particular, their physical performance by measuring their efficiency in withstanding environmental loads (known to exist in their natural habitat) and loads from self-weight. *Petioles* are subject to both bending and torsion and so the efficiency of both of them are studied individually, as well as the combined efficiency of torsion and bending. In addition to unknown facts about palm *petiole* structure and material, gaps in the knowledge exist for torsion efficiency performance indicators for cross sections other than elliptical and rectangular shapes and there is scope to improve the *shape transformer* and acquisition methods to increase the accuracy of the data and efficiency of data collection.

The objectives of the thesis are as follows:

1) Map the 2D and 3D distribution of vascular bundles in the *T. fortunei* palm *petiole* and relate to the stiffness of the *petiole*.
2) Relate the external profile of the *T. fortunei* palm *petiole* to its flexural and torsional stiffness through *shape transformers* and physical bending and torsion tests. This palm is readily available for material testing as it is not a protected species.
3) Design an effective and inexpensive method to obtain shape profiles of living natural structures with a measurement error of less than 1%.
4) Develop a *shape transformer* to reduce inaccuracies in the conventional *shape transformer* model.
5) Design a method to break down 2D shapes to smaller components to identify significant contributors of shape to bending and torsion stiffness.
6) Map the contribution of shape within the *petioles* of different species of *palmate* and *costapalmate* palm.

1.6 Structure of thesis

Four publications have been produced by the author of this thesis. This work is incorporated into the methods, results and discussion sections, becoming part of the narrative.

The chapter layout is as follows:

- Chapter 1 Introduction. The reasons why palm *petioles* were chosen as the subject for study are described here in botanical and environmental context together with a brief methodology for shape analysis and the aims and objectives of the work.
- Chapter 2 Literature Review. Topics follow the order of internal structure, material properties and shape which is continued throughout the thesis. This is preceded by a section on the background to palms.
- Chapter 3 Methodology and Methods. The following methods are novel and so are preceded by methodologies to explain the reasoning behind the methods: shape acquisition, bi-layered model, the *shape transformer* envelope and the associated shape edge mapping methods.

  Profiles of two dimensional transverse sections along the longitudinal axis of seven species of *palmate* and *costapalmate* palm *petioles* are imaged using a new profiling method. Shape data in relation to the functional requirements of the *petioles* are extracted and related to their environmental conditions for use in engineering design and biomimetics.

  Further to determining the material properties of a *T. fortunei* palm *petiole* and relating this to its shape, the internal structure of this heterogeneous and anisotropic palm *petiole* is modelled and related to its overall mechanical efficiency.

  The novel data collection procedure and theoretical method for processing the data has also overcome the problem of primary data masking as a result of natural variations in size, material, shape and aspect ratio. Part of this research methodology is to separate transverse section profiles into simpler components to identify significant performance contributors. *shape transformers* for bending and torsion efficiency have been introduced for sections of complex shapes using palm *petioles* as a case study.
- Chapter 4 Results and Analysis. The results of both the novel and conventional

methods employed in this research are presented here together with verifications of new techniques and statistical analyses.

- Chapter 5 Discussion. The discussion critically evaluates the significance of the results in relation to previous work and identifies further work.
- Chapter 6 Conclusions. The conclusions highlight the contribution to knowledge claimed in this thesis.
- Chapter 7 References. References to work referred to within this thesis including the four of the author's own publications
- Chapter 8 Appendices. The raw *petiole* profile data is here for all the palm sections and the subsequent processed images are included for a subset of the data, namely for the TfP (*T. fortunei* Proximal) section.

2 Literature review

2.1 Introduction

Herewith is a study of the literature related to the aims and objectives set out in the Introduction. Broadly speaking, these are to map the internal structure of the palm *petiole*, to measure its material properties and lastly to analyse the contribution of shape to its mechanical performance.

Biomimetics is the study of the structure and function of biological systems as models for the design and engineering of materials and structures. Vincent (Vincent, 2008), says that the intelligent use of structure, from molecules to ecosystems, not energy, creates exceptional functionality in plants and animals, driven by chemical composition and morphology derived from DNA. This is in line with Rich (Rich, 1987) who says that chemical composition of cell walls is more likely to change under environmental forces than cell and tissue structure. However, this goes against what Niklas (Niklas, 1992) says in that it is easier for a plant to change geometry than its constituent materials. In addition to the curious phenomena that take place at *boundary layer*s, Barthlott and Koch (Barthlott & Koch, 2011) say that a focal point in biomimetics is in the study of the many materials with micro and nano structures, so both structure and material are important avenues of research.

The subject of study in this thesis is the arborescent palm, the unique features of which are subsequently discussed.

2.2 Palmate palm petioles – structure to accommodate bending and twisting

The *palmate* palm *petiole* can be approximated to a tapered beam and is supported by a sheath which completely or partially surrounds the palm stem. According to Vogel, this promotes bending stiffness and low torsional rigidity if the layers of sheath can move relatively easily against each other (Vogel, 1992). The *vascular bundles* contained within may be likened to reinforcing rods embedded within concrete, sometimes separate, but they can also be fused together. They are set in a matrix of compressible *parenchyma* cells which in turn are surrounded by epidermis cells at the *petiole*/air interface (Figure 6 and Figure 7). The part of the *petiole* in closest proximity to a corrugated leaf blade is often elliptical in transverse section, allowing the leaf blade to rotate as the corrugations in the leaf blade hinder its rotation (Niklas, 1992).

2.2.1 Cellular structure of the petiole

Figure 5 shows the juxtaposition of the main tissues that can be found in a transverse section of a typical *monocotyledon petiole* for reference with items discussed below.

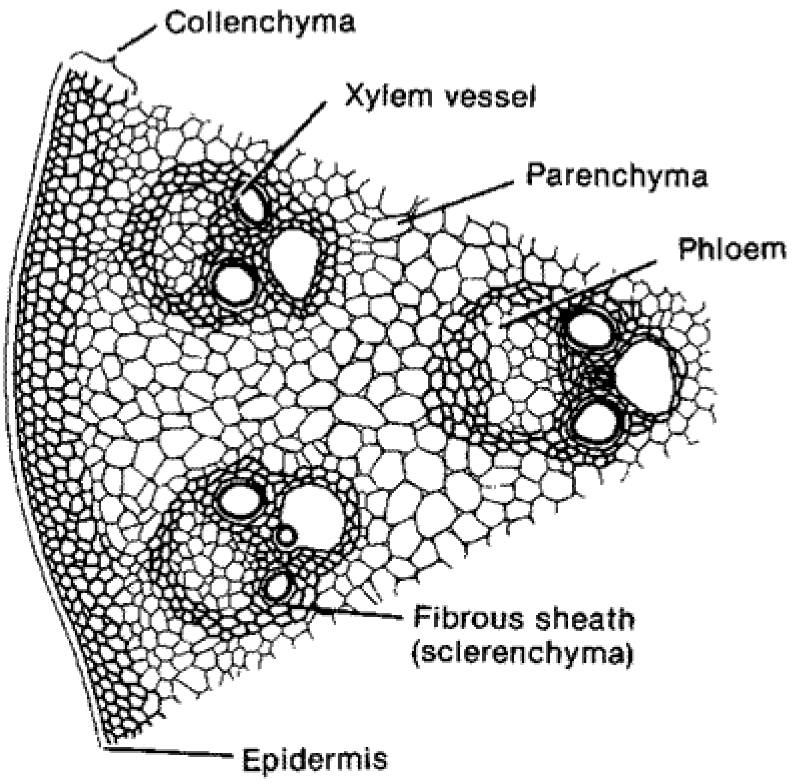

Figure 5 Diagram to show relative placement of *petiole* tissues

Petioles are comprised of the following cellular structures:

1) **Strong skin** – The epidermis (outer skin layer) and the layers of cells underneath this are thickened in some plants and this may be the case with palms. Palm leaves often are quite tough to tear, the question is if this results from a thick epidermis or lignified cells (Cutler, 2005).
2) ***Xylem*** – In addition to conducting water, the *vessels* and *tracheids* (both constituting the *xylem*) function mechanically. *Transpiration*, whereby water evaporates from the plant, has an effect of causing forces on the *xylem* which are counterbalanced by increasing the *xylem* wall thickening. Tracheids contain annular or helical thickening allowing for elongation while retaining lateral strength. Vascular bundles have an outer sheath of fibres. In the vascular bundles of *Monocotyledon*s, the number of *xylem* cells does not increase after maturity and in

palms in particular, this number is determined before the trunk starts elongating. The mechanical support from the *phloem* cells is small but the support from the associated fibres may be significant (Cutler, 2005). Tracheids are a fibre-reinforced composite whereby cellulose fibres are embedded in a matrix of lignin and hemi-cellulose as well as other polymers. The aspect ratio of softwood *tracheids* is about 75 compared to the hardwood *vessels* with aspect ratio of about 50, making softwoods, better at transferring stress longitudinally. However, these strength properties are influenced by moisture. Further research on the length of palm *tracheids* would shed light on their ability to transfer stress down the trunk and *petioles*.

3) **Fibres** – Their primary function is to provide strength. Lignin permeates the cellulose of the cell wall although these cells may remain flexible (Cutler, 2005).

4) **Lignified *parenchyma*** – Cells of this type make up the majority of strengthening tissue in bamboos (Cutler, 2005). Perhaps lignified *parenchyma* is present in palm *petioles*.

5) **Fibres and Composite Structures** – Extra xylary fibres can usually be found grouped as axial strands in the stem or bark and in leaves tracking the vein direction. They are grouped strategically in order to strengthen leaf margins and reinforce soft tissues having rod like forms. However, thick walled cells create a large demand for energy and in plants the distribution and amount has been very fine tuned to be efficient. The main veins act rather like ribs in a cantilevered structure (Cutler, 2005).

6) **Sclerids** – These are cells with very thick lignified walls. Together with fibres they form the *sclerenchyma*. Sclerids are shorter and may be branched, sinuous or just short with a fairly constant diameter. The longer sclerids can often be found sheathing veins especially at the end of the finer vein branches. With age, the outer part of the plant often becomes more sclerified (Cutler, 2005).

7) **Collenchyma** – Collenchyma is a sub-epidermal supporting tissue in leaf *petioles* and vein ribs formed before vascular differentiation. Collenchyma is primarily cellulosic and unlike fibres, grows with the surrounding tissue. Collenchyma is more flexible than fibre if it remains un-lignified. After the main growth has occurred in trees, collenchyma may become lignified in which case it would function much as fibres do (Cutler 2003). The natural polymer material with highest ratio of Young’s Modulus (in tension) to density is cellulose. It is higher than that of steel by a factor of about 2.5 which is due to the highly oriented state of semi-crystalline chains.

8) **Cellulose and water** – The cellulose surrounding cells is thin in growing tips and roots where water turgidity creates *turgid* pressure. When thick lignin becomes incorporated, it

strengthens the cells without having to make the structure *turgid*. As a consequence, the structure becomes heavier (Cutler, 2005).

2.2.2 Vascular bundle distribution within palm petioles

Vascular bundles (*VBs*) within palm *petioles* are comprised of *xylem* and *phloem* cells which are aligned with the longitudinal axis of the *petiole*. The *xylem* and *phloem* cells are conduits for water and nutrients respectively and are partially or wholly surrounded by hardened, lignified, *sclerenchyma* cells for which the only function is strength and support.

The arrangement of the *VBs* at the periphery of the palm stem are more parallel to the stem axis compared to the helically arranged *VBs* in the centre (Zimmermann & Tomlinson, 1972). A similar *VB* arrangement may be found within the palm *petiole*, an area for further research.

The diameter of *VBs* at the periphery of the stem of six rain forest arborescent palms, were found to be larger than those within the central core of the stem, forming a radial density and modulus gradient (Rich, 1987). However, the *VBs* of the *T. fortunei* palm *petiole*, show the diameter of *VBs* decreasing towards the periphery (Windsor-Collins, et al., 2008). The *VB* distribution and size gradient within the *T. fortunei* palm stem, is an area for future study to determine if the *VB* gradient is opposite to that of its *petiole*.

Micrographs of the transverse sections of a *petiole* from the arboresecent palm, *Chamaerops humilis,* show the spatial distribution of *VBs* within the *parenchyma* matrix, from which Gibson et al concluded that the *VBs* were uniformly distributed radially (Gibson, et al., 1995). However, looking at the section they refer to in their paper (Figure 6), it can be seen that the *VBs* are more concentrated nearer the periphery of the transverse section, in addition to being smaller.

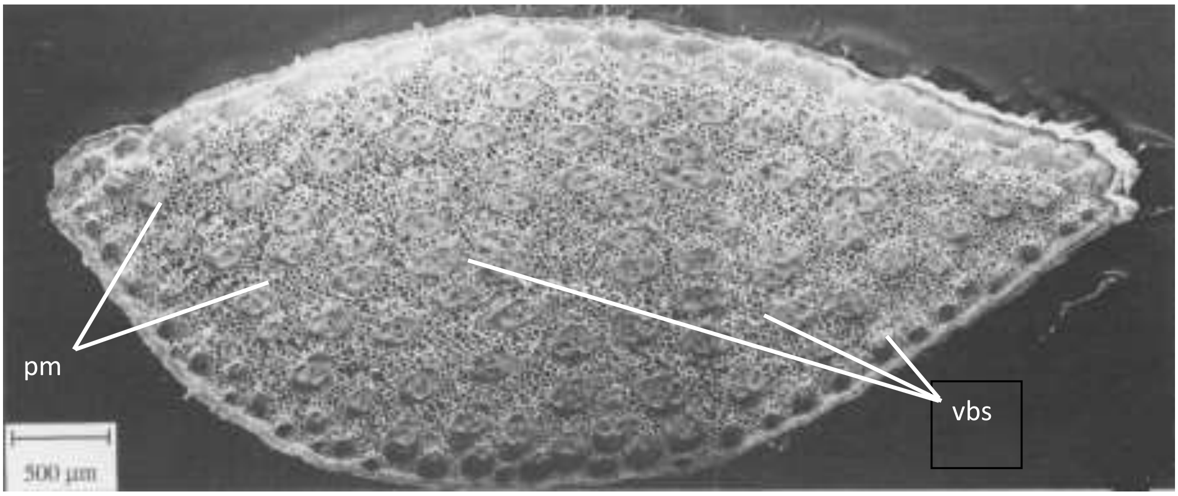

Figure 6 Micrograph of a *petiole* transverse section from the palm (*Chamaerops humilis*) showing the distribution of the vascular bundles, vbs, in the *parenchyma* matrix, pm, adapted from Gibson et al 1995.

The alignment of the longitudinal axis of the *VBs* and *parenchyma* cells are concluded to be parallel to the longitudinal axis of the *petiole* (Gibson, et al., 1995). However, in this paper the length of the longitudinal section observed was 1 mm, too short to observe changes over the whole length of the *petiole*. They may appear aligned over short lengths but in reality they may twist as do the *VBs* in many palm stems.

The *VBs* within the base of the *petiole* surrounding the stem, probably continue to provide structural support as the tree gets older. The tensile modulus of isolated dehydrated *VBs* is astonishing at about 100 GN/m^2 (Niklas, 1992) and on the death of the palm leaf blade, two centri-parallel layers of *VBs* remain. Later it was found that *T. fortunei* has three centri-parallel layers (Zhai, et al., 2011).

2.2.3 Structural gradients

Stiffness gradients within the fibre caps of *VBs* in the centre of the stem of the arborescent palm, *Washingtonia robusta,* were shown using Synchrotron X-ray diffraction and UV-microspectrophotometry (Figure 7 a). However, the fibre caps on the stem periphery were found to have constant high stiffness (Figure 7 b), with no gradient. The stiffness gradient prevents high local stresses between the *parenchyma* and the caps which may be beneficial for trunk dampening (Ruggeberg, et al., 2008).

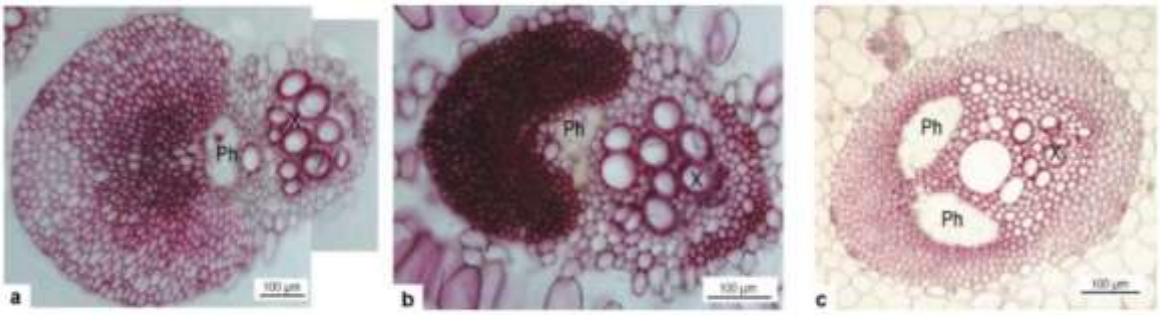

Figure 7 Cross-sections of a leaf trace from (a) the subcortical zone of the central stem of *Washingtonia robusta* (Mexican fan palm) (b) from the periphery of the stem c) *Vascular bundle* from a *petiole*. All sections are stained with phloroglucinol/hydrochloric acid. Ph, *phloem*; X, *xylem*. From Ruggeberg et al, (Ruggeberg, et al., 2008).

Figure 7 c shows a *VB* from the *petiole* having caps on both sides of the *VB*, making it stiff even though the caps are not as heavily lignified as the bundle in the stem periphery. No structural gradient can be seen within the cap, although the caps on either side do have different levels of lignification. The external shape the palm *petiole* will also contribute considerably to the high flexural stiffness of the *petiole* and although the caps are not as heavily lignified as in the stem, other strengthening materials such as cellulose may be present (Cutler, 2016).

The proportion of fibre in the *VBs* of *T. fortunei* were shown to be inversely proportional to the size of the *VB*. Young's modulus, E, and the tensile strength of the bundle also increases with decrease in *VB* size in the *T. fortunei* palm (Zhai, et al., 2011).

The leaf sheath of the *T. fortunei* is a convenient structure to obtain single strands of *VBs* as when the leaf blade senesces, or is removed, the fibres of the sheath remain while the *parenchyma* disappears. Three layers of fibres constitute the leaf sheath as shown in Figure 8. The fibre bundles in the middle layer had a larger diameter (418.0 µm) than the inner and outer layers (202.1 and 342.5 µm respectively), meaning that the middle layer had the lowest Young's modulus and tensile strength (Zhai, et al., 2011). However, the confidence intervals for the size of the *VBs* in the middle and outer layers mean that the data are indistinguishable, so it can only be said that the inner layer had *VBs* of smaller diameter and therefore greater tensile strength and Young's modulus. The bundles within the three layers could be traced to specific areas within the *petiole*, to indicate which bundles have the highest tensile strength and elastic modulus. It could be that the inner layer of the *T. fortunei* leaf sheath follows through to the outer layer of the *petiole*, an area for further research.

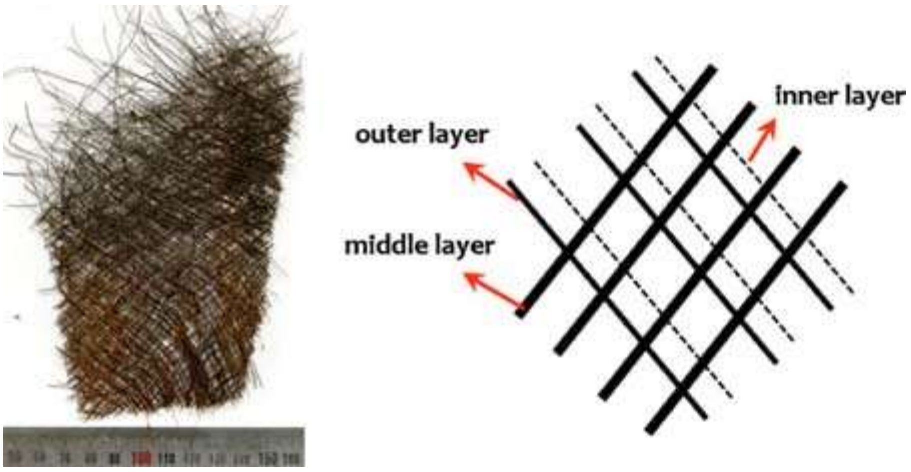

Figure 8 Leaf sheath taken from a *T. fortunei* palm. Left, a small piece of one sheet of leaf sheath with scale (cm). Right, a model of fibre bundle variance in one sheet of leaf sheath. The different layers of fibre bundles are characterized by differences in diameter, orientation and location (Zhai, et al., 2011).

Bending stiffness increases with graded structures. Wegst (Wegst, 2011) introduces the gradient *shape factor* which describes how much a plant's bending stiffness is increased through grading of the shape of structures. This is then used in combination with *shape factor*s in other hierarchical levels; the microstructural *shape factor* and the macroscopical *shape factor* to be used as a measure of overall bending performance as a result of shape only. *Shape factor*s are discussed in chapter 2.4 of this thesis.

Mechanical efficiency is the mechanical performance per unit mass and palms and bamboos perform exceptionally well as both are cellular materials reinforced with fibres. Density and modulus gradients increase the flexural stiffness of plants per unit mass, mass being a measure of metabolic investment into the construction of the organism. According to Wegst (Wegst, 2011), one of the main reasons for palms to have a high mechanical efficiency is because their fibres are aligned parallel to the stem, but in actual fact they are helically arranged in the centre and only on the periphery, are they more parallel to the longitudinal axis of the stem (Zimmermann & Tomlinson, 1972). This however will contribute to the mechanical efficiency but possibly with respect to torsion, even more so because the orientation of the helical bundles opposes one another.

2.2.4 Micro modelling

Materials from woods, palms and bamboos are among the most mechanically efficient, having composite and cellular micro structure whereby the cell walls are just composites. Gibson et al (Gibson, et al., 1995) analyses this microstructure using performance indices. The values for Young's modulus and relative density gives rise to their exceptional performance. The results from the model of the composite cell wall and the cellular structure in wood suggest that the lower the relative density of the material, the higher the mechanical efficiency of the material will be.

The *T. fortunei* palm *petiole* has a much more pronounced *VB* areal density and size gradient than the *Chamaerops humlis petiole*, so *VB* distribution varies significantly between palm species.

By increasing the volume fraction of fibres towards the periphery of a fibre composite cross-section, the flexural rigidity increases as long as the fibres are uniformly distributed. Although density and Young's modulus gradients are not utilised normally in engineering materials, this would be beneficial. However, thin walled sections do not benefit from this (Gibson, et al., 1995). The required uniform distribution of the *VBs* in the periphery of the transverse section may be linked with the uniform stress principle as notch stresses cause local failure.

The internal shape of cell walls if optimised (smooth) results in higher ultimate strength than if not optimised. Factors governing fatigue failure are not only alternating and mean stresses, load frequency, environmental conditions and macroscopic structure but also include microstructure geometry (Abad, et al., 2012). Periodic loading has a detrimental impact on the resistance of lattice materials. The unit internal cell wall shape effect on the fatigue strength of square and hexagonal lattices is determined using a method based on asymptotic homogenisation theory. It was found that cells with inner cell walls of continuous and minimum curvature geometry had better fatigue resistance compared to cells described by basic lines and arcs in bending dominated lattices. It was proved experimentally and theoretically using metallic and polymeric cellular materials, that if the insides of the cell walls are smooth, (optimised), the stress in the cell walls is distributed uniformly along the cell struts and these cells have higher yield and ultimate strength than those with non-optimised cell walls.

Parenchyma cells in palm *petioles* are roughly hexagonal. They are randomly arranged meaning that they are more like foams than lattices and because it is a natural material it is assumed that the internal cell wall shape is optimised. The smooth shape of the internal wall of the *parenchyma* cells in Figure 7c implies this.

2.2.5 Microstructure of biological hard tissues

The mechano-sensing system of live bamboo, its strength and its structure was investigated by Nogota (Nogata & Takahashi, 1995). They showed that living bamboo cells do not just respond to external mechanical stimuli, but that they sense information and can re-model hard tissue. As most of the *VB* contents are dead, collenchyma is the material for which this has the most impact as they are alive. As collenchyma cells are nearest the edge of the *petiole* and are comprised of thick cell walls this may allow the *petiole* to change its external shape.

The shape and structure of bamboo was analysed in relation to the forces which act upon it in its natural habitat. Like with the synthesis of bone on the application of stress, bamboo displays similar traits in that when stress is applied, a voltage is incurred and matter is deposited, so that uniform strength is maintained by re-modelling. Together with tension tests, the Young's modulus and density of very small sections of bamboo were measured along the longitudinal and radial axes and mapped. The macro structure of the bamboo was related to wind loading and the arrangement of the *VBs* was correlated with the photoelastic stress patterns around holes of similar shape and size in an infinite plate model under uniaxial tension. Bamboo was found to be graded and to have uniform strength radially, axially and transversely (Nogata & Takahashi, 1995). Relating the photoelastic stress pattern around a hole (representing the voids within the *xylem* and *phloem*) in an infinite plate model under uniaxial tension with the pattern of the *xylem* and *phloem* within the bundle, suggests that the direction of compressive stress correlates to the longest axis of the fibre bundle transverse section. Similar kinds of patterns in the palm *petiole* should be sought.

In order to determine how sensitive the bamboo was, external stress was applied to the bamboo and the induced biological signal was recorded on an electrocardiograph machine used for the human body. The machine was attached with adhesive paste. Electrocardiogram spikes observed during application of bending moments on the bamboo were thought to trigger adaptive growth related to the regions of stress as the higher voltage was recorded on the compressive side of the bamboo cantilever. As no signal was received from dead specimens, it was deduced that living plant material did not just respond to external mechanical stimuli, but that it senses information such that it can re-model hard tissue.

The first line of the Introduction states that “Examining some biological load carriers such as plant and tree stems, animal bones and other biological hard tissues, we see that their geometry changes under loading to match mainly stress- or strain-dependent requirements.” (Nogota and Takahashi, 1995). The word ‘match’ would be better replaced with the words ‘at least match’ as it is widely known, even at the time of writing the paper, that biological systems over compensate to be able to withstand stresses yet to occur. In a book called ‘Trees’ by Ennos (Ennos, 2001), the reasons for trees being pre-stressed is explained. “[…] wood is only about half as strong when compressed as when stretched, as the cells tend to fail along the so-called compression crease. […]. Trees prevent this happening to their trunks and branches by pre-stressing them”.

Fibres are consistently mentioned in the paper as the only support component of bamboo. However, sclereids (also part of *sclerenchyma*) and trachieds and *vessels* (from the *xylem*) also play significant support roles. Mechano-sensing can only occur in bamboo that is alive, as opposed to dead, and the fibres, when mature are dead according to (Mauseth, 2012). Therefore ‘fibres’ should be replaced by ‘vascular bundles’. *Sclerenchyma* provides the main structural support to a plant and its cells have thick lignified secondary walls and often die when mature. However, collenchyma cells have thin primary walls with some areas of secondary thickening. Collenchyma provides extra structural support, particularly in regions of new growth. Collenchyma, being alive, is therefore worth examining as a cell type where electrical signals are being induced, rather than the dead cells in the *VBs*, in particular the mature *VBs*.

The statement by Nogata and Takahashi in the results and discussion section (Nogata & Takahashi, 1995), “So, it is found that bamboo is a self-optimizing graded structure constructed with a sensing system of external mechanical stimuli; we may call this an intelligent adaptive modelling system” can be partly deduced from the data. It was proved to be graded laterally, but not vertically, as only two vertical sections were examined. It was also proved that when alive, bamboo responds electrically to external stimuli, but it cannot be deduced from the data that bamboo is self-optimising. In order to prove self-optimisation, tests must be done over several days / months and on several bamboo specimens.

The last sentence of the abstract (Nogata & Takahashi, 1995) where it states “It is concluded that a bamboo structure is designed to have uniform strength at all positions in both the radial direction on the transverse section and the lengthwise direction […]” is incorrect as the strength changes in both of these directions. The key errors with the article are as follows: more than two transverse sections should have been analysed to describe a gradual gradient of fibre density along the stem. The sample sizes along the cross section were too small as the *vessels* were of the same order of magnitude. More samples should have been taken so that the variation in the data could be observed. The Young’s modulus for the fibre was different to the stated value when using the Rule of Mixtures and the data from the graphs. The procedure for the calculated strength should be shown. The measured strength was said to be consistently 25 – 30 times as much as the calculated strength.

Electrical impulses produced by bamboo stems under stress can only do so within live cells as confirmed within this paper (Nogata & Takahashi, 1995). An examination into these growth areas deriving from live cells within the *VB* versus the relative contracted compressed woody cells also within the *VB* and resulting stress strain map requires further examination.

The authors (Nogata & Takahashi, 1995) suggest spending more time and money on developing functionally graded materials which are governed by uniform strength, which could be interpreted as uniform stress, it is unclear. This would be achieved by optimising the placement of structural fibres, microstructures, porous and cellular structures.

The shape of the *VBs* within palm *petioles* should now be examined as a result of this paper. It should be noted how eccentric the ellipse is to which the *VBs* could be approximated and if there are any trends in shape as a result of their placement within the *petiole*.

Wood toughness is greatly enhanced by the arrangement of the wood microfibrils. In the middle layer of the cell walls (called the S2 layer), the microfibrils are arranged at an angle of 20 degrees to the longitudinal axis of the cell such that they form a helix. This makes it hard to pull the fibres out of the matrix when stressed, making it tough. When wood is cut across grain, the cells do not break straight across, the cell walls buckle parallel to the fibres and the cell wall layers uncoil. This process uses a lot of energy, enhancing its toughness and making it one hundred times tougher than fibreglass (Ennos, 2001). Following on, this process occurs when the wood is subjected to lateral loads, effectively bending along the longitudinal axis. A different kind of toughness, fracture toughness, measures the resistance of a material to the propagation of a crack. If a material has high fracture toughness, and therefore has high resistance to the propagation of a crack, it may alternatively undergo plastic, ductile fracture. Brittle fracture is very characteristic of materials with low fracture toughness. One major advantage of wood is that it has high work of fracture (Ennos, 2013). Work of fracture is proportional to the square of the stress intensity factor (at which a thin crack in the material begins to grow) divided by Young's modulus.

Natural cellular materials e.g. palm all have low densities (0.1-1 mg/m^3) resulting from the high volume fractions of its voids. The prismatic shape of the cells of wood results in the stiffness and strength being higher along the grain than cross-grain (Ashby, et al., 1995). The relative mechanical properties for solid and micro-structured engineering materials are shown in

Table 2 (Burgess & Pasini, 2004):

Table 2 Microstructure - Equivalent mechanical properties between solid engineering materials and microstructures

Property	**Solid (*s*) Shaft**	**Micro-structured Material**
Density, ρ	ρ_s	**ρ decreases**
Radius, *r*	r_s	***r* increases**
Second Moment of Area, *I*	I_s	***I* increases**
Mass, *m*	***m***	***m* remains the same**

The second moment of area, *I*, increases with the square of the ratio ρ_s/ρ and as the strength and Young's modulus of the material decreases linearly with the ratio ρ_s/ρ, it means that micro-structure results in higher structural efficiency. The largest values of ρ_s/ρ can be found in very low density woods such as balsa wood where ρ_s/ρ is ten so it can be said that microstructure is beneficial in lower density wood. Hollow cells in plant material are usually hexagonal and about 50µm in diameter (Burgess S. P., 2004). Although microstructure results in lowering the bulk density as the material is placed away from the neutral axis, making the structure more structurally efficient, when a material is compressed, the altered microstructure matrix containing voids can make a material weak or buckle. Honeycomb structures in aircraft, layered materials allowing for internal slippage under stress without affecting the whole structure and air pockets in metal, reducing the overall density, are all examples are of engineering materials which have been constructed based on natural microstructure (Burgess & Pasini, 2004). According to Pasini and Burgess (Pasini & Burgess, 2002), wood is three times stronger in tension than in compression because the cells can buckle under axial load. However, because of pre-stressing, the wood is normally compressed, perhaps being the reason for this difference in strength.

2.2.6 Hierarchy in bio-structures

A paper by S. Ganeriwala on the relationship between morphology and mechanical properties of the tobacco leaf lamina showed that anisotropy and inhomogeneity are apparent at microscopic scale but at the macroscale, they look uniform (Ganeriwala, 1990). During stress-strain tests on two types of tobacco leaf, scanning electron microscopy showed uneven stress distributions and anisotropy in the deformed samples. However, 'the macroscale phenomenological results indicated a harmony in its mechanical behaviour'. Size hierarchy is therefore integral to the study of bio structures.

Structural hierarchy connects a point source to a much larger surface area. The higher the hierarchy, the more direct the load path will be, making it structurally efficient and reducing bending moments (Burgess & Pasini, 2004). As structural members are small in length in a hierarchal structure, there are fewer critical buckling loads and the load on each individual member is much less. One of the roles of the palm *petiole* is to accommodate the increase in number of *VBs* distally along the longitudinal axis of the *petiole*.

Generally, at every order of magnitude of size, in biology, there is a different hierarchical level. It was found that sizes around 1mm were mainly effected by material and those from 1mm to 10cm were more effected by structure. Above this length scale, communities were the main influence. (Vincent, 2008). This research suggests that by looking for alignment in structures, hierarchical levels can be identified. Splitting of the data into hierarchical levels in design is a method currently used for ease of manipulation of similar data. In engineering, the different levels of hierarchy correspond to heterogeneity. Usually, the smaller scale structure is destroyed and re-designed in a different way. Stiffness takes no account of hierarchy as it is not affected by size or scale. However, stiffness is affected by shape and in this research, shape is classed as hierarchical. One of the advantages of hierarchical structures is that they can have different functions at different length scales for instance, stiffness is controlled at nanometre levels and resistance to fracture (fracture toughness, the ability of a material containing cracks to resist fracture) at micrometre to centimetre length scales. These properties can therefore be independently manipulated. One of the main lessons to be learned is to introduce heterogeneity over a range of length scales. The volume fractions of data have been split and independently analysed. However, stiffness of the various volume fractions of composites can be isolated and controlled such as with the shear-lag model in nacre (Jackson, et al., 1988) developed for platey composites whereby the pull-out of the platelets is the main mode of failure. Interfaces are where the strain energy is absorbed when under tensile stress and the more hierarchal levels there are, the more interfaces there are. Strain energy can be absorbed at one hierarchical level to protect another hierarchical level from damage under that strain.

Only about 12% of engineering designs are fully based on the biological solutions to problems and this is a result of hierarchy in biological systems.

2.2.7 Tapering in long organs of plants

Shanley (Shanley, 1943) recognised the need for high strength to weight ratios for beams through tapering. There are major shortcomings in applying classical beam theory in the design of aeroplanes as the shear stresses caused by axial bending result in cross-sections moving out of plane. The shear beam which tapers in length was of special interest to designers at the time.

Some palm trunks are tapered and others are straight (Tomlinson, 2004). By observation, maximum tapering on a palm could reasonably be said to be half the width at the top compared to the bottom. However, some palms are thicker at the top, so material and internal structure must account for this difference (Fahn, 1990).

The tapering of tree branches produces a uniform stress distribution in the outer fibres, ensuring efficient use of material (Burgess & Pasini, 2004), which leads us to expect that the *petiole* form will also adopt uniform stress distributions (Windsor-Collins, et al., 2007a). The nature of the variant transverse sectional shape along the *palmate* and *costapalmate* palm *petiole* axis is one of the reasons for looking in depth at how its shape determines its performance. Palm *petioles* taper in cross-sectional area towards the leaf blade, usually having a groove or ridge(s) running along the top (upper) surface. They are roughly symmetrical about the vertical plane.

2.2.8 Adaptive structures

Tree trunks are usually tapered with adaptive growth creating the final form. The maximum compressive and bending stresses are found at the trunk/air interface and are determined by self-weight (effects of the gravitational constant, g) and bending loads, for example multidirectional wind forces. The outer fibres of trees are pre-loaded and bending stresses are superimposed upon this (Pasini & Burgess, 2002). Trees adapt their shape in response to stress, in particular compressive stress, resulting in living material being used in the most optimal way during growth. Optimisation occurs in the longitudinal and transverse shapes of structures and in the joints between the components of the structures. Palm *petioles* adapt to stress by changing certain aspects of their shape (Tomlinson, 2004), whether it is possible to identify the palm species by these shapes is a matter for further research and is discussed further in section 2.5.6 'Differentiating *petioles* by shape'.

Genetics limits the stem diameter of palms. However, there is evidence for adaptive growth in *petioles*, stems and roots in palms (Tomlinson, 2004). Tapering branches and trunks of trees in general, are a way of using the most efficient amount of material required for a uniform stress distribution on the surface (Tomlinson, 2004). As palm *petioles* can respond to compressive stress by adding material, then the shape of the *petiole* will reflect these stresses but it will also be influenced by the temporal torsional and bending forces on it for its survival.

The uniform stress postulate is an accepted design theory for natural section shapes subject to loading. The two ways in which biomechanical structures react and adapt to applied loads are through: 1) trial and error through better designs brought about accidentally (a slow process) and 2) adaptive growth through self-repair. Adaptive growth reduces the notch stresses and distributes the stress on the surface of a structure (Mattheck & Tessari, 2003).

Two Finite Element Methods (FEMs), Computer Aided Optimization (CAO) and Computer Aided Internal Optimisation (CAIO) have been developed to transfer biological optimisation mechanisms (adaptive growth and fibre placement) to engineering and design (Mattheck & Tessari, 2003). CAO simulates the principle of adaptive growth. Past stresses are replaced with thermal expansion in the computer program such that high stress causes thermal expansion and low stress results in the material being removed. The result is a homogeneous stress on the surface of a model. An example where this has been successful is with orthopaedic screws, designed to be free of notch stresses and achieving up to twenty times as much repetitive bending before dysfunction. CAIO determines optimum arrangements of fibres by making fibres coincident with force flow. For example, fibres bypass holes to avoid notch stresses. The performance of fibre placement is optimised with force flow to avoid shear stresses between fibres. The *VB* arrangement in palm *petioles* should be analysed in this context.

Although CAO and CAIO are able to mimic the adaptive growth caused by localised compressive stress, they model the entire 3D structure and individual factors may be overlooked. A method is required to break down the 3D structure into smaller components to identify significant contributors, an area of research in this thesis.

Branch and *petiole* shape is an important factor in withstanding external stresses. The diameter of tree branches is proportional to the wind load and the square of the diameter of the branch is proportional to the load as a result of self-weight. Growth rings are thicker on the underside of branch cross-sections because this is where the most compressive stress is situated and where most cells are produced. Elongated sections of branches are much better at support by a factor of ten compared to circular sections of the same cross-sectional area (Burgess & Pasini, 2004). The point at which self-weight and wind loading contribute equally to the load would result in the branches being circular in transverse section. Therefore, any increase in loading would be from self-weight only and would result in vertically elongated branches.

2.2.9 Pre-stressing

Pre-stressing in tree trunks and branches occurs by the relative shrinking of tubes of long thin-walled wood cells to adjacent cells. As new cells are formed, towards the outside of the trunk, they are fully hydrated and are joined to the adjacent older wood cells. During maturation, these new wood cells dry out, shrink and shorten. Because they remain attached to already shrunken cells in the inside it causes the more recent cells to become more tensioned as shown in Figure 9.

The result is the same effect as pre-stressing. If these cells were not pre-stressed, they would buckle across a compression crease when flexed. According to Zhai et al (Zhai, et al., 2011) the *VBs* of the inner layer of the *T. fortunei* palm leaf sheath (with a moisture content of between 8 and 10%) have a max tensile strength of 113.72 MPa and a Young’s modulus of 1249.70 MPa. The tensile strength of the main VB of the coconut palm leaf midrib is of the same order being 0.17 to 0.3 GPa (Niklas, 1992) which supports the value by Zhai et al.

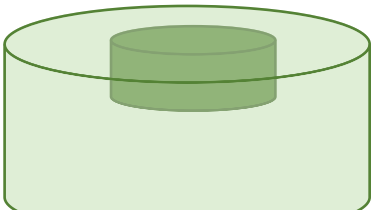

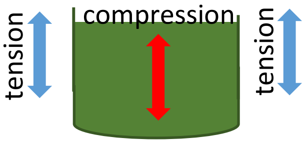

Figure 9 Pre-stressing in wood schematic

When a tree is flexed, wood cells on the concave surface are not compressed, but some of the pre-tension is released. Consequently, whole tree trunks were used by shipwrights for centuries for masts (Ennos, 2001). As palms often not vertical, they may have more pre-stressing than dicot trees. Wind is the most significant load on *dicotyledonous* trees and all their structural elements are cantilevers. Wind velocity typically increases with height from the ground and as the tree gets bigger with age, the loading also increases. The highest bending moments are where different structural elements join for example where the branches meet the trunk and where the trunk meets the ground, this latter junction being the largest bending moment. The self-weight of trees creates compressive forces on the trunk and if not vertical, it can cause the tree to buckle (Pasini & Burgess, 2002). Tall palms on the other hand are *Monocotyledon*s and are typically branchless. They are often not vertical, so it is possible that they counteract buckling by having more pre-stressing than *dicotyledonous* trees.

Sclerenchyma (which is the strengthening tissue) of the small plant, *Aristolochia macrophylla*, was tested for tensile strength over a series of loading and unloading cycles (Spatz, et al., 1999). Three types of deformations were distinguished from one another: elastic, viscoelastic and plastic. After the first cycle, the structure partially or wholly returned to its original state slowly. The reason for this was shown to be internal microstructural pre-stresses. A bi-phasic stress-strain relationship was found which is analogous to stiff fibres within a less stiff matrix. The stress strain plots show a distinct gradient change between the two phases, this being the case for many sample tests, even though the resultant elastic modulus varied by more than an order of magnitude. The first cycle shows plastic deformation, but subsequent cyclical loadings show very little plastic deformation, just elastic and viscoelastic behaviour. The elastic modulus also changed between first and second loadings, meaning that the material had changed. This was coincident with the change in orientation of the microfibrils in the *sclerenchyma* from 22° to 18° with respect to the longitudinal axis even after 24 hours. Polarized microscopy was used to image the microfibrils and this was confirmed with x-ray analysis. As the fibres and matrix are not strained equally when stresses are unloaded, it may be that the fibres become pre-stressed as the unloading follows a different path to loading causing the fibres to be in tension and the matrix to be in compression along the longitudinal axis.

Pre-stressing sometimes occurs in the same material in engineering by compressing locally. Although pre-stressing is common in engineering materials such as reinforced concrete beams, usually composite materials are used. In biological structures however, pre-stressing can occur within the same material. In some engineering structures, the material is locally compressed for example at the surfaces of some holes and shafts to create residual stress (Burgess & Pasini, 2004).

Pre-stressing in palm *VBs* makes them resistant to fatigue. Insight to fatigue may be gained from palm *petioles* as many *palmate petioles* survive tropical storms intact. Burman (Burman, 1998) has worked on sandwiching PMI foam and polymeric PVC materials between panels for the aerospace industry and concludes that a negative maximum stress to minimum stress ratio means that the material has much less resistance to fatigue. So, for that to happen in palm *petioles*, the maximum and minimum stresses must both be either positive or negative. *dicotyledonous* plants are pre-stressed caused by new layers of cells which are formed on the outside of stems and branches (in the cambium ring of *VBs*), adhering to the old layers of cells towards the inside of the stem. As the new cells dry out and shrink, they compress the older, inner layers, pre-stressing them because they are attached to them. In *Monocotyledon*s, there is no cambium ring of *VBs* at the periphery of the trunk or branch, instead, the *VBs* are spread throughout the *petiole*. As the *vessels*, sclereids, fibres and trachieds die, they shrink, so the *VBs* within which they are situated, may become pre-stressed and better able to resist compression relative to the surrounding cells. In the light of the Burman 1998 paper (Burman, 1998), it would be expected that minimum and maximum stress will always be positive as a result of pre-stressing within the *VBs*. There is ample literature on how this is achieved in *dicotyledonous* trees, but not on *Monocotyledon*ous trees. Periodic arrangements of cells are termed foams if they are randomly distributed and a lattice if systematically spread throughout the material. The *parenchyma* tissue in the palm *petiole* is more like a foam than a lattice as its cells are arranged randomly.

2.3 Torsional rigidity and bending stiffness of petioles

2.3.1 Material properties of the petiole – Young's modulus, strength and density

The juxtaposition of materials in wood accounts for its exceptional properties, not the individual material properties (Ashby, et al., 1995). There is nothing unusual about the cellulose in wood which has a Young's modulus, E similar to polythene and the lignin-hemicellulose matrix which has an E of about 20% of that of epoxy. Material property charts are a way of comparing properties of natural and engineering materials and performance indices are plotted on these charts, enabling the identification of applications for which each material is suited (Ashby, et al., 1995). Material property charts plot one material property against another (e.g. Young's modulus versus density) and performance indices are a combination of properties (e.g. the ratio of Young's modulus to density) which, when maximised, optimises some aspect of the performance of the material in a given application. In order to evaluate the efficiency of a material for a particular application, the performance indices are plotted on the material charts.

Natural materials show a high variation in properties which can vary within one organism, between organisms and between species (Ashby, et al., 1995). They are made from a small number of polymeric and ceramic components or building blocks, some of which are composites. In wood, the matrix comprises hollow prismatic cells amongst other shapes (Gibson, et al., 1995). Therefore, generally speaking, palms and *dicotyledonous* woods have a tensile Young's modulus, E, to density, ρ, ratio close to mild steel and it is in bending that palm and wood perform well in terms of their stiffness to density ratios. Ashby in (Ashby, et al., 1995), describes the material performance indices, M_1, M_2 and M_3 for the three modes of loading: tie in tension, beam in flexure and plate in flexure as shown in equations (15), (16) and (17) respectively:

$$M_1 = E/\rho \tag{15}$$

$$M_2 = E^{1/2}/\rho \tag{16}$$

$$M_3 = E^{1/3}/\rho \tag{17}$$

Palm and wood from *dicotyledonous* trees have high values of $E^{1/2}/\rho$ so can well resist both bending and elastic buckling and are better than most engineering materials (Table 3 and Figure 10).

Table 3 Modulus–density performance indices comparing palm to other natural materials and steel. Adapted from (Ashby, et al., 1995).

Material	E / GPa	ρ / Mgm^{-3}	M_1 / GPa(Mg m^{-3})$^{-1}$ for tie in tension	M_2 / GPa$^{0.5}$ (Mg m^{-3})$^{-1}$ for beam in flexure	M_3 / GPa$^{1/3}$ (Mg m^{-3})$^{-1}$ for plate in flexure (longitudinal modulus only as anisotropic)
Palm (*Iriartea*)	3.5	.15	23	12.5	10.1
Palm (*Welfia*)	11.0	.55	20	6.0	4.0
Dry coconut timber	7.0	.5	14	5.3	3.8
Single cellulose fibre	100.0	1.5	67	6.7	3.1
Teak	12.0	0.65	18	5.3	3.5
Pine	11.0	0.5	21	6.3	4.2
Plywood	8.0	0.6	13	4.7	3.3
CFRP Laminate	50.0	1.5	33	4.7	2.5
Mild Steel	210.0	7.9	27	1.8	0.8

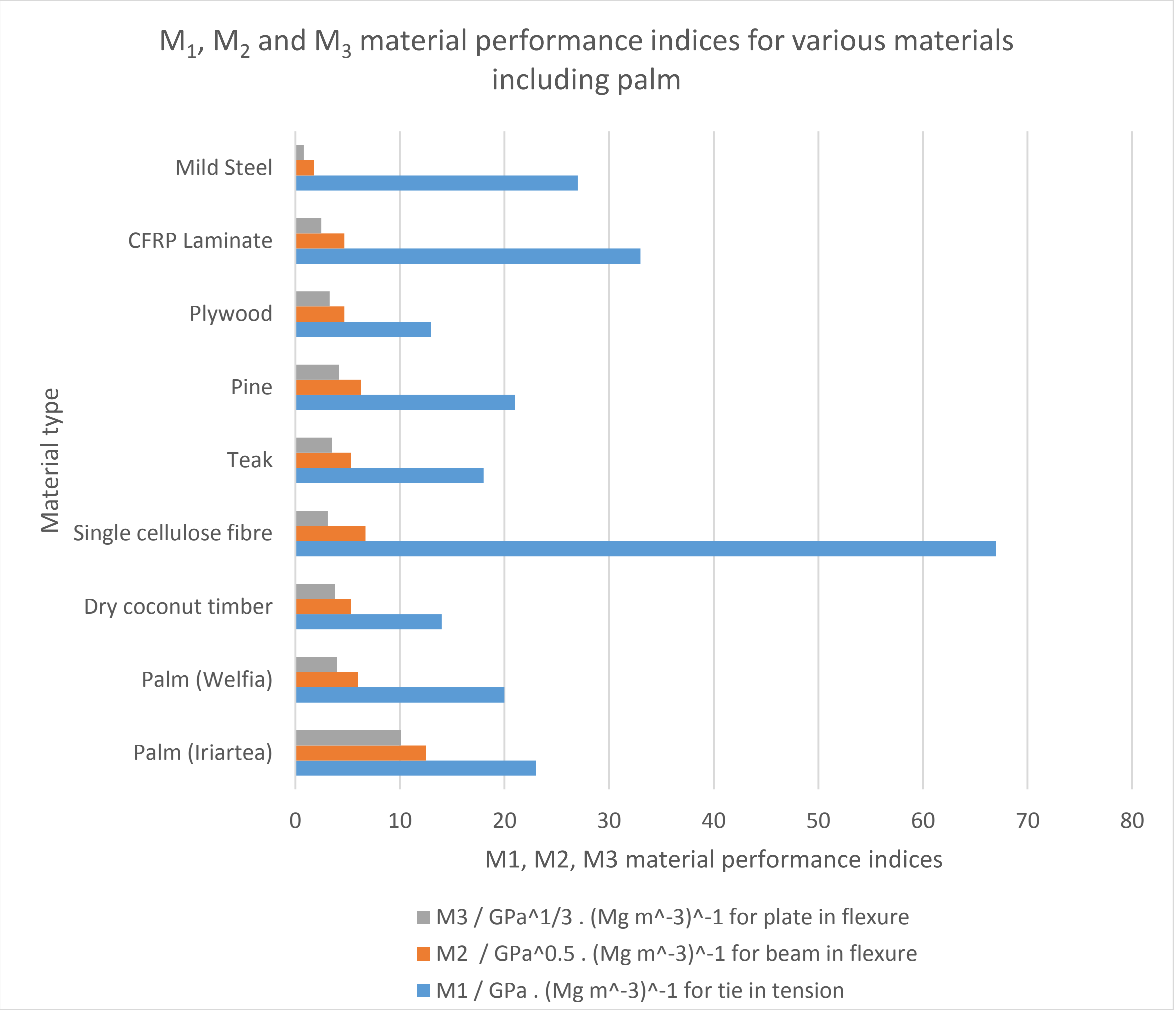

Figure 10 Material performance indices for different palm species compared to other materials commonly used in structural design

Late wood is three times the density of the early wood (Hunt, 2004). The oldest wood in palms is at the top of the tree as it grows from the base. Unless the palm trunk is used without it being sawn (apart from removing the roots and leaves), it is not used in building as it is too anisotropic (Tomlinson, 2004). To summarise, palm macro-material generally resists flexing and torsion efficiently compared to other woods and steel with respect to density.

2.3.2 Loading on leaf petioles and palm petioles

Self-weight and loads from wind are the forces that act on branches and trunks (Gibson, et al., 1995). However, from a personal communication with Professor Cutler (Cutler, 2016), rain (precipitation) loading may have more of a significant effect on the 'branches' or '*petioles*' of palms than wind.

Generally, wind loading on a tree increases with height from the ground and blows laterally. The wind loading, F_w, on a tree is a product of the density of the air, ρ, the drag coefficient, C_d, the frontal area, A_f and the wind velocity, v in equation (18):

$$F_w = 0.5\rho C_d A_f v \tag{18}$$

At high wind speeds when the Reynold's number is very high, the form drag is more significant than viscous friction (Burgess & Pasini, 2004). Reducing form drag is therefore something that the palm that survives hurricanes does well, by aligning the *petioles* with the wind (although turbulent) and by streamlining the wind over the leaf blades along the corrugations for example.

The compressive loading in the main trunk resulting from the weight of the tree is relatively small compared to that derived from wind loading (Burgess & Pasini, 2004). The total net effect of loading on branches in *dicotyledonous* trees does not usually result in any significant bending stress at the root of the trunk, but local bending stresses occur for instance where large horizontal branches join the trunk resulting from self-weight (Burgess & Pasini, 2004). The base of the palm '*petioles*' are supported by the harder older leaf bases (Tomlinson 1990) and so have a very different method of attachment to the trunk / stem. As a result of the non-vertical orientation of most branches, self-weight is an important contributor to the bending load (Burgess & Pasini, 2004). This applies to the longitudinal axis of the palm *petiole*. As *petioles* are situated high up on tall arborescent palms, significant bending stress at the root/foundation interface resulting from wind loading may occur compared to *dicotyledonous* trees with thicker, shorter stems.

The shape of the structure is of vital importance as well as material properties. In *palmate* palm leaves for example, the corrugated shape of the leaf blade enables the *petiole* to support a much larger weight than it would if the leaves were simple. The *petiole* functions in three main ways as follows (Table 4) to counteract loading, adapted from (Cutler, 2005):

Table 4 *Petiole* functions

	Function	**Consequence**
1)	Strong cantilever	To support the leaf which encloses *vessels* to transport water and nutrients.

2)	Arranges orientation of leaves	The *petiole* perhaps helps the leaf blade to track the sun.
3)	Allows leaf blade to twist	Elasticity helps its self-righting ability.

Usually, structural design in engineering involves designing for strength or stiffness (Pasini & Burgess, 2002). High strength and low stiffness enables flexibility which is useful when minimising the damage from forced convection. The axial groove on the upper side of some *petioles* allows high torsional flexibility and high resistance to bending. This is very effective in minimising aerodynamic loading which is proportional to the frontal area (Pasini & Burgess, 2002). Tensile loads are also important in high winds.

In the stipes of four wave-exposed seaweeds, it was found that 42 – 52% of the loading energy was dissipated during tension as a result of plastic and viscoelastic processes (Harder, et al., 2006). It was found that single material properties did not correlate with the size or habitat position of any of the four seaweed stipes (Harder, et al., 2006). However, the orientation of the samples taken from the stipes were always tangential in the outer cortex and always radial in the central medulla, so a representative selection of samples was not taken. The extent of the grading of material properties of plants can change with the age of the plant.

2.3.3 Twist-to-bend ratio

Flexural stiffness or flexural rigidity is a composite variable which measures the resistance to bending of a beam. It is a product of the material property, E, Young's modulus and the geometrical quantity, I, the second moment of area about the neutral plane of bending. Torsional stiffness or torsional rigidity is another variable that is composite but measures the resistance to twisting of a beam. It is a product of the material property, G, the shear or rigidity modulus and the geometrical quantity, J, the polar second moment of area about the axis of twisting (Vogel, 1992). Bending or flexural stiffness is therefore expressed as EI and torsional stiffness as GJ.

The *petiole*, representative of a cantilevered beam supported at one end by the stem is subjected to bending and torsion loads in its natural habitat. Both of these actions on the leaf blade usually occur simultaneously and so the ratio of bending stiffness, EI, to torsional stiffness, GJ, is a shape performance measure of interest where E is the Young's modulus, I is the second moment of area, G is the rigidity modulus and J is the polar second moment of area.

The ratio of resistance to bending to resistance to twisting of a structure is expressed as EI/GJ which for convenience is called the ‘twist-to-bend ratio’, which is easier to say than ‘resistance to bending to resistance to twisting ratio’. A structure with a high $EI\!:\!GJ$ can therefore twist more than bend and a low value [of less than one] indicates that the structure can bend more than twist (Vogel, 1992). This is a dimensionless index and so is independent of the size of the structure. Therefore, structures of all different sizes may be compared using the twist-to-bend index.

2.3.4 Twist-to-bend ratio in palm petioles

According to Vogel (Vogel, 1992), free standing palm *petioles* twist more than bend with a twist-to-bend ratio ranging from 2.2 to 7.7, the twist-to-bend ratio, increasing the less circular a shape becomes.

Separate *VBs* enable torsion in *petioles* (Ennos, 1993); (Ennos, et al., 2000). According to Isnard and Rowe (Isnard & Rowe, 2008), to maximise bending stiffness the *VBs* were concentrated around the perimeter of the cross-section. Isnard and Rowe go on to say that because the bundles are separate, it follows that the *petiole* of *Plectocomia* has a low resistance to torsion. However, it can be seen in Figure 11 that all the bundles in the climbing palm stem of *Plectocomia,* are not separate longitudinal strengthening elements but are connected together forming a tube, which is the best structure for resistance to torsion. The ability of free standing palm *petioles* to twist more than bend could therefore be more of a consequence of their macro shape and macro internal structure, an area for further study in this research.

Figure 11 Light micrograph of transverse section of rachis (R1) of *Plectocomia himalayana*, with outer rind of *VBs* (Bar = 1 mm) (Isnard & Rowe, 2008)

2.4 Shape factors – separating shape from size

2.4.1 Models, dimensional similarity and structural indices

In 1943, results from small scale models took precedence over structural indices, but at very small scales sheet metal could sometimes be impractically thin and time consuming to make with the design of very small rivets and screws. For small structures in particular, the use of dimensional similarity was encouraged by Shanley (Shanley, 1943), whereby each dimension is multiplied by a numerical factor to predict strength, stiffness and behaviour.

Structural indices were guides only, based on ideal conditions, after which the structure would be easily converted to practical dimensions (Shanley, 1943). Shanley states that "…if the original structure happened to be the most efficient type for the particular conditions involved, the expanded structure would also represent the optimum type for the new conditions". This highlights that it was not known at the time that structures behave in different ways at different length scales depending on their mass.

Structural indices used by Shanley were for the shapes of 3D structures readily available from the manufacturers and comparisons could not be made between structures from different structure shape families.

2.4.2 Merit indices – objectives and constraints

The selection of material and cross sectional shape for a load bearing engineering component depends on its functions, objectives and constraints. Its function may be transmitting torque or carrying bending moments for example. Its objective is to minimise or maximise something for example minimising weight and/or cost or maximising safety. Function and objective limits are both subject to constraints which may be geometrical (as in fixed dimensions) or functional (such as safety factors and cost limitations) (Weaver & Ashby, 1996).

The paper by Ashby (Ashby, 1991) provides a procedure for the selection of section shape and material of load bearing components for a particular mechanical purpose (torsion, bending and axial loading) with aim of optimising a performance criterion such as mass, volume or energy storage. However, the shapes compared were only those commonly available such as solid sections, tubes and I-beams and the material varies in the way of density, modulus and strength.

Merit Indices, combining material properties and shape show the relative performance in shafts, beams and ties. These Merit Indices are upgraded by Ashby et al in 1995 as shown in section 2.3.1 of the Literature Review (Ashby, et al., 1995) and defined in equations (15), (16) and (17)

2.4.3 Shape factors for structures dimensionally constrained

Ashby in 1991 (Ashby, 1991) defined four *shape factor*s to isolate shape from material and to find the direct contribution of shape only. They are dimensionless and have a value of one for beams or shafts of solid circular sections. They are for elastic bending, φ_B^e (equation (19), and torsion, φ_T^e (equation (21)), and for failure in bending, φ_B^f, and torsion, φ_T^f which are irrelevant for this thesis. The *shape factor* for elastic bending may be as high as 30 for shapes such as thin walled tubes or slender I-beams (Ashby, 1991).

Later in 1996, Weaver and Ashby defined a further *shape factor* for buckling, resulting from compression (Weaver & Ashby, 1996). They found that in the early stages of design, the maximum values for *shape factor*s are very useful to allow comparison of performance of [some] combinations of material and shape.

*Shape factor*s for elastic bending of beams and elastic torsion of shafts are derived in the next section.

Bending *shape factor*s and material indices by Ashby (Ashby, 1991) are developed by Burgess (Burgess, 1999) so that beam height dimensions are constrained. Likewise, torsion *shape factor*s and material indices are developed so that shaft diameter dimensions are constrained, both useful functions in integrated machinery where space for components is specified. Constraining the height of the beam or the diameter of the shaft has a significant effect on the optimal selection of material and shape.

In addition to reducing cost and impact on the environment, lowering the mass of beams and shafts increases performance such as increasing natural frequency (which changes the dynamic characteristics of the structure) and lowering inertial loads.

2.4.3.1 Constrained height in beams

As soon as the stiffness requirement reaches a certain level as a result of the height constraint, the constrained optimisation is sub-optimal compared to the un-constrained optimisation (Burgess, 1999). This stiffness requirement depends on the material of the structure for example, aluminium reaches the height at much lower stiffness than steel because of its lower density. It also depends on the section shape. Another objective function and *shape factor* are therefore required for the restrained height and the *shape factor*, $\varphi^{e}_{B(h)}$, which is equal to one for solid circular beam, is shown in equation (19) It differs from the *shape factor* for unconstrained elastic bending as it contains the height constraint, h. The second moment of area, I, is usually approximated to simplify the calculations (Ashby, 1991).

$$\varphi^{e}_{b(h)} = \frac{16I}{h^2A} \tag{19}$$

Unlike the unconstrained *shape factor*s, when constrained by height many become a constant value for a given type of cross section. The only sections where there is more than one design solution are I, H and T sections and open walled rectangular and elliptical sections, resulting from the dependency of the *shape factor* on the ratio between the overall width and web thickness (Burgess, 1999).

The highest performance index for restrained height, shape and material, MS, is shown in equation (20) and what was found was that constrained height results in lower efficiency as it limits the second moment of area, I.

$$MS = \left(\frac{E}{\rho}\right)\left(\varphi^{e}_{b(h)}\right) \tag{20}$$

It was found that higher density materials perform better in constrained height structures.

As it is not possible to directly compare unconstrained to constrained *shape factor*s, the complete objective functions have to be used for comparison.

2.4.3.2 Constrained diameter in shafts

Burgess (Burgess, 1999) derives torsion *shape factor*s and material and shape indices for constrained diameter shafts.

As soon as the stiffness requirement reaches a certain level as a result of the diameter constraint, the constrained optimisation is sub-optimal compared to the un-constrained optimisation. This stiffness requirement depends on the material and shape of the structure for example, aluminium reaches the diameter at much lower stiffness than steel because of its lower density. It also depends on the section shape. Another objective function and *shape factor* is therefore required for the restrained diameter and the *shape factor*, $\varphi^{e}_{T(d)}$, which is equal to one for solid circular shaft, is shown in equation (21). It differs from the *shape factor* for unconstrained elastic torsion as it contains the diameter constraint, d (Burgess, 1999).

$$\varphi^{e}_{T(d)} = \frac{8K}{d^2 A} \tag{21}$$

Unlike unconstrained *shape factor*s, when constrained by diameter, many become a constant value when the cross section is scaled in thickness alone.

The only sections where there is more than one design solution are for the hollow rectangular and elliptical sections, resulting from the dependency of the *shape factor* on the initial ratio between the overall width and height.

The highest performance index for restrained diameter, shape and material, $MS(d)$, is shown in equation (22) and it was found that constrained diameter results in lower efficiency as it limits the torsional second moment of area, K (Burgess, 1999).

$$MS(d) = \left(\frac{G}{\rho}\right)\left(\varphi^{e}_{T(d)}\right) \tag{22}$$

As with height constraints in bending, it was found that higher density materials perform better in constrained diameter structures, this time because density is relatively highly weighted in the material index.

As it is not possible to directly compare unconstrained to constrained *shape factor*s, the complete objective functions have to be used for comparison. The objective functions show that mass increases with the square of the diameter constraint. This is overcome by *shape transformers* described in chapter 2.5 of the literature review

As with height restraint *shape factor*s, a problem with constrained diameter *shape factor*s is that they have to be especially derived for each cross section type.

2.4.4 Micro shape factors

Ashby (Ashby, 1991) explains that both microstructure and macrostructure when combined provide very efficient structures. The total *shape factor* is the product of the micro *shape factor* and the macro *shape factor*. The micro *shape factor* for elastic bending is the ratio of the density of the solid part of the microstructure to the overall density of the macro structure. An example is made of wood whereby it has a micro-*shape factor* of 15. Ashby says that if wood is shaped into an I-section, box section or tube (with a macroscopic *shape factor* of about 10), the combined *shape factor* could be as high as 150, higher than any simple shaped section available to an engineer at that time. The assumption is that wood is homogeneous and isotropic, which is not the case, but that is not to say that homogeneous isotropic material can be made. Ashby goes on to say that *shape factor*s for wood should be made transversely and longitudinally to the grain of the wood to allow for anisotropy. Later in 2004, Burgess (Burgess & Pasini, 2004) states that micro *shape factor*s allow us to determine the relative strength of different woods independently from any specific loading and show how bending strength increases with beneficial microstructure. It is possible to obtain equivalent density, stiffness, strength and area of a material as well as micro *shape factor*s for bending stiffness, torsional rigidity, bending strength and torsional strength. Some natural materials (e.g. bamboo) have both a micro and macro shape whereby the combined *shape factor* is the product of the micro and macro *shape factor*s. However, material shape indices are used for solid material properties (Burgess S. P., 2004).

2.4.5 Shape factor scaling of beams of rectangular cross section

Pasini, Burgess and Smith (Pasini, et al., 2001) introduce q, the non-proportional scaling parameter to calculate the performance index in bending for rectangular cross sections that are scaled differently to each other horizontally and vertically are of different materials. A graphical method is introduced to optimise mass and bending stiffness, k. It was still not possible to separate Young's modulus, E from the second moment of area, I; a project for future work.

For the first time non-proportional scaling of rectangular cross section beams is incorporated into performance indices for material and shape selection of beams. This is opposed to only either vertical or horizontal scaling, or proportional scaling of the cross section of beams of different materials for comparison (Pasini, et al., 2001).

The paper introduces the shape envelope dimensions, D and shape, S, as design variables such that when the performance index, p, is a measure of mass efficiency, it is expressed as a function of four parameters: function, F, size, D, shape, S, and material, M in equation (23).

$$p = f(F, D, S, M) \tag{23}$$

The paper was only concerned with D and M as variables as the shape remained rectangular and the function was that of resistance to bending of a cantilever beam subjected to an end load. In the performance index for material and shape whereby mass is minimised, the D for horizontal, vertical and proportional scaling is represented as a power of Young's modulus, E. The aim of the paper was to find q, which is a function of D to create the non-proportional scaling performance index. Two linear multipliers, u and v are defined as the relative change in width and height respectively between cross sectional envelopes of different materials. The new performance index, p, for low mass and high bending stiffness is related to Young's modulus, E, density, ρ and q which is a function only of the scaling vector of the two rectangular cross sectional envelopes of different materials being compared in equation (24), where q is defined in equation (25).

$$p = E^{q} \rho \tag{24}$$

$$q = \ln uv / \ln uv^{3} \tag{25}$$

A new graphical way of determining the stiffness performance index of a rectangular beam was also presented whereby the cross sections of rectangular beams of the same material could be compared, which was not possible with the performance index, p, in equation (24). This is because the constituents of q, (u and v), were multipliers of the rectangular cross section dimensions. Height was plotted against width and two curves, one for constant mass (which was represented by area in this case) and the other for constant stiffness (the product of E and I) were plotted. Areas between the curves refer to co-ordinates of optional shapes of same bending stiffness with lower mass. In 2001, when this paper was written, Pasini et al states 'However, in stiffness design (unless some assumptions are made about the dimensions of the cross sectional shape), the second moment of area, I, is not separable from the material property (E). Young's modulus determines the space that cross-sections must occupy in order to meet the functional requirement, k'. Further work must be done to be able to separate E from I.

2.4.6 Designing shape factors

Bouwman et al (Bouwman, et al., 2004) calculates how to find the optimal combination of *shape factor*s to describe granule shape. There are many types of *shape factors* and it is possible to design shape *factors* in 2D and 3D.

In a paper by Bouwman et al (Bouwman, et al., 2004), the optimal combination of *shape factor*s to describe granule shape and roughness are identified including two new *shape factor*s; the projection *shape factor* and a new mass *shape factor*.

Eight different *shape factor*s were analysed with the aim of differentiating between granules made of one of four types of material. These were aspect ratio, circularity, e_R (a combination of circularity and aspect ratio), radial *shape factor*, One-Plane-Critical-Stability (OPCS), Stoke's *shape factor* and the two new *shape factor*s for projection and mass. The roughness factor, R, which is not a *shape factor*, was also defined. Different parameters are required to describe roughness and shape otherwise they are indistinguishable, so protrusions in the surface of less than 60μm were defined as roughness as opposed to shape. All of the *shape factor*s defined in the paper, excepting e_R, ranged in value between zero and one where one represented a sphere. e_R, ranged from one, again the perfect sphere, to negative infinity which corresponded to extreme elongation or rough shapes.

Various *shape factor*s resulted in problems; the aspect ratio could not distinguish between circles and squares, circularity had problems with measuring the perimeter of the shape as a result of the 'Coastline of Britain Problem' and the radial *shape factor* does not apply to re-entrant features. However, the new projection parameter overcomes the perimeter measurement problem by projecting the image of the shape using lines originating at the centre of gravity, projecting out every five degrees. The perimeter is taken as the smooth perimeter eliminating the effect of roughness.

The Stoke's *shape factor* analyses the 3D image as opposed to the 2D image and measures the sedimentation velocity of the granules relative to the velocity of spheres of the same mass and volume. Mass is compared with the projected 2D image to create another 3D *shape factor*. 2D and 3D *shape factor*s can therefore be designed from any variable / parameter that is of interest. It was found that for the purposes of differentiating between granules, that circularity and the projection *shape factor* were fit for purpose.

Thomas and Qidwai's paper (Thomas & Qidwai, 2004) shows a method for developing a *shape factor* to combine independent subsystem variables, to reduce redundancy in subsystem materials and functions.

By combining independent functions of a shape into one entity, it is possible to improve the system performance in a way that is not possible by optimising each subsystem variable. The paper by Thomas and Qidwai (Thomas & Qidwai, 2004) describes the procedure to design indices to look at the effect of the individual composite component's geometry and properties on the overall system performance. First the design requirements have to be defined, then an objective function has to be developed, the free variables identified, a constraint equation using equalities or non-equalities must be developed and finally, obtain an expression for the cross section which is modulus weighted, using *shape factor*s in terms of the free variables. After substituting this parameter into the constraint equation, solve it for the free variables and then substitute this into the objective function. The objective function is then regrouped into independent variable groups to express the design objectives and lastly the index is maximised or minimised to optimise the performance of the component. Log-log plots can then be used to rank various composite designs.

A problem with *shape factor*s is that they have to be specifically derived for each cross section type which is very time consuming and makes comparison very difficult if at all possible.

2.5 Shape transformers, performance indices and the torsion scaling problem

Figure 10 shows that palms and woods have performance indices for beams and plates in flexure equal to or greater than nearly all engineering materials (Ashby, et al., 1995). Palms are therefore worthy of shape transformer analysis, although this is challenging for natural shapes as discussed in the following subsections of this chapter.

2.5.1 Shape transformers – the use of the envelope to normalise shape

Area, second moment of area and polar second moment of area are geometric quantities of 2D shapes that can be normalised by dividing these by the same quantities of the circumscribed rectangular envelopes. The resulting *shape transformers* are described in equations (2), (1) and (26) below where ψ_{JT} is the torsion *shape transformer*, J_T is the torsional constant of the shape and J_{TD} is the torsional constant of the circumscribed rectangular envelope (Singh, et al., 2011). The methodology of *shape transformers* is explained in section 1.2 of the Introduction.

$$\psi_{JT} = \frac{J_T}{J_{TD}} \tag{26}$$

Using these *shape transformers*, the geometrical properties of shapes are being compared to the geometrical properties of rectangles.

shape transformers are different to *shape factor*s in that they normalise the shape for the purposes of comparison. These enclosed shapes may be solid, hollow or have re-entrant features. *shape transformers* range between the values of zero and one.

2.5.2 Performance indices with no scaling applied

In a paper by Pasini, Smith and Burgess (Pasini, et al., 2003), the envelope efficiency parameter, λ_{IA}, is introduced for beams in bending. Rectangular and square envelopes are used to plot the mass-efficiency of shape whereby *shape transformers*, ψ_I and $\psi_A$are plotted against each other (Figure 12). Only rectangular envelopes with the same aspect ratio are plotted here as they cannot be relatively scaled at this point.

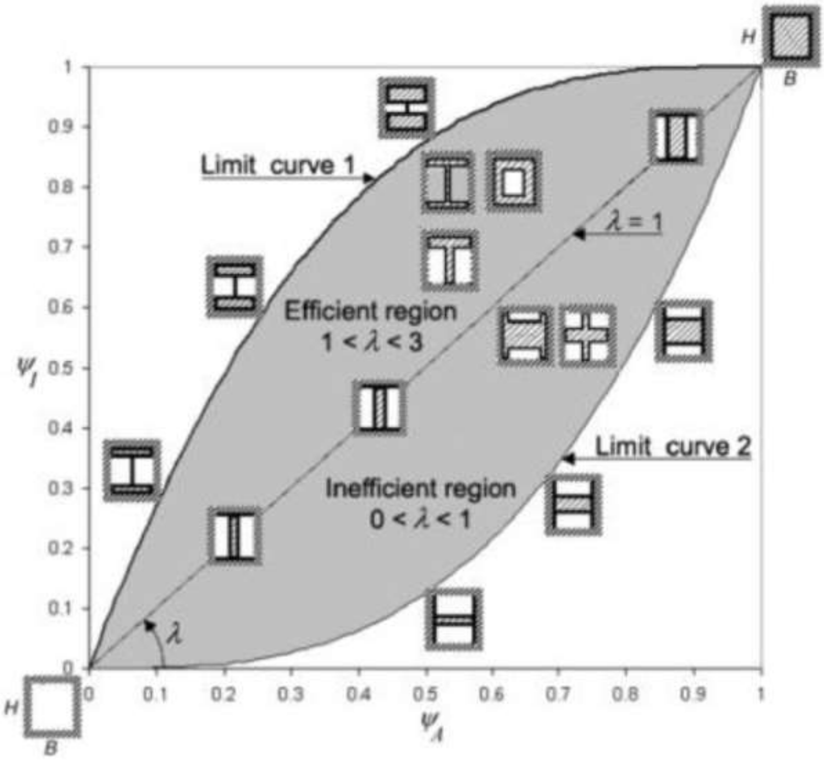

Figure 12 Rectangular envelope efficiency map where the grey region depicts the area where all cross sectional shapes that are surrounded by the same rectangular envelope, lie. The bisector divides mass-efficient shapes from inefficient shapes when used as cross sections of cantilevers for bending (Pasini, et al., 2003).

An envelope efficiency parameter, λ_{IA}, is introduced for the structural efficiency of beams in terms of two *shape transformers*, ψ_I and ψ_A (equations (2), (1) and (27)). These *shape transformers* are the ratio of the area and second moment of area of a transverse section of a beam to the same of the smallest rectangle that will enclose that section shape (Pasini, et al., 2003). This rectangular area is called the rectangular design space.

$$\lambda_{IA} = \frac{\psi_I}{\psi_A} \tag{27}$$

λ_{IA} varies between zero and three for the rectangular envelope and between zero and two for a square envelope. The envelope efficiency parameter, λ_{IA}, therefore depends on the shape of the envelope as well as the shape of the section within it.

The mass-efficiency of currently available standard cross sections subject to bending are shown on a structural efficiency map (Figure 12) for rectangular envelopes, where all of the shapes are bounded by two curves: one is the limit for cross sections with mass as far away from the neutral axis as possible, and the other curve is the limit for cross sections where the mass is as close to the neutral axis as possible. The graph bisector where λ_{IA}=1, divides the efficient from the inefficient shapes with respect to the efficiency of the solid rectangle, so the higher the gradient the more efficient the section.

Cross sectional shapes within a given class, for example, the hollow ellipses, have their own range of ψ_I, ψ_A and λ_{IA} depending on the thickness of the ellipse wall and have their corresponding efficient and inefficient regions. They all lie within the two aforementioned limiting curves labelled 'Limit curves 1 and 2' in Figure 12.

When ψ_I is the same as ψ_A for a shape, it means that when compared to the smallest rectangle that can encapsulate the shape, the shape is not more or no less mass-efficient than the rectangle by way of changing the shape. Efficiency maps could be made for envelope shapes other than rectangles and squares as seen in this paper.

All of the above shapes are encapsulated by rectangular envelopes of the same size, but to meet particular stiffness requirements in particular design spaces, the sections need to be scaled using the scaling parameter, q (Pasini, et al., 2001). The placement of the two limiting curves on the efficiency maps vary depending on the aspect ratio of the encapsulating rectangular envelope.

The above analysis applied only to beams bending elastically, calculations for other loading conditions are for further research.

2.5.2.1 Bending stiffness modelling

When the objective is to minimise the mass of the beam, equation (28) shows its relationship to the performance index λ_{IA} in equation (27) for the shape bending stiffness mass-efficiency of a section of uniform and isotropic material (Pasini, 2007). The higher the bending stiffness efficiency parameter, λ_{IA}, the lighter and stiffer the cross-section is in shape bending. This assumes a constant Young's modulus, E, density, ρ and I_D/A_D (the ratio of the second moment of area to the area of the envelope) between the samples being compared. These equations apply to non-scaled cross sections only.

$$\frac{bending\ stiffness}{mass} = \frac{EI}{\rho A} = \frac{EI_D\psi_I}{\rho A_D\psi_A} \tag{28}$$

The stiffness and buckling load of a laminate plate with embedded fibres was simultaneously optimised forming part of the set of solutions for a Pareto front, possible as they were found to be generally unrelated (Nik, et al., 2012). The embedded fibres in the composite plate can be likened to the *VBs* in the palm *petiole* which vary in size and areal density along the *petiole*.

2.5.2.2 Torsion stiffness modelling

When the objective in equation (29) is to minimise the mass of a shaft, equation (30) shows the torsional constant performance index λ_{JTA} for the shape torsional rigidity mass-efficiency of a section of uniform and isotropic material (Pasini, 2007). The higher λ_{JTA} is, the lighter and stiffer the cross-section is in shape torsion assuming constant rigidity modulus, G, ρ and J_{TD}/A_D (the ratio of torsional constant to the area of the envelope) between the samples being compared. These equations apply to non-scaled cross sections only.

$$\frac{torsion\ stiffness}{mass} = \frac{GJ_T}{\rho A} = \frac{GJ_{TD}\psi_{JT}}{\rho A_D \psi_A} \tag{29}$$

$$\lambda_{JTA} = \psi_{JT}/\psi_A \tag{30}$$

2.5.2.3 Bending to torsion stiffness ratio modelling

In the case of bending to torsion stiffness modelling, the objective (equation (31) is to minimise the torsional rigidity. Equation (32) shows the performance index, λ_{IJT}, which measures the bending to torsional stiffness efficiency of a section of uniform and isotropic material (Pasini, 2007). The higher the λ_{IJT} is, the more likely a section is to twist than bend assuming constant E, *G* and J_{TD}/I_{TD} between the samples being compared. These equations apply to non-scaled cross sections only.

The performance index, λ_{IJT}, in equations (32) and (31) is highest when the torsion flexibility is maximised for a given flexural stiffness assuming constant *E, G,* and I_D/J_{TD} between the samples being compared. The ratio I_D/J_{TD} here is only constant if the envelope of each cross section has the same aspect ratio in order to compare like with like or as is found in this thesis, if the envelope is circular.

$$\frac{bending\ stiffness}{torsional\ rigidity} = \frac{EI}{GJ_T} = \frac{EI_D\psi_I}{GJ_{TD}\psi_{JT}} \tag{31}$$

$$\lambda_{IJT} = \frac{bending\ shape\ stiffness}{torsional\ shape\ rigidity} = \frac{\psi_I}{\psi_{JT}} \tag{32}$$

2.5.3 Proportional scaling

Charts for the selection of materials and shape for shafts in torsion which are not restrained at either end and are free to warp are developed by Mirjalili and Pasini (Mirjalili & Pasini, 2007). Scaled rectangular cross sections (open and closed wall sections) were tested but only proportionally scaled ellipses with constant wall thickness were examined.

Mirjalili and Pasini (Mirjalili & Pasini, 2007) claim that previous methods of generating structural alternatives at the concept stage of design are inefficient and alternative structures are difficult to generate and select. They thereby develop a technique to optimise material and shape for stiff shafts in the early stages of design by producing selection charts.

Two families of shapes only, the ellipses and the rectangles are tested in torsion. Open and closed wall sections of the rectangle family were tested. For the ellipses, only proportionally scaled and constant thickness classes were examined.

In order to formulate the *shape transformers*, the correct torsional constant had to be applied. The torsional constant, J_T, should be found using the Saint-Venant semi-inverse method whereby the warping function of the surface is integrated over the surface area (Mirjalili & Pasini, 2007). However, only approximate values for the shapes tested were used, derived by Roark (Young & Budynas, 2002) and Ashby (Ashby, 2005) with up to 4% error (Young & Budynas, 2002).

The *shape transformer* for the torsional constant, ψJ_T is defined in equation (26) where *D* is the property of the rectangular envelope.

The mass-efficiency of torsion shafts was modelled. They were unrestrained at both ends, a uniform torque condition and so warping was negligible in these calculations. Further details on warping are described in section 2.6 ‘The Warping Factor Problem’. Rectangular envelopes were used to form material and shape indices for scaled rectangular sections (open and closed wall sections) and only proportionally scaled elliptical sections of constant wall thickness. It was found that closed walled rectangular sections were 10^3 times stiffer in torsion than open walled sections (Mirjalili & Pasini, 2007).

2.5.4 Scaling in shape transformers and q

When cross sections are scaled, an envelope scaling factor has to be calculated and applied to the individual samples when circumscribed by rectangular envelopes (Pasini, 2007). The relative scaling of a cross-section with rectangular envelope breadth and height, *B* and *H*, respectively, relative to a reference envelope with dimensions, B_0 and H_0, is described using two scaling multipliers, *u* and *v* as in equation (33):

$$u = B/B_0,\ v = H/H_0 \tag{33}$$

When cross sections have the same sizes, $u = v = 1$. The equations (27), (30) and (32) are only relevant for comparing shapes that have envelopes with the same aspect ratio and size, such that the geometric quantities of the envelope are constant. The scaling parameter, q, is derived from u and v and is shown in equation (34):

$$q = \ln(uv)\,/\ln(u^{1.55}v^{2.45}) \tag{34}$$

For example, if the material is prescribed, the performance factor for resistance to bending mass efficieny, $\dot{p}_{s,}$ for shape selection for scaled cross sections is shown in equation (35) (Pasini, 2007):

$$\dot{\mathrm{p}}_s = \psi_I^q/\psi_A \tag{35}$$

For co-selection of shape and material using scaled envelopes for bending stiffness, shape efficiency plots now display lines of iso-performance using logarithmic scales. As well as just displaying shape options in bending stiffness, it is possible to co-select shape and material using scaled envelopes. Section 1.3 in the Introduction section of this thesis shows the methodology for shape and material selection (Pasini, 2007).

The problem whereby shapes with rectangular envelopes of different aspect ratios were incorrectly compared with each other previously, is overcome by using scaled s*hape transformer* techniques allowing for scaling of cross-sections in two directions. A new feature of this method is that of the space envelope as a design parameter. The materials are assumed to be homogeneous and isotropic and Young's modulus the same in compressions as it is in tension. This approach uses rectangular envelopes for pure bending stiffness only (Pasini, et al., 2001) and it does not apply to torsion.

Defining shape properties that are invariant to scaling can be advantageous when describing failure mechanisms. Performance indices were created for the design of beams and selection charts provided a visual representation of this. The samples used in this research were all geometrical shapes, but it could have been applied to natural section shapes also.

The paper by (Singh, et al., 2011) selects a Pareto front of shape and material combinations of lightweight shafts that are subject to bending, shear and torsional loads. Rectangular envelopes are used to create *shape transformers* and scaled sections, using envelope multipliers. The shapes compared were only those used commonly in structural design. Rectangular envelopes were again used but this time with scaling applied to model multi-objective selection problems integrating shape and material into the model. Torsional rigidity was considered as a restraint but again using rectangular envelopes creating warping factors and approximations to the polar second moment of area of up to 3% error relative to experimental results (Singh, et al., 2011).

To minimise mass in a torsional rigidity design, shape efficiency maps are used (Singh, et al., 2011). In the single objective case, the shape is selected first for a prescribed envelope and then a scaled envelope. For a cross-section of prescribed size and material equation (36) is used. The higher the efficiency parameter λ_{JT}, the lighter and stiffer the cross-section is in torsion. Shapes that have the design requirement of a specific torsional rigidity can be identified on the ψ_{JT} versus ψ_A selection chart.

$$\lambda_{JT} = \frac{\psi_{JT}}{\psi_A} \tag{36}$$

For a scaled envelope, straight iso-performance lines are plotted on a logarithmic scaled chart with axes for log ψ_{JT} and log ψ_A as can be seen in Figure 13.

This is done by taking the logarithm of the performance index monomial (equation (37), creating a straight line on a log-log graph as in Figure 13. The performance index, PI, is known and is that of the iso-performance line. q is known and is user defined and a range of ordinates for ψ_{JT} are set up to obtain the corresponding ordinates for ψ_A. When q is known (when there is a geometric constraint) the intercept on the y axis will directly give the PI, the shape performance (Singh, et al., 2011).

$$log\psi_{JT} = \left(\frac{1}{q}\right) log\psi_A + (1/q)logPI \tag{37}$$

So, for a non-proportionally scaled shape, q is known because u and v are known. From the known slope of the selection guideline, the y intercept $(1/q \; log \; PI)$ can be selected and ultimately the performance PI can be determied.

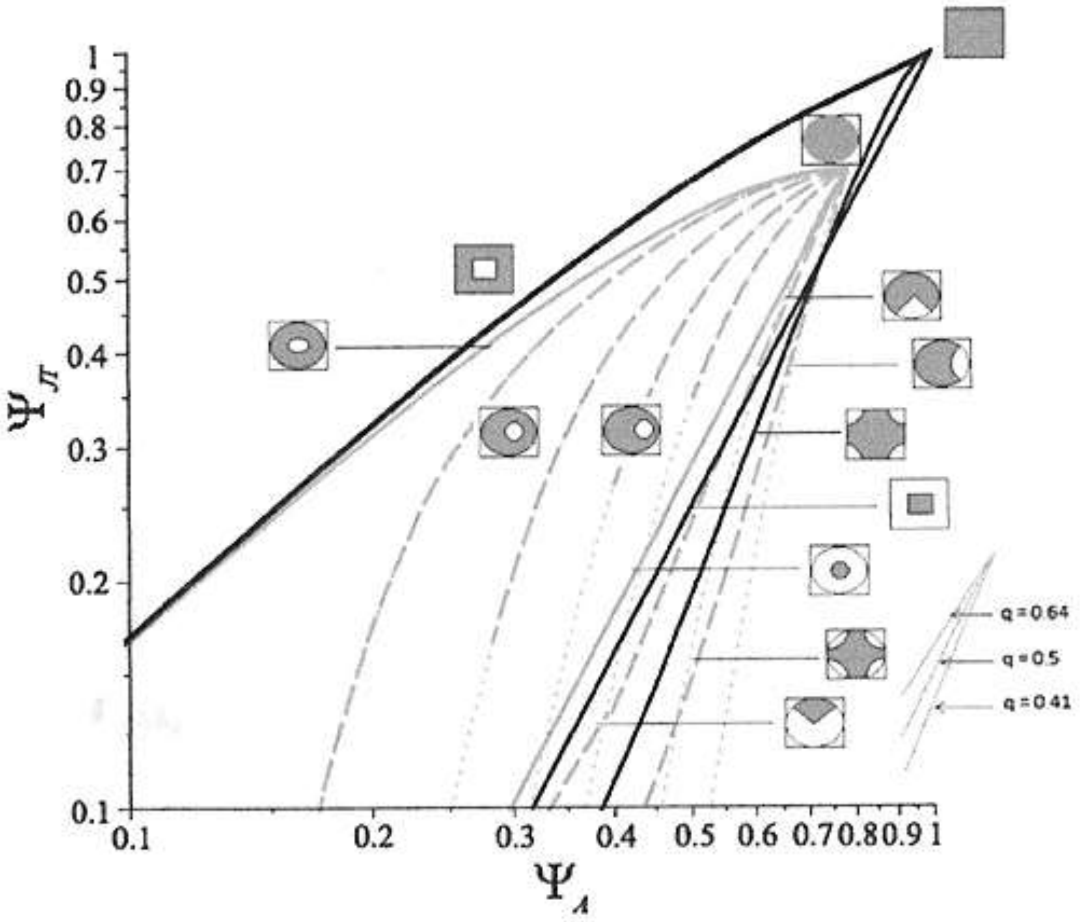

Figure 13 Efficiency map for scaled cross-sections (closed-wall cross-sections), logarithmic scale reproduced from (Singh, et al., 2011)

2.5.5 The torsion scaling problem

The paper by Singh, J., Mirjalili, V. and Pasini, D (Singh, et al., 2011), states that “In torsion the efficiency limits are dependent on the relative scaling of the envelope, which is governed by α, the angle between the horizontal base of the rectangle and the diagonal line between the two opposing corners of it. This is a result of the fact that Ψ_{JT} is a function of the angle α as opposed to Ψ_I which is not. In most cases such as hollow rectangles, the performance increases when the envelope tends to be square (i.e. $\alpha = 45°$), but for practical values of α, the increase is less than 5%. Hence, at the conceptual stage of design, Ψ_{JT} (and thus, efficiency parameter) could be assumed to be constant.”

If by using rectangular envelopes, it is decided that the process takes too long and it is not considered important to lose 5% of the performance efficiency, then firstly, a more time efficient solution should be sought and secondly, a more precise performance index should be used. By using circular envelopes, calculated values of performance are not compromised. This will be discussed further in the novel methods chapter.

Pasini & Mirjalili (Pasini & Mirjalili, 2006) acquired data for ten *dicotyledon petiole* transverse-sections and compared these with idealised ellipse and semi ellipse shapes to make an analysis of shape efficiency. The bending stiffness was plotted against the torsional rigidity for rhubarb *petiole* transverse-sections to examine the ability of living organisms to twist without bending (Pasini, 2008). However, in the first paper (Pasini & Mirjalili, 2006), the *shape transformers* were not scaled as they should have been as the aspect ratio of the envelopes was not constant. Scaling is required if rectangular envelopes are used with various aspect ratios and the *shape transformers* are plotted on the same efficiency chart.

Firstly, the transverse section shapes were compared with idealised ellipse and semi-ellipse shapes for shape efficiency analysis. A more direct way of doing this would be to use circular envelopes, the higher the performance index, the more like a solid circular cross section, the shape is. Secondly, scaling of the bending to torsion performance index may not be required with a circular envelope.

2.5.6 Differentiating petioles by shape

Petiole anatomy was used to differentiate between species of laurel (Kamel & Loutfy, 2001). The shape of the *upper edge* of the *petiole* only, was used in the analysis. It is good for discriminating between taxa within the same genus, but not between distantly related genera. However, Kamel and Loutfy are actually looking at a combination of shape and size. If shape was separated from size, differences between species and distantly related taxa may become more apparent.

A paper by (Kamel & Loutfy, 2001) used three methods to classify and differentiate between species of laurel. The first was SDS-PAGE analysis based on seed storage protein files, the second was leaf *Cuticle* features, whereby epidermal peels are investigated for cell shape and thickness, *Stoma*ta and special features. Lastly, *petiole* anatomy was used to differentiate between *some* species. Transverse sections of 20μm width were cut using a hand microtome and stained with *Safranin* to highlight the woody lignin in red and *Light green* to stain trichomes (epidermal hairs on the *petiole* which may be single or multi-cellular). *Petiole* transverse section shape (upper edge only), distribution and shape of trichomes, shape of epidermal cells, hypodermis structure, distribution of oil cells, location of pigmented cells and *VB* distribution were all aspects of the *petiole* that were analysed. It was found that *petiole* anatomy was good for discriminating between taxa belonging to the same genus, but not between distantly related genera. Further work should look into more detailed aspects of the *petiole* shape to define the taxa better by extracting shape from size. The shape of the lower edge of the *petiole* was not investigated and the shape of the upper edge was determined by cutting sections of *petiole* rather than measuring the profile externally. Further work should consider analysing the lower edge of the transverse sections also and the process of 3D imaging.

2.6 The warping factor problem

When subjected to torsion, every transverse-section of a circular shaft remains plane and undistorted. Conversely, cross-sections of non-circular shafts are distorted when subject to torsion. So while the circular cross-sections along a shaft rotate (when the shaft is subject to torsion) each cross-section rotates as a solid rigid slab. When a bar of square cross-section is subject to torsion, its various sections become warped and do not remain plane. Consequently, circular cross-sections remain plane when shear stress is applied to a transverse section of a shaft, but rectangular cross-sections do not.

2.6.1 Approximating the torsional constant

Techniques are laborious and modelling of the shape and mechanical function of complex structures is inaccurate. When comparing the torsional stiffness of shapes, this laboriousness is partly overcome, by simplifying the equations for the torsional constant, J_T (a function of warping) rather than performing a surface integration over the surface area using the Saint-Venant semi-inverse method. However, doing this, incurs an error of up to 4% for the rectangle (Young & Budynas, 2002). To reduce the laboriousness and the error, it should be noted here that J_T, for circular shapes is equal to the polar moment of area J meaning that no approximation to J_T is required.

The time intensive modelling is exemplified when measuring natural structures, where correlation between shape and mechanical function between simple natural 2D shapes varies randomly resulting from similar and slightly independent scaling variations, so each shape has to be individually scaled.

2.6.2 Warping: torque and shear stress

When torque is applied to a shaft of non-circular cross-section, warping always occurs (Ryder, 1955). When shear stress is applied to a transverse section of a shaft of non-circular cross-section, the resulting shear strain causes a distortion to the cross-section called warping.

At high angles of twist ϴ, shafts experience non-linear stiffening and strengthening effects caused by longitudinal stresses induced by the axial shortening of longitudinally arranged fibres.

Shear stress causes shear strain and the distribution of this about the shape centroid determines the extent of distortion. The following analysis of shear stress in rectangular and circular sections shows that the shear stress is constant on the edge of the circular section, but not so with the rectangular sections, causing the latter to distort out of plane.

2.6.3 Torque applied to a shaft – effects of warping, elastic and plastic deformation

The torque, T, at distance z along a shaft axis in equilibrium is given in equation (38) where G is the rigidity modulus, E is the Young's modulus, w is the warping section constant, l_n is the section property described as a nonlinear 'Wagner' constant and lastly, $\partial\theta/\partial z$ is the rate of rotation with respect to the z axis. The second term represents the warping effects of the cross section (which reduces the torque required to twist the shaft) and the third term represents the plastic deformation of the shaft. The third term for non-linear plastic torsion rarely occurs in practice and is negligible for small deformations (Mirjalili & Pasini, 2007).

$$T = GJ_T\frac{d\Theta}{dz} - Ew\left(\frac{d^3\Theta}{dz^3}\right) + \left(\frac{1}{2}\right)EI_n\left(\frac{d\Theta}{dz}\right)^3 \tag{38}$$

The second term in equation (38) describing the effect of warping within the cross section, is required when warping is prevented at the support (which is the case with the palm *petiole*). Warping restraint like this causes longitudinal stresses to occur within the shaft, which otherwise would not occur. This term is negligible for shafts with a length to depth ratio of more than six (providing that both ends are free to warp) (Mirjalili & Pasini, 2007). Warping therefore occurs in plant *petioles* as at least one end is attached to the rest of the plant and restrained. How this is reflected in the torsion *shape transformer* is part of the area of research in this thesis.

Equation (39) is the formula for torsional deformation of a shaft of length L, the torsional constant, J_T is equal to the polar second moment of area, J only for circular cross sections.

$$\theta = \frac{TL}{J_T G} \tag{39}$$

For all other non-circular cross sections, J_T is less than J and may be only a very small fraction of J (Young & Budynas, 2002). This is therefore an area requiring further research.

2.7 Summary of the literature review

The overall purpose of the literature review was to analyse current research methods suitable for this research, demonstrate gaps in the literature to be addressed and finally to achieve new insight into shape performance problems in structures.

Five gaps are identified in the literature review which the following research will aim to address. Generally, there is a need to understand how arborescent palms compensate for extreme stresses. Specific gaps in the knowledge internally are the 3D distribution of *VBs* within the *petiole* and the degree of lignification of the outer layer of the *petiole*. In terms of acquiring shape data from *petioles* non-destructively, so that the data from endangered species can be included, a method to obtain palm *petiole* profiles in vivo, does not exist in the literature. Conventional *shape transformers* used to isolate shape from size and normalise shape incur up to 4% error as a result of the shape of the shape envelope. A method does exist to overcome this, but it is too laborious to use. The method is also slowed down because each shape has to be independently scaled, so there is an opportunity to propose a simpler *shape transformer* method. Up to now, only whole transverse sectional shapes are tested for contributions to bending and twisting; no independent upper and lower edge shape mapping of transverse sections exists. Lastly, further techniques are required for the taxonomic classification of plants.

The literature review has provided insight into the micro and macro structures of the arborescent palm to identify what the important aspects of their success in survival are: namely hierarchy of structures, graded structures, internal and external shape and their adaptability to their mechanical environment. Palm material was reviewed as this is closely linked with structure to provide the mechanical responses observed. The effects of warping in shafts and their impact on *shape transformers* was researched and scope for designing new *shape transformers* to compensate for this was identified. The inaccurate scaling factors and laborious methods for calculation applied for the purposes of comparing shapes were researched, providing guidelines for better solutions. Additionally, there is scope for designing a more detailed shape analysis technique which identifies the contributions to bending and torsion from the upper or lower edges of the shape as opposed to the whole shape. Approximations are inherent in the rectangular shape of the envelope used in the *shape transformers*, for which there is scope to overcome. Plant species classification is achieved partly by the analysis of the combined shape and size of the upper edge of *petioles* although distantly related genera cannot currently be distinguished from each other. It would be worth investigating if an analysis of shape only could solve this problem and if the analysis of both edges could give a 100% success rate.

The following is an action list for this research resulting from what has been learned in this literature review. The number in parenthesis after each item corresponds to the same objective number (listed under 'Aims and objectives' in section 1.5 of the Introduction chapter).

- Design a novel method to acquire palm *petiole* profiles in vivo (Objective 1).
- Develop author's idea of using circular envelopes in *shape transformers* to reduce effect of warping so that shape technology from biological optimisation mechanisms can be more accurately and easily transferred to mechanical engineering and design (Objective 2).
- Develop idea of using circular envelopes in *shape transformers* to negate requirements for scaling in the *shape transformers* $\psi_A, \psi_I\ and\ \psi_{JT}$. For all non-circular cross sections, J_T is less than J and may be only a very small fraction of J (Young & Budynas, 2002). This is therefore an area requiring further research (Objective 2)
- Although CAO and CAIO are able to mimic the adaptive growth caused by localised compressive stress, they model the entire 3D structure and individual factors may be overlooked. A method is required to break down the 3D structure into smaller components to identify significant contributors to bending and torsion stiffness. Design a SEM system to determine contribution to torsion and bending from upper and lower edges of cross sections (Objective 3)
- The cell wall cellulose of the extra xylary fibres present in the *petiole*, where their primary function is providing strength is permeated by lignin. However, these cells may remain flexible (Cutler, 2005). The arrangement of the fibres within the *petiole* transverse section and along the longitudinal axis of the *petiole* should be examined (Objective 5)
- The size gradient of the *VBs* across the transverse sections in relation to the stiffness of the *petiole* should be analysed (Objective 5).
- As the *VBs* in the thin outer layer of the *T. fortunei petiole* appear fused (Windsor-Collins, et al., 2007a), create a bi-layered model using Young's modulus derived from material tests and the change in shape of the layers along the *petiole* to calculate the Young's modulus of the two layers and therefore answer the question as to whether the outer layer is lignified or made of thick epidermis (Cutler, 2005) (Objective 5).
- Calculate *VB* area density for the six transverse sections of the *T. fortunei* palm *petiole* from the same palm used for the flexural and torsion tests in this research and compare to the elastic and shear moduli data (Objective 5).

- As structural members are small in length in a hierarchal structure, there are fewer critical buckling loads and the load on each individual member is much less. One of the roles of the palm *petiole* may be to accommodate the increase in number of *VBs* distally along the longitudinal axis of the *petiole* (Objective 5).
- The nature of the variant transverse sectional shape along the *palmate* and *costapalmate* palm *petiole* axis is one of the reasons for looking in depth at how its shape determines its performance. Palm *petioles* taper in cross-sectional area towards the leaf blade, usually having a groove or ridge(s) running along the top (upper) surface. They are roughly symmetrical about the vertical plane (Objective 6).

2.8 Hypotheses

I. The size, orientation and distribution of *VBs* within the *parenchyma* matrix may contribute to the mechanical efficiency of the *petiole*.

II. It may be possible to estimate material properties of the individual layers of a palm *petiole* by using its shape and its bulk material properties.

III. Using circular envelopes in *shape transformer* analysis provides more accurate torsion performance indices.

IV. The independent *petiole* configurations are well suited to the function of the *petiole* as a whole. There may be a strong correlation between the properties and the transverse-section shapes of palm *petioles*.

3 Methodology and methods

3.1 Overview of chapter and flow chart

The hypotheses put forward after reviewing the literature point to three areas for further research into the *palmate* palm *petiole*: histology (*VB* size, shape and distribution), material properties and morphology (the external shape of the *petiole*). Each of these areas of research has a subheading of the same name under which the methodologies and methods are described. The methodologies provide the background theory for an in depth understanding of the procedures later described for replicating the tests. A methods flow chart (Figure 14) shows how the three areas of research follow through to the methods which in turn link to the appropriate hypothesis.

Methods map

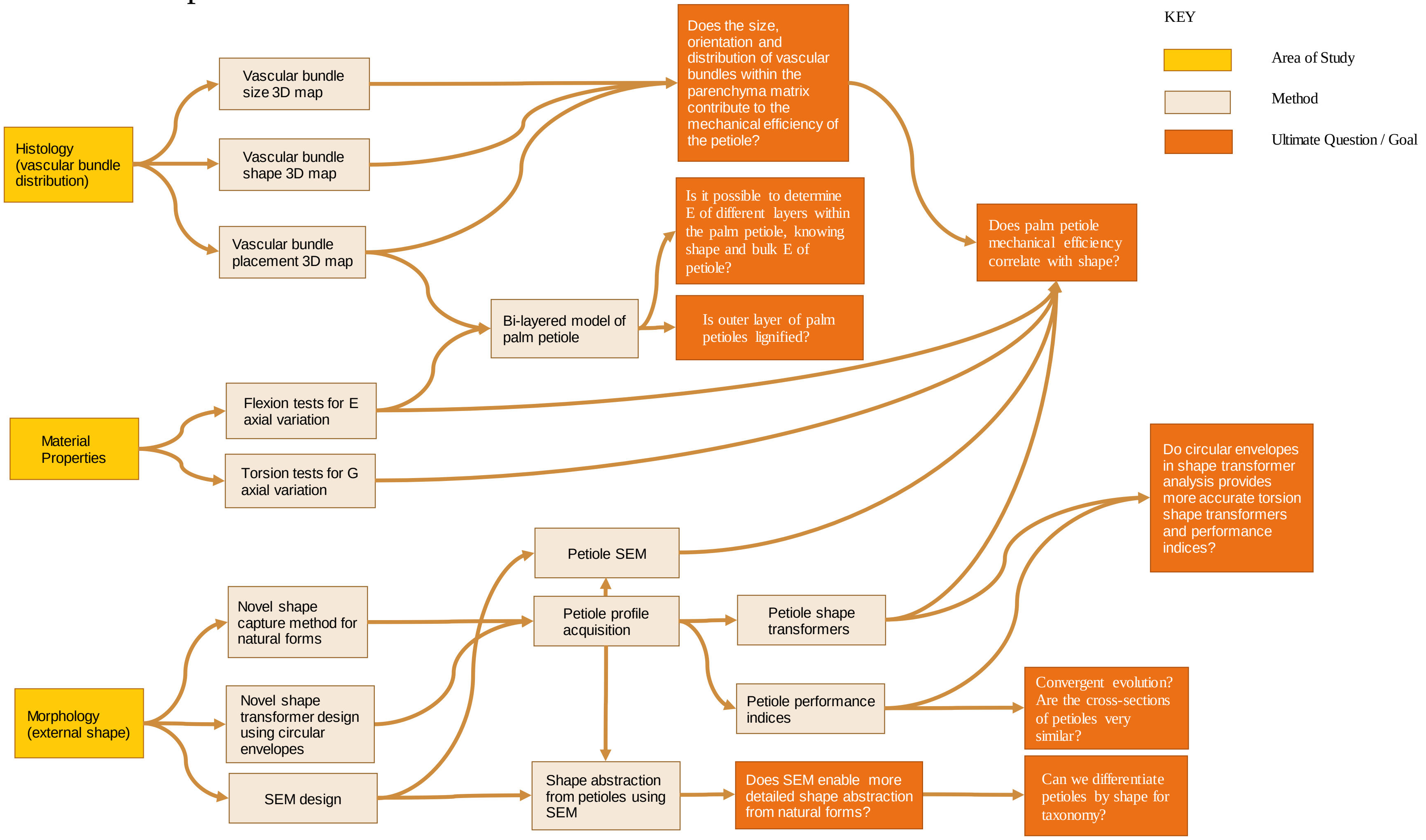

Figure 14 Methods flow chart

3.2 Histology - vascular bundle size, shape, count and gradients

3.2.1 Methodology

The size, shape and number of *VBs* (*VBs*) in the transverse cross section and along the longitudinal axis of the *T. fortunei* arborescent palm *petiole* has implications for its bending and torsion performance. In terms of *VB* size, Zhai et al points out that smaller *VBs* have a higher E and a higher proportion of fibres than larger ones (Zhai, et al., 2011). It is inferred by the author of this thesis through the work of Nogata and Takahashi (Nogata & Takahashi, 1995) that the orientation of the principal axis of the elliptical shaped *VBs* is aligned with the main direction of stress. According to Gibson et al, the *VBs* are concentrated in areas of high flexural rigidity and so their distribution affects the flexural rigidity (Gibson, et al., 1995). Gradients of these distributions indicate an efficient use of energy required to make the materials (Ruggeberg, et al., 2008) and so these are measured for size and areal distribution.

3.2.2 Method

A fresh *petiole* from the *T. fortunei* arborescent palm was taken with leaf blade intact. As soon as the *petiole* was removed from the tree, the cut end was immersed in water to help maintain hydrostatic pressure and to stop the *petiole* from dehydrating and shrinking. Six samples (P1 to P6) of 3 cm in length were cut using a scalpel every 171mm along the length of the *petiole* such that samples of approximately 5mm in length were collected equidistantly as shown in Figure 15 (Windsor-Collins, et al., 2006).

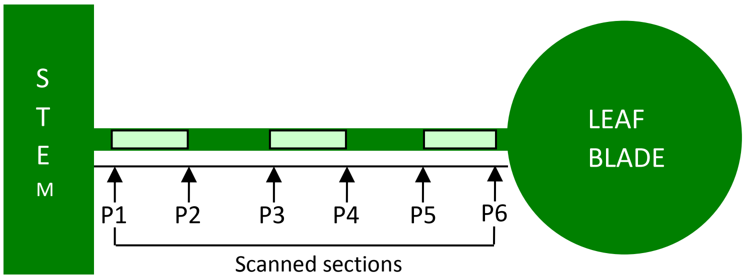

Figure 15 Palm *petiole* schematic showing the relative placement of scanned sections P1 to P6 – figure adapted from (Windsor-Collins, et al., 2006)

To evaluate the internal structure of a fresh *T. fortunei petiole*, cut sections were mounted in wax (Figure 16) and scanned at a resolution of 1200dpi revealing the arrangement of *VBs* (Windsor-Collins, et al., 2006).

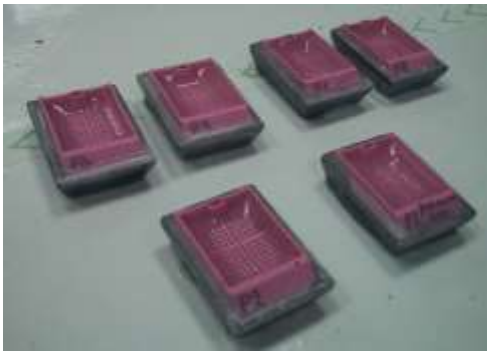

Figure 16 Setting the *petiole* sections in wax

The specimens were then dehydrated using 70%, 90%, 95% and 100% ethanol, each step taking two hours. The alcohol was then driven out by using two baths of Histoclear, which is miscible with wax. Each sample was embedded in wax to enable cutting thin layers from the sample with a microtome (Figure 17). The samples were infiltrated in two baths of molten paraffin wax at 60°C and mounted into paraffin blocks. The samples were then sectioned using a microtome.

Figure 17 Cutting the *petiole* sections with a microtome

The *petiole* was often too hard for the microtome to cut intact slices from the samples. However, the remainder of each section which was embedded in the wax after removal of some transverse section slices with the microtome, provided a clean cut surface (Figure 18).

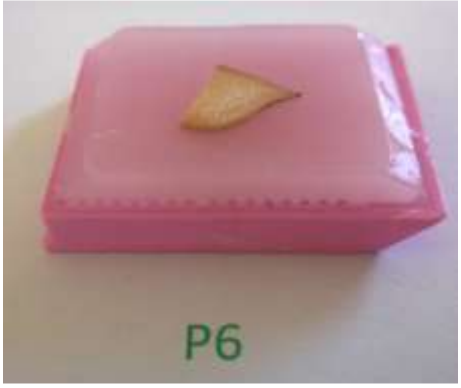

Figure 18 *petiole* section P6 embedded in wax after being cut with the microtome

A scanner was used to show the size, shape and areal density of *VBs* along the longitudinal axis of the *petiole*, the *petiole* sections of which are shown in Figure 19. Each section was scanned at 1200 dpi (Windsor-Collins, et al., 2006).

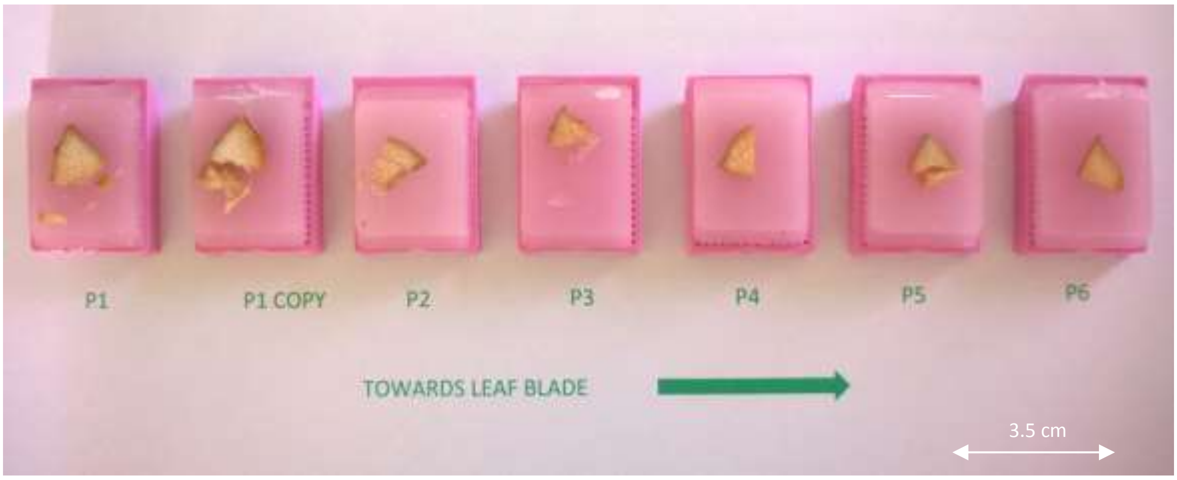

Figure 19 Series of 2D *petiole* sections P1 to P6 along the *T. fortuneii petiole* axis

The sizes of the *VBs* were determined by relative comparison with the scale bar pictured on the images at high magnification on the computer. Each *VB* was approximated to an ellipse and the length of both the major and minor axes of the visible ellipses were measured. In addition, the orientation of the longitudinal axis of the ellipses were observed and recorded.

The vertical *VB* distribution within the *petiole* is described using the thin white line YY shown in Figure 20 as a reference. The thicker white line, XX running laterally, perpendicularly bisects YY. The *VBs* on either side of line XX were counted with the aid of a graticule. Using Adobe Photoshop® software, a 0.25 mm grid was placed over each section image so that the number of *VBs* could be counted within each unit of the grid to establish the areal density across the *petiole* transverse sections. Whole *VBs* that were entirely present within the graticule, were counted as integers whereas those that were partially within the grid were summed and divided by two.

The total number of *VBs* within the transverse sections P1 to P6, were calculated using the same counting method as for the vertical distribution. This procedure was followed for the viewable area of each section.

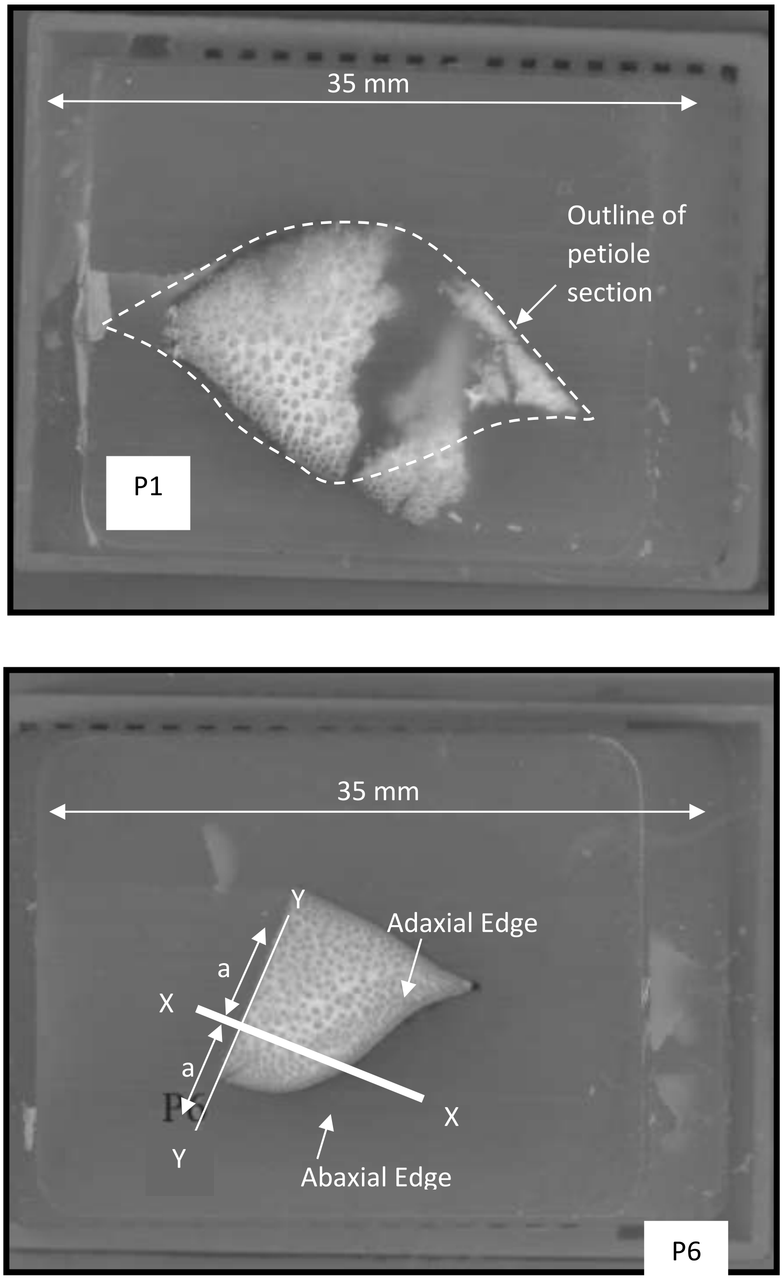

Figure 20 Photograph showing sections P1 and P6 embedded in wax. P1 was torn while cutting the hard sample using a scalpel. Lines XX and YY are used for reference later where XX perpendicularly bisects YY. Adapted from (Windsor-Collins, et al., 2008)

3.3 Material properties

3.3.1 Methodology

The aim of the flexural tests was to determine the variation of Young's modulus, E_L along the longitudinal (L) axis of the *T. fortunei* palm *petiole*. This was for comparison with shape from the *shape transformer* results ultimately to understand the *petiole* function and as one of the input parameters for the bi-layered model.

The output of the torsion tests provided the variation of the rigidity modulus, G, of the *T. fortunei* palm *petiole* along its longitudinal axis again for comparison with shape. As wood is anisotropic, three rigidity modulus constants describe the elastic behaviour of wood G_{LR}, G_{LT} and G_{RT} where the wood axes are annotated as: longitudinal (L), tangential (T) and radial (R). However, in these tests, palm *petiole* material was assumed to be isotropic and homogeneous as they were tested as a whole. A general value of G was therefore required.

Although the *petioles* used for the bending and torsions tests were from the same palm, the tests were performed on different *petioles* because firstly, the tests may have damaged the *petiole* and secondly, the test specimens would not be of the same freshness for the two tests, freshness being an important contributor to *petiole* mechanical performance.

A paper by Windsor-Collins et al (Windsor-Collins, et al., 2007b) highlights the fact that vascular bundles are sometimes more concentrated towards the external boundaries of the *petiole*, but are not necessarily arranged concentrically. Following on from this, it has been noted that the transverse sectional area of the palm *petiole* could be separated into two regions of differing material properties. There is an obvious colour density difference between these two regions (Figure 21) which shows that on closer examination this is coincident with a higher spatial density of *VBs* towards the periphery of the *petiole*. The *VBs* have relatively high tensile strength relative to the supporting *parenchyma* tissue which consists of relatively thin walled 'packing' cells.

A bi-layered model was designed to predict separate values of E for the inner and outer regions of the *petiole*, based on values of EI for the whole *petiole* from the flexural test results. The outer layer of the palm *petiole* consists of an epidermis, under which is the hypodermis, normally made up of compactly arranged *sclerenchyma* cells without intercellular spaces. It was not known if this outer layer consisted of a thick epidermis or lignified cells (Cutler, 2005) so estimating an E for these two, thin, combined outer layers should signify if they are lignified or not as the values of E for lignin are widely known.

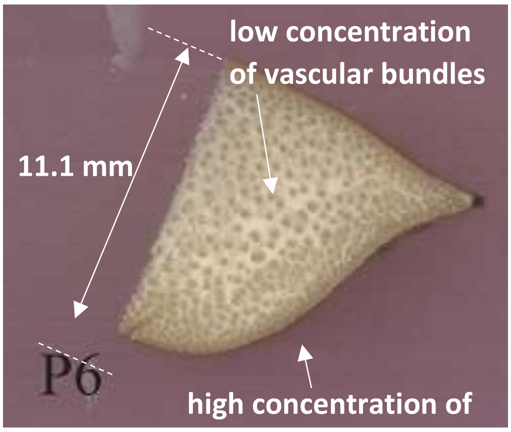

Figure 21 Transverse section 'P6' of a *T. fortunei* palm *petiole* embedded in wax showing how the distribution of vascular bundles is more concentrated towards the edges

3.3.2 Empirical flexural test method and petiole preparation

The flexure test was carried out on six *petioles* each divided equally into three sections: *P, C* and *D* along the length of the *petiole*; the proximal, central and distal segments respectively.

For each *petiole* tested, three mild steel receptacles, specially machined for this purpose, were clamped with the concave side oriented upwards in readiness for the epoxy resin adhesive and the embodiment of one end of each of the three *petiole* sections P, C and D. Each *petiole* was cut to a total length of about 85 cm. The cut ends were quickly submerged in water to help retain the material properties and freshness. Using a fine toothed saw, each *petiole* was divided into five equal sections. Each section had a 20 mm margin at one end to embed in the epoxy resin. As a result, each tested section was 171 mm in length. Using a sharp, hard (hardness 'H') pencil, the transverse profiles of the ends of the sections were recorded to later calculate the second moment of area using the CAD package, Rhinoceros® NURBS modelling for Windows®. The clamp receptacles were degreased with FKS UN3295, a non-alcoholic, fast-evaporating solvent to help prevent slippage. They were then filled with epoxy resin adhesive (Araldite® 2013 AV 144-2/HV997) and the *petiole* sections were potted within the paste. With the aid of a spirit level, the sections were then held vertically in clamps as shown in Figure 22. To help prevent water loss, the free ends of the sections were dipped in melted wax and the sides were covered with cellulose film and secured with tape.

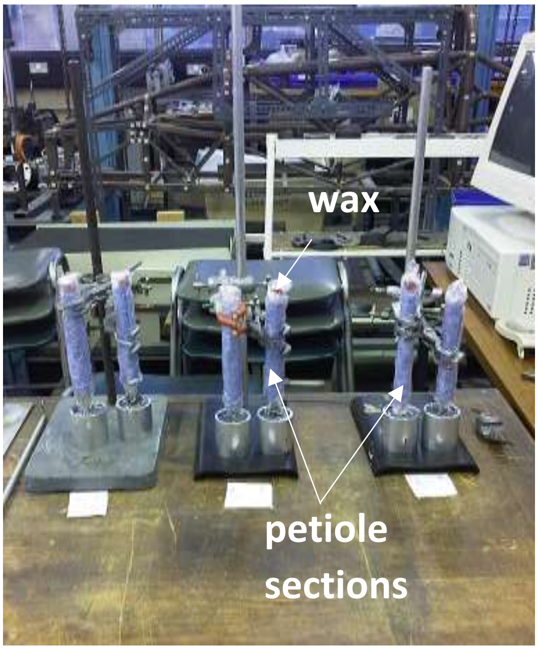

Figure 22 Potted *petiole* sections from two *petioles* covered in cellophane and wax at tips

After waiting for 24 hours for the epoxy resin to cure, the *petiole* sections and their receptacles were removed from the clamps. Each segment in turn was set up in the magnetic clamp as shown in Figure 23. A displacement transducer (with range 0 – 50 mm) was positioned 20 mm from the loading point on the *petiole* in the direction of the clamp. The length of each segment was recorded together with the temperature of the room and the time taken between potting and testing. The depth transducer was zeroed before any force was applied to the end of the *petiole*. Readings of the loads and resulting deflections were recorded and the loads were applied in increasing steps of to first the upper edge of the *petiole*, then the lower edge by inverting the *petiole*, up to a maximum load of 13 N. The loading point was positioned 10 mm from the free end of the *petiole* segment and the incremental loads applied at 15 second intervals.

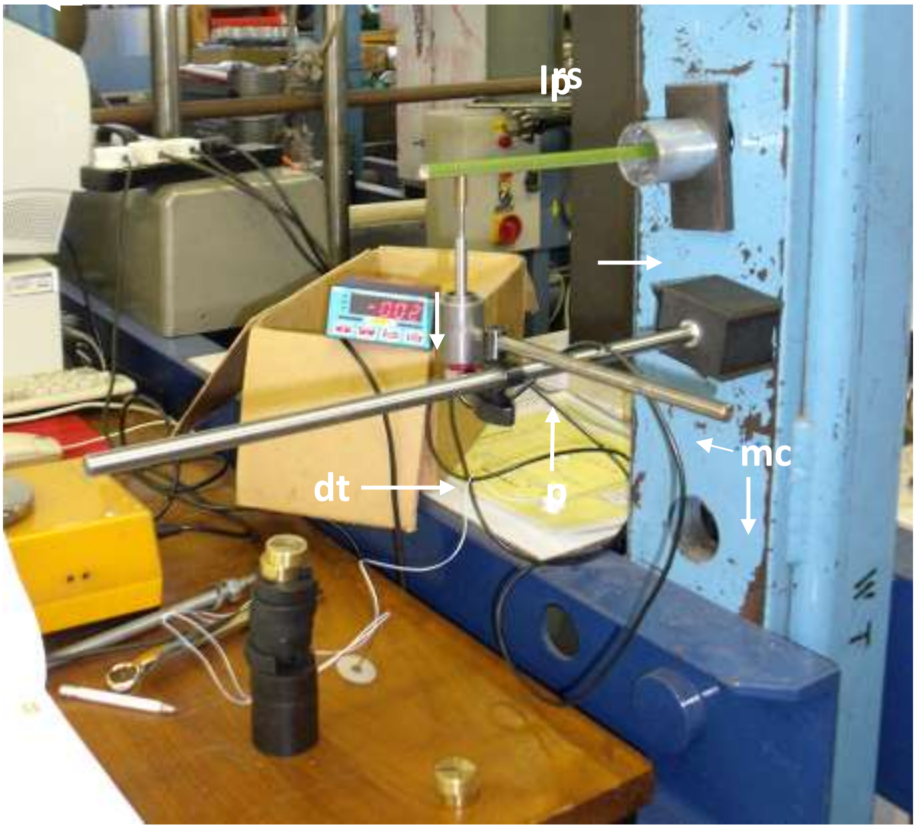

Figure 23 Bending Test Equipment showing roof support, *rs*, with attached magnetic clamp, *mc*, supporting the displacement transducer, *dt*, which is placed 20 mm from the loading point, *lp*, which in turn is placed 10 mm from the free end of the *petiole*, *p*. The load, *l*, was supported by the load carrier, *lc*.

A schematic diagram for the flexural test is shown in Figure 24 where the *petiole* beam (which is equal to length L plus the distance from the loading point to the end of the beam) is supported at one end. The load, F, is applied at the loading point, lp, causing the *petiole* to deflect with a displacement, δ. The Euler-Bernoulli equation for elastic bending of beams is shown in equation (40) and was used to determine E_L.

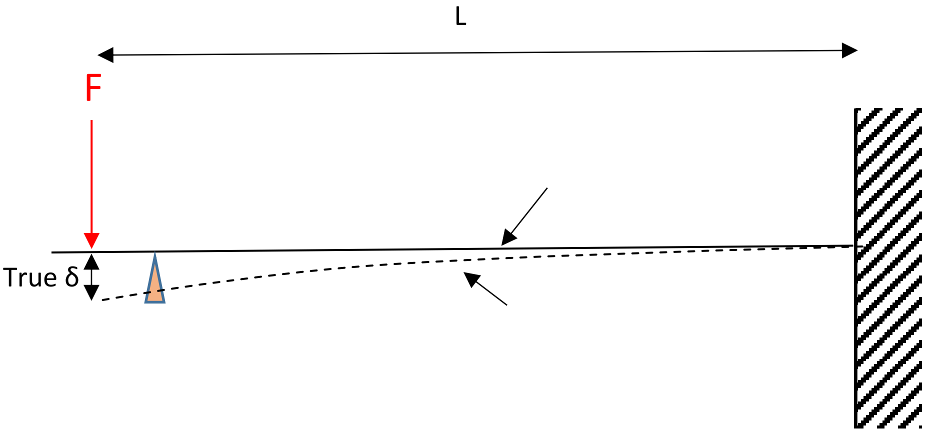

Figure 24 Flexural Test Schematic Diagram

Equation (40) shows the relationship between the deflection, *δ,* and the load, *F*, applied at a distance, *L,* from the support for the beam with second moment of area, *I,* and Young's modulus *E*.

$$\delta = \frac{FL^3}{3EI} \tag{40}$$

The flexural test was performed with the *petiole* segment oriented in two opposing directions such that the axis of symmetry of the transverse section was in the bending plane. The *petiole* segment was thus tested with the lower edge facing down and again with the lower edge facing up in order to satisfy number 5) of the Euler-Bernoulli beam equation conditions listed as follows (Bauchau, O.A. *et al.,* 2009):

1) The beam is subject to pure bending.
2) The material is isotropic and homogeneous.
3) The material obeys Hooke's law.
4) The beam is initially straight with a constant transverse section throughout the beam length.
5) The beam has an axis of symmetry in the plane of bending.
6) The proportions of the beam are such that it would fail by bending rather than by crushing, wrinkling or sideways buckling.
7) Cross-sections of the beam remain plane during bending.
8) E is the same in tension and compression.
9) Effects of local and general buckling are neglected.
10) The lengths of the beam are less than or equal to a tenth of the other two dimensions.

The independent variable was the load and the measured dependent variable, the displacement. The length, Young's modulus and the second moment of area were the fixed variables. Young's modulus, E_L, for each segment was derived from the mean distal and proximal second moment of area of the segment ends, the true deflection, segment length and load applied to the free end using the Euler-Bernoulli formula for cantilever beams.

FL^3 versus $3\delta I$ was plotted for each test and E (specifically E_L, Young's modulus along the longitudinal axis of the *petiole* segments) was calculated from the gradient in the elastic portion of the graph. 95% confidence intervals for E_L were calculated and shown on the plots and the data analysed for its significance.

The same method was repeated for all six *T. fortunei petioles* and the results compared.

3.3.3 Empirical torsion test method

The torsion test was performed on two tapered *petioles* from the same *T. fortunei* palm, the same palm from which the *petioles* were taken for the bending test. They were each divided into three segments so that the transverse sections of the test specimens were as uniform as possible along the length of the section. The most proximal part of the *petiole* was not tested (the 100 mm length of *petiole* nearest the palm stem) as this part of the *petiole* varies the most in cross-sectional area and shape compared to the rest of the *petiole* axis. The torsion equation, which was used to calculate the rigidity modulus, *G,* applies to circular cylinders only, so the remainder of the *petiole* was tested in segments of similar sectional area (not varying by more than +/- 8% in area). However, it was important to reduce the effect of clamp ends by keeping the length of the *petiole* segments as long as possible, so a compromise was made on the length of the test section.

Two disease-free *petioles* of 850 mm length were cut from the palm and the cut ends were immersed in water as soon as practicable to sustain freshness and maintain physical properties. Each *petiole* was divided into five equal lengths of nominally 160 mm. Only the first (P), third (C) and fifth (D) segments were used for this test. Two *petioles* and therefore six segments were tested.

As 20 mm of each segment end was to be embedded in epoxy resin, effectively part of the clamp, the tested length *L*, was 120 mm. The size and shape of the segment ends were recorded by tracing around the edges with a sharp pencil. This was to later calculate the polar second moment of area *J*, using the CAD program Rhinoceros® NURBS modelling for Windows®. Cellulose film was wrapped around each cut end to maintain freshness prior to it being embedded in epoxy resin.

Machined mild steel receptacles were degreased with FKS UN3295, a non-alcoholic, fast-evaporating solvent to help prevent slippage of the epoxy resin relative to the receptacle. Epoxy resin was placed into six receptacles and 20 mm of one end of each segment was inserted into the epoxy resin and held vertically in a clamp with the aid of a spirit level. After curing for 24 hours, the other ends of the segments were potted in the same way and left to cure for a further 24 hours (Figure 25).

Figure 25 Six *petiole* segments embedded in epoxy resin and covered in cellulose film prior to torsion testing

The receptacles were inserted into the torsion rig and the torsion rig was aligned by ensuring that the protractor and spring balance read zero simultaneously and the pivot arm was horizontal by observing the spirit level contained within the arm (Figure 26).

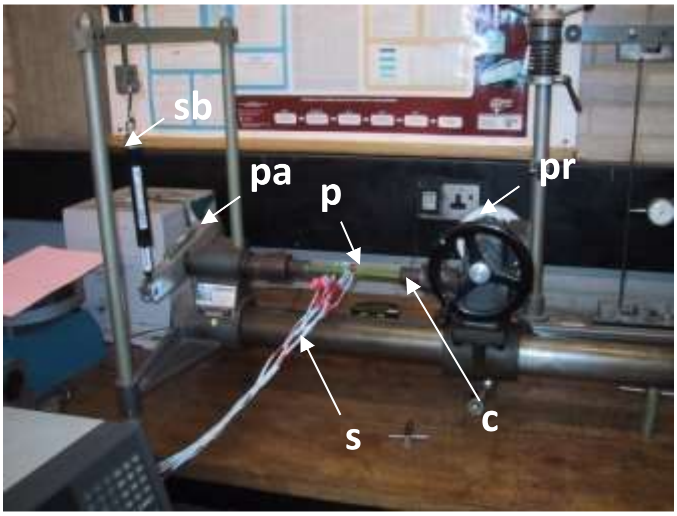

Figure 26 Torsion rig setup showing *petiole*, *p*, clamps, *c*, protractor, *pr*, to measure the angle of twist, strain gauge wires *s*, (used for further testing but not in this work), pivot arm, pa and spring balance, sb. Adapted from (Windsor-Collins, et al., 2008)

Torque was applied by rotating a handle that was fixed to the protractor shown in Figure 26. For each reading, the segment was twisted by one degree. The force shown on the spring balance and the angular twist readings were manually recorded at ten second intervals. After the tests, the *petioles* looked intact externally. Readings for force on the spring balance were also taken for decreasing angles of twist and the whole test was repeated on the same *petiole*.

The length of the pivot arm of the torsion rig and the spring balance offsets were recorded in order to derive the torque values from the forces recorded on the spring balance.

The shaft, in this case the *petiole* of length L, was fixed at one end as shown in the schematic diagram in Figure 27. The rigidity modulus, *G* was determined by rearranging the terms in equation (41) which shows how the torque *T* per angle of twist, *ϴ,* varies with rigidity modulus, *G*, polar second moment of area, *J*, and length, *L,* of the shaft.

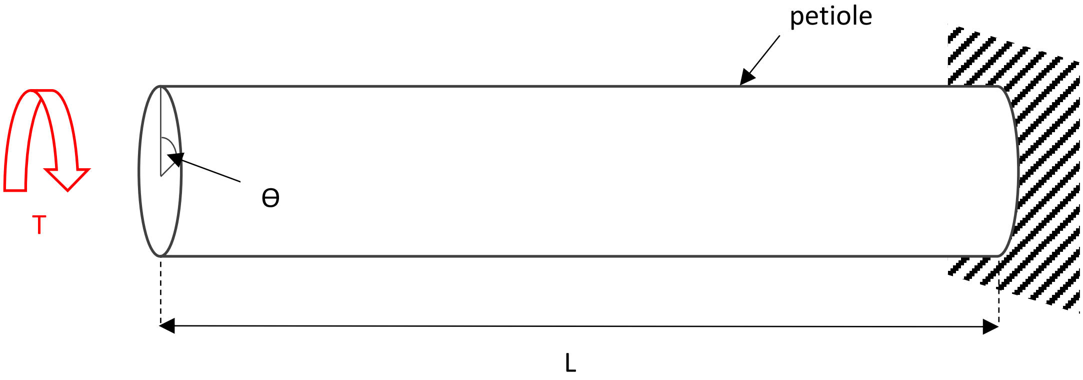

Figure 27 Torsion test schematic diagram

$$\frac{T}{\theta} = \frac{GJ}{L} \tag{41}$$

To satisfy the torsion equation (equation (41), the following assumptions were made (Ryder, G., 1955):

1) The shaft is subject to pure torque about its polar axis.
2) The material is isotropic and homogeneous.
3) The transverse section of the shaft is circular.
4) All points lying on the radius before twisting remain on the radius.

By plotting torque, *T*, against angle of twist, *ϴ*, the rigidity modulus, *G*, for each segment could be determined from the gradient of the graph by calculating the mean polar second moment of area, J, of each end and knowing the length, *L*, of the specimen.

The segment end profiles were scanned and transcribed into a CAD package (Rhinoceros® NURBS modelling for Windows) enabling the area, centroid, second moment of area and polar second moment of area to be processed accurately. Using equation (41), G was calculated and plotted for each segment together with 95% confidence intervals. The data were subsequently analysed for significance.

3.3.4 Poisson’s ratio

The values for the rigidity modulus, *G,* and Young’s modulus, *E,* from the torsional and flexural tests were used to determine Poisson’s ratio, v, of the *T. fortunei* palm *petiole* material equation (42). Only the Young’s modulus results for Tests 5 and 6 were used as these were the same *petioles* as used as in the torsion tests.

$$v = \left(\frac{E}{2G}\right) - 1 \tag{42}$$

3.3.5 Bi-layered palm petiole model method

The results from the flexural test were used from two segments of the flexural test, the P (proximal) and D (distal) segments of the *T. fortunei petiole* in the bi-layered model. This enabled Young’s Modulus, E_1 and E_2 in the two regions to be determined as demonstrated in Figure 28 where I_1 and I_2 are the second moment of area of the outer and inner sections of the *petiole* and t is the thickness of the outer layer.

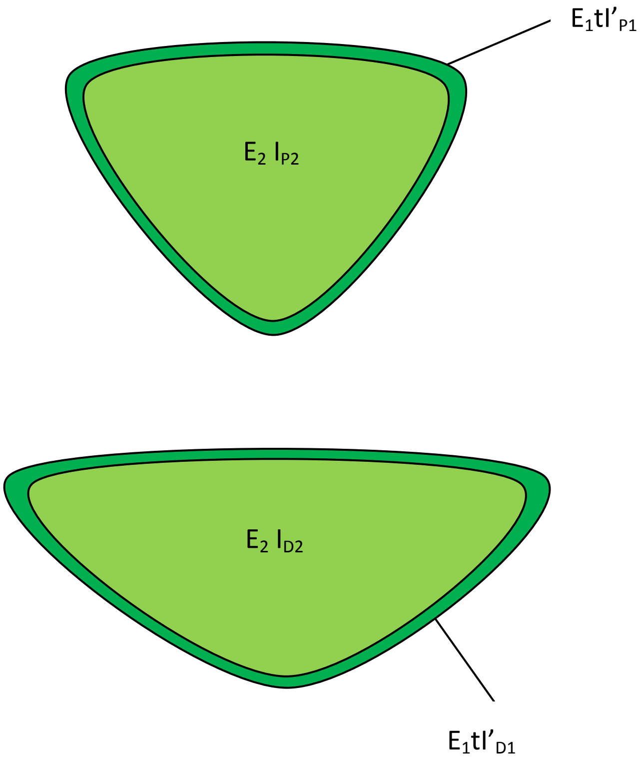

Figure 28 Young's modulus, E and second moment of area, I notation used in bi-layered *petiole* model

It was assumed that E_1 and E_2 did not change along the *petiole* axis. E_1 relates to the Young's modulus of the epidermis and the hypodermis, normally made up of compactly arranged *sclerenchyma* cells. It is not known if these cells are heavily lignified or not (Cutler, 2005), and it may be possible to find out using the bi-layered model designed for this research. Therefore, estimating E_1 for these two, thin, combined outer layers should signify if they are lignified or not as the values of E for different degrees of lignified material are widely known.

Formulae for flexural stiffness in the proximal, P, and distal, D, segments using the notation in Figure 28 can be found in equations (43) and (44) where *EI* is the combined flexural stiffness.

$$\boldsymbol{EI_P = E_1 tI'_{P1} + E_2\, I_{P2}} \tag{43}$$

$$\boldsymbol{EI_D = E_1 tI'_{D1} + E_2\, I_{D2}} \tag{44}$$

EI was found using equations (45) and (46) for the *petiole* flexure tests as detailed in this thesis in sections 3.3.2 and 4.2.1, the empirical flexural test method and results.

$$\boldsymbol{\frac{FL^3}{3EI} = \delta_D} \tag{45}$$

$$\boldsymbol{\frac{FL^3}{3EI} = \delta_P} \tag{46}$$

Mean values for *petiole* deflections were calculated resulting from tests performed using diametrically opposite forces causing the deflections as indicated in equations **(47)** and **(48)**

$$\boldsymbol{\delta x_P = \frac{\delta_0 + \delta_{180}}{2}} \tag{47}$$

$$\boldsymbol{\delta x_D = \frac{\delta_0 + \delta_{180}}{2}} \tag{48}$$

Flexural stiffness was measured for two segments along the *petiole* axis enabling us to use the following two simultaneous equations (49) and (50) to calculate E_1 and E_2.

$$\boldsymbol{E_1 t I'_{P1} + E_2 I_{P2} = \frac{FL^3}{3\delta_P}} \tag{49}$$

$$\boldsymbol{E_1 t I'_{D1} + E_2 I_{D2} = \frac{FL^3}{3\delta_D}} \tag{50}$$

I_1 and I_2 were measured in Rhinoceros® NURBS modelling for Windows. Only E_1 and E_2 were unknown. The thin outer layer detail is shown in Figure 29.

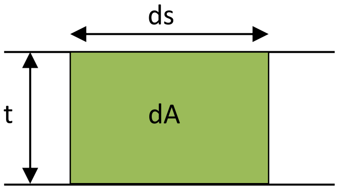

Figure 29 Detail of thin outer layer in bi-layered *petiole* model

The thickness, t, of the outer region was assumed to be very small, such that it could be assumed to be negligible when considering I_2, so I_2 was assumed to be the I of the whole shape.

Within the definition of I_{P1} in equation (31), the integral was shown as an open integral for the curve of the *petiole* perimeter. Likewise, the same applies to I_{D1}.

$$\boldsymbol{I_{P1} = \int y^2 t ds} \tag{51}$$

As t is not a function of the curve s, it can be taken out of the integral, changing I to I' as shown in equation (52). The definition of I'_{P1} is shown in equation (53) and so the units of I'_{P1} are mm^3 as opposed to I_{P1} which are mm^4.

$$\boldsymbol{I'_{P1} = \int y^2 ds} \tag{52}$$

$$\boldsymbol{I'_{P1} = I_{P1}/t} \tag{53}$$

Values for I_{P1} versus t were plotted for a range of very small thicknesses of t. Gradients of I_{P1} vs t as well as I_{D1} vs t were plotted for each test.

$$k_P = E_1 \, tI'_{P1} + E_2 \, I_{P2} \tag{54}$$

$$k_D = E_1 \, tI'_{D1} + E_2 \, I_{D2} \tag{55}$$

The parameters in red font in the simultaneous equations of equations (**54**) and (55) highlight the two unknowns, $E_1 t$ and E_2 which could then be found. As t was very small it was assumed that I_{P2} and I_{D2} were equal to I of the entire section. E_1 would be very large if t was very small, so a range of values for E_1 were obtained from a range of likely values for t.

3.4 Morphology

In nature, the two most common simple geometric structures to be found are the hollow cylinder and the solid cylinder, the former being more mass-efficient as the mass is further away from the neutral axis which is where the stress is highest (Burgess, 2005). Three methods have been designed in this thesis to extract clear trends in *shape transformer* data. If conventional *shape transformer* methods are used on natural section shapes, relatively few trends can be ascertained in the scattered *shape transformer* data. Circular envelope *shape transformer* analysis, Shape Edge

Mapping (SEM) and shape abstraction which is an application of SEM, are all methods designed as part of this research.

The question is how are the difficulties and inaccuracies of modelling natural section shapes overcome? When comparing shapes with reference to their ability to rotate under torsion, an error in the polar second moment of area, J, of up to 4% (Young & Budynas, 2002) results from using approximations of the torsional constant, J_T (a function of warping), for rectangles. Circular envelopes overcome this error as J_T equals J for circles.

Shapes of structures of the same type in nature, are variable so as to make accurate correlation between shape and ability to withstand torsion and/or bending very difficult as there is so much 'interference'. The work in this thesis has resulted in a technique called SEM which isolates physical parts and/or properties of an 2D natural form producing *shape transformer* data with clear trends. The scattered data is split first by 1) separation of edges (upper or lower) and 2) torsion or bending resistance shape mass efficiency.

In addition to overcoming the difficulties and inaccuracies of modelling natural section shapes, shape abstraction was performed using SEM, whereby families of theoretical data are created by adding variables to forms seen in nature, using this novel technique in section 3.4.7.

3.4.1 Novel procedure for acquiring petiole transverse section shape

3.4.1.1 Methodology

Prior to this research, the only methodology used that could be found in the literature to gather shape profiles of natural structures were Computed Tomography (CT) and Magnetic Resonance Imaging (MRI) and which although effective in terms of producing profiles (as well as internal images), are laborious and expensive to use. The new methodology designed for this research employs the use of two fine resolution metal contour profiling gauges brought together from the top and bottom edges of the *petiole* to form the *petiole* profile non-destructively.

Plant imaging using µCT scanning (X-ray computed tomography) works by attenuating X-rays as they pass through an object and so is a direct result of the object's density and chemical composition.

Using absorption-based synchrotron radiation microtomography (SRCT), a 1 μm^3 spatial resolution may be obtained. Small wood samples have a very weak absorption contrast but however produce significant phase shifts using X-ray beams. This is called phase-contrast tomographic microscopy where a 3D reconstruction of the refractive index from 2D phase images is produced (Trtik, et al., 2007).

Non-invasive Magnetic Resonance Imaging (MRI) has been used for the first time in 2015 to image *VBs* in live plants in three dimensions by researchers from the Plant Biomechanics Group of the University of Freiburg, Germany. In particular, *VB* spatial density and their branching was imaged together with their deformation when stress was applied. This technique is in its early stages, but it is the first time that it has worked on live plant tissues.

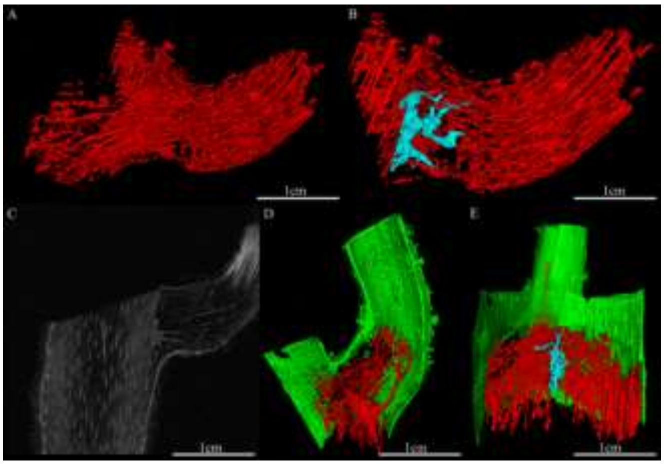

Figure 30 MRI scans of plant ramifications (credit: Linnea Hesse, (Hesse, et al., 2016))

Compared to other histological techniques and µCT scanning, the preparation prior to and post scanning is considerably less in MRI.

Non-destructive measurements of shape, such as MRI and CT could be valuable but would have been very difficult to carry out due to time and cost constraints.

A more cost effective methodology for non-destructively obtaining palm *petiole* profiles was used for the first time in this research using two fine toothed metal contour profiling gauges (Figure 31).

Figure 31 Profiling equipment used to measure the section shape of the *petioles*

3.4.1.2 Method

A summary of the shape capture profile method protocol is shown in Figure 32. Before the profiles were acquired, the two profilers (Figure 31) were aligned such that the profiling fingers were perpendicular to the holder and not skewed.

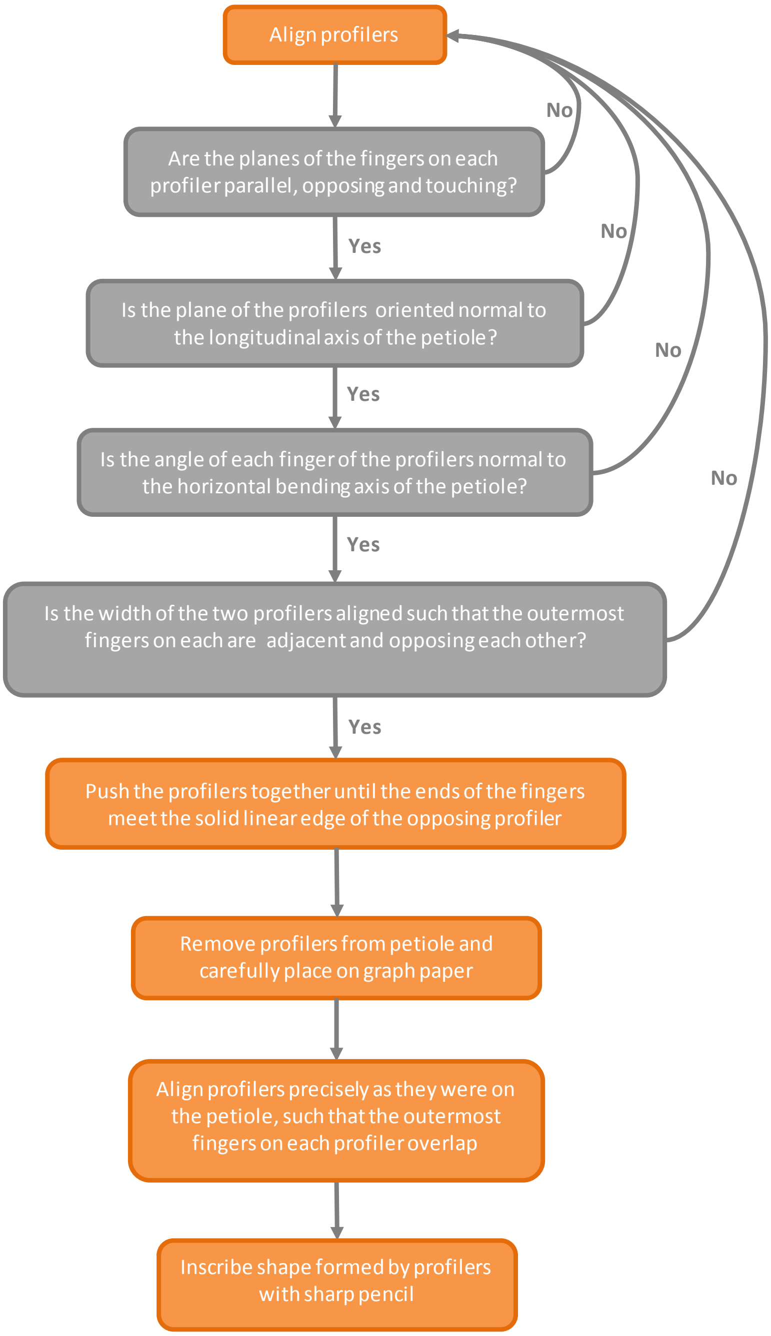

Figure 32 Shape capture protocol diagram

The profilers were pushed on to the upper and lower edges of the *petiole* in the following way:

1) The planes of the fingers on each profiler were parallel, opposing and touching.
2) The plane of the profilers was oriented normal to the (local) longitudinal axis of the *petiole* as sometimes the longitudinal axis of the *petiole* was curved slightly.

3) The angle of each finger of the profilers was normal to the horizontal bending axis of the *petiole*, such that the profilers moved in a direction normal to the transverse plane of the section.
4) The width of the two profilers were aligned such that the outermost fingers on each were adjacent and opposing each other.

The profilers were pushed until the ends of the fingers met the solid linear edge of the opposing profiler. The profilers were taken from the *petiole* and carefully placed on corrugated card board mounted with graph paper cut slightly larger than the board and secured with tape (Figure 33).

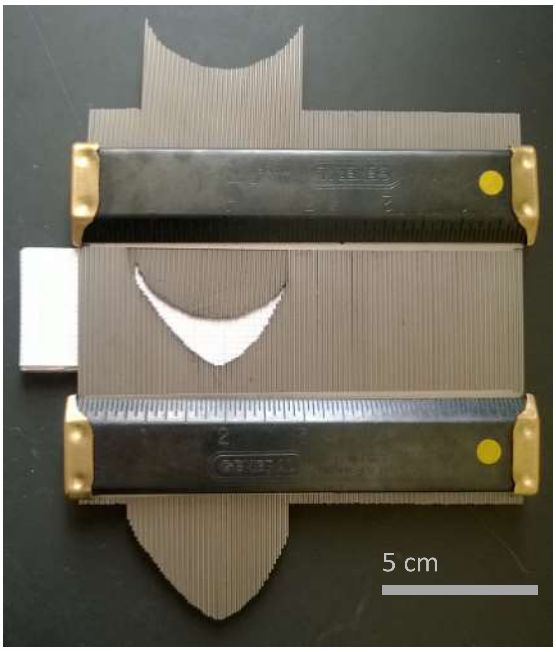

Figure 33 Profilers arranged on specially designed board mounted with graph paper ready for imaging with a fine pencil

The profilers were aligned precisely as they were on the *petiole*, such that the outermost fingers on each profiler overlapped. The ends of the fingers gently contacted the linear solid edge of the opposing profiler such that the outer fingers were aligned over each other. Using a sharp, pencil of hardness ‘H’, the outline of the *petiole* was drawn, by inscribing the shape formed by the profilers. Extra care had to be taken not move the fingers of the profilers, otherwise the profile had to be acquired again. The corresponding identification of the section was written on the results sheet for reference.

3.4.1.3 Verification of new profile acquisition method

The measurement error of the shape profilers was determined in two ways. Firstly, the linear measurement and secondly an area measurement.

Standard gauge blocks were used to compare with the profiler linear measurements. The blocks were put on a steel flat bed and the width readings taken twelve and eight times respectively for the 8mm and 30 mm blocks. The mean and standard deviation were calculated.

To calculate the accuracy of the proposed shape analysis method, the transverse section of a cylinder of known shape and size was tested using the new shape profiling method as described in section 3.4.4 of the Methods, ‘Acquiring the *shape transformer* data for palm *petioles*.

The size of transverse section of the cylinder was selected to be of a similar order to that of the tested *petioles*. Of the sampled *petiole* sections, *Latania vershaffeltii* (LvZ) had the largest proximal section area which measured 762 mm^2. The smallest transverse section area was that of the distal section of *T. fortunei* (*Tf*) which measured 64 mm^2. Many of the transverse sections had arc shaped upper and lower edges. As a result, a circular cylinder with a diameter of 25 mm (area 490 mm^2) was selected.

The diameter of the cylinder was measured five times using Vernier callipers at five equidistant positions along the length of the longitudinal axis of the cylinder. The temperature of the room was recorded before and after the measurements were taken.

The profile shapes of the circular cylinder were acquired using the shape profilers 20 times to calculate the measurement error of the shape profilers when measuring an area. The area of the profiles of the standard shapes using the profilers was compared to the known values of the same using Vernier callipers. The standard deviations and confidence intervals were calculated and discussed.

3.4.2 Method for petiole profile acquisition and associated blade and petiole dimensions

3.4.2.1 Selecting the palms to test

A selection of *palmate* and *costapalmate* palms had to be made of which there are many in the Palm House at the Royal Botanic Gardens, Kew, London. Palms from the three tropical and subtropical areas of the world where palms are indigenous i.e. regions from the Americas, Asia Pacific and Africa narrowed the selection down. As described in the paper by Windsor-Collins et al (Windsor-Collins, et al., 2007a), only palm *petioles* that could easily be reached with a step ladder were selected for measurement but only mature palms were sampled as juvenile palms may have different properties compared to their mature relatives. Only *petioles* with no apparent disease were sampled as those with disease may have different structural / material properties although, as would be expected, at Kew there was no sign of disease. Only *petioles* which were free from contact with any other vegetation were selected which would hinder adaptive growth (please refer to section 2.2.8 'Adaptive structures' in the Literature Review).

After the pre-selection filters had been applied, the transverse section shape profiles of *petioles* were taken from the following seven palm species: *Sabal minor* (Jacq.); *Leucothrinax morrisii* (H. Wendl.); *Latania vershaffeltii* (Lem.); *Pritchardia kaalae* (Rock.); *Kerriodoxa elegans* (Dransfield); *Borassodendron machadonis* (Ridley) and *Trachycarpus fortunei* (Hook). These palms are shown in Figure 34 with one of the measured *petioles* indicted with a white arrow.

(a) S. minor *(b) L. morrisii*

(c) L. vershaffeltii *(d) B. machadonis* *(e) K. elegans*

(f) P. kaalae *(g) T. fortunei*

Figure 34 Photographs of the palms at The Palm House, RBG Kew, from which profiling data were acquired ((Windsor-Collins, et al., 2007a)

3.4.2.2 Location and frequency of sampling

With regards to *petiole* sampling adequacy, the profile shape and transverse sectional area of each *petiole* was sampled at three equidistant locations along the axis; P, C and D. The shapes of the *petioles* measured changed smoothly along the axis, tapering towards the leaf blade. The three measurements taken at equidistant points from each other over the length of the *petiole* is therefore statistically satisfactory.

For the purposes of economy and focus, one *petiole* was chosen from each palm species. The selected *petioles* were estimated to be of typical dimension and shape and were visually disease free. The research data were non-dimensionalised and so the various sizes of the *petioles* on each palm are irrelevant. The fact that not all *petioles*, sizes and locations are presented is therefore not an issue.

One *petiole* was tested from each of the seven palms. Each *petiole* was sampled at three equidistant locations along the longitudinal axis. They were marked with a piece of string tied around the *petiole* and named P (proximal), C (central) and D (distal) as shown in Figure 35.

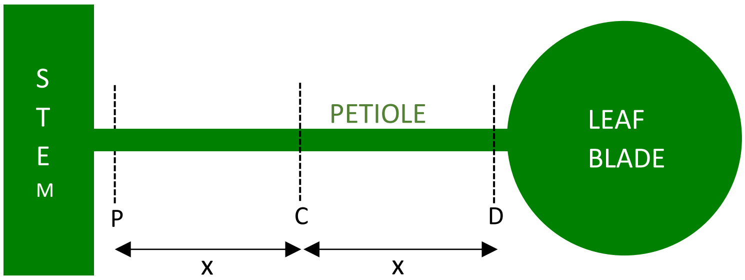

Figure 35 Palm *petiole* schematic showing the relative placement P, C and D profiles – figure adapted from (Windsor-Collins, et al., 2007a)

For the *shape transformer* measurements, four of the seven palms were tested. Thirty-two profiles were taken using the method in 3.4.4 ‘Acquiring the *shape transformer* data for palm *petioles*’ for each transverse section with the aim of making the measurement error less than 1%, currently expected as a minimum in engineering measuring devices. An illustration showing the profiles for one *petiole* from *K. elegans* is shown in Figure 36.

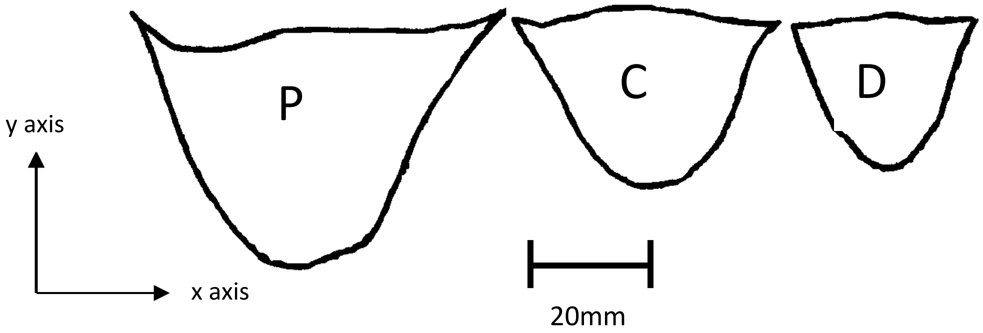

Figure 36 Profiles P, C & D from one *K. elegans petiole* – figure adapted from (Windsor-Collins, et al., 2007a)

3.4.2.3 Method for recording associated blade and petiole data

Palm profile samples were acquired using the novel method described in section 3.4.1.2. As described in the paper by Windsor-Collins et al (Windsor-Collins, et al., 2007a), associated dimensions were gathered relating to the palm from which the *petiole* profile samples were taken. These were *petiole* length, stem diameter, distance from ground along the stem to where *petiole* emerges from stem and the length and width of the blade. The *petiole* length was measured from the *hastula* (Figure 37) to a point along the longitudinal axis of the *petiole*, 20 cm in-line with the main part of the *petiole* from the palm stem. This was done for consistency as the structure of the interface between the *petiole* and stem can vary between palm species and to discount the most curved part of the *petiole*. Associated measurements for *Ke*, *Lv*, *Pk* and *Tf* were recorded on pro-forma data sheets in Figure 109, Figure 110, Figure 111 and Figure 112.

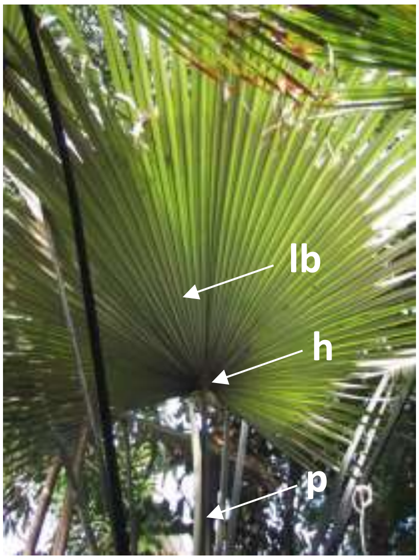

Figure 37 Leaf blade and *petiole* of the palm *K. elegans* showing the location of the *hastula*, *h*, in relation to the *petiole*, *p*, and the leaf blade, *lb*. Figure adapted from (Windsor-Collins, et al., 2007a)

3.4.3 Circular envelope shape transformer methodology

The shape, S, of a transverse section of a *petiole* that is circumscribed by a circular envelope, D, is shown in Figure 38 which demonstrates the juxtaposition of the shape and the new envelope.

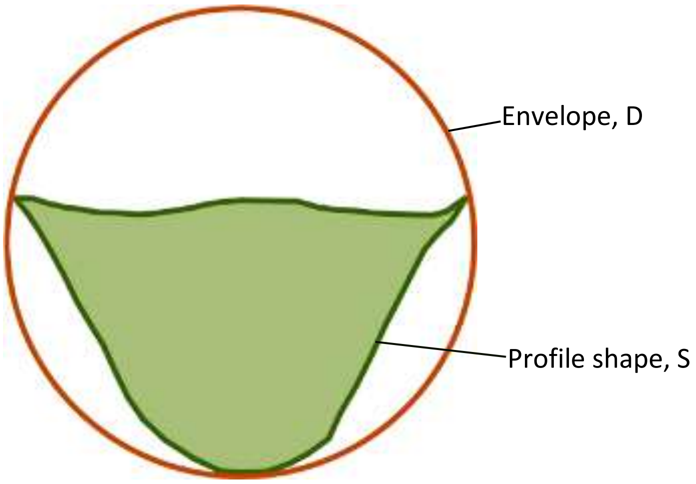

Figure 38 Profile, S, in relation to the circular envelope shape, D.

Pasini & Mirjalili (Pasini & Mirjalili, 2006) acquired *petiole* transverse-section data for ten *Dicotyledon petioles* (not palm) using rectangular envelopes and compared these with the efficiency of idealised ellipse and semi ellipse shapes. Following on from this, shapes can be compared to circles directly by using circular envelopes, simplifying the process.

Generally, *shape transformers* are used to quantify differences in shape between cross-sections by normalisation. For a given cross-section, a *shape transformer*, ψ_G is defined where G is the normalised geometric quantity of either: area, A, second moment of area, I, or polar second moment of area, J, as defined equations (2), (1) and (26). However, the normalised *shape transformer* for torsion using circular envelopes is more accurate than the conventional term.

The torsional constant, J_T for non-circular shapes is found exactly by using the Saint Venant semi-inverse method requiring the surface integration of a warping function over the surface.

Replacing rectangular envelopes with the new circular envelopes in the design of the new *shape transformer* for torsion, ψ_{JT}, eliminates the error in J_{TD} as it is no longer approximated. For circular envelopes J_{TD} can be simply replaced by J (which is J_C for a circle), thereby not incurring any warping factor approximation for the envelope. The simplified equations for J_T using rectangles involve an approximation, with a resulting error of up to 4% (Young & Budynas, 2002). ψ_{JT} is defined in equation (56) where J_T is the torsional constant of the shape. Circular envelopes therefore reduce the total error as still, the J of the shape, if not regular should ideally be J_T.

$$\Psi_{JT} = J_T/J_C \tag{56}$$

3.4.3.1 Disadvantages of rectangular envelopes

Warping constants should be taken into consideration for the rectangular envelope when calculating the polar second moment of area. There are instances in the literature where J_T of the rectangle is assumed to be J as in (Pasini, 2008).

J_T is a measure of how stiff a shaft is in turning for a given G. It increases, the harder it is to twist. When rectangular envelopes are used, J_T can be very different for rectangles of different aspect ratio, J_T being smaller, the greater the aspect ratio of the rectangle is. As the aspect ratio of circular envelopes is always unity, this approximation to J_T which varies with aspect ratio is not encountered.

Rectangular envelopes were used when calculating the *shape transformers* for flexural stiffness and torsional stiffness for palm *petioles* in a paper by Windsor-Collins et al (Windsor-Collins, et al., 2007a) and these were compared to *shape transformers* using rectangular envelopes of *Dicotyledon*s calculated by Pasini & Mirjalili (Pasini & Mirjalili, 2006). However, although the method used to calculate the *shape transformers* was the same in both papers, neither (incorrectly) applied relative scaling factors which are dependent on the aspect ratio of the envelope.

3.4.3.2 Significance of warping when analysing palm petioles

For shafts of non-circular section, warping of the cross-section takes place under the action of torque (Ryder, 1955). However, when subjected to torsion, every cross-section of a circular shaft remains plane and undistorted.

Warping in relation to torque and shear stress is explained whereby the torque, T, applied to a circular shaft, produces complimentary shear stresses in the longitudinal plane causing a distortion of filaments and a cross sectional warping distribution. The assumed points on the radius r remain on the radius after twisting which is justified by the symmetry of the circle. The shear stress, τ, is proportional to the distance along the radius, ρ, and for τ_{max}, this equals the radius, r as shown in equation (57):

$$\tau = \frac{\boldsymbol{Tr}}{\boldsymbol{J}} = \boldsymbol{\tau max} \tag{57}$$

The corresponding formula for the angle of twist, θ, is shown in equation (41).

For circular sections, the shear stress, τ, is equal to the maximum shear stress, τmax, at the same radial distances from the centre as shown in Figure 39

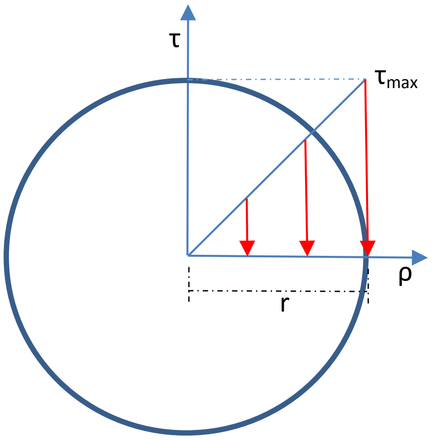

Figure 39 Distribution of shear stress, τ, within a circular cross-section where ρ is the distance along the radius, r

Shear stress varies linearly with the radial position within the circular section. The sum of the moments from the internal stress distribution is equal to the torque on the shaft at the section resulting in equation (57) for circular sections.

New methods and applications are required to produce better approximations to shape with respect to torsion and warping constants so that shape technology from biological optimisation mechanisms to mechanical engineering and design can be more accurately and easily transferred.

The reason why the warping term is relevant when testing the palm *petioles* in this research is explained. The second term of the 'Torque of a shaft in equilibrium' equation (38) describes the effect of warping within the cross section. It is required when warping is prevented at the support. This is the case with the palm *petiole* at one end, when in vivo, and at both ends in the torsion test.

The warping term is negligible for shafts with a length to depth ratio of more than six (providing that both ends are free to warp) (Mirjalili & Pasini, 2007). The palm *petiole* sections tested had a length to depth ratio of more than six, but as they were restrained, warping is significant. The second term in equation (38) must therefore be included.

The *hastula* (Figure 37 and Figure 40), a structure located at the interface between the *petiole* and the leaf blade, of the *palmate* palm, may act as a warping restraint, resisting its ability to twist, as its main flange is orientated normal to the *petiole* axis, an area for further research. Currently it is not known what the purpose of the *hastula* is (Dransfield, 2003). Such a warping restraint causes longitudinal stresses to occur within the shaft, which otherwise would not occur making it stiffer to rotate.

Figure 40 *Palmate* palm showing the *hastula* taken at Fairchild Botanic Garden, Florida

For non-circular cross –sections, there are no exact analytical equations to work out the torsional constant, although approximate solutions are obtainable for many shapes. For example, the torsional constant, J_T, for a solid rectangular cross section is given in simplified form in equation (43) where $2a$ and $2b$ are the length of the long and short sides of a rectangle respectively involving an approximation, with a resulting error of up to 4% (Young & Budynas, 2002).

$$J_T = ab^3[\frac{16}{3} - 3.36\left(\frac{b}{a}\right)\left(1 - \left(\frac{b^4}{12a^4}\right)\right] \; for \; a \geq b \tag{58}$$

As a worked example, using equation (58), if a = 2 m and b = 1 m then J_T = <u>7.234 m^4</u>. A slightly different value for J_T is obtained when Ashby's definition of J_T is used (Ashby, 1991). For a rectangle where $h > b$, J_T is calculated to be <u>7.573 m^4</u> in equation (59) where the height of the rectangle, h, is 4 m and the width, b, is 2 m (the same example as applied to in the Young and Budynas in equation (59).

$$J_T = (b^3h/3)(1 - 0.58\left(\frac{b}{h}\right)) \tag{59}$$

Table 5 and Figure 41 show how J varies with J_T for the two approximations to J_T which show that the J_T derived by Young and Budynas (Young & Budynas, 2002) is slightly different to that derived by Ashby (Ashby, 1991) but not significantly different.

Table 5 *J* vs *J_T* for rectangles of aspect ratios from 1 to 10

Rectangle height, h / m where h>b	Rectangle breadth, b / m	h/b	J / m^4	J_T / m^4 (formula from Ashby 1991)	J_T/J as a % (Ashby 1991)	J_T / m^4 (formula from Young and Budynas formula, 2002)	J_T/J as a % (Young and Budynas, 2002)
1	1	1	0.17	0.14	84	0.14	85
2	1	2	0.83	0.47	57	0.46	55
3	1	3	2.50	0.81	32	0.79	32
4	1	4	5.67	1.14	20	1.12	20
5	1	5	10.83	1.47	14	1.46	13
6	1	6	18.50	1.81	10	1.79	10
7	1	7	29.17	2.14	7	2.12	7
8	1	8	43.33	2.47	6	2.46	6
9	1	9	61.50	2.81	5	2.79	5
10	1	10	84.17	3.14	4	3.12	4

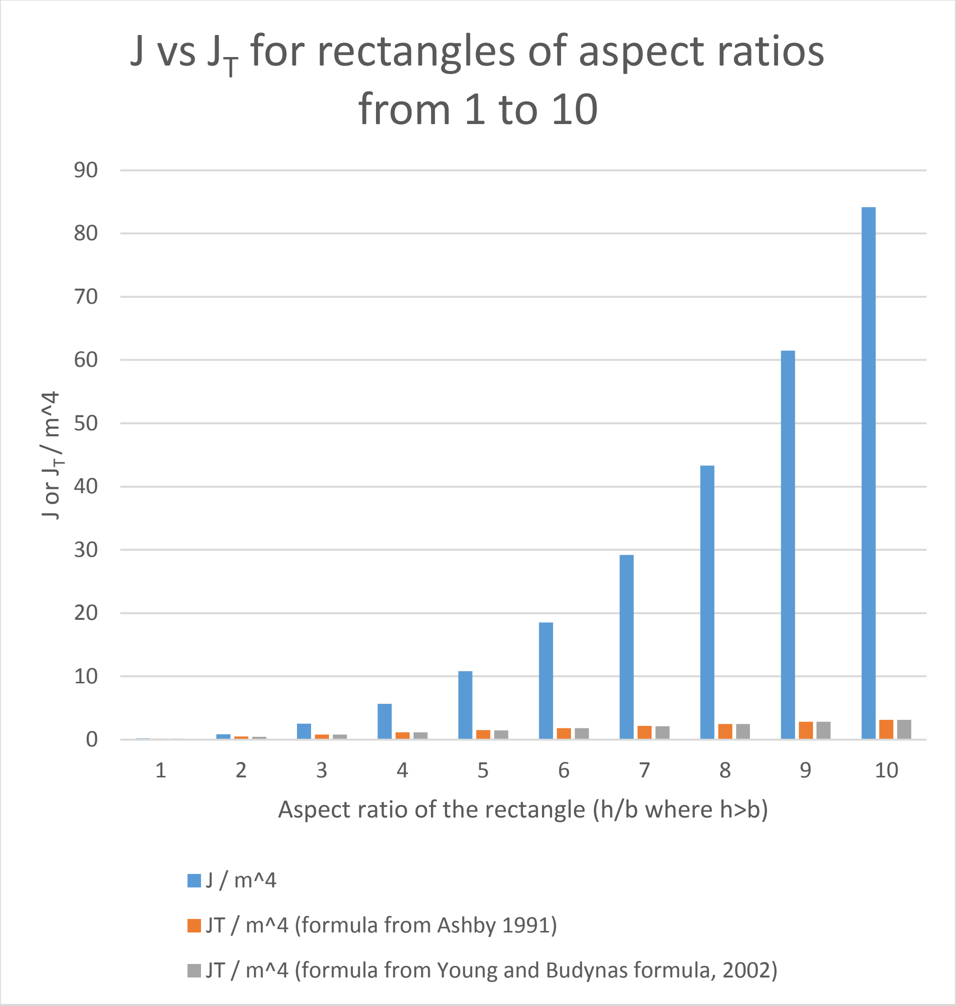

Figure 41 J versus J_T for rectangles of aspect ratios from 1 to 10

3.4.3.3 Scaling or not of the circular envelope shape transformers

The aspect ratio of rectangular cross section envelopes which circumscribe *petioles* varies in relation to the slenderness ratio of the natural shapes as is common in nature. Comparisons are not valid between shapes using rectangular envelopes if these envelopes have different aspect ratios and have not been scaled. Work previously done by Pasini and Mirjalili (Pasini & Mirjalili, 2006), and Windsor-Collins et al (Windsor-Collins, et al., 2007a) who used the same method, did not apply scaling to the envelopes as should have been done.

Circular envelopes however, do not require scaling as their aspect ratio is always unity, so when *shape transformers* are compared, shapes are compared that are within the same envelope shape.

3.4.3.4 Methodology for performance indices and efficiency charts

Efficiency charts (whereby ψ_I versus ψ_{JT} are plotted) were produced for the three sections of *petioles* of four species of arborescent palm using the circular envelopes developed in this research. The more efficient the structure was in terms of shape, the lower the shape's torsional resistance and the higher the shapes bending resistance (twist-to-bend ratio) compared to a solid circle. ψ_I versus ψ_A and ψ_{JT} versus ψ_A were also plotted on flexural and torsional mass-efficiency charts respectively showing how mass-efficient the *petiole* transverse-sections were for a given bending or twisting ability compared to a solid circle.

3.4.4 Acquiring the shape transformer data for palm petioles

One *petiole* from each of four species of palm were sampled. Transverse-sections (P, C and D) from each *petiole* were sampled 32 times as described in section 3.4.1.2. The profiles were scanned and subsequently transcribed using Adobe Illustrator into a CAD package (Rhinoceros® NURBS modelling for Windows®) enabling the area, centroid, second moment of area and polar second moment of area to be processed of the profile and the circumscribed circular envelope, for which the *shape transformers* were calculated. The standard deviations and percentage standard deviations and 95% confidence intervals of the *shape transformers* were then recorded.

3.4.4.1 Profile scanning method

The transverse section profiles of *petioles* were scanned at 600 dpi and saved as .bmp files. To ensure that the scaling remained at 100% throughout the scanning process, a 1cm^2 square was drawn on the same piece of graph paper as the *petiole* profile, the area of which was later checked in Rhino.

3.4.4.2 Profile digitising method

The scanned profiles were opened in Adobe Illustrator and using the pen tool (of one 'point' thickness), the shapes were digitised, taking care to digitise the inner edges of the profiles and the points nearest to the centre of the profile to take into account the thickness of the profiler fingers. The 1cm^2 square was also digitised to later verify in Rhino, that no scaling had occurred during the scanning and digitising process. The old images of the profiles were then deleted, the file saved and exported from Illustrator as .ai files, ensuring the box for 'use compression' was unticked.

3.4.4.3. Shape analysis in Rhino

Rhinoceros® NURBS modelling for Windows® was opened during which the units in Rhino were changed to 1mm = 1 Rhino unit in the dialogue box. The *petiole* profiles and the 1cm^2 square .ai files were then opened. Each *petiole* shape was rotated such that visually, the line of symmetry was vertical resulting in an equal second moment of area about the bisecting y axis. The area of the imported square was determined in Rhino using the analyse tool and checked, the procedure only proceeding if the two areas were the same verifying that no scaling occurred during the scanning and digitisation processes.

Surfaces were created for the profiles and the area, second moment of area and polar second moment of area of each profile was obtained using the Analysis – Mass Properties – Area Moments tool.

The palm *petiole* transverse-sections were circumscribed with a circle. Surfaces were created for the circumscribed circles and the A, I and J of the envelopes were determined again using the Area Moments tool. The ratio of A, I and J of the profile with that of the circular envelope was then calculated producing *shape transformers* ψ_A, ψ_I and ψ_{JT} in equations (2), (1) and (26) respectively.

Figure 42 shows samples of the *petiole* transverse-section profile sections P, C and D for *Kerriodoxa elegans*, along with their circular envelopes.

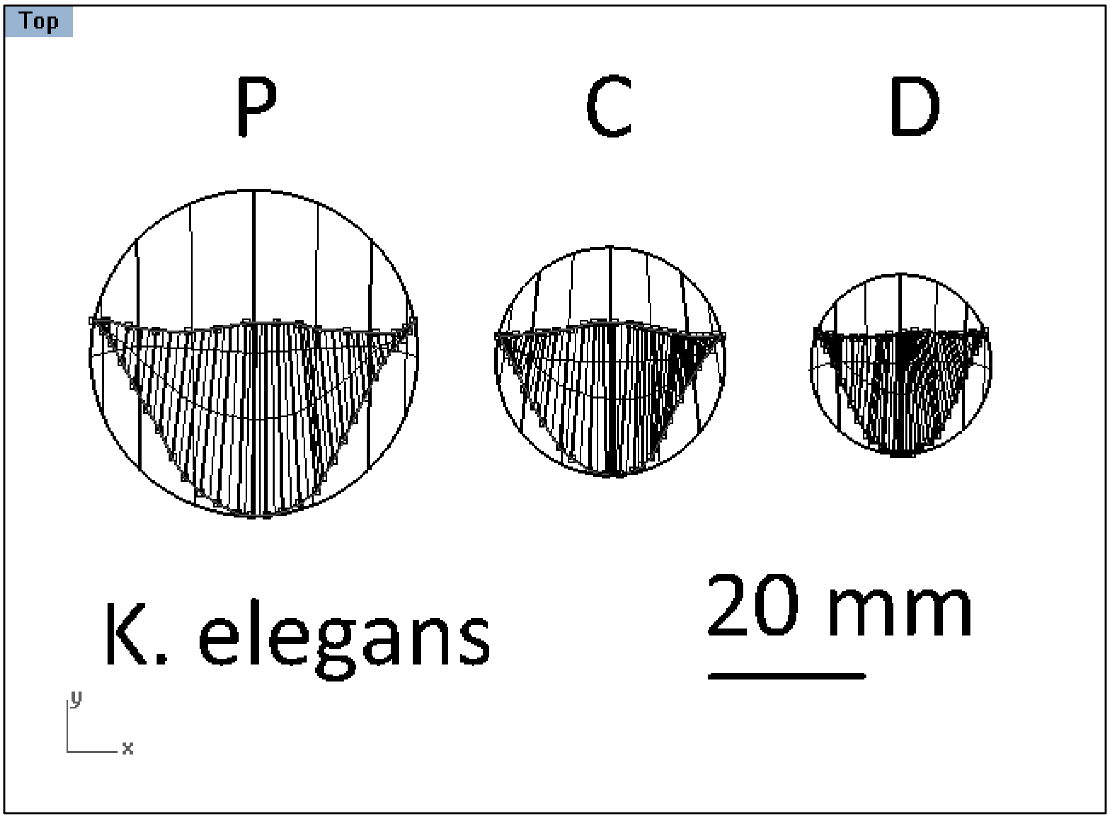

Figure 42 Profiles P, C and D of *Kerriodoxa elegans*

From these *shape transformers*, three types of efficiency charts were created for the *petiole* transverse-sections as follows:

1) ψ_I versus ψ_A for bending resistance mass (area) efficiency with respect to a circle
2) ψ_{JT} versus ψ_A for torsion resistance mass (area) efficiency with respect to a circle
3) ψ_I versus ψ_{JT} for shape twist-to-bend ratio with respect to a circle

Performance indices λ_{IA}, λ_{JAT} and λ_{IJT} were calculated from the *shape transformers* as defined in equations (27), (30) and (32) respectively.

3.4.5 SEM Shape Edge Mapping

3.4.5.1 SEM methodology

The SEM technique developed in this research employs the use of circular envelopes to extract torsion and flexural *shape transformer* data, from the edges of bi-lateral, non-regular, cross-section shapes of natural section shapes such as palm *petiole* transverse sections. As with shape analysis using circular envelopes, SEM uses *shape transformers* to separate shape from size by normalising geometric quantities. SEM was used to identify the contribution of the shape of the separate upper and lower edges of a *petiole* transverse section to the performance of the whole section in terms of resistance to torsion and bending and mass-efficiency as a result of shape.

The closeness of fit of the data to a quadratic curve trend line to the *shape transformer* data was recorded. A quadratic curve was used for consistency on all *shape transformer* plots and is sensitive enough to filter the data sufficiently. The more aligned the *shape transformer* data is to the trend line, the more that portion of the *petiole* is adapted to the role described by the *shape transformer*. Families of similar shapes can then be abstracted for further analysis.

Figure 43 and Figure 44 illustrate how this conclusion was made and how the individual breakdown of the components is useful:

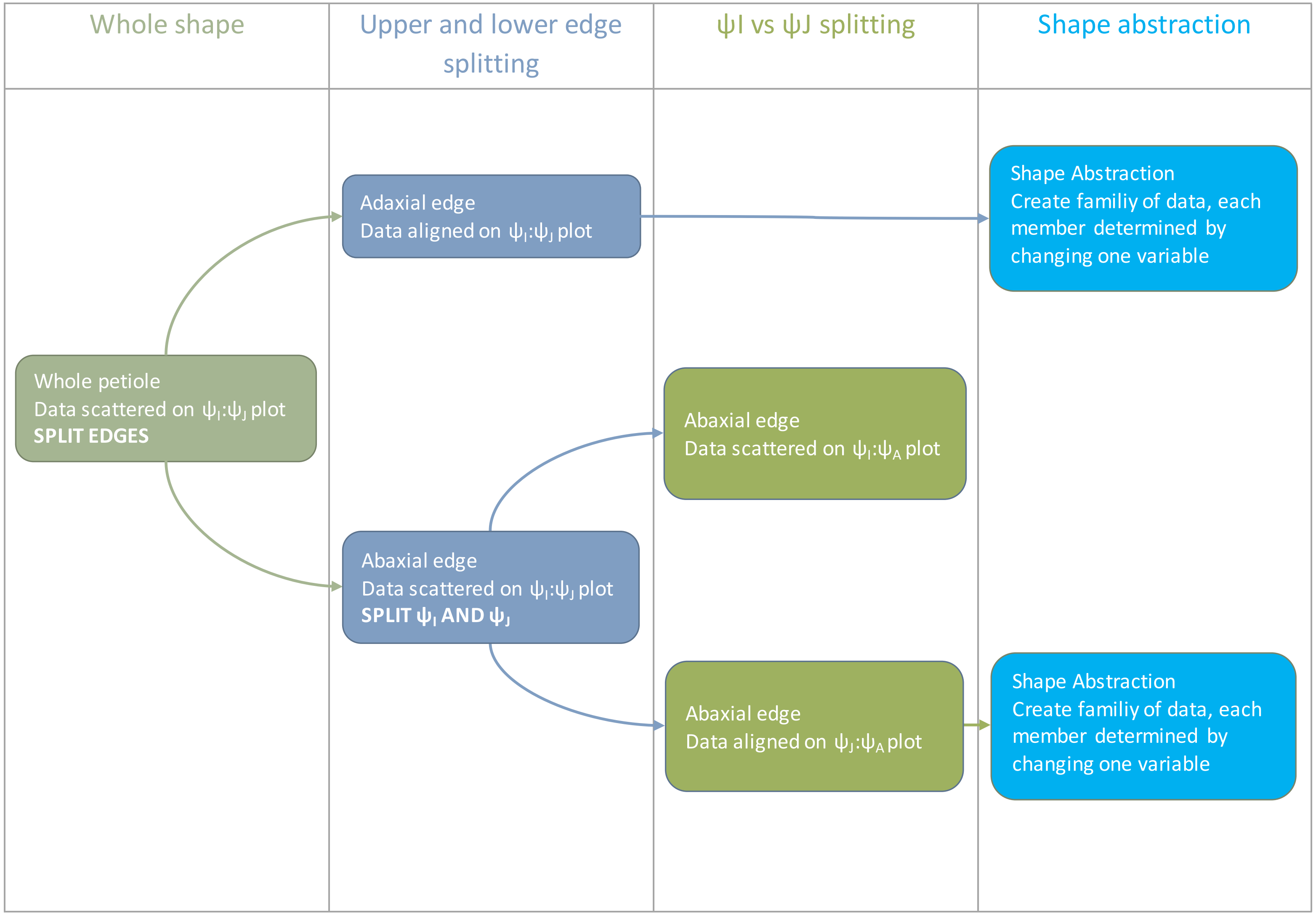

Figure 43 SEM methodology with palm *petiole* example

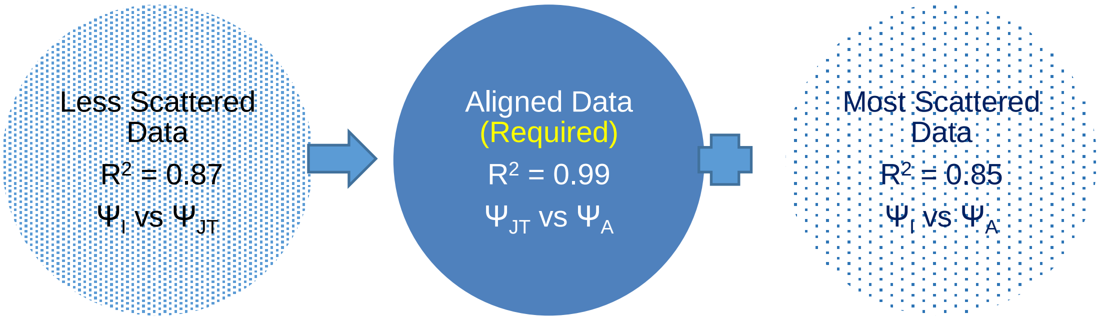

Figure 44 SEM technique data scatter sorting mechanism schematic example

3.4.5.2 SEM method

Each *petiole* profile was divided into its upper and lower edge. Each edge was made into a closed shape by joining it up with a circular arc which coincided with the circle to circumscribe the modified *petiole* shape. The *shape transformers* of these modified shapes indicated the contribution of each edge to the shape function of the whole *petiole* transverse section.

The Shape Edge Mapping (SEM) method designed in this research, constitutes three main steps; shape data acquisition, shape edge splitting and identification of trends in *shape transformers* as follows:

1) The *petiole* profiles were acquired and transcribed using the method in section 3.4.4.

2) The upper edges of each transverse section shape was separated from the lower edges in Rhino at the two most lateral extents. The removed lower edge was then replaced with the arc of the circle that would circumscribe the retained edge. Likewise, the removed upper edge was then replaced with the arc of the circle that would circumscribe the retained edge. Figure 47 shows how these edges were then re-constructed into 2D shapes. *shape transformers* for the re-constructed 2D shapes were then obtained using the same method as for the whole *petiole* cross-sections using circular envelopes.

3) *shape transformer* trends were identified by plotting the three different *shape transformer* coordinate combinations relevant to torsion and bending i.e. Ψ_I vs Ψ_A and Ψ_{JT} vs Ψ_A *and* Ψ_I vs Ψ_{JT}.

The closeness of fit of the data to a quadratic curve trend line was recorded and discussed. Quadratic curves were used on all *shape transformer* plots for consistency and is sensitive enough to filter the data sufficiently. To illustrate this third stage of SEM, actual *shape transformer* data from the lower *petiole* edges and circular arc upper edges are used in Figure 44.

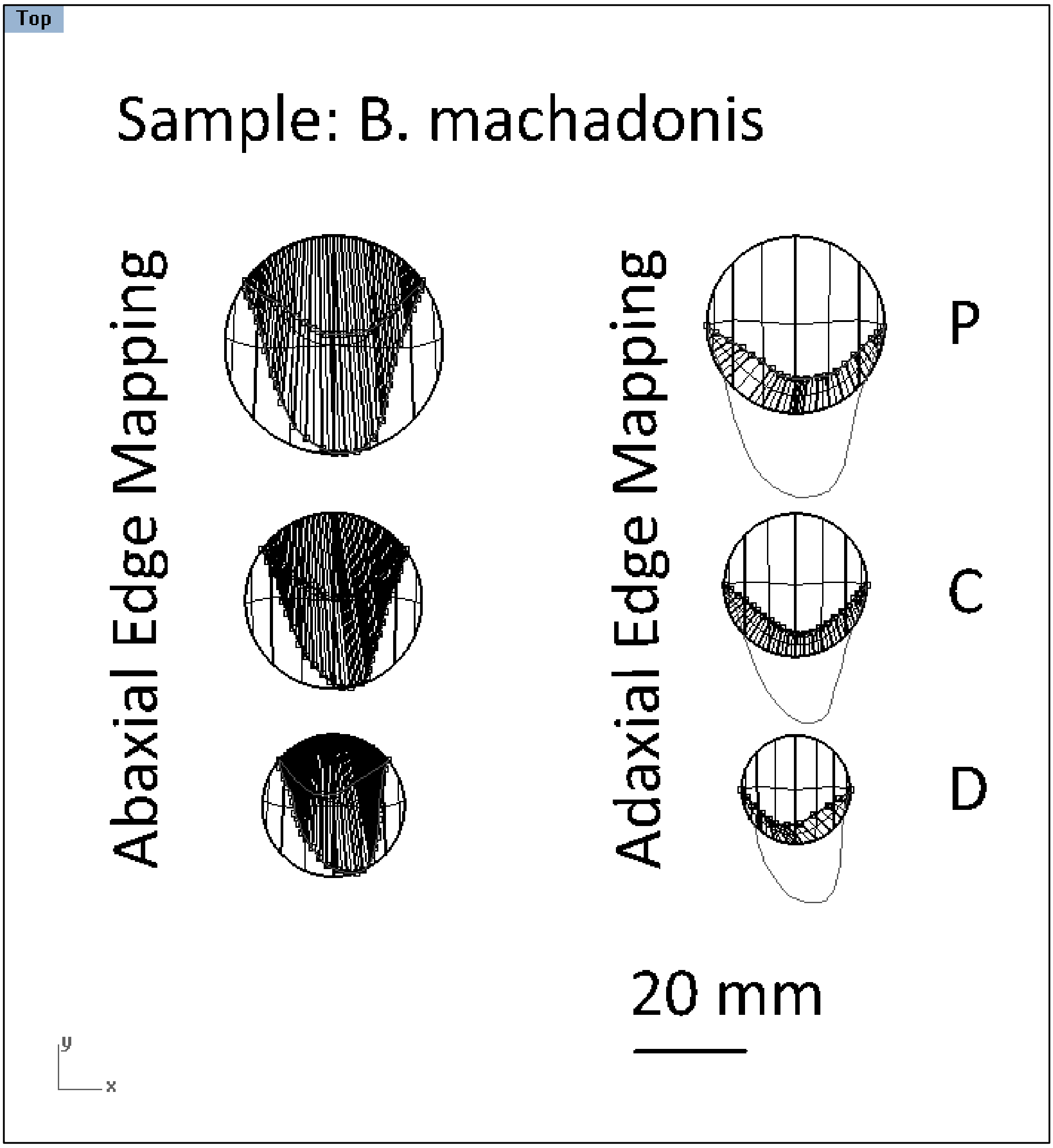

Figure 45 *Borassodendron machadonis* sample Rhinoceros® profiles showing shape edge splitting

3.4.5.3 Verification of SEM with regular shapes

Shape Edge Mapping, SEM, was verified by applying it to regular shapes. The shapes selected were the circle, equilateral triangle, square and hexagon. Using the SEM method in section 3.4.5.2, the regular shapes were split into the upper and lower edges, each edge being then reformed into a shape with a circular arc, coincident with the circular envelope. Figure 46 shows the orientation of the shapes with respect to the x axis and the envelopes in Rhino. *shape transformers* ψ_A, ψ_I and ψ_J and performance indices λ_{IA}, λ_{JA} and λ_{IJ} were calculated for each of the derived shapes.

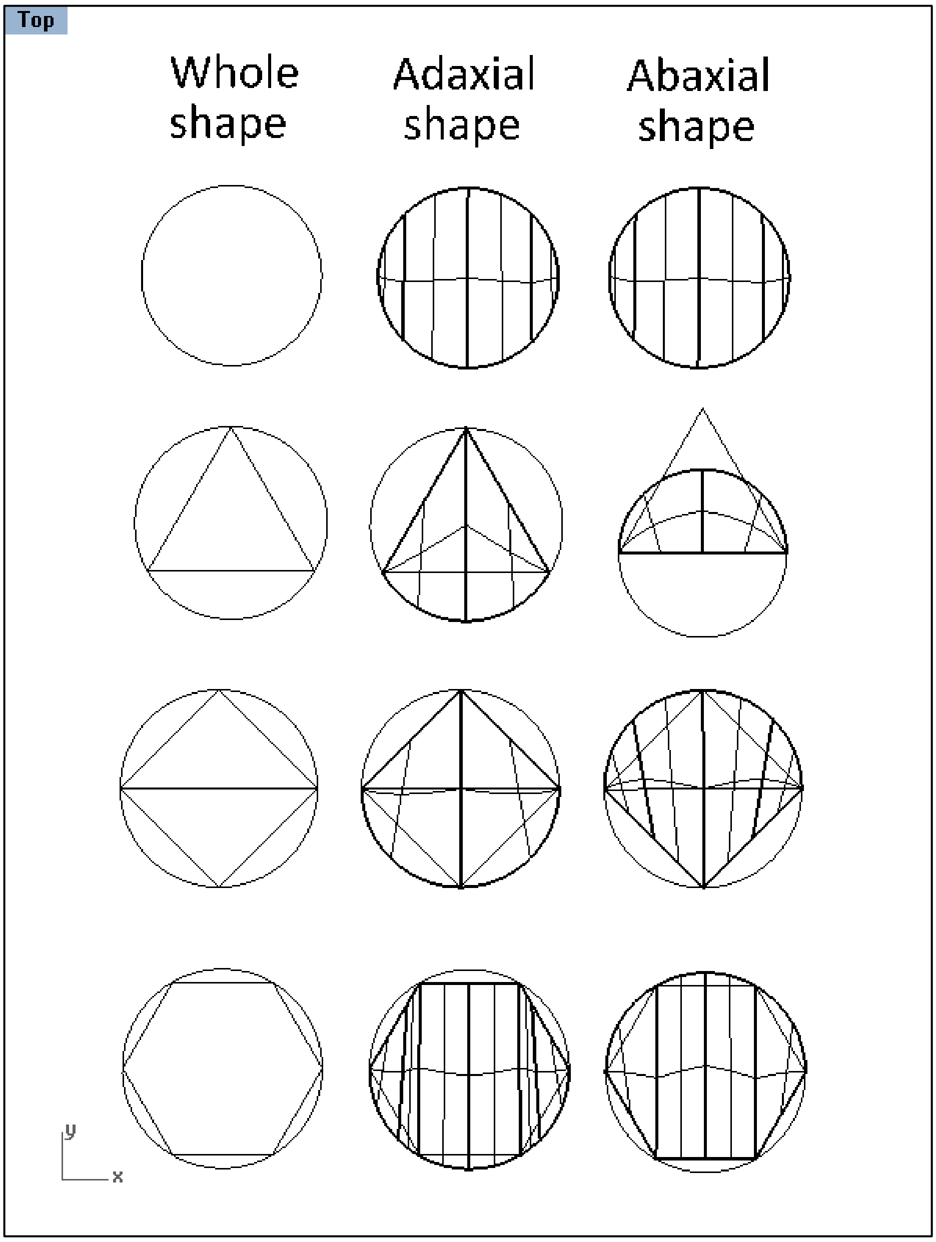

Figure 46 Regular shapes in Rhino showing derivative SEM shapes and envelopes

3.4.6 Shape abstraction methodology using SEM

It was noted that the number and depth of the grooves and ridges on the tops of *petioles* varied along the *petiole* and between palm species. Grooves and ridges observed on the *adaxial* (upper) edges of palm *petioles* were modelled by representing them as Non Uniform Rational B Spline (NURBS) curves.

Families of these shapes, were made by varying the height of the ridges and troughs only. *shape transformers* and performance indices were then analysed. Further to this, hypothetical families not observed in the *petioles*, but part of the same theoretical set, were processed in the same way.

Petioles from seven species of palm were observed (Figure 47). These species were, *Sabal minor*, *Sm*, *Leucothrinax morrisii*, *Lm*, *Latania vershaffeltii*, *Lv*, *Pritchardia kaalae*, *Pk*, *Trachycarpus fortunei*, *Tf*, *Kerriodoxa elegans*, *Ke* and *Borassodendron machadonis*, *Bm*. The classification for *Thrinax morrisii* has changed during this research to *'Leucothrinax morrisii'* and although the new name is represented in this thesis, some of the original acquisition data may refer to the previous name.

A way of defining the ridges and grooves was necessary for reference purposes. Wavenumber, defined as the spatial frequency of a wave, in cycles per unit distance in the physical sciences, was used in this research to avoid the confusion with temporal wavelength.

More specifically, the magnitude of a wave vector is the wavenumber of the wave which is inversely proportional to the wavelength. The direction of the wave vector is usually the direction of wave propagation and is not relevant in this research. The wavenumber 'k' (spatial angular frequency) describes the number of oscillations per unit of space and is related to wavelength 'λ' by the equation: $k = \frac{2\pi}{\lambda}$. Table 6 shows the relationship between wavelength and wavenumber for the four families observed in palm *petioles*.

Table 6 Wavenumber families observed in families and their wavelength analogy

Wavenumber k families (spatial equivalent)	'Wavelength' λ (temporal analogy)
4π	0.5
2π	1
1.333π	1.5
π	2

The height (equivalent to 'amplitude') of static waveforms was the variant making up the members of each family. Approximations to static wave forms observed on the upper edge of *palmate* and *costapalmate* palm *petioles* were 0.5, 1, 1.5 and 2 'wavelength forms' (Figure 47).

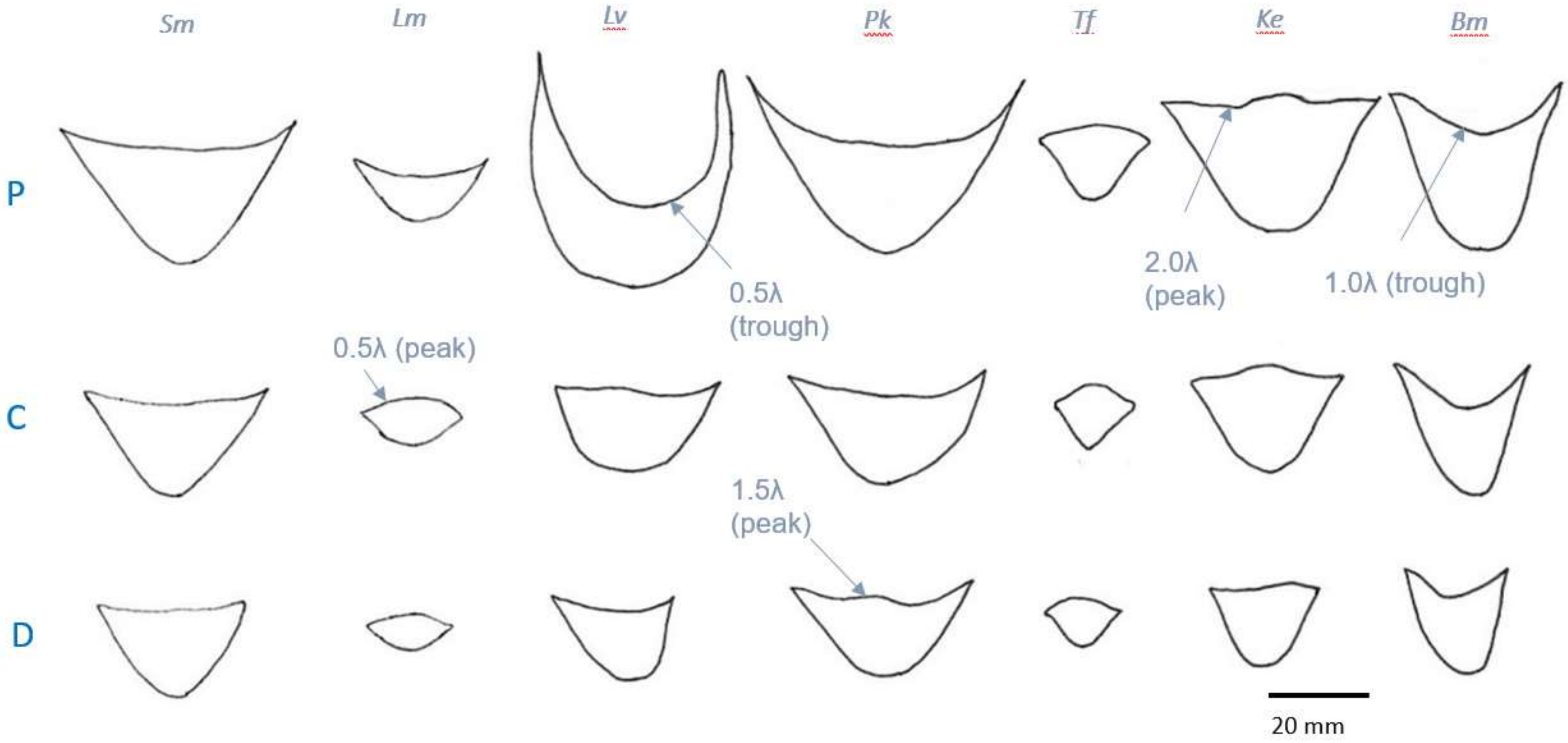

Figure 47 Seven palm petiole profiles observed for shape abstraction

3.4.7 Shape abstraction method

The details of the SEM technique may be seen in Figure 43 and Figure 44. First, the 2D shape profiles are studied to identify patterns in their forms and selected. Next, the edges of the forms are isolated using SEM and the 2D shape re-formed by adding a circular arc to the isolated edge. Shape resistance to bending versus shape resistance to torsion data are then plotted. If the data align, then families of similar data can be created for efficiency selection charts for ψ_I versus ψ_A, ψ_J versus ψ_A and ψ_I versus ψ_J. If the ψ_I versus ψ_J data do not align to a second order or first order curve, then ψ_I versus ψ_A should be plotted. If the data are aligned, then families of similar data can be created for efficiency selection charts for combinations of ψ_I versus ψ_A and ψ_J versus ψ_A. If the ψ_I versus ψ_A and ψ_J versus ψ_A data do not align to a second order or first order curve, then ψ_J versus ψ_A should be plotted. If the data are aligned, then families of similar data can be created for efficiency selection charts for ψ_J versus ψ_A. If the ψ_J versus ψ_A data do not align to a second order or first order curve, then the form of the profiles has to be studied again and a less complex edge selected for SEM.

Examples of how three static waveform families were created in Rhinoceros® NURBS modelling for Windows are shown in Figure 48. They show the waveform shapes circumscribed by circular envelopes. Static waveform nodes were positioned at each end of the diameter of the circular envelope. The static amplitude ranged from zero to the maximum possible within the circumscribed circular envelope. The amplitude increased in 1 mm increments to create family members.

shape transformer charts ψ_I versus ψ_A, ψ_{JT} versus ψ_A *and* ψ_I versus ψ_{JT} and performance indices λ_{IA}, λ_{JTA} *and* λ_{JTI} for the different 'amplitudes' and wavenumber families were analysed.

Initially, only families for 'waveforms' observed on *petioles* were plotted. A notable trend for the 1.5λ family was observed, so hypothetical 1.2, 1.4, 1.6 and 1.8λ families either side of the 1.5λ family were compared on *shape transformer* charts.

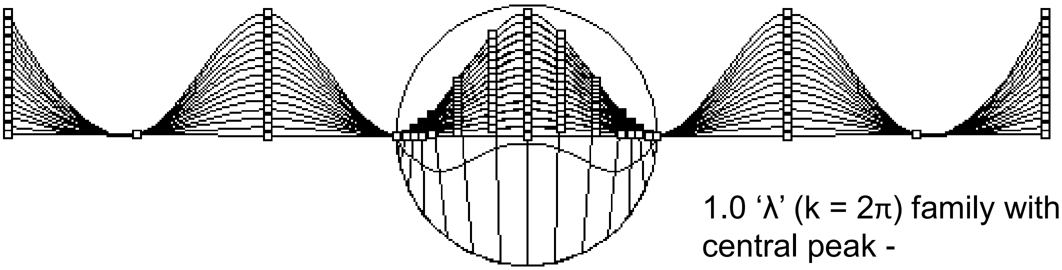

1.0 ‘λ’ (k = 2π) family with central peak - ‘amplitudes’: 0-14 mm

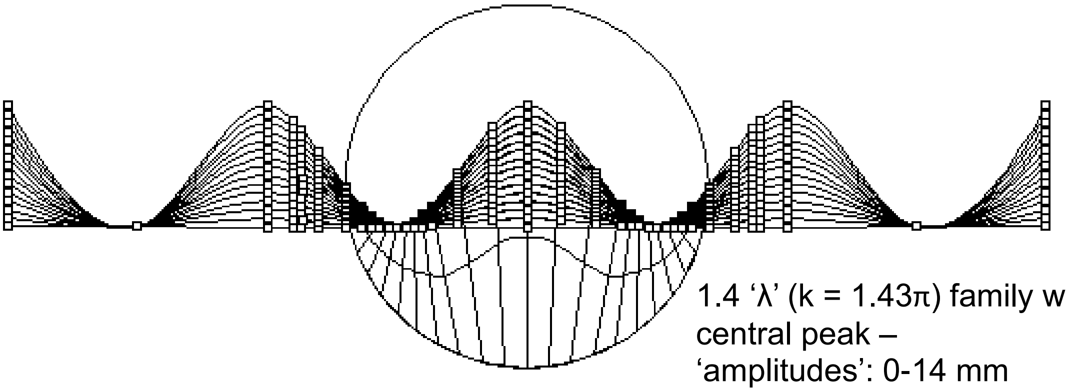

1.4 ‘λ’ (k = 1.43π) family with central peak – ‘amplitudes’: 0-14 mm

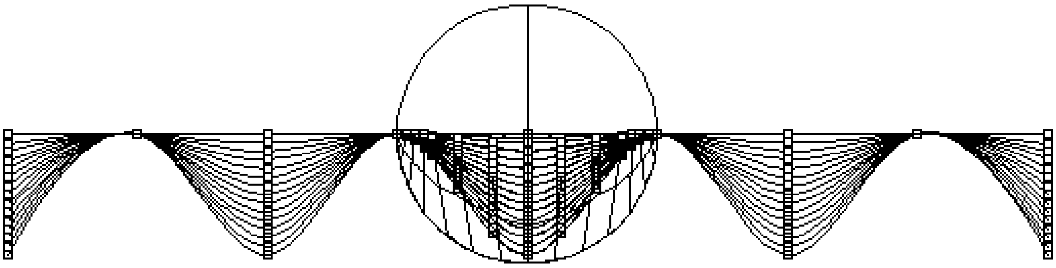

1.0 ‘λ’ (k = 2π) family with central trough – ‘amplitudes’: 0-14 mm

Figure 48 Relation of circular envelope to static amplitudes and edges of waveform families

3.5 Summary of methods developed in this research

The methods are broadly divided in to three areas: histology, material and morphology of the palm *petiole*. As most of these methods are novel, methodologies describe the theory before the methods are laid out.

The *petiole* histology was primarily concerned with *VB* distribution, size and shape across and along the longitudinal axis of the *petiole*. Gradients in quantities and their direction relative to parts of the *petiole* were measured for later discussion and correlation with shape and material properties of the *petiole*.

Elasticity in bending and torsional rigidity, represented by Young's modulus, E, and the rigidity modulus, G, respectively were the aspects of *petiole* material that were tested using standard procedures. However, to predict E of the inner and outer layers of the *petiole*, the novel bi-layered model and method which was designed in this research was used. The input for the model was E from the flexural tests and the outer profile shape, specifically the second moment of area I.

Petiole morphology constituted the bulk of the thesis research, with new methods used for shape profile analysis in terms of more appropriate *shape transformers* as well as a novel method for acquiring the shape profiles in vivo. The process for obtaining the *shape transformers* and performance indices for palm *petioles* is described. The methodology and method for Shape Edge Mapping (SEM), a novel technique designed in this research is described here such that it can be repeated precisely the way it was carried out in this research. Finally, the methodology and method for shape abstraction using SEM and waveform representation as an example of its application is described in this chapter whereby families of theoretical shapes are abstracted from palm *petioles*. Optimum shapes could then be identified on efficiency selection charts for a given function requirement.

4 Results and analysis

The results and analysis follow the same order as the methods from which they were derived in the 'Methodology and methods' section of this thesis.

Confidence intervals at the 95% significance level are displayed in the plots and the number of samples is represented by the 'n' value given for each data group. The Student-t distribution was used for all data sets less than 31 samples otherwise the normal z distribution was used to calculate the probabilities. For this research it was important to compare values relative to each other, so confidence intervals are displayed as opposed to p-values to provide information about a range in which the true value lies with 95% probability.

4.1 Petiole histology results

According to Gibson (Gibson, 2012), the combination of high cell wall properties and high relative density of the *VBs* in parts of the arborescent palm stem (specifically the arborescent palm stems of *Welfia georgii* and *Iriartea gigantea*), gives rise to high Young's modulus of about 30 GPa and high strength of about 300 MPa. It follows, that although the subject of this research was not on stems of palms, attempts to section a palm *petiole* from the *T. fortunei* palm may be challenging to cut as a result of similar high strength and density to the palm stem. Many attempts at sectioning the *petiole* with a scalpel and microtome were made and it was difficult to obtain complete sections as shown in a paper by Windsor-Collins et al (Windsor-Collins, et al., 2006). As a result, some of the palm *petiole* specimens were not complete, but it was possible to make an informative analysis.

4.1.1 Vascular bundle size and distribution

The *VB* shape was approximated to an ellipse to estimate the areas of both the internal and peripheral *VBs* at either end of the *petiole* (sections P1 and P6, proximal and distal respectively). The results are shown in Table 7. The Student's t-distribution was used to calculate the margin of error and the 95% confidence intervals as the sample numbers were less than 31.

Table 7 *Vascular bundle* internal and external transverse area distribution

Internal *VBs* (section P1) n = 24	**Mean**	**Margin of error (95% confidence level)**
Longitudinal axis length / mm	0.467	0.051
Transverse axis length / mm	0.350	0.033
Area of *VB* ellipse / mm^2	0.257	0.055
External *VBs* (section P1) n = 22	**Mean**	**Margin of error (95% confidence level)**
Longitudinal axis length / mm	0.266	0.032
Transverse axis length / mm	0.216	0.029
Area of *VB* ellipse / mm^2	0.090	0.024
Internal *VBs* (section P6) n = 27	**Mean**	**Margin of error (95% confidence level)**
Longitudinal axis length / mm	0.285	0.033
Transverse axis length / mm	0.241	0.020
Area of *VB* ellipse / mm^2	0.108	0.022
External *VBs* (section P6) n = 25	**Mean**	**Margin of error (95% confidence level)**
Longitudinal axis length / mm	0.124	0.015
Transverse axis length / mm	0.124	0.015
Area of *VB* ellipse / mm^2	0.024	0.006

These results in Table 7 are summarised in Table 8 and visualised in a bar chart (Figure 49) showing 95% confidence intervals.

Table 8 Summary of *Vascular bundle* transverse area distribution with MOE

Area of *VB* ellipse / mm^2	**Mean**	**Margin of error (95% confidence level)**
P1 internal	0.257	0.055
P1 external	0.090	0.024
P6 internal	0.108	0.022
P6 external	0.024	0.006

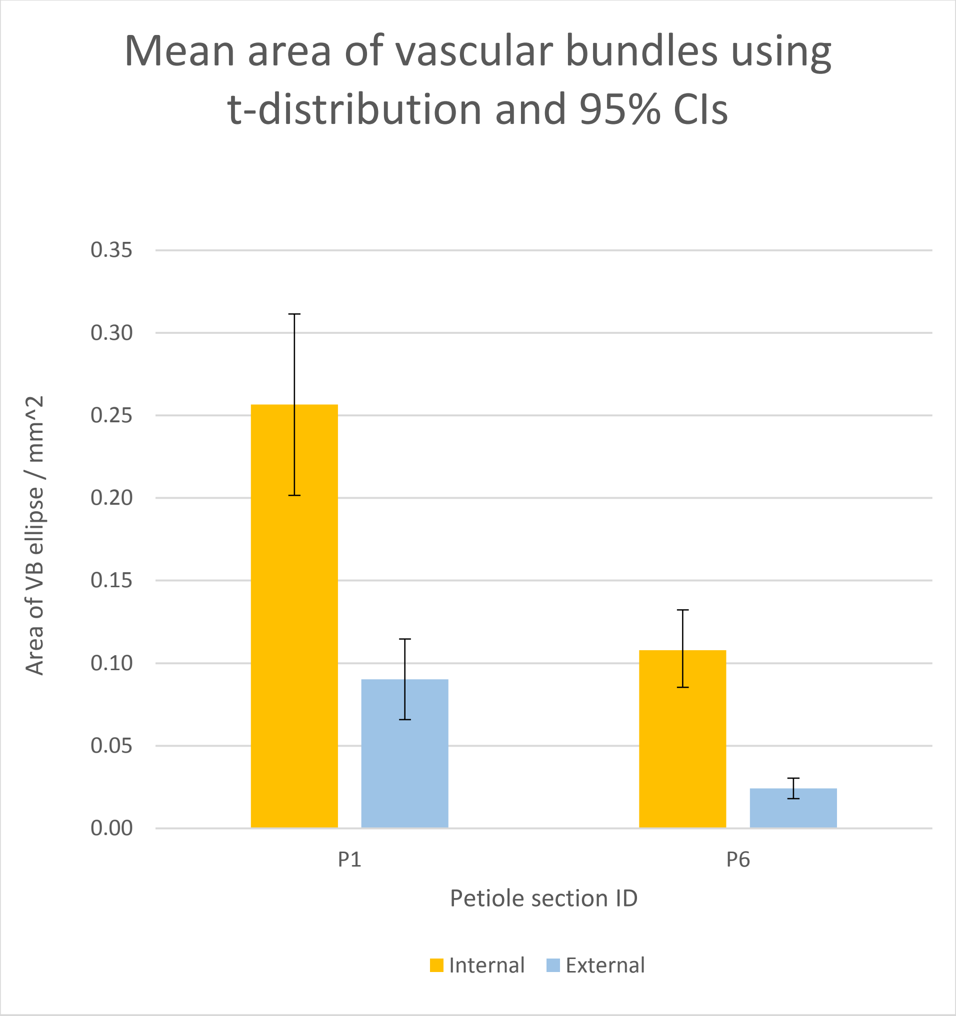

Figure 49 Area of *Vascular bundle* ellipse approximation along and across *petiole*

4.1.1.1 Axial gradient

The area of the *VBs* decreased in the direction from the stem towards the leaf blade. Looking in more detail at the outer *VBs*, the areas in section P1 nearest to the stem, were 375% larger than those in section P6 nearest the leaf blade. However, for the inner *VBs*, the areas at P1, were calculated to be only 238% larger than those at P6.

4.1.1.2 Radial gradient

The images of two transverse sections of the *petiole*, P1 and P6 at the extreme ends of the *petiole* are displayed in Figure 20. A marked difference in size can be observed between the internal and peripheral *VBs*. The change in area along the radius was not gradual, but changed abruptly at a constant distance from the *petiole* edge. The transverse gradient in *VB* area shows that at both ends of the *petiole*, the inner bundles were shown to be larger than the outer ones. The size difference between inner and outer bundles was larger at P1 than at P6. The outer *VBs* of P1 were 35% of the area of the inner ones whereas at P6, the outer *VBs* were relatively smaller and only 22% of the area of the inner ones. Table 9 summarises these results in prose form.

Table 9 *Vascular bundle* transverse area overview

Size attribute	Gradient direction
Area of outer *VBs*	Decreased towards leaf blade
Area of inner *VBs*	Decreased towards leaf blade to a lesser extent than the outer *VBs*
Difference between inner and outer *VB* area	Decreased towards leaf blade

Table 10 shows how the *VB* areas compare to those in a paper by Zhai et al (Zhai, et al., 2011) in which he shows images of *VBs* in the three layers of the *T. fortunei* leaf sheath.

Table 10 Comparison of *VB* size with *T. fortunei* leaf sheath as measured by Zhai et al (Zhai, et al., 2011).

	Longitudinal axis length / µm	Transverse axis length / µm	Mean diameter / µm	Layer in *T. fortunei* that these results correspond to in Zhai et al
Internal *VBs* (all that could be seen in section P1)	467	350	408	Middle layer 307-385 µm
External *VBs* (all that could be seen in section P1)	266	216	241	Outer layer 221-356 µm
Internal *VBs* (all that could be seen in section P6)	285	241	263	Outer layer 221-356 µm
External *VBs* (all that could be seen in section P6)	124	124	124	Inner layer 42-164 µm

4.1.2 Vascular bundle orientation

As with the *VB* size distribution, the images of the two transverse sections of the *T. fortunei petiole*, P1 and P6 at the extreme ends of the *petiole* displayed in Figure 20 were used to determine the orientation of the main axis of the *VB* cross sections.

The orientation of the *VBs* was described as the angle that the major axis of the ellipse which approximated to the *VB* cross section shape made with a known reference point. In this case, the reference point was either the centroid or the nearest lateral extent of the *petiole*. The *VBs* were approximated to an ellipse (either eccentric or circular) shapes. The major and minor axes of the ellipses were measured and Table 11 provides a summary of the orientations of the major axes of the *VB* cross sections for the inner and outer regions of the *petiole* for sections P1 and P6.

Table 11 *Vascular bundle* orientation summary

Location of *VBs*	Predominant orientation of *VB* major axis
Inner *VBs* (section P1) n = 24	Eccentric elliptical *VBs* aligned with centroid of *petiole* cross section
Outer *VBs* (section P1) n = 22	Eccentric elliptical *VBs* aligned with centroid of *petiole* cross section
Inner *VBs* (section P6) n = 27	Eccentric elliptical *VBs* aligned with the nearest one of the two points which constitute the furthest lateral extents of the *petiole* cross section
Outer *VBs* (section P6) n = 25	Circular (zero ellipse eccentricity), so not orientated in any direction

4.1.3 Vascular bundle number count (distribution)

4.1.3.1 Vertical transverse VB areal concentration

The vertical distribution of *VBs* within the transverse section of a *T. fortunei petiole* was evaluated using reference lines to count and calculate the relative concentration of *VBs*. The reference line *yy* shown in Figure 50 and Figure 51 extends between the upper and lower surfaces of the transverse section and is coincidental with the vertical axis of symmetry. The reference line, *xx* perpendicularly bisects *yy*. The *VBs* were counted above and below line *xx* to evaluate their vertical distribution for the only two sections that were complete; P4 and P6 (Figure 50 and Figure 51).

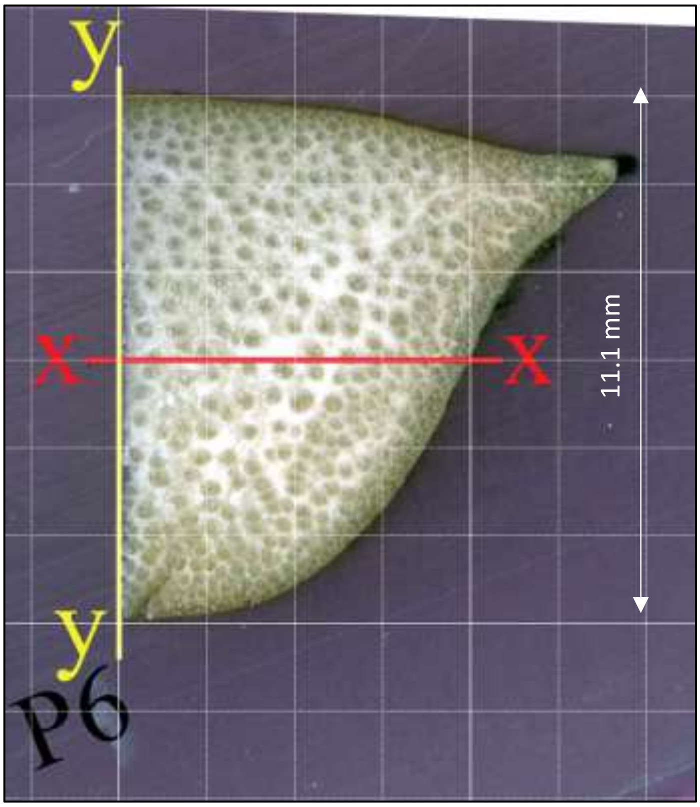

Figure 50 P6 *petiole* section of *T. fortunei* with reference lines xx and yy – adapted from (Windsor-Collins, et al., 2006)

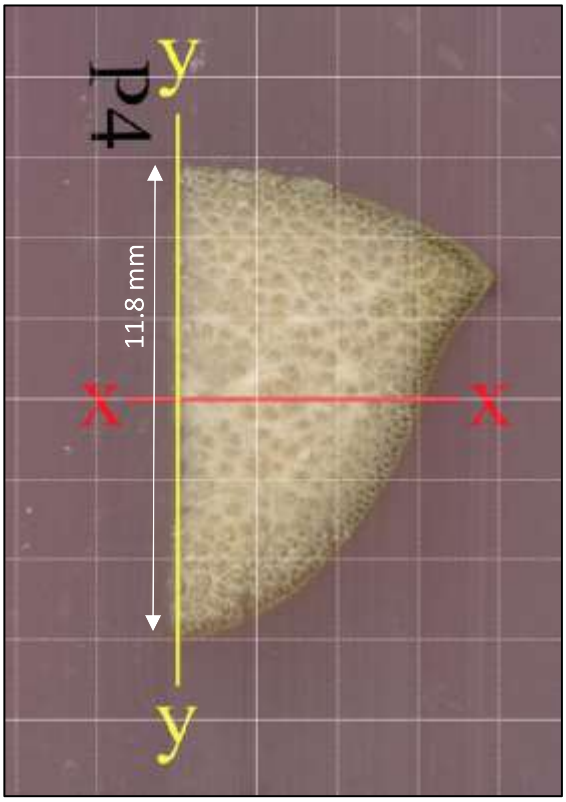

Figure 51 P4 section of *T. fortunei petiole* with grid showing reference lines *xx* and *yy*

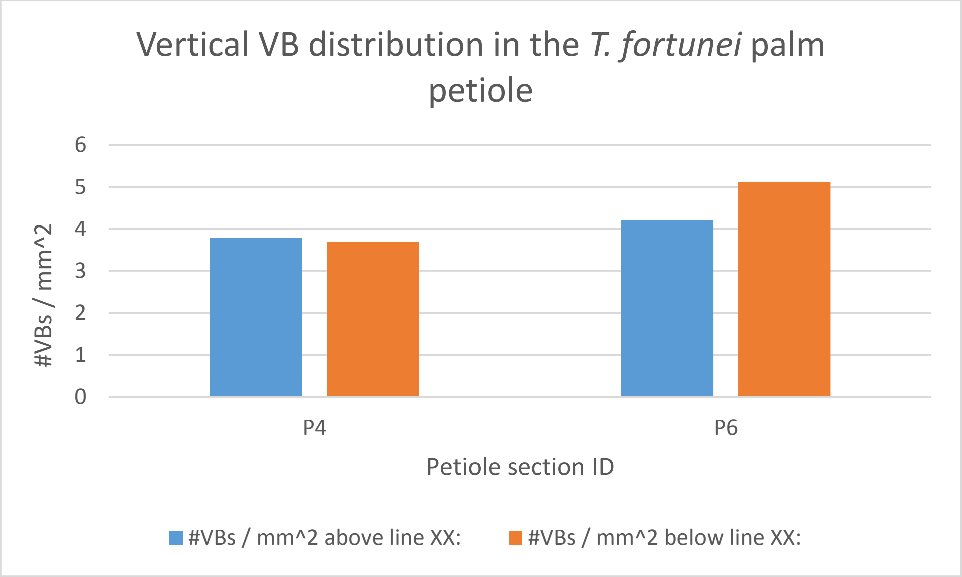

Figure 52 Vertical *Vascular bundle* distribution in the *T. fortunei* palm *petiole* (n=1, hence no CIs shown)

The results shown in the paper by Windsor-Collins et al show that although there were 47% more *VBs* in P6 above line *xx* than below it, 80% more of the cross-sectional area of the *petiole* section was above line *xx* than below it. The result of this is that there was a higher areal density of *VBs* on the lower side of this *petiole* in section P6, nearest the leaf blade (Windsor-Collins, et al., 2006).

Further analysis in this research (Figure 52) shows that in P4, the number of *VBs* per mm above and below line *xx* was 3.78 and 3.68 respectively, a percentage *decrease* of 3%. In P6, after re-processing the above results in the Windsor-Collins et al paper (Windsor-Collins, et al., 2006), the number of *VBs* per mm above and below line *xx* was 4.21 and 5.12 respectively a percentage *increase* of 18%.

Table 12 P4 vertical *VB* count

Section P4

Number of separate *VBs* counted per grid square

Alphanumeric grid coordinates	**1**	**2**	**3**	**4**	**Row sum**
A	16	11	6	0	**33**
B	13	16	17	15	**61**
C	12	13	14	3	**42**
D	11	15	9	0	**35**
E	14	11	2	0	**27**
F	14	5	0	0	**19**

Sum of visible *VBs* above line XX:	136
Sum of visible *VBs* below line XX:	81

62% of the cross-sectional area of the *petiole* section was above Line *XX*

63 % of the *VBs* within the transverse *petiole* section were above Line *XX*

	Number whole squares	**Number part squares**	**Number of squares**	**Square area / mm^2 (2 mm x 2 mm)**	**Area / mm^2**
Above line XX:	6	6	9	4	**36**
Below line XX:	3	5	5.5	4	**22**

#*VBs* / mm^2 above line XX:	3.78	(3% > below line xx)
#*VBs* / mm^2 below line XX:	3.68	

Table 13 P6 vertical *VB* count

Section P6

Number of separate *VBs* seen per grid square

Alphanumeric grid coordinates	**1**	**2**	**3**	**4**	**5**	**6**	**Row sum**
A	21	19	15	13	2	0	**70**
B	15	13	13	13	12	0	**66**
C	13	10	11	15	2	0	**51**
D	12	9	18	8	0	0	**47**
E	13	18	15	2	0	0	**48**
F	20	19	6	0	0	0	**45**

Sum of *VBs* above line XX:	187
Sum of *VBs* below line XX:	140

62% of the cross-sectional area of the *petiole* section was above Line *XX*

57 % of the *VBs* within the transverse *petiole* section were above Line *XX*

	Number whole squares	**Number part squares**	**Number of squares**	**Square area / mm^2 (1.85 mm x 1.85 mm)**	**Area / mm^2**
Above line XX:	9	8	13	3.42	**44.46**
Below line XX:	5	6	8	3.42	**27.36**

#*VBs* / mm^2 above line XX:	4.21	
#*VBs* / mm^2 below line XX:	5.12	(18% > above line xx)

4.1.3.2 Axial VB areal concentration

A count of the *VBs* per unit area was achieved by overlaying a graticule on each of the six *petiole* sections, P1 to P6 using the digital imaging software, Adobe Photoshop as shown the paper by Windsor-Collins et al (Windsor-Collins, et al., 2006). The transverse area of each section was estimated by counting the number of whole squares and adding this to half the number of squares partially filled by the *petiole* image. Damaged parts of the sections were totally discounted. Figure

50, Figure 51 and Figure 53 to Figure 56 show the *petiole* sections P1 to P6 and Table 14 and Figure 57 show the areal density of *VBs* along the longitudinal axis of the *T. fortunei petiole*.

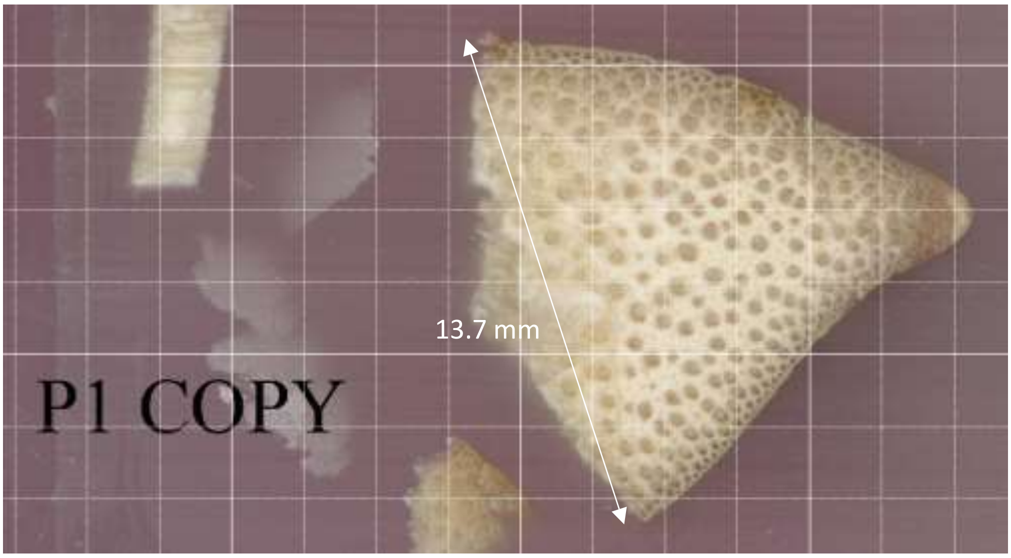

Figure 53 P1 section of *T. fortunei petiole* showing *VB* placement and graticule grid

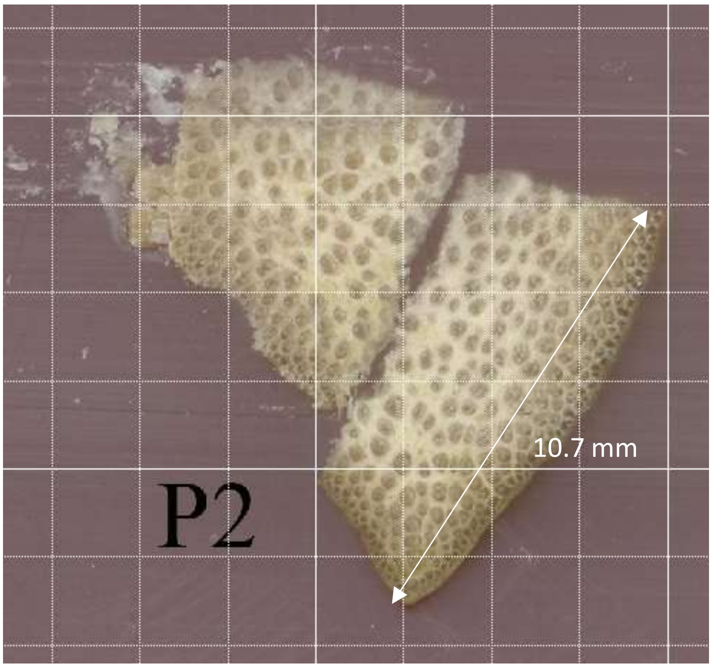

Figure 54 P2 section of *T. fortunei petiole* showing *VB* placement and graticule grid

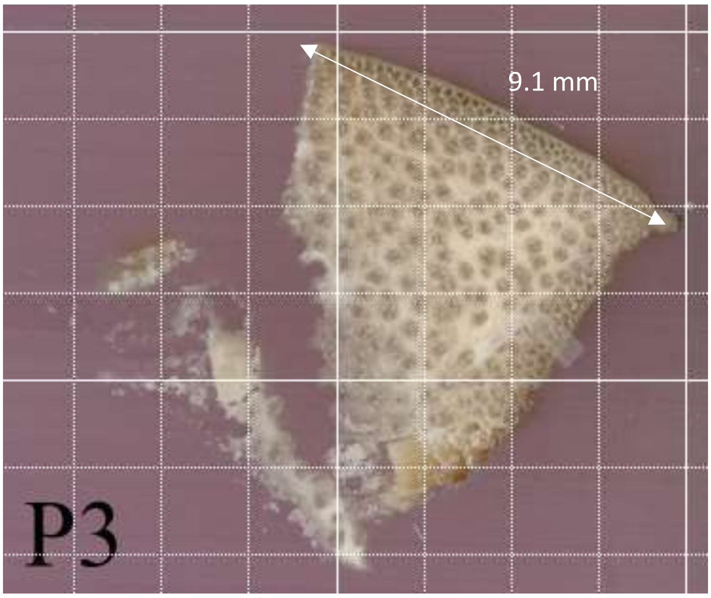

Figure 55 P3 section of *T. fortunei petiole* showing *VB* placement and graticule grid

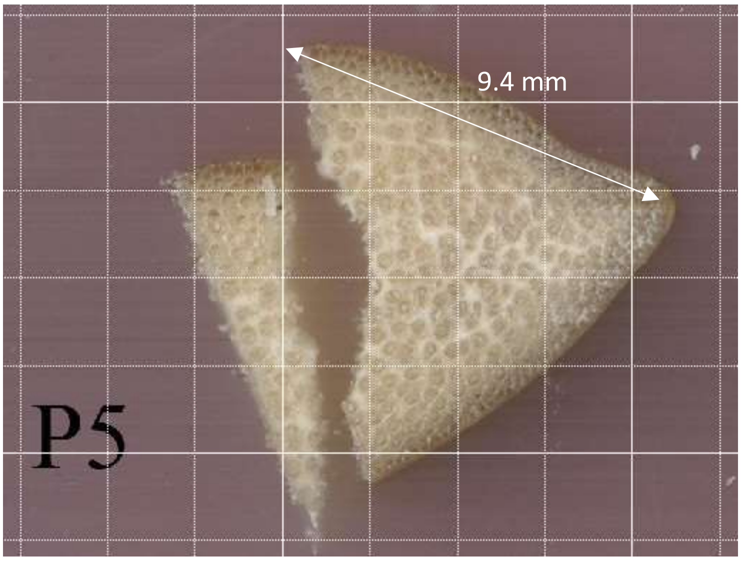

Figure 56 P5 section of *T. fortunei petiole* showing *VB* placement and graticule grid

Table 14 Number of *VBs* per square mm for sections P1 to P6

Petiole section	Distance from P1 / mm	Number of *VBs* / mm^2
P1	0	1.98
P2	171	3.43
P3	342	3.62
P4	513	3.74
P5	684	3.76
P6	855	4.55

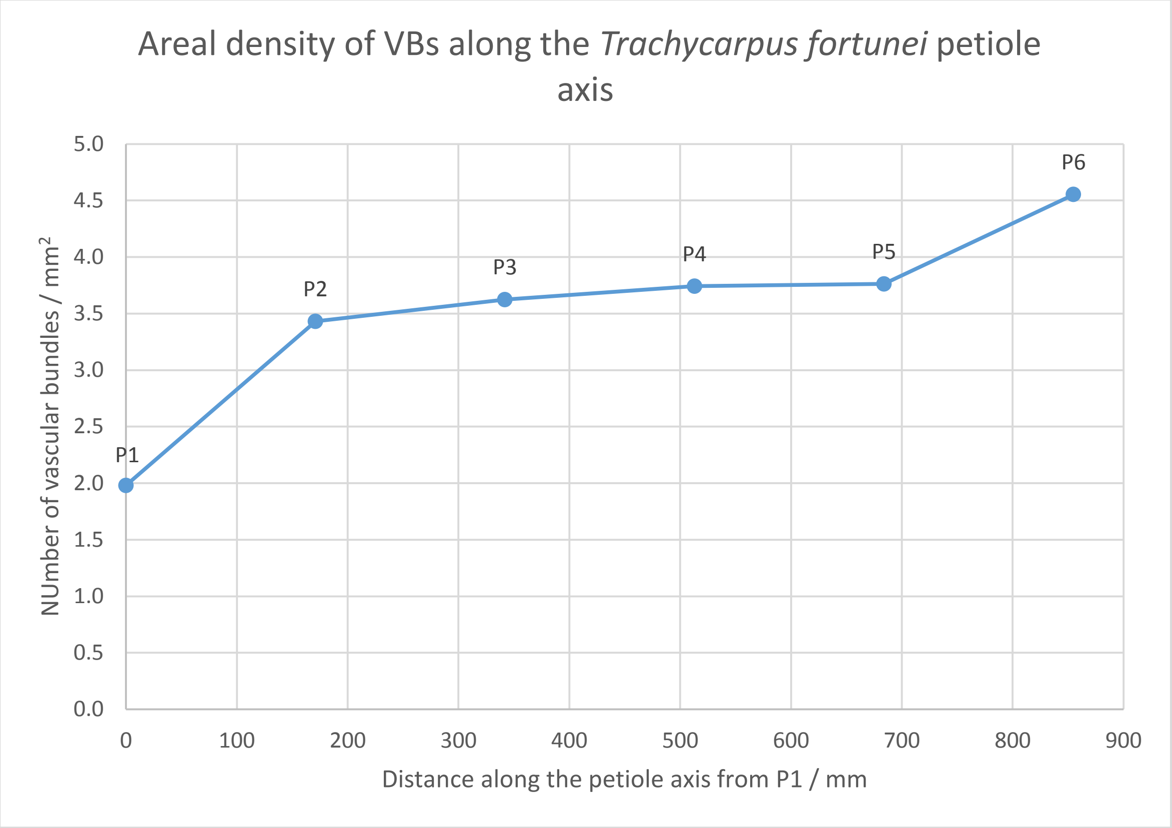

Figure 57 Areal density of vascular bundles along the axis of the *T. fortunei petiole* (n = 1) – adapted from (Windsor-Collins, et al., 2006)

It was found that the areal density of *VBs* increased towards the leaf blade, but most of all between sections P1 and P2 and between P5 and P6. It was effectively linear between sections P2 and P5.

4.2 Petiole material results

4.2.1 Empirical flexural test results

The mean longitudinal Young's modulus (E_L) values for each segment, P, C and D, of the *T. fortunei* palm *petiole* are shown in Figure 58 with the 95% confidence intervals shown using the *t*-distribution. The mean values for E_L were derived from six *petioles* tested with both the *abaxial* edge facing upwards and again facing downwards. Table 15 summarises the results in numerical form.

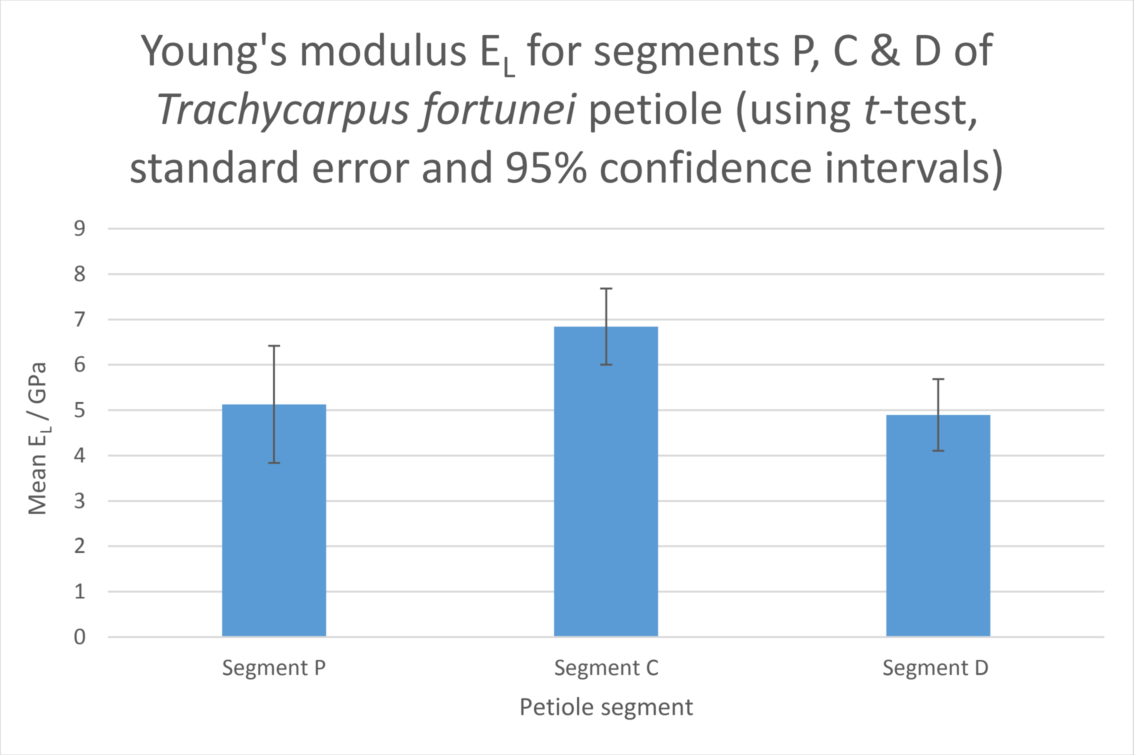

Figure 58 Young's modulus results from flexural tests (n=12)

The values for E_L, show that with 95% confidence, the material in its central section C had a higher Young’s modulus than section D all six *petioles* tested. It cannot be concluded from the results that the P section had a higher flexural stiffness or not than any of the other sections.

The mean E_L values for the fresh (green) material of the *T. fortunei petioles* tested ranged from 2.25 GPa in segment P Test 1 to 8.49 GPa in segment C Test 5. This range is within that found in green coconut palm timber which Ashby et al (Ashby, et al., 1995) quotes as between 0.7 GPa to 9 GPa.

Table 15 Young's Modulus Values from Empirical Flexural Tests

Segment P	*Abaxial* side down						*Abaxial* side up								
	Test 1	**Test 2**	**Test 3**	**Test 4**	**Test 5**	**Test 6**	**Test 1**	**Test 2**	**Test 3**	**Test 4**	**Test 5**	**Test 6**	**Sample mean E**	**Standard Error**	**Margin of Error (using t_{11} = 2.20099)**
E_L /GPa	2.25	6.25	5.03	3.39	7.93	5.66	2.41	6.67	5.29	2.67	8.02	5.94	5.13	0.59	1.29

Segment C	*Abaxial* side down						*Abaxial* side up								
	Test 1	**Test 2**	**Test 3**	**Test 4**	**Test 5**	**Test 6**	**Test 1**	**Test 2**	**Test 3**	**Test 4**	**Test 5**	**Test 6**	**Sample mean E**	**Standard Error**	**Margin of Error (using t_{11} = 2.20099)**
E_L /GPa	4.57	6.99	7.74	6.71	8.49	7.48	4.07	6.5	7.4	6.72	8.07	7.38	6.84	0.38	0.84

Segment D	*Abaxial* side down						*Abaxial* side up								
	Test 1	**Test 2**	**Test 3**	**Test 4**	**Test 5**	**Test 6**	**Test 1**	**Test 2**	**Test 3**	**Test 4**	**Test 5**	**Test 6**	**Sample mean E**	**Standard Error**	**Margin of Error (using t_{11} = 2.20099)**
E_L /GPa	3.24	5.13	4.84	4.63	6.90	6.13	2.70	4.27	4.48	4.26	6.30	5.89	4.90	0.36	0.79

4.2.2 Empirical torsion test results

The values for the general rigidity modulus, G, of the *T. fortunei petiole* given in a paper by Windsor-Collins et al (Windsor-Collins, et al., 2008) were derived from torsion tests measuring torsion in response to increasing angles of twist (Figure 26). It showed that G increased towards the leaf blade. However, the new tests performed in this thesis are better, but contradict what the author did previously, the reasons for which follow: In the original test, the torsion values resulting from decreasing angles of twist were recorded, but the derived results for G were not processed and subsequently not published. Furthermore, G was not derived from the results of a repeat of the torsion tests on the same *petioles*. As a result, four times as much acquired data was available to process.

On a visit to the Fairchild Tropical Botanic Garden Research Center in Florida, during a private interview with Professor P. B. Tomlinson (Tomlinson, 2004), Tomlinson suggested that *petioles* on the same palm plant may vary in material properties as there is evidence for adaptive growth in *petioles*, stems and roots. However, the G from both *petioles* was averaged in the paper by Windsor-Collins et al (Windsor-Collins, et al., 2008) whereas the G from both *petioles* may have been significantly different. Subsequently, the data were re-processed using torsion data acquired for decreasing angles of twist and the repeated tests to increase the number of samples by four. The result was four-fold data for two separate *petioles* (called Test 5 and Test 6) as opposed to two-fold data for one hypothetical *petiole*. Figure 59 and Table 16 show with 95% confidence that the rigidity modulus, G, decreased towards the leaf blade for both *petioles* (tests), but it can be said with 95% confidence that the absolute G values for *petiole* segments C and D for the two *petioles* were different. Consequently, the data from the two *petioles* were compared not averaged.

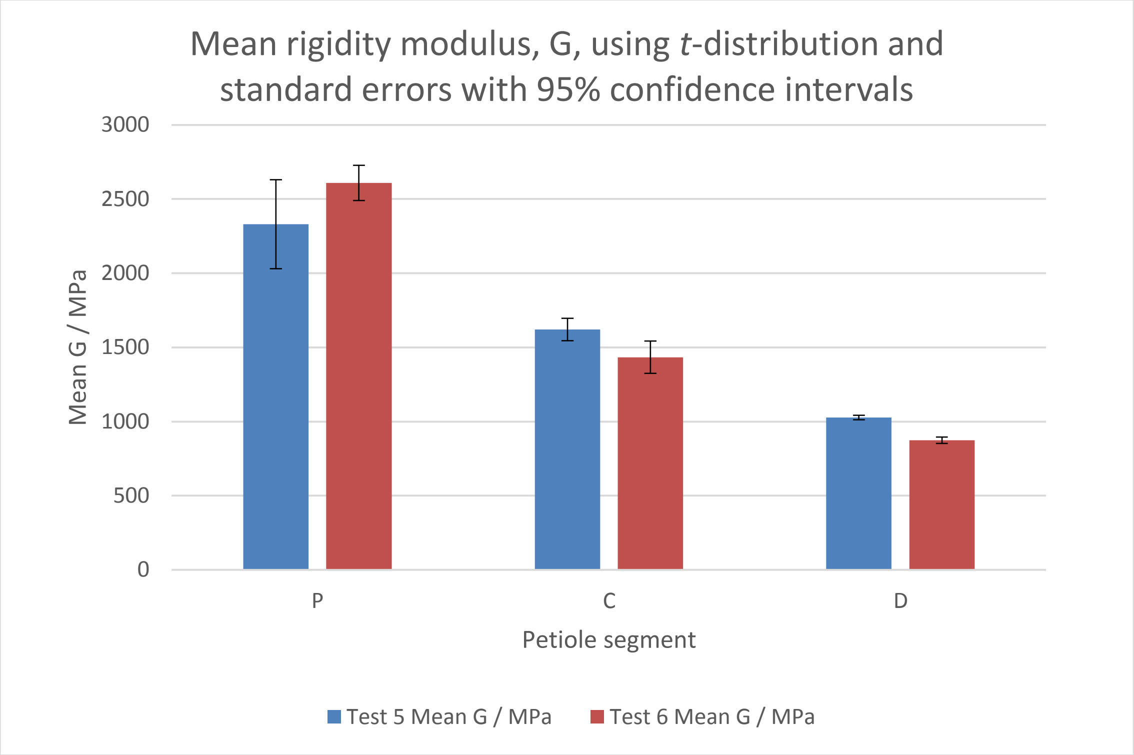

Figure 59 Mean rigidity modulus, G for two *petioles* using 95% confidence intervals (n = 4)

Table 16 Rigidity modulus, G for two *petioles* of *T. fortunei*

Test 5

Segment	G (increasing load) / MPa	G (decreasing load) / MPa	G (increasing load repeat) / MPa	G (decreasing load repeat) / MPa	Mean G / MPa	Standard Error	Margin of Error (using t_3 = 3.18245)
P	2391	2145	2566	2219	**2330**	94	299
C	1632	1556	1669	1623	**1620**	24	75
D	1039	1029	1017	1021	**1027**	5	15

Test 6

Segment	G (increasing load) / MPa	G (decreasing load) / MPa	G (increasing load repeat) / MPa	G (decreasing load repeat) / MPa	Mean G / MPa	Standard Error	Margin of Error (using t_3 = 3.18245)
P	2683	2521	2655	2576	**2609**	37	118
C	1514	1395	1464	1362	**1434**	34	109
D	873	888	855	876	**873**	7	22

Vogel (Vogel, 1995) lists the G values for several dry woods ranging from 105 MPa for wisteria to 915 MPa for bamboo culm. The G values for fresh (green) *T. fortunei petiole* material overlapped with those for dry woods quoted by Vogel and was *up to* three times as resistant to torsion as bamboo, the dry wood with the highest value for G tested by Vogel. Only section D of Test 6 had a lower G than that of bamboo.

4.2.3 Poisson's ratio results

Poisson's ratio for two *T. fortunei petioles* was derived using equation (41) using the bulk E and G values from the bending and torsion tests on the same *petioles*, the results for which may be found in sections 4.2.1 and 4.2.2 of this thesis. The results are shown in Figure 60 and Table 17.

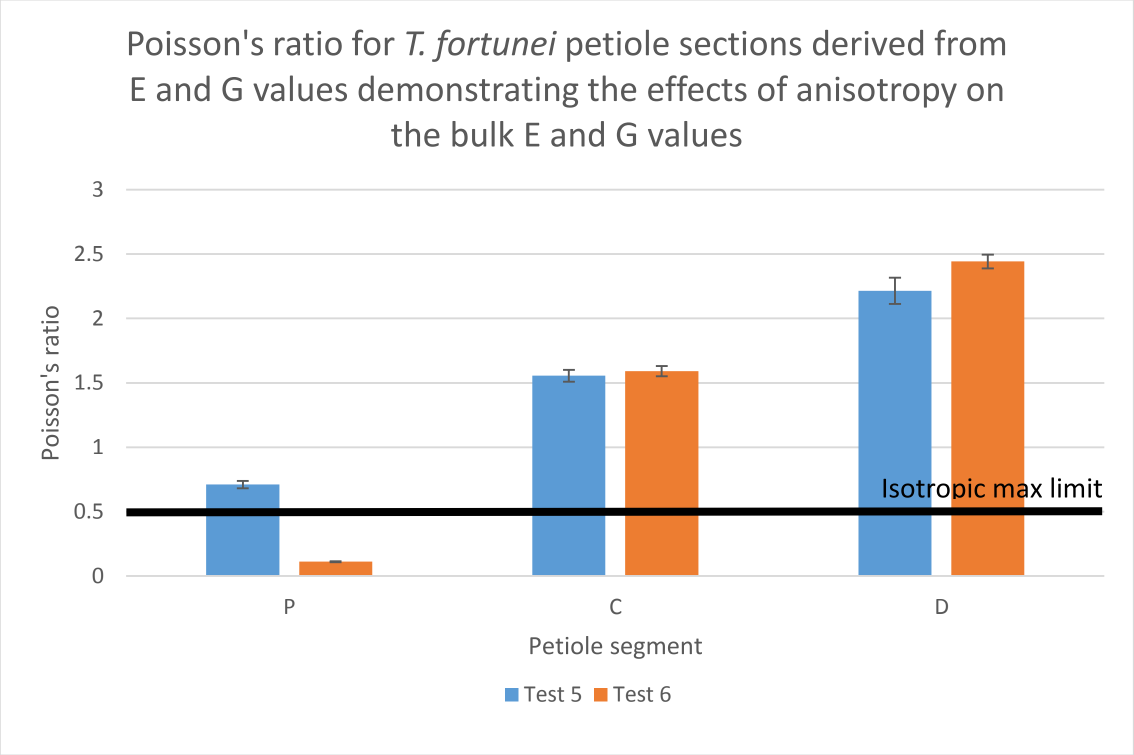

Figure 60 Poisson's ratio for the *T. fortunei petiole* highlighting undesirable effects of anisotropy in the bulk E and G values used to calculate it (95% confidence intervals, n = 4)

Table 17 Poisson’s ratio calculation from values of bulk E & G from flexural and torsion tests

Test 5	Mean E / MPa (n = 4)	Standard Error for E	Mean G / MPa (n = 4)	Standard Error for G	Poisson's ratio, v (n = 4)	Standard Error for v
P	7975	45	2330	94	**0.71**	0.03
C	8280	210	1620	24	**1.56**	0.05
D	6600	300	1027	5	**2.21**	0.10

Test 6	Mean E / MPa (n = 4)	Standard Error for E	Mean G / MPa (n = 4)	Standard Error for G	Poisson's ratio, v (n = 4)	Standard Error for v
P	5800	140	2609	37	**0.11**	0.00
C	7430	50	1434	34	**1.59**	0.04
D	6010	120	873	7	**2.44**	0.05

For reference to other people’s work which demonstrate the same problem with anisotropic and heterogeneous nature of wood, Vogel (Vogel, 1995) provides E and G for various woods, a subset of which is shown in Table 18, the resulting Poisson’s ratio is between 3.25 and 8.15.

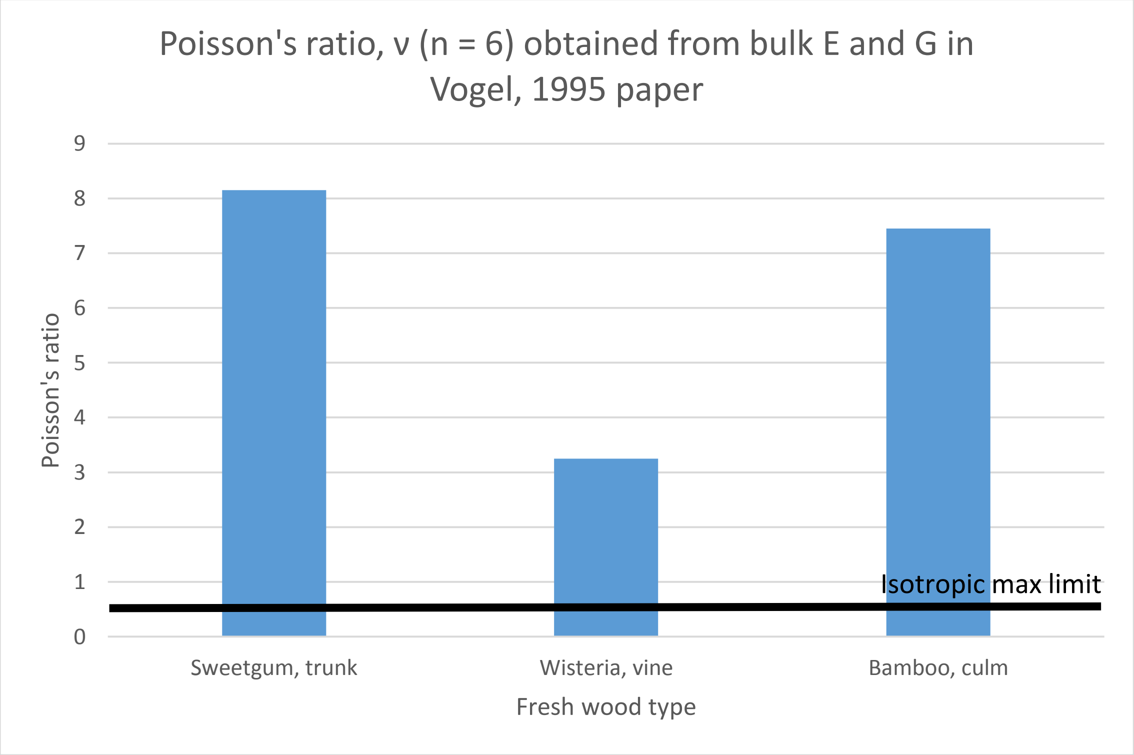

Figure 61 Poisson's ratios for fresh wood samples derived from bulk E and G, the latter published by (Vogel, 1995)

Table 18 Poisson's ratios derived from bulk E and G of fresh woods, the latter published by (Vogel, 1995)

	Mean E / MPa (n = 6)	Mean G / MPa (n = 6)	Poisson's ratio, v (n = 6)
Sweetgum, trunk	5580	305	**8.15**
Wisteria, vine	892	105	**3.25**
Bamboo, culm	15460	915	**7.45**

No individual margins of error were presented in this paper (Vogel, 1995), hence them not being presented here. Only the number of samples are indicated by the n value.

4.2.4. Bi-layered model results

Table 19 shows the derived values for *EI* from the flexural tests performed on segments *P* and *C* of Test 5. These values were then input into equations (49) and (50).

Table 19 Flexural Stiffness k (EI) derivation for Test 5 segments P and C from the flexural tests

Test 5 *EI* derivation for Segments *P* and *C* from flexural tests

Segment	Mean E / Nmm^{-2}	SE E / Nmm^{-2}	Mean I / mm^4	SE I / mm^4	EI / Nmm^2
P	7.975×10^{-6}	4.5×10^{-8}	1011	349	8059×10^{-6}
C	8.28×10^{-6}	21×10^{-8}	355	51	2939×10^{-6}

I_1, the second moment of inertia of the outer layer about the x axis was plotted against the thickness of the outer *petiole* layer, t at both ends of segments *P* and *C* (proximal and distal) as shown in Figure 62 to Figure 65. These curves were linear at low values of t and consequently, the gradients of the linear trend lines through the data were obtained from the equation displayed on the charts. The gradient, I', was equal to I/t as shown in equation (53). The R^2 values shown on each chart are above 0.99 showing a very close fit of the data to the linear trend line. The gradient, I', decreased towards the leaf blade and the mean values for each segment are shown in Table 20.

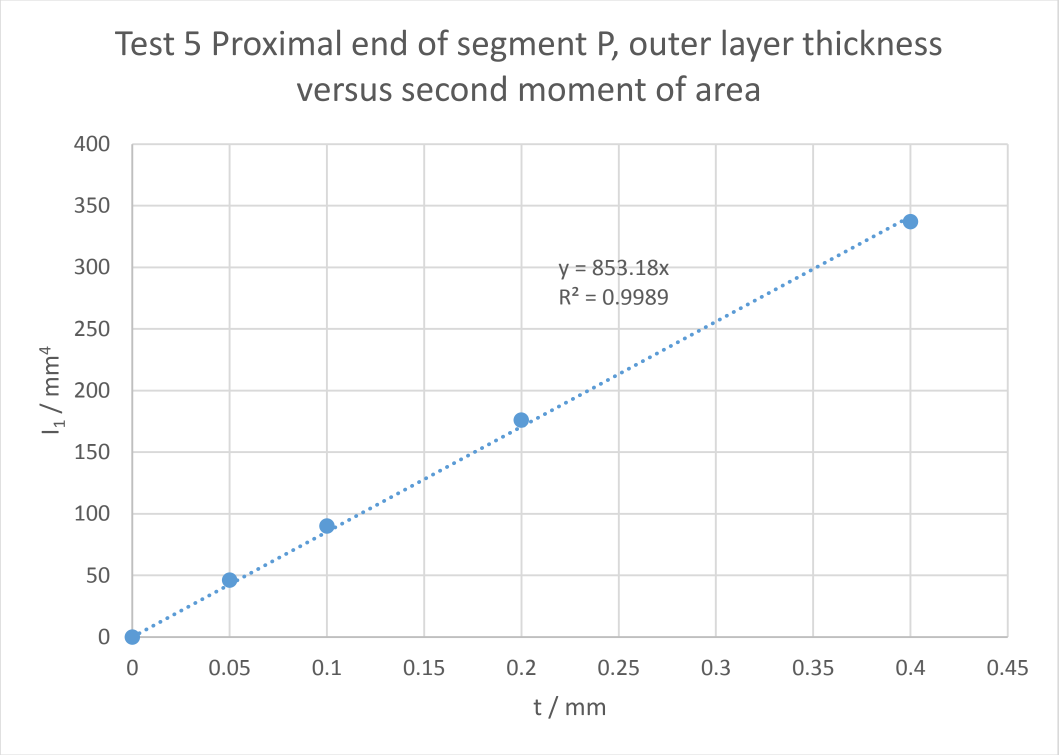

Figure 62 I_1 vs t for Test 5 segment P proximal section

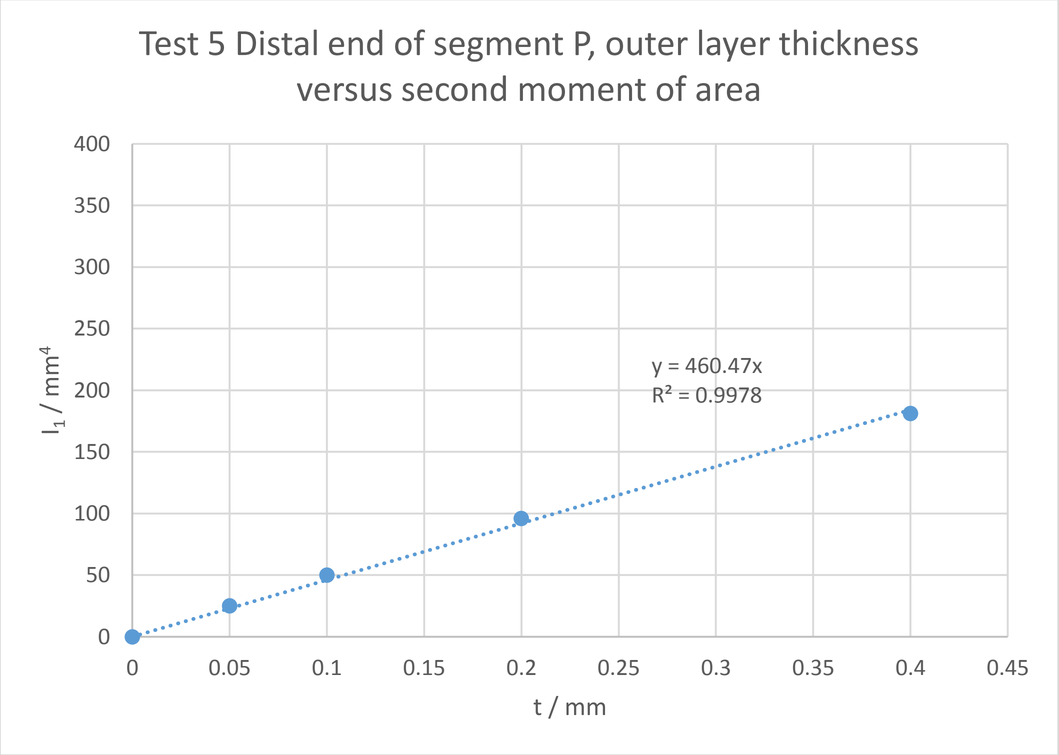

Figure 63 I_1 vs t for Test 5 segment P distal section

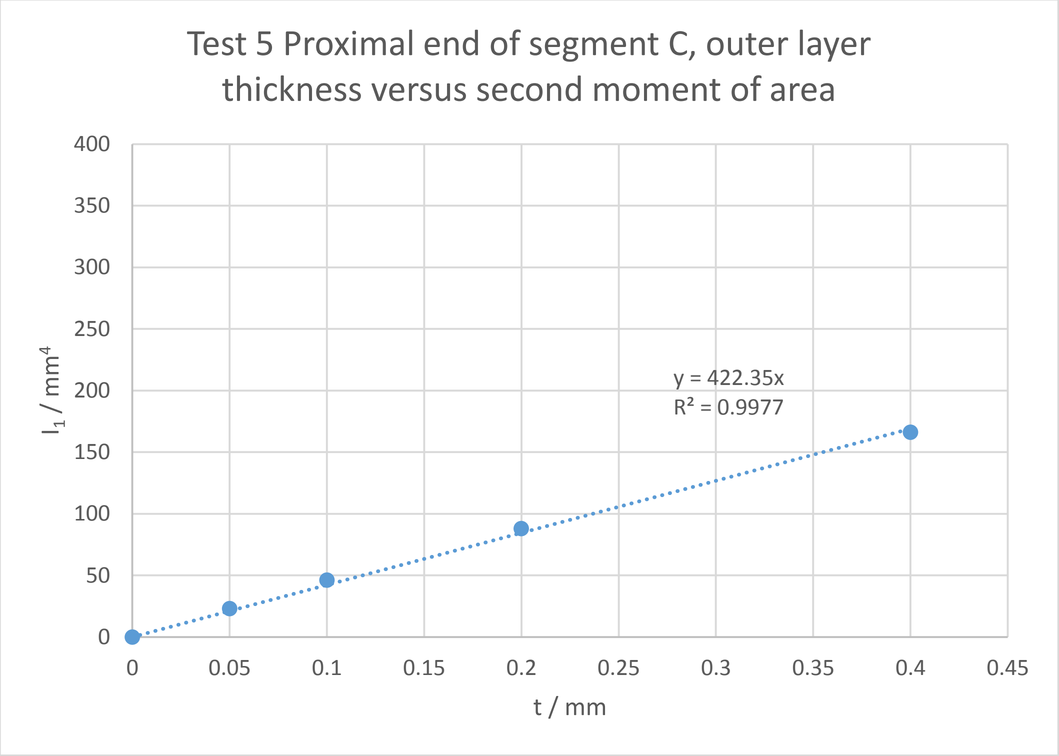

Figure 64 I_1 vs t for Test 5 segment C proximal section

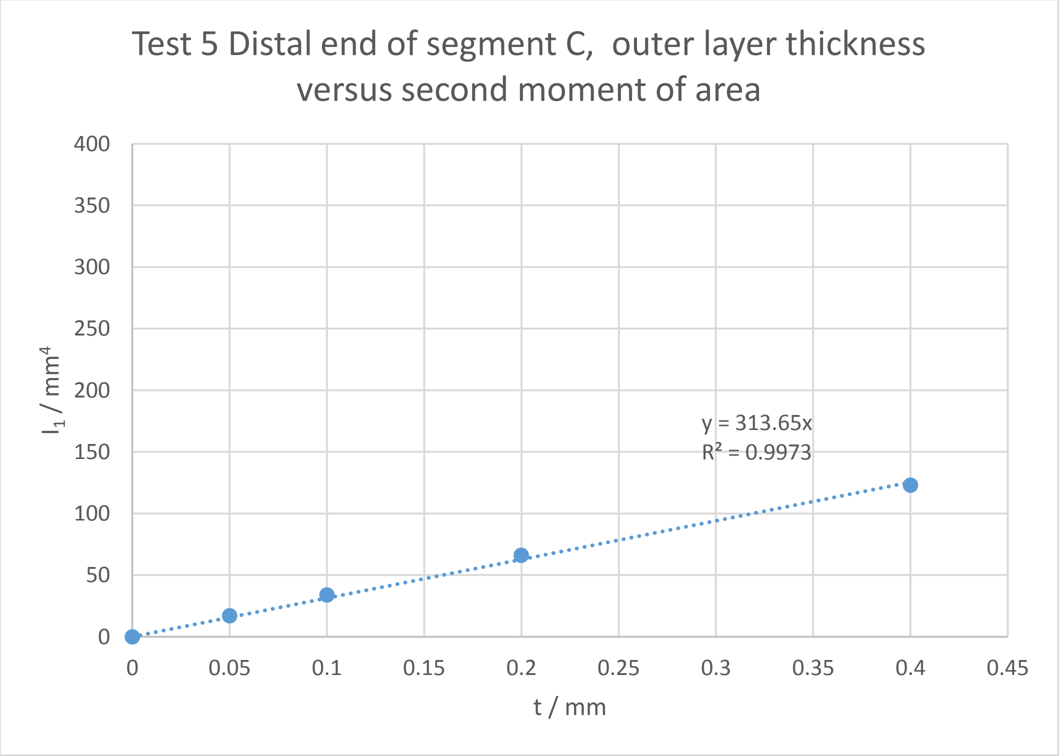

Figure 65 I_1 vs t for Test 5 segment C distal section

Table 20 Mean values for I' for segments P and C of Test 5

	Gradient, I' (proximal) / mm^3	Gradient, I' (distal) / mm^3	Mean I' / mm^3
Segment P	853	460	**657**
Segment C	422	314	**368**

To find the two unknowns E_1t and E_2, simultaneous equations (**54**) and (55) were populated with the *EI* values from Table 19 and *I'* values from Table 20. As *t* was very small, it was assumed that I_2 was the same as *I* of the whole cross-section. As it was not possible to derive E_1 (as it would have been very large if *t* was very small), a range of values for E_1 was obtained from a range of likely *t* values.

For Segment P from equation (**54**):

$EI_P = E_1t * I_{1P}' + E_2 I_{2P}$

$8059 \times 10^{-6} = (E_1t \times 657) + 1011E_2$

For Segment C from equation (55):

$EI_C = E_1t * I_{1C}' + E_2 I_{2C}$

$2939 \times 10^{-6} = (E_1t \times 368) + 355E_2$

$E_1t = (2939 \times 10^{-6} - 355E_2) / 368$

E_2 was obtained by substituting E_1t into equation (**54**):

$8059 \times 10^{-6} = (E_1t \times 657) + 1011E_2$

$8059 \times 10^{-6} = (((2939 \times 10^{-6} - 355E_2) / 368) \times 657) + 1011E_2$

$\underline{E_2 = 7.5 \text{ GPa}}$

E_1t was obtained by substituting E_2 into equation (55):

$E_1t = (0.002939 - 355E_2) / 368$

$E_1t = (0.002939 – (355 \times 0.0000075) / 368$

$\underline{E_1t = 7899 \times 10^{-10} \text{ N/mm}}$

Table 21 shows the range of E_1 values calculated from a likely range of *t* values:

Table 21 Range of E_1 values from likely range of *t* values calculated from bi-layered model

E_1t / Nmm^{-1}	t / mm	E_1 / Nmm^{-2}	E_1 / Nm^{-2}
7.899E-07	0.025	0.0000315960	31.60
7.899E-07	0.05	0.0000157980	15.80
7.899E-07	0.1	0.0000078990	7.90
7.899E-07	0.2	0.0000039495	3.95
7.899E-07	0.4	0.0000019748	1.97
7.899E-07	0.8	0.0000009874	0.99

E_2 was calculated using the bi-layered model to be 7.5 GPa; less than the value for $\bar{E}$ for the whole of either the *P* or *C* segment derived from the flexural test which amounted to 8.0 GPa and 8.3 GPa respectively. It would be expected therefore for E_1 to have a higher value than E_2. It can be seen from Table 21, that the thickness of *t* of 0.2 mm or greater, results in values of E_1 lower than 7.5 GPa. Therefore, the results suggest that the thickness of the outer layer is less than 0.2 mm.

4.3 Petiole morphology results

4.3.1 Shape profiler verification using regular shapes

4.3.1.1 Linear accuracy of shape profilers

The precision of the shape profilers was 0.35 mm as the width of each finger was 0.7 mm. The error of the shape profiler was therefore +/- 0.7mm.

The given widths of the two gauge blocks to be measured by the shape profilers were 8 mm + 0.15 µm and 30 mm – 0.10 µm.

The widths of the two gauge blocks were measured using the shape profilers. The inscribed pencil outline was then scanned. Digitised using Adobe Illustrator software and the images imported into Rhino. The mean values and standard deviations are tabulated in Table 22 and are summarised as follows:

Width of 8 mm gauge block using shape profilers:	8.9 mm (s = 0.8 mm)
Width of 30 mm gauge block using shape profilers:	30.2 mm (s = 0.7 mm)

Table 22 Gauge block widths as measured by shape profilers

Width of 8 mm gauge block / mm (n = 12)												Mean, µ / mm	Standard deviation, s / mm
9.4	9.1	9.9	10.0	9.4	9.6	7.9	7.6	7.8	7.9	8.9	9.1	8.9	0.8

Width of 30 mm gauge block / mm (n = 8)								Mean, µ / mm	Standard deviation, s / mm
30.9	30.6	30.9	30.7	29.7	29.6	29.4	29.5	30.2	0.7

Therefore, the linear measurements using the shape profilers were 0.67% and 11.24% more than the standard widths of the 30mm and 8 mm gauge blocks respectively.

4.3.1.2 Comparison of area of circular cylinder transverse cross section derived from shape profilers and Vernier callipers

Table 23 Circular cylinder profiler comparison with Vernier callipers

Mean area of transverse section of cylinder calculated in Rhino and using the shape profilers /mm^2 (n = 20)																				mean / mm^2	sd / mm^2	% sd
1351	1352	1367	1381	1322	1349	1370	1366	1339	1354	1353	1371	1333	1321	1339	1340	1329	1323	1331	1378	1348	19	1

The temperature of the room before and after the measurements were taken was 18.8°C and 18.9°C.

Diameter of cylinder using Vernier calipers / mm (n = 5)					mean / mm	standard deviation / mm	% standard deviation
42.08	42.06	42.04	42.08	42.08	42.07	0.02	0.00

The mean area of transverse section of cylinder derived from Vernier caliper measurement of diameter in Table 23 = 1390 mm^2

The mean area of transverse section of cylinder calculated in Rhino using the shape profilers = 1348 mm^2

Therefore, the area of the circular cylinder measured by the shape profilers was 3.02% less than the area when measured using Vernier callipers.

4.3.2 Petiole profiles

All of the *petiole* profiles are shown in Appendix 9.2. Thirty-two (32) samples were taken for each profile and are hence too numerous to be presented in the main body of this thesis. However, a subset of all of the *petiole* profiles in Appendix 9.2 are shown in Figure 66 so that the reader can observe the relative shape and size of the *petioles* at a glance. Their *shape transformer* measurements are presented in section 5.3.5.

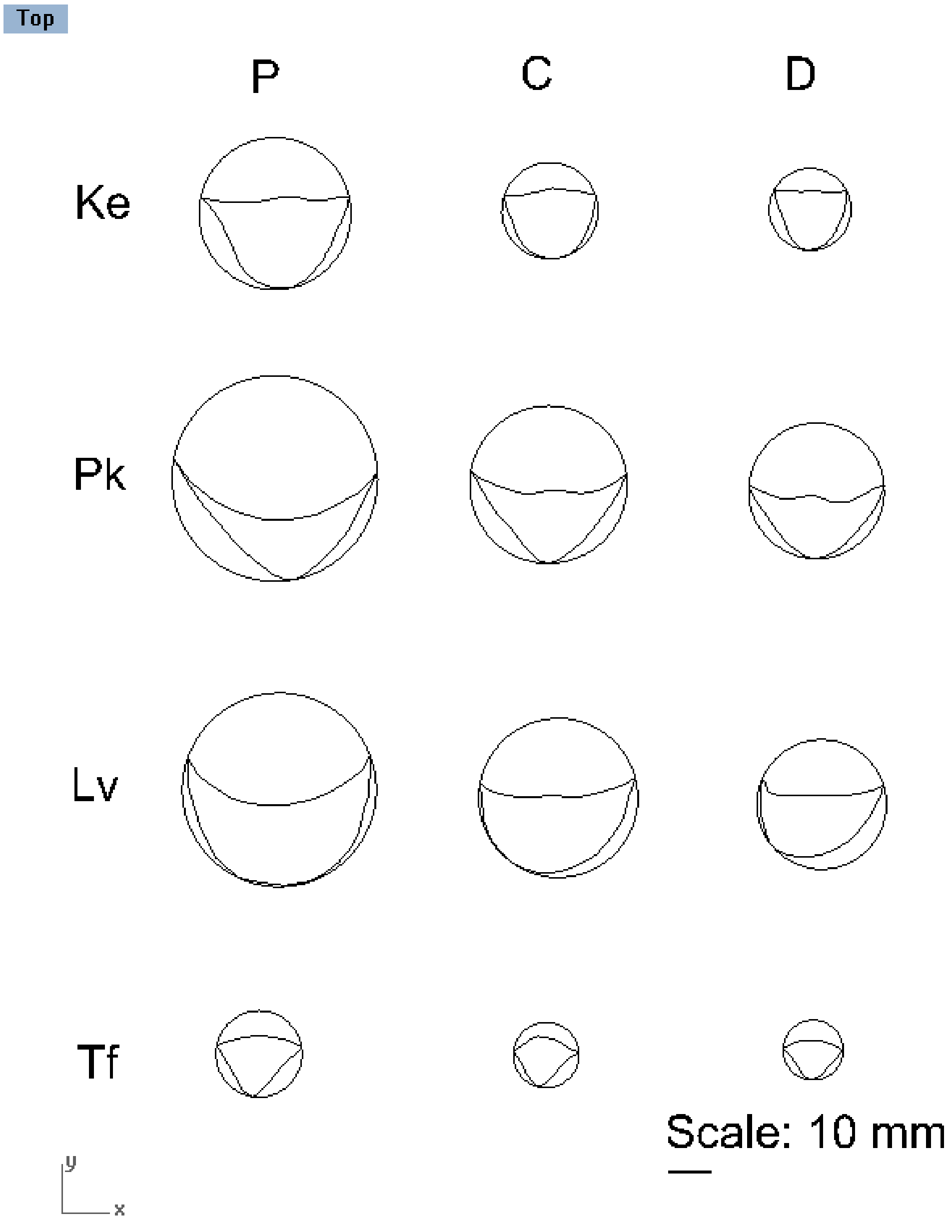

Figure 66 One sample from each palm *petiole* transverse section tested

4.3.3 Associated palm dimensions and habitats

As described in the paper by Windsor-Collins et al (Windsor-Collins, et al., 2007a), a record was made of the blade type, dimensions and the angle that the *petiole* made with the palm stem. Data sheets were copies of the original field data sheets for the *Ke*, *Lv*, *Pk* and *Tf* palm *petioles* are shown in Appendix 9.1, a summary of which is shown below in Table 24 and Figure 67. The palm habitats are also shown here and referred to in the discussion section in connection with shape mass-efficiency for torsion and bending resistance.

Table 24 Summary of associated palm dimensions and habitats

Palm species	Petiole length / cm	Stem diameter / cm	Blade width / cm	Blade length / cm	Height of *petiole* base above ground / cm	Habitat
Ke	134	25	212	125	90	Sheltered, forest understorey, Thailand
Pk	80	16	120	105	60	Windswept ridges, tropical storms, Hawaiian Islands
Lv	103	32	220	150	50	High winds and heavy rainfall, Rodrigues island, Mauritius
Tf	90	24	100	65	191	Mountainous regions, heavy snow cover, China

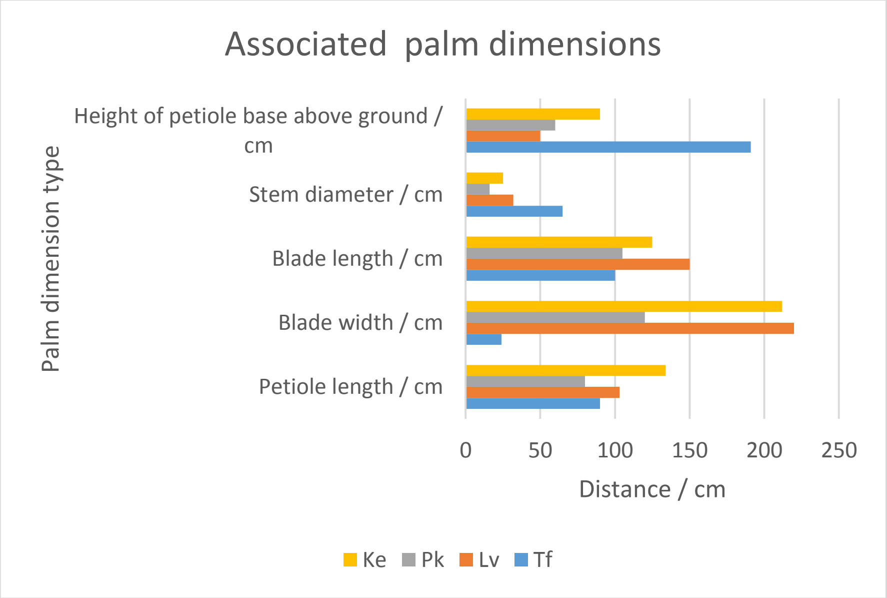

Figure 67 Comparison of associated palm dimensions

4.3.4 Shape transformers and SEM

4.3.4.1 Mass-efficiency in bending, ψI vs ψA

Table 25 ψI vs ψA whole *petiole* and SEM results

ψI vs ψA for all whole *petiole* sections				
mean (n = 32)	**ψA**	**ψI**	ψA margin of error	ψI margin of error
Ke P	0.481	0.193	0.004	0.003
Ke C	0.605	0.318	0.006	0.006
Ke D	0.609	0.363	0.008	0.010
Pk P	0.209	0.036	0.004	0.002
Pk C	0.337	0.084	0.000	0.000
Pk D	0.347	0.082	0.004	0.002
Lv P	0.443	0.135	0.006	0.004
Lv C	0.444	0.120	0.008	0.005
Lv D	0.443	0.128	0.004	0.003
Tf P	0.495	0.220	0.005	0.005
Tf C	0.532	0.265	0.006	0.006
Tf D	0.500	0.210	0.010	0.008

ψI vs ψA for all *adaxial petiole* sections				
mean (n = 32)	ψA	ψI	ψA margin of error	ψI margin of error
KeP	0.479	0.126	0.006	0.003
KeC	0.541	0.176	0.006	0.004
KeD	0.485	0.131	0.013	0.006
PkP	0.281	0.049	0.006	0.002
PkC	0.387	0.078	0.005	0.002
PkD	0.407	0.087	0.005	0.002
LvP	0.263	0.042	0.010	0.003
LvC	0.387	0.076	0.007	0.003
LvD	0.381	0.072	0.006	0.003
TfP	0.605	0.236	0.007	0.006
TfC	0.674	0.334	0.009	0.009
TfD	0.628	0.265	0.015	0.013

ψI vs ψ_A for all *abaxial petiole* sections				
mean (n = 32)	ψ_A	ψ_I	ψA margin of error	ψI margin of error
KeP	0.855	0.822	0.006	0.012
KeC	0.875	0.851	0.009	0.017
KeD	0.822	0.809	0.012	0.023
PkP	0.854	0.760	0.020	0.035
PkC	0.863	0.783	0.009	0.017
PkD	0.891	0.817	0.009	0.016
LvP	0.944	0.940	0.013	0.029
LvC	0.903	0.823	0.016	0.032
LvD	0.846	0.718	0.008	0.014
TfP	0.787	0.668	0.009	0.015
TfC	0.799	0.678	0.010	0.017
TfD	0.842	0.745	0.020	0.034

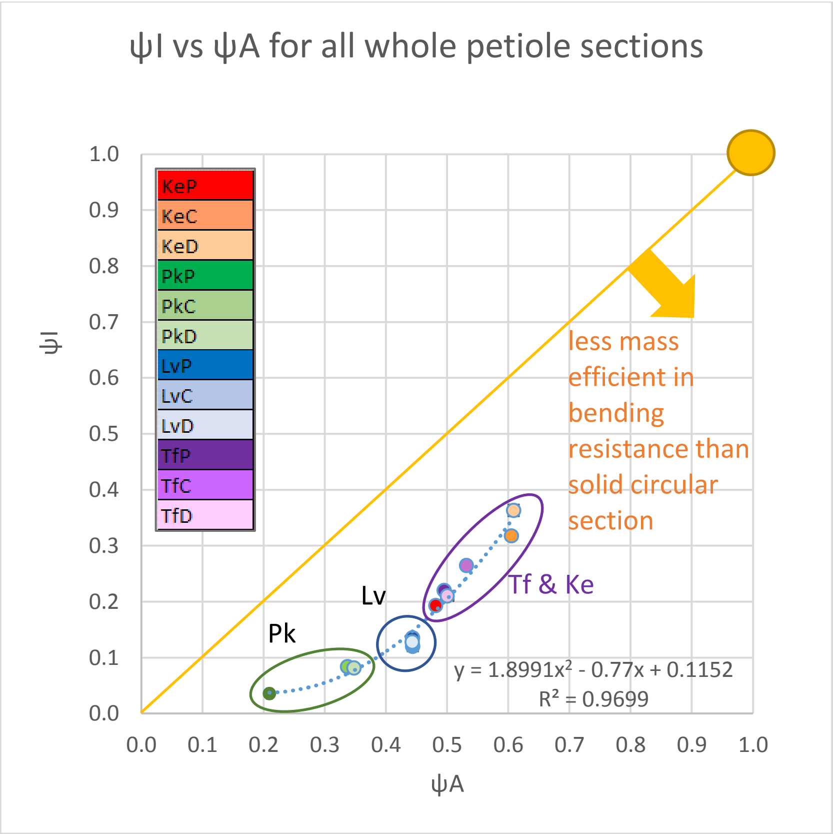

Figure 68 ψ_I vs ψ_A for whole *petiole* sections (including 95% confidence intervals)

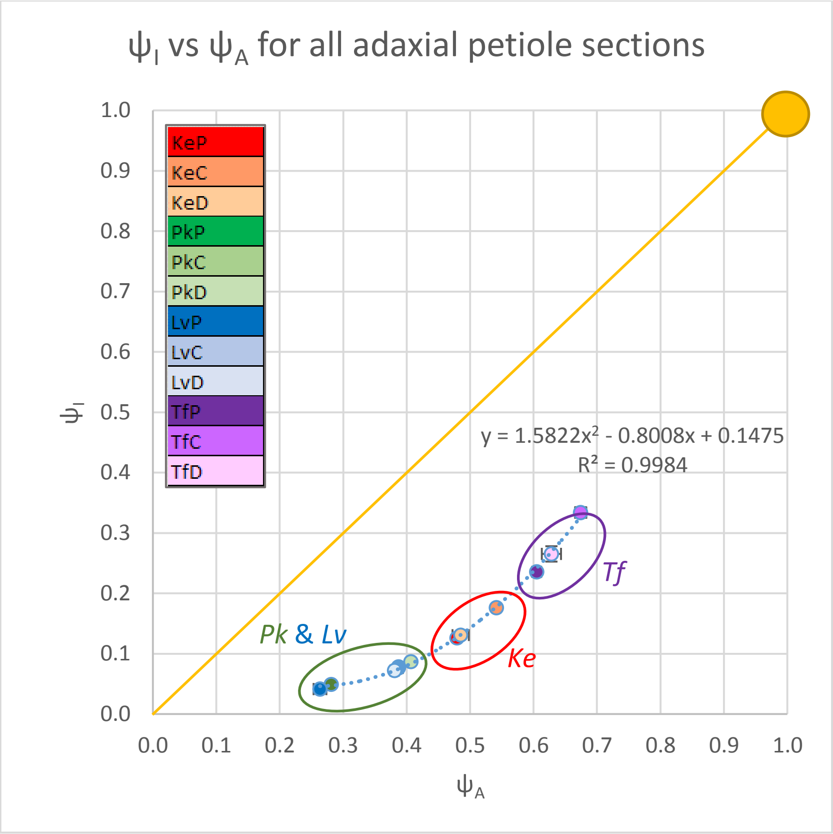

Figure 69 ψ_I vs ψ_A for *adaxial petiole* sections (including 95% confidence intervals)

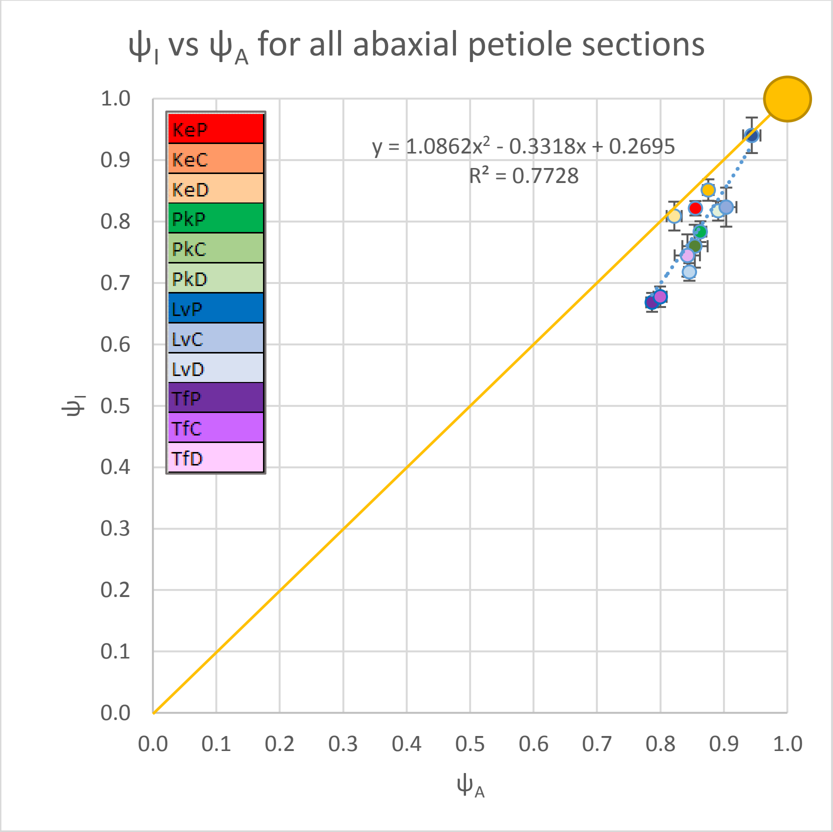

Figure 70 ψ_I vs ψ_A for *abaxial petiole* sections (showing 95% confidence intervals)

4.3.4.2 Mass-efficiency in torsion, ψJ vs ψA

Table 26 $ψ_J$ vs $ψ_A$ whole *petiole* and SEM results

ψJ vs ψA for all whole *petiole* sections				
mean (n = 32)	**ψA**	**ψJ**	ψA margin of error	ψJ margin of error
Ke P	0.481	0.267	0.004	0.004
Ke C	0.605	0.394	0.006	0.007
Ke D	0.609	0.402	0.008	0.010
Pk P	0.209	0.088	0.004	0.003
Pk C	0.337	0.164	0.000	0.000
Pk D	0.347	0.175	0.004	0.004
Lv P	0.443	0.293	0.006	0.008
Lv C	0.444	0.268	0.008	0.009
Lv D	0.443	0.258	0.004	0.005
Tf P	0.495	0.282	0.005	0.006
Tf C	0.532	0.308	0.006	0.007
Tf D	0.500	0.279	0.010	0.011

ψJ vs ψA for all *adaxial petiole* sections				
mean (n = 32)	ψA	ψJ	ψA margin of error	ψJ margin of error
KeP	0.479	0.302	0.006	0.007
KeC	0.541	0.350	0.006	0.007
KeD	0.485	0.307	0.013	0.015
PkP	0.281	0.183	0.006	0.007
PkC	0.387	0.239	0.005	0.005
PkD	0.407	0.253	0.005	0.006
LvP	0.263	0.164	0.010	0.008
LvC	0.387	0.232	0.007	0.008
LvD	0.381	0.222	0.006	0.007
TfP	0.605	0.412	0.007	0.010
TfC	0.674	0.481	0.009	0.013
TfD	0.628	0.432	0.015	0.021

ψJ vs ψ_A for all *abaxial petiole* sections

mean (n = 32)	ψ_A	ψ_J	ψA margin of error	ψJ margin of error
KeP	0.855	0.750	0.006	0.011
KeC	0.875	0.778	0.009	0.015
KeD	0.822	0.697	0.012	0.020
PkP	0.854	0.743	0.020	0.034
PkC	0.863	0.756	0.009	0.016
PkD	0.891	0.802	0.009	0.016
LvP	0.944	0.894	0.013	0.025
LvC	0.903	0.822	0.016	0.029
LvD	0.846	0.726	0.008	0.014
TfP	0.787	0.645	0.009	0.015
TfC	0.799	0.665	0.010	0.017
TfD	0.842	0.727	0.020	0.034

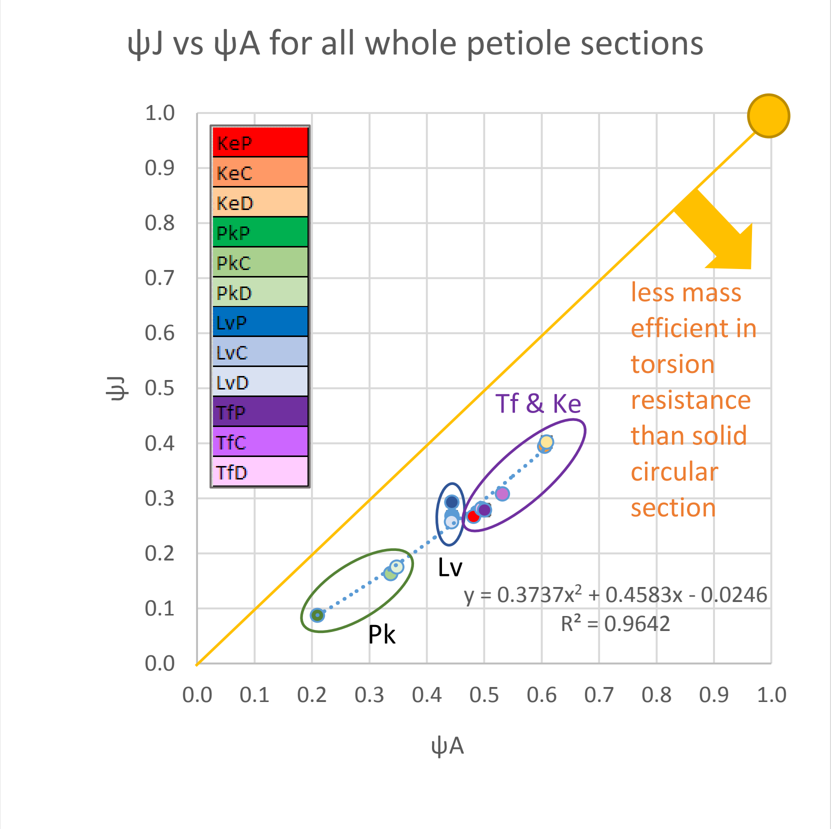

Figure 71 ψ_J vs ψ_A for whole *petiole* sections (showing 95% confidence intervals)

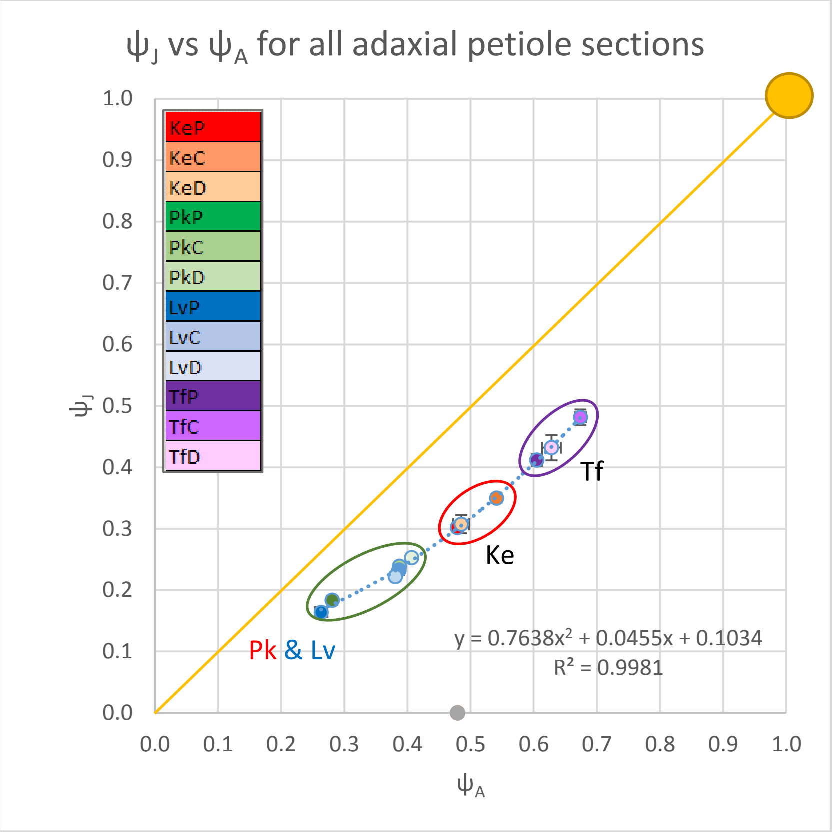

Figure 72 ψ_J vs ψ_A for *adaxial petiole* sections (showing 95% confidence intervals)

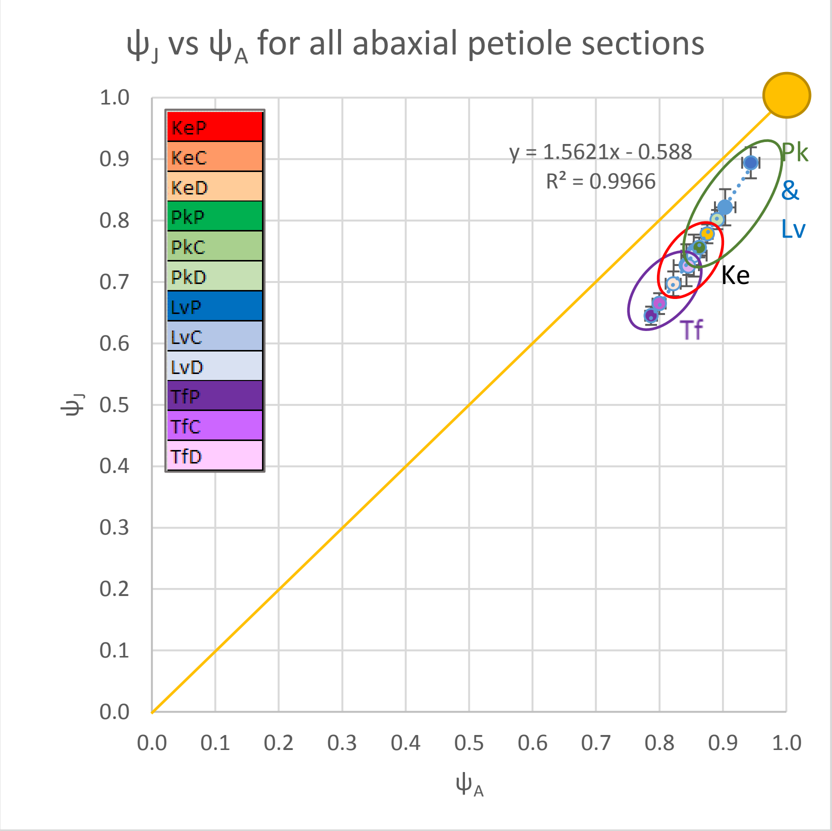

Figure 73 ψ_J vs ψ_A for *abaxial petiole* sections (showing 95% confidence intervals)

4.3.4.3 *Twist-to-bend ratio,* ψ_I *vs* ψ_J

Table 27 ψ_I vs ψ_J whole *petiole* and SEM results

ψ_I vs ψ_J for all whole *petiole* sections				
mean (n = 32)	ψ_J	ψ_I	ψ_J margin of error	ψ_I margin of error
Ke P	0.267	0.193	0.004	0.003
Ke C	0.394	0.318	0.007	0.006
Ke D	0.402	0.363	0.010	0.010
Pk P	0.088	0.036	0.003	0.002
Pk C	0.164	0.084	0.000	0.000
Pk D	0.175	0.082	0.004	0.002
Lv P	0.293	0.135	0.008	0.004
Lv C	0.268	0.120	0.009	0.005
Lv D	0.258	0.128	0.005	0.003
Tf P	0.282	0.220	0.006	0.005
Tf C	0.308	0.265	0.007	0.006
Tf D	0.279	0.210	0.011	0.008

ψ_I vs ψ_J for all *adaxial petiole* sections				
mean (n = 32)	ψ_J	ψ_I	ψ_I margin of error	ψ_J margin of error
KeP	0.302	0.126	0.003	0.007
KeC	0.350	0.176	0.004	0.007
KeD	0.307	0.131	0.006	0.015
PkP	0.183	0.049	0.002	0.007
PkC	0.239	0.078	0.002	0.005
PkD	0.253	0.087	0.002	0.006
LvP	0.164	0.042	0.003	0.008
LvC	0.232	0.076	0.003	0.008
LvD	0.222	0.072	0.003	0.007
TfP	0.412	0.236	0.006	0.010
TfC	0.481	0.334	0.009	0.013
TfD	0.432	0.265	0.013	0.021

ψ_I vs ψ_J for all *abaxial petiole* sections				
mean (n = 32)	ψ_J	ψ_I	ψ_J margin of error	ψ_I margin of error
KeP	0.750	0.822	0.011	0.012
KeC	0.778	0.851	0.015	0.017
KeD	0.697	0.809	0.020	0.023
PkP	0.743	0.760	0.034	0.035
PkC	0.756	0.783	0.016	0.017
PkD	0.802	0.817	0.016	0.016
LvP	0.894	0.940	0.025	0.029
LvC	0.822	0.823	0.029	0.032
LvD	0.726	0.718	0.014	0.014
TfP	0.645	0.668	0.015	0.015
TfC	0.665	0.678	0.017	0.017
TfD	0.727	0.745	0.034	0.034

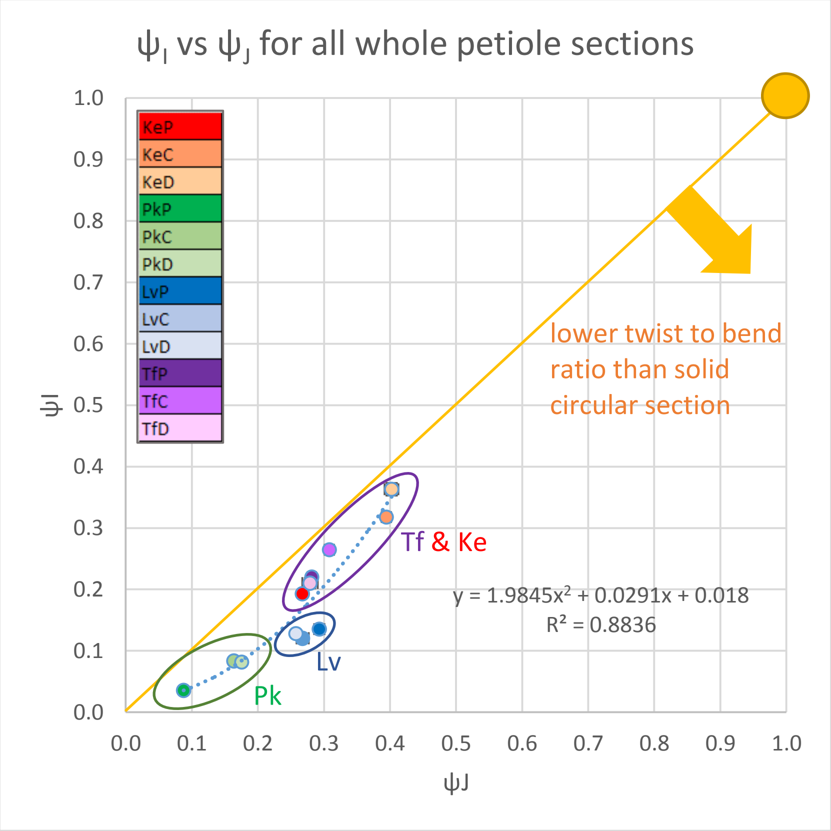

Figure 74 ψ_I vs ψ_J for whole *petiole* sections (showing 95% confidence intervals)

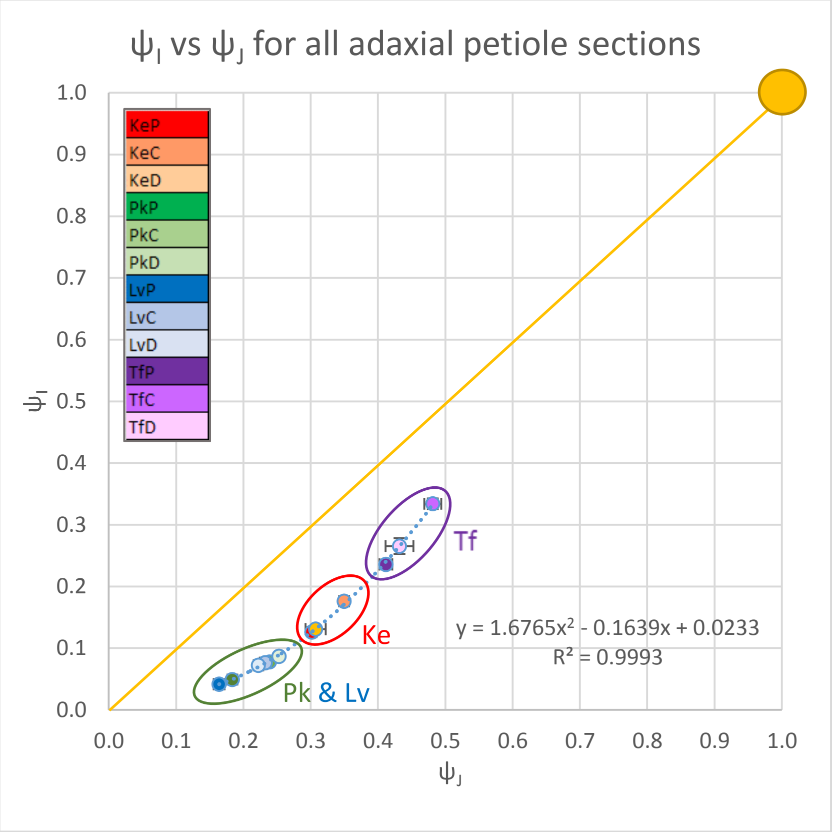

Figure 75 ψ_l vs ψ_J for *adaxial petiole* sections (showing 95% confidence intervals)

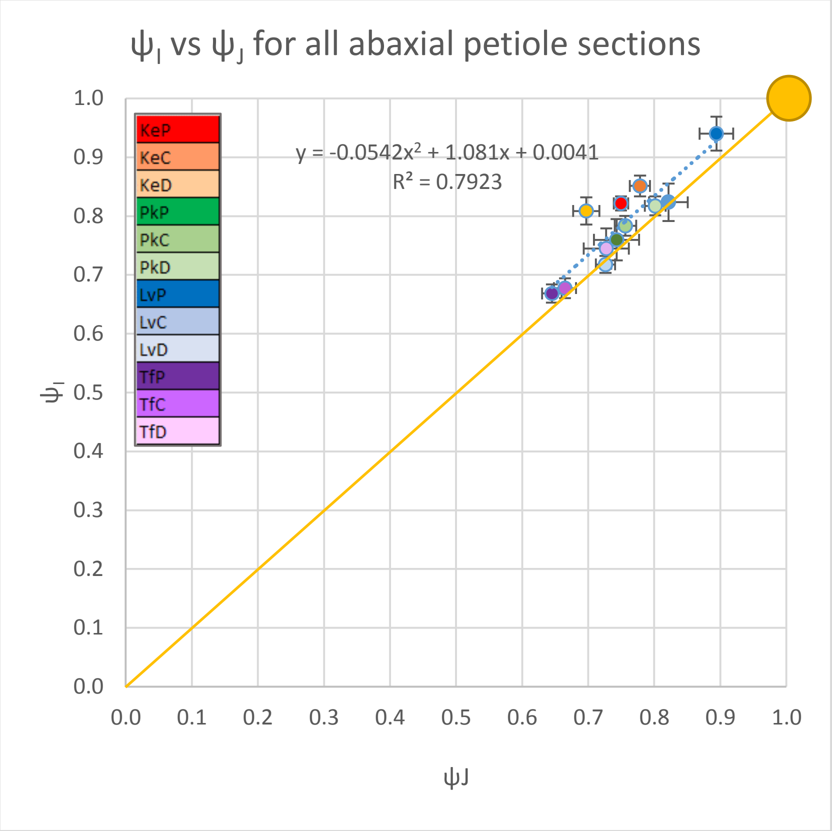

Figure 76 ψ_l vs ψ_J for *abaxial petiole* sections (showing 95% confidence intervals)

4.3.5 Performance indices

4.3.5.1 Performance index λ_{IA}

The values of λ_{IA} for the whole *petiole* are significantly different between palm species and changes the most along its length in the palm species (Table 28 and Figure 77). This is also true for the *adaxial petiole* apart from *Pk* and *Lv* which are indistinguishable in all but the distal (D) sections (Table 29 and Figure 78). The *abaxial petiole* λ_{IA} is effectively constant for all sections of all species tested (Table 30 and Figure 79). The *abaxial petiole* λ_{IA} of 0.9 for all *petioles* and sections is very close to the λ_{IA} of 1.0 for the solid circle.

Table 28 λ_{IA} whole *petioles*

Whole *petioles*		
λ_{IA}	mean (n = 32)	margin of error
Ke P	0.402	0.007
Ke C	0.524	0.012
Ke D	0.595	0.018
Pk P	0.171	0.008
Pk C	0.249	0.006
Pk D	0.235	0.006
Lv P	0.305	0.011
Lv C	0.270	0.013
Lv D	0.288	0.006
TfP	0.444	0.011
TfC	0.496	0.013
TfD	0.419	0.019

Table 29 λ_{IA} *adaxial petioles*

Adaxial petioles		
λ_{IA}	mean (n = 32)	margin of error
KeP	0.263	0.007
KeC	0.325	0.008
KeD	0.269	0.015
PkP	0.175	0.008
PkC	0.201	0.006
PkD	0.214	0.006
LvP	0.157	0.012
LvC	0.198	0.009
LvD	0.190	0.008
TfP	0.389	0.010
TfC	0.495	0.014
TfD	0.423	0.023

Table 30 λ_{IA} *abaxial petioles*

Abaxial petioles		
λ_{IA}	mean (n = 32)	margin of error
KeP	0.961	0.016
KeC	0.972	0.022
KeD	0.983	0.032
PkP	0.889	0.046
PkC	0.909	0.022
PkD	0.918	0.020
LvP	0.996	0.034
LvC	0.911	0.039
LvD	0.849	0.019
TfP	0.850	0.022
TfC	0.847	0.012
TfD	0.884	0.046

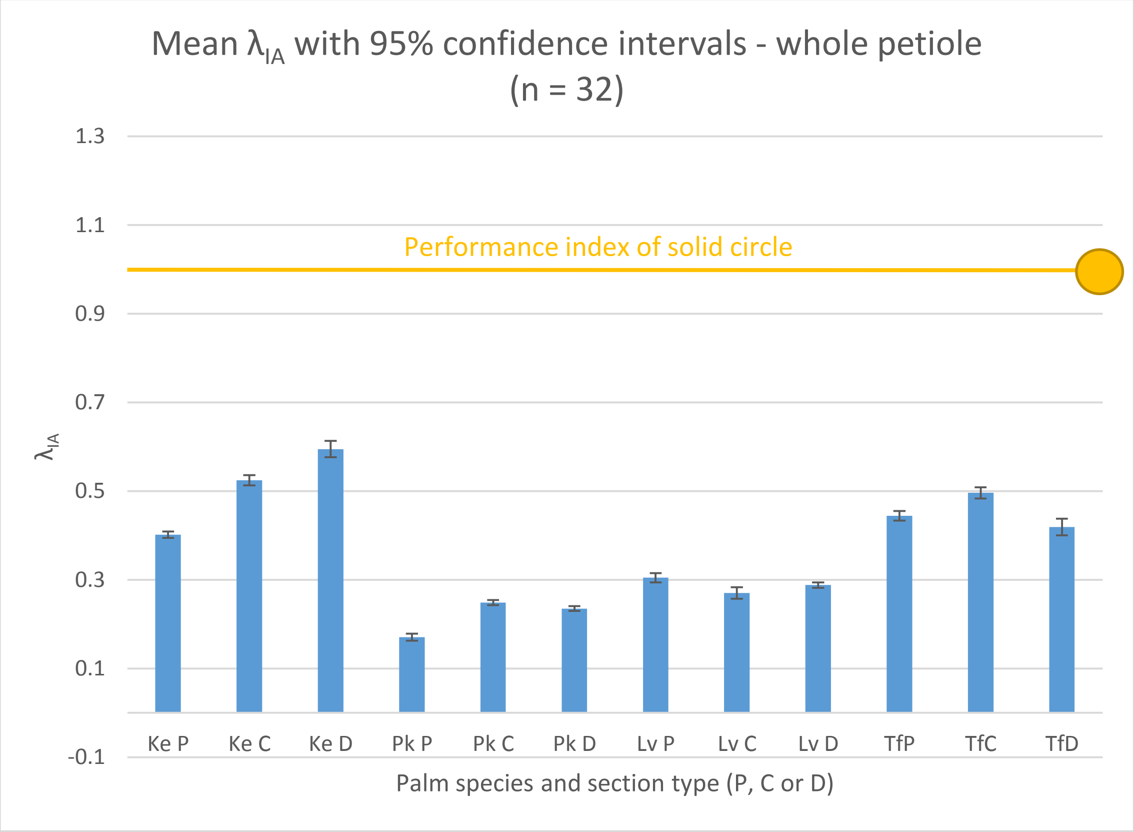

Figure 77 λ_{IA} whole *petioles*

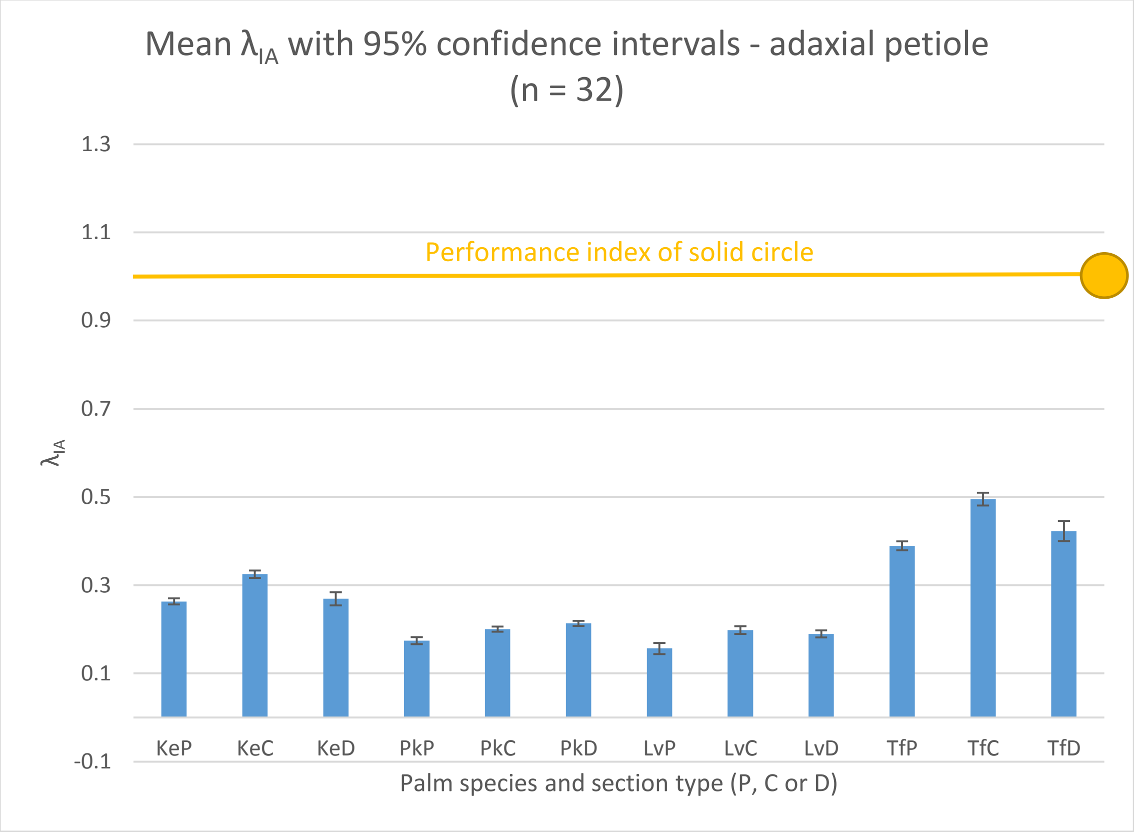

Figure 78 λ_{IA} ***adaxial petioles***

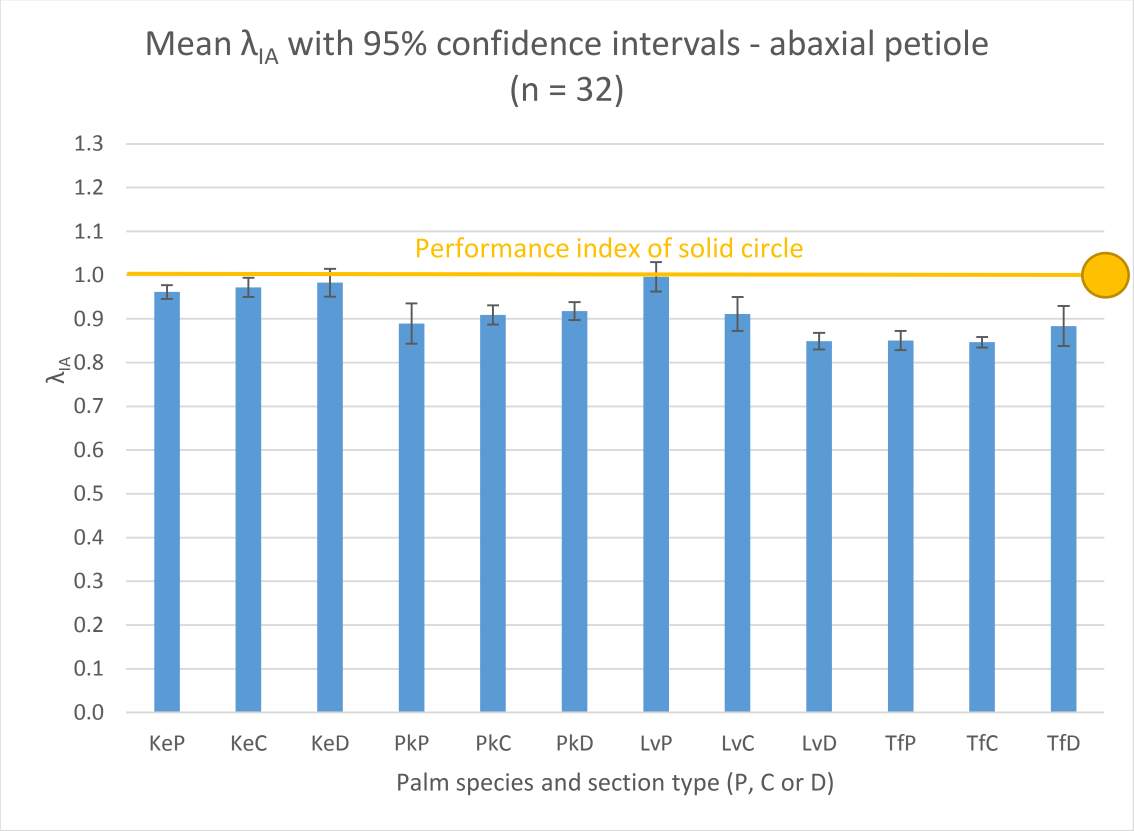

Figure 79 λ_{IA} ***abaxial petioles***

4.3.5.2 Performance index λ_{JA}

The whole *petiole* λ_{JA} sections between species are distinct from one another (Table 31 and Figure 80) whereas the *abaxial* and *adaxial petiole* shapes in Table 32, Table 33, Figure 81 and Figure 82 show effectively constant λ_{JA} across all species as a result of their overlapping 95% confidence intervals.

Table 31 λ_{JA} whole *petioles*

Whole *petioles*		
λ_{JA}	mean (n = 32)	margin of error
Ke P	0.556	0.010
Ke C	0.651	0.013
Ke D	0.660	0.019
Pk P	0.418	0.019
Pk C	0.486	0.011
Pk D	0.505	0.012
Lv P	0.660	0.019
Lv C	0.602	0.024
Lv D	0.581	0.013
TfP	0.568	0.013
TfC	0.579	0.015
TfD	0.556	0.026

Table 32 λ_{JA} *adaxial petioles*

Adaxial petioles		
λ_{JA}	mean (n = 32)	margin of error
KeP	0.630	0.015
KeC	0.646	0.015
KeD	0.633	0.035
PkP	0.652	0.030
PkC	0.617	0.016
PkD	0.622	0.016
LvP	0.622	0.039
LvC	0.601	0.024
LvD	0.583	0.021
TfP	0.681	0.018
TfC	0.714	0.021
TfD	0.688	0.037

Table 33 λ_{JA} *abaxial petioles*

Abaxial petioles		
λ_{JA}	mean (n = 32)	margin of error
KeP	0.877	0.014
KeC	0.889	0.020
KeD	0.848	0.027
PkP	0.870	0.045
PkC	0.877	0.021
PkD	0.900	0.020
LvP	0.947	0.030
LvC	0.909	0.036
LvD	0.859	0.019
TfP	0.820	0.021
TfC	0.831	0.012
TfD	0.863	0.045

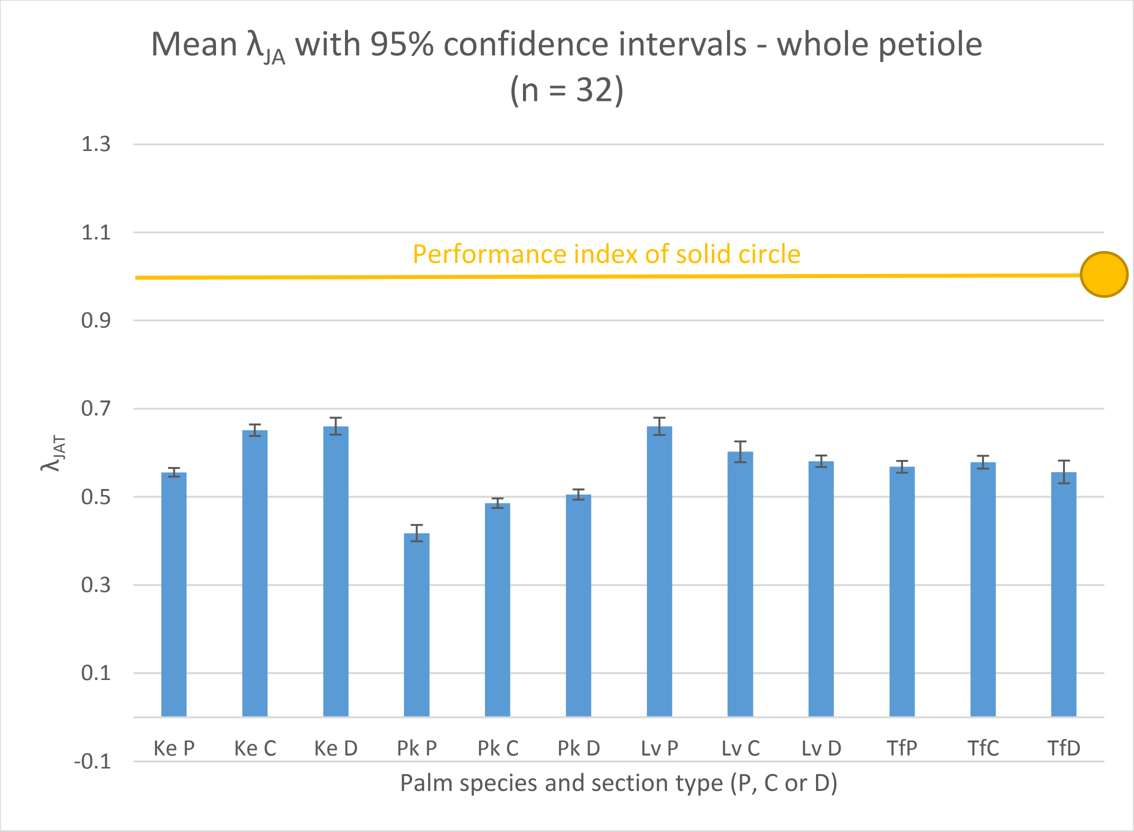

Figure 80 λ_{JA} whole *petioles*

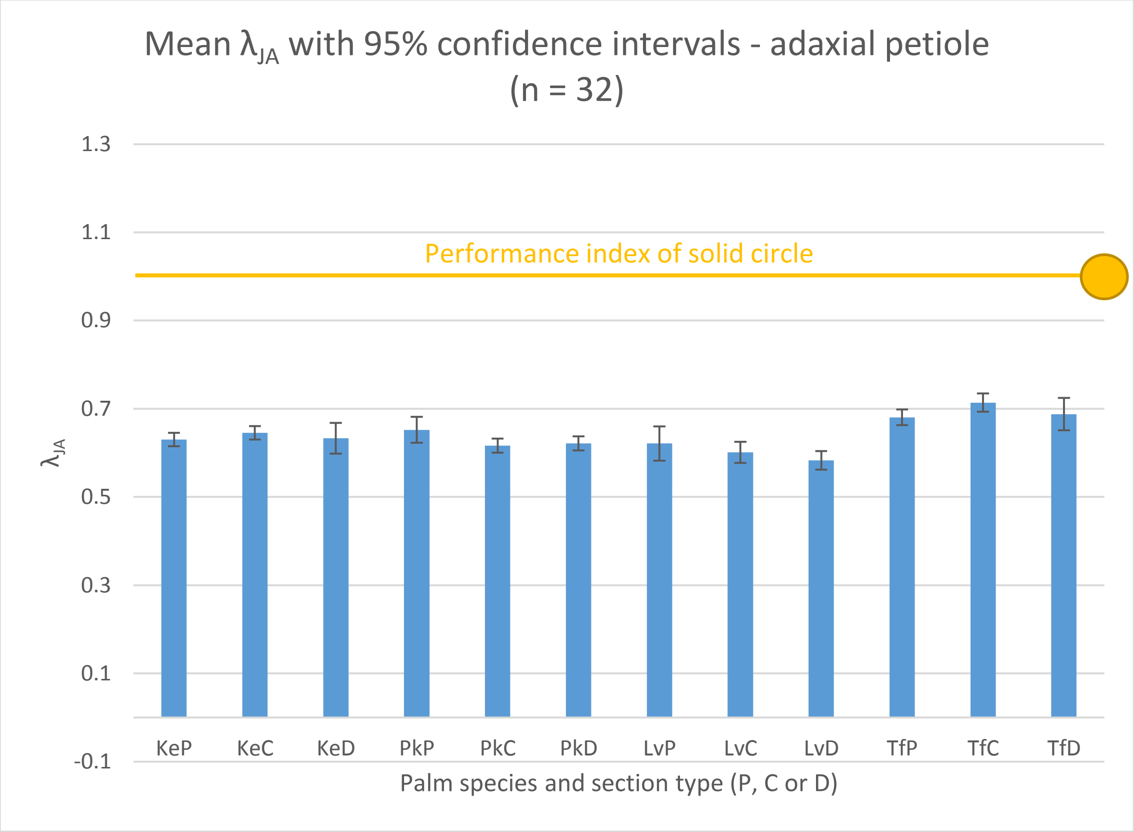

Figure 81 λ_{JA} ***adaxial petioles***

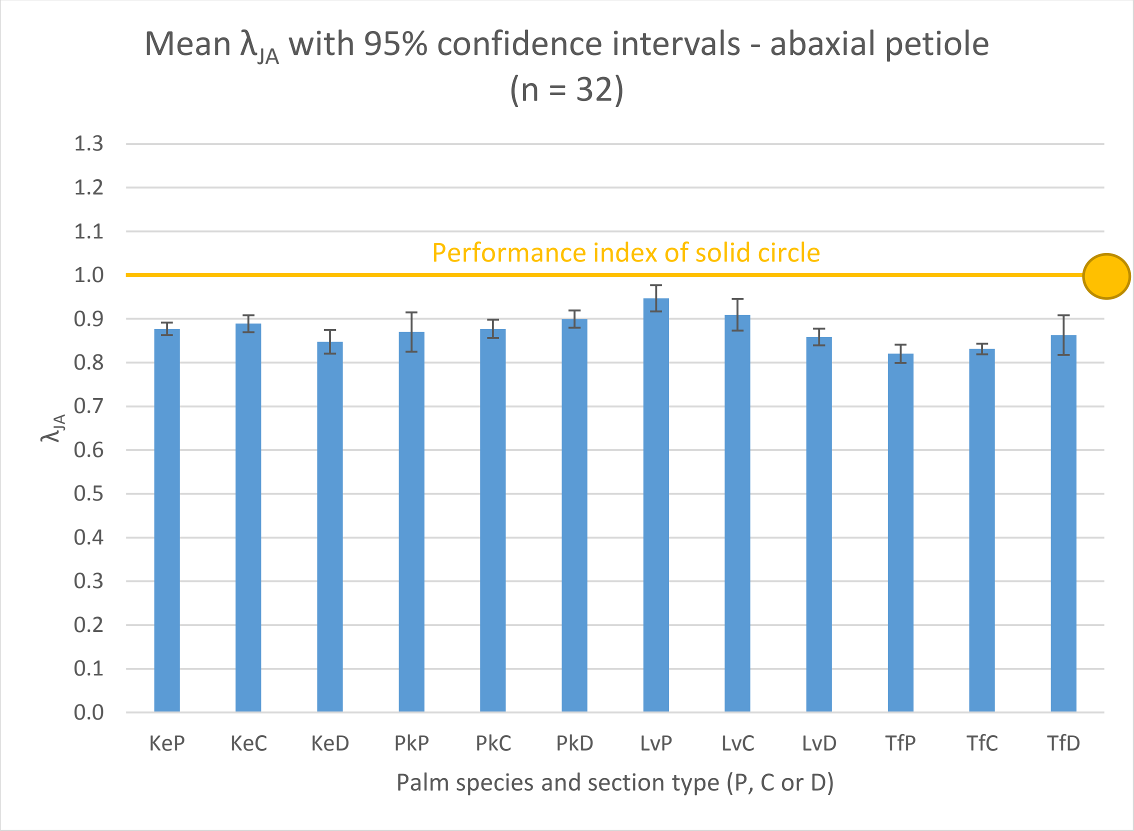

Figure 82 λ_{JA} ***abaxial petioles***

4.3.5.3 Performance index λ_{IJ}

The values of λ_{IJ} for the P, C and D sections is highest in the *Ke* and *Tf* palm *petioles* (Table 34 and Figure 83) and the λ_{IJ} of 1.05 for the *abaxial petiole* exceeds the performance of that of the solid circle at 1.0 (Table 36 and Figure 85).

Table 34 λ_{IJ} whole *petioles*

Whole *petioles*		
λ_{IJ}	mean (n = 32)	margin of error
Ke P	0.723	0.016
Ke C	0.805	0.022
Ke D	0.902	0.034
Pk P	0.408	0.024
Pk C	0.512	0.014
Pk D	0.465	0.014
Lv P	0.462	0.019
Lv C	0.450	0.025
Lv D	0.497	0.014
TfP	0.782	0.024
TfC	0.858	0.028
TfD	0.754	0.043

Table 35 λ_{IJ} *adaxial petioles*

Adaxial petioles		
λ_{IJ}	mean (n = 32)	margin of error
KeP	0.418	0.014
KeC	0.503	0.016
KeD	0.426	0.029
PkP	0.268	0.015
PkC	0.325	0.011
PkD	0.343	0.012
LvP	0.252	0.022
LvC	0.329	0.017
LvD	0.325	0.016
TfP	0.572	0.019
TfC	0.694	0.026
TfD	0.614	0.042

Table 36 λ_{IJ} *abaxial petioles*

Abaxial petioles		
λ_{IJ}	mean (n = 32)	margin of error
KeP	1.096	0.022
KeC	1.094	0.031
KeD	1.160	0.047
PkP	1.023	0.067
PkC	1.036	0.031
PkD	1.020	0.028
LvP	1.052	0.044
LvC	1.002	0.053
LvD	0.988	0.028
TfP	1.036	0.034
TfC	1.019	0.018
TfD	1.024	0.067

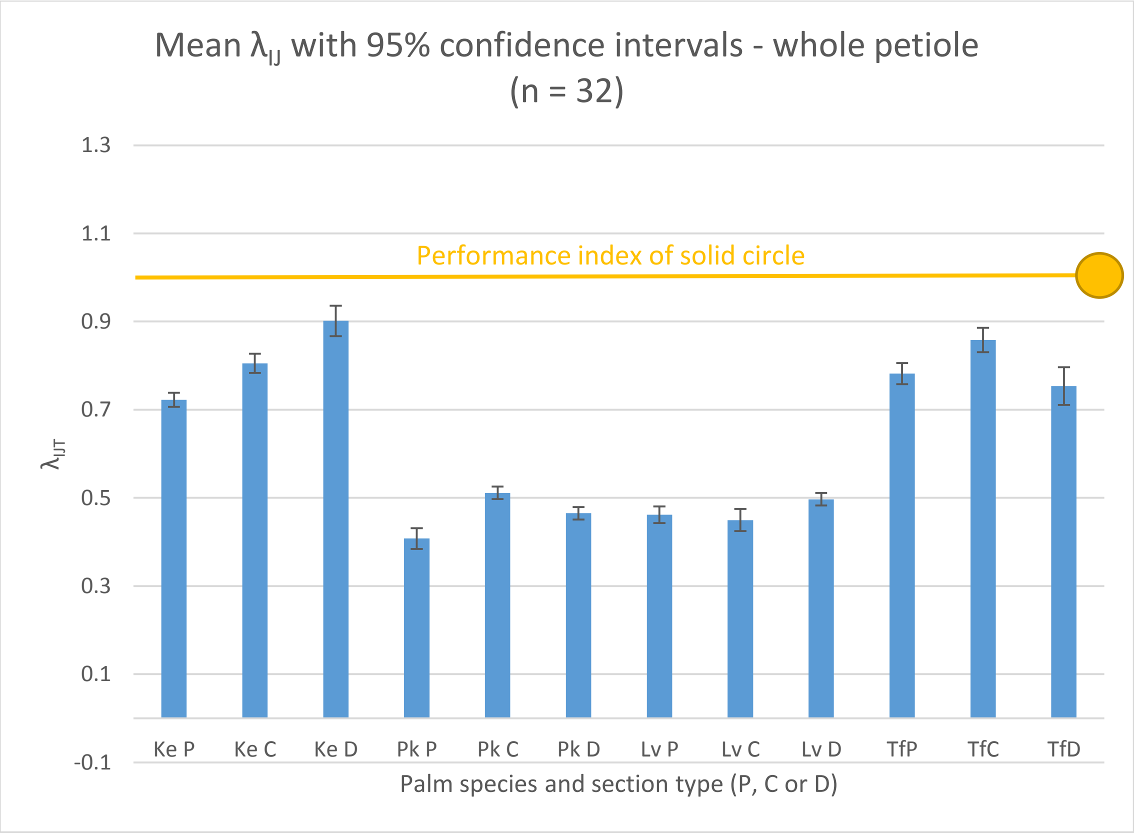

Figure 83 λ_{IJ} whole *petioles*

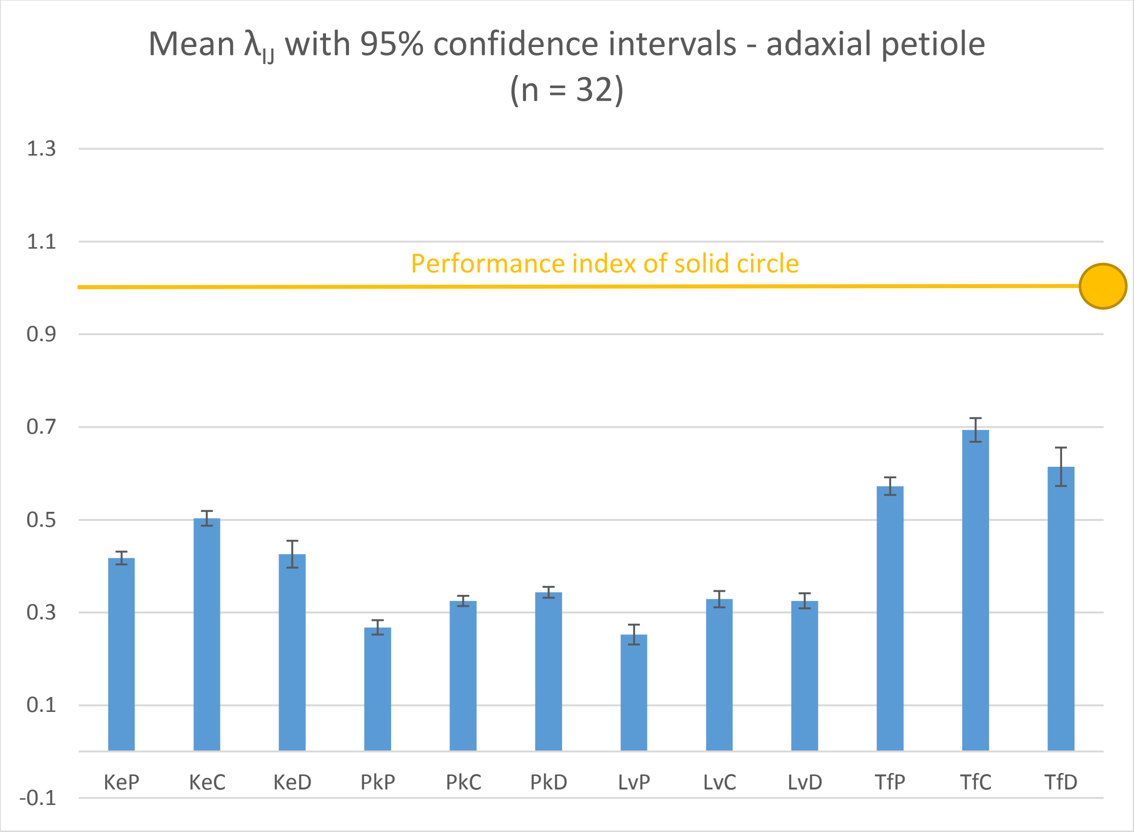

Figure 84 λ_{IJ} ***adaxial petioles***

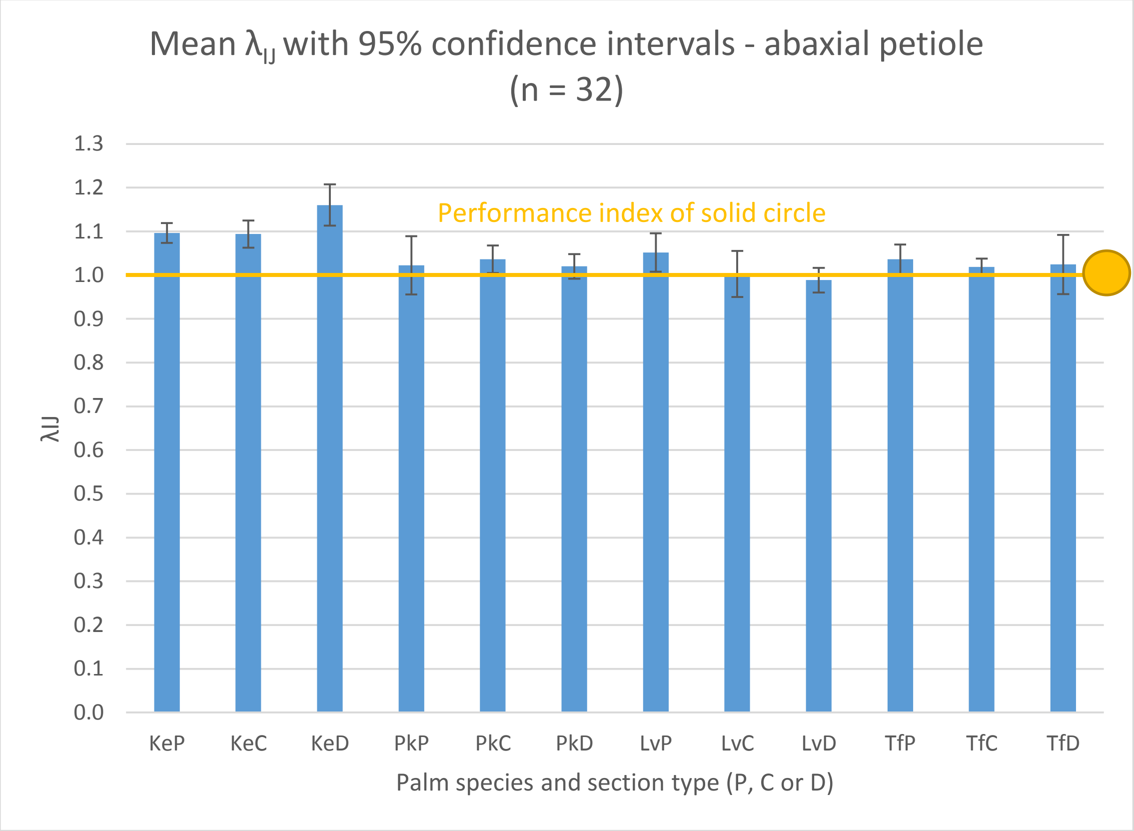

Figure 85 λ_{IJ} ***abaxial petioles***

4.3.6 Verification of SEM with regular shapes

Table 37 *shape transformers* and performance indices for regular shapes using SEM

Whole shape	ψ_A	ψ_I	ψ_J	λ_{IA}	λ_{JA}	λ_{IJ}
Circle	1.00	1.00	1.00	1.00	1.00	1.00
Equilateral triangle	0.41	0.21	0.21	0.50	0.50	1.00
Square	0.64	0.42	0.42	0.67	0.67	1.00
Hexagon	0.83	0.69	0.69	0.83	0.83	1.00

Adaxial regular shape	ψ_A	ψ_I	ψ_J	λIA	λJA	λIJ
Circle	1.00	1.00	1.00	1.00	1.00	1.00
Equilateral triangle	0.61	0.49	0.41	0.80	0.67	1.19
Square	0.82	0.66	0.68	0.80	0.84	0.96
Hexagon	0.92	0.84	0.84	0.91	0.92	0.99

Abaxial regular shape	ψ_A	ψ_I	ψ_J	λIA	λJA	λIJ
Circle	1.00	1.00	1.00	1.00	1.00	1.00
Equilateral triangle	0.50	0.14	0.32	0.28	0.64	0.43
Square	0.82	0.66	0.68	0.80	0.84	0.96
Hexagon	0.91	0.83	0.83	0.91	0.92	0.99

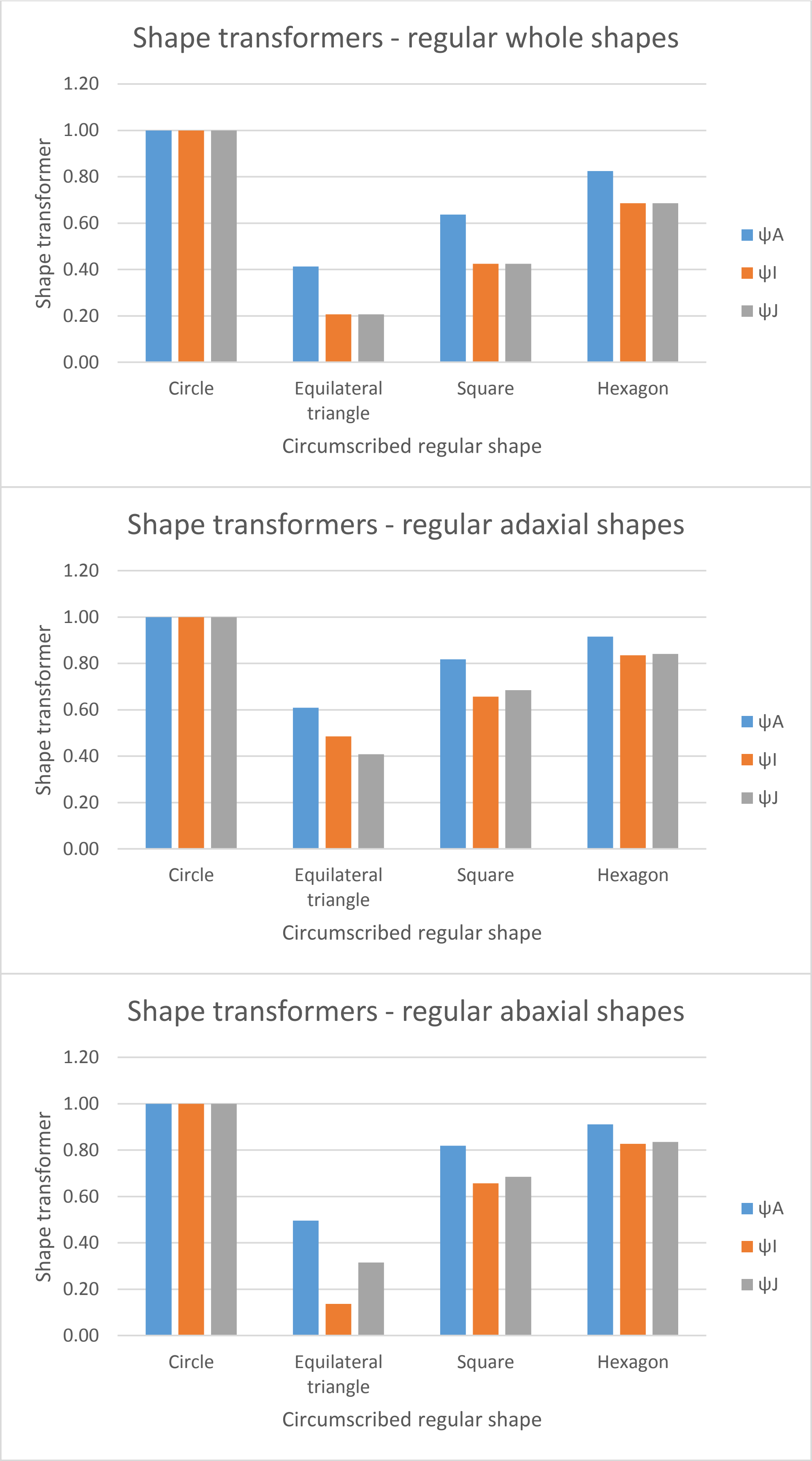

Figure 86 Shape transformers of regular shapes using SEM (n=1, hence no CIs shown)

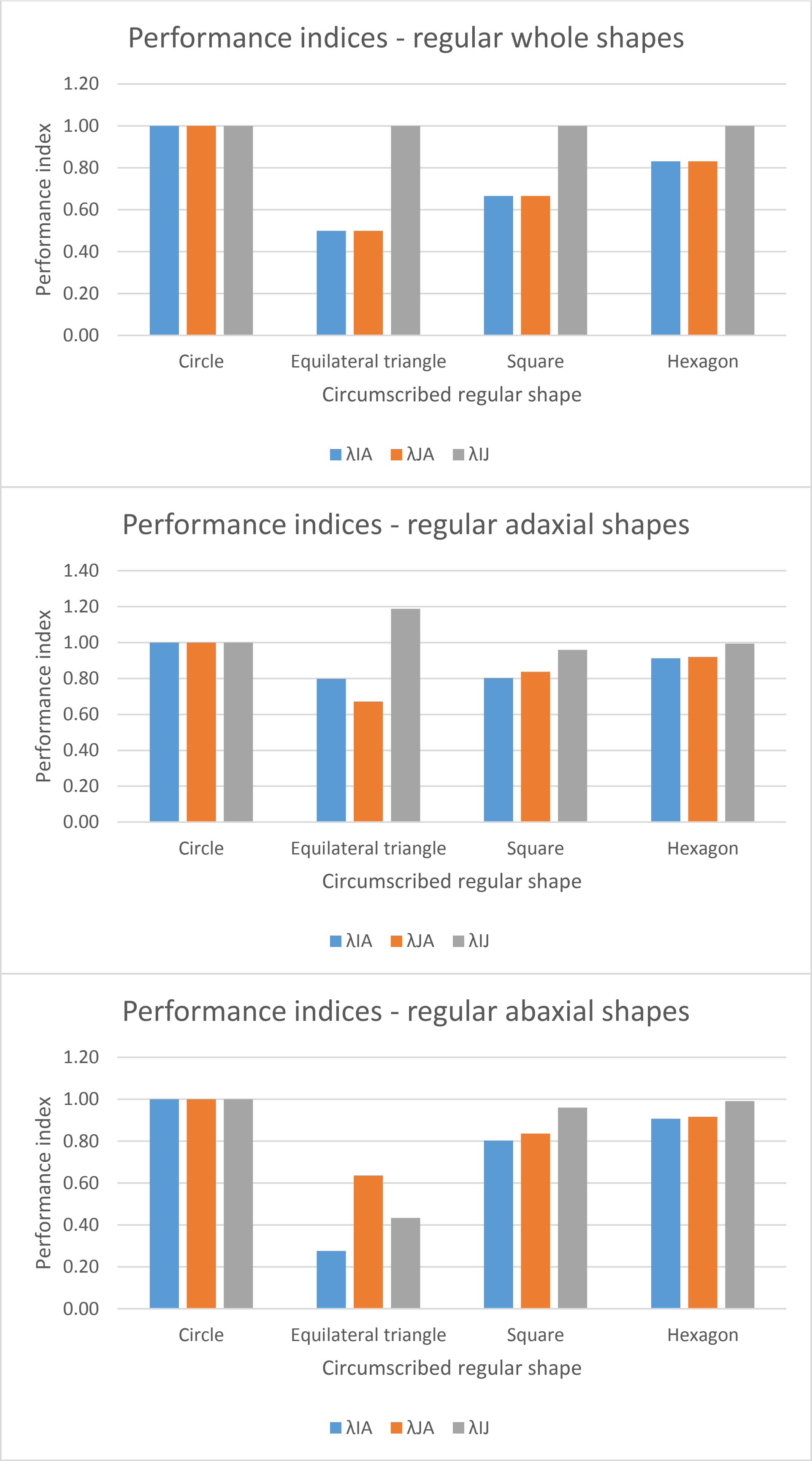

Figure 87 Performance indices of regular shapes using SEM (n=1, hence no CIs shown)

4.3.7 Comparison of rectangular and circular envelopes using SEM

Shape Edge Mapping (SEM) was carried out on four of the *Sabal minor* (*Sm*) palm *petioles*, W, X, Y and Z, using both scaled rectangular envelopes and circular envelopes (which do not require scaling). The *adaxial* (upper) edge of the *petiole* sections were analysed keeping the lower edge, the shape of the envelope, an example of which is shown in Figure 88.

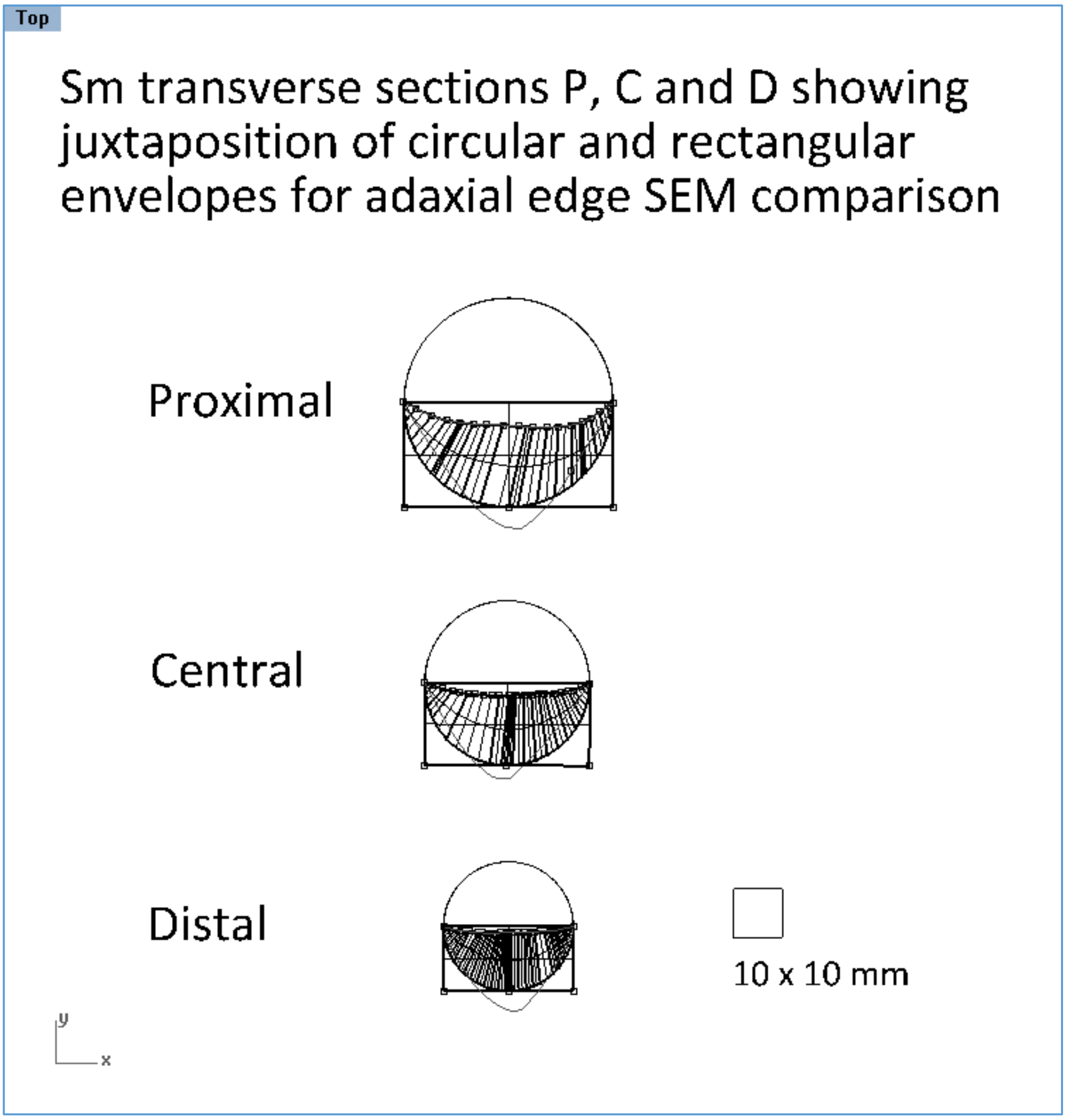

Figure 88 Rhino representation of *Sm adaxial* transverse-sections from one of the four *petioles*, SmW, with circular and rectangular envelope lower edges

shape transformers for resistance to torsion which take into account scaling had not been developed at the time of writing; only for hollow shafts as can be seen in the paper, '*Shape factor*s and material indices for dimensionally constrained structures Part 2: shafts' by Burgess (Burgess, 1999). Therefore, only the bending performance index, λ_{IA} was compared, the results of which are presented in Table 38 to Table 41.

Table 38 Scaled performance index for *adaxial* upper edge and rectangular envelope lower edge of SmW

SmW	P	C	D
A / mm^2 of shape (SmW)	572	393	257
Ix/ mm^4 of shape (SmW)	13,438	6,427	2,792
Iy/ mm^4 of shape (SmW)	68,775	29,125	11,742
Iz / mm^4 of shape (SmW)	82,212	35,552	14,534
A / mm^2 of rectangular envelope	939	580	357
Ix/ mm^4 of rectangular envelope	36,802	14,030	5,260
Iy/ mm^4 of rectangular envelope	146,982	56,160	21,539
Iz / mm^4 of rectangular envelope	183,784	70,190	26,799
Breadth of rectangular envelope / mm	43	34	27
Height of rectangular envelope / mm	22	17	13
u (x axis)	43	34	27
v (y axis)	22	17	13
ln uv	6.84	6.37	5.87
ln uv^3	12.99	12.04	11.04
q	0.5267	0.5289	0.5318
ψ_A	0.61	0.68	0.72
$\psi_I^{\,q}$	0.59	0.66	0.71
λ_{IA} ($\psi_I^{\,q}$ / ψ_A)	0.97	0.98	0.99

Table 39 Scaled performance index for *adaxial* upper edge and rectangular envelope lower edge of SmX

SmX	P	C	D
A / mm^2 of shape (SmW)	543	348	358
Ix/ mm^4 of shape (SmW)	12263	5007	5636
Iy/ mm^4 of shape (SmW)	63930	23259	21097
Iz / mm^4 of shape (SmW)	76194	28266	26733
A / mm^2 of rectangular envelope	930.63	528.16	465.56
Ix/ mm^4 of rectangular envelope	36201	11592	8940
Iy/ mm^4 of rectangular envelope	143885	46614	36490
Iz / mm^4 of rectangular envelope	180087	58207	45430
Breadth of rectangular envelope / mm	43	32	31
Height of rectangular envelope / mm	22	16	15
u (x axis)	43	32	31
v (y axis)	22	16	15
ln uv	6.83	6.27	6.14
ln uv^3	12.98	11.86	11.57
q	0.53	0.53	0.53
ψ_A	0.58	0.66	0.77
$\psi_I^{\,q}$	0.57	0.64	0.78
λ_{IA} ($\psi_I^{\,q}$ / ψ_A)	0.97	0.97	1.02

Table 40 Scaled performance index for *adaxial* upper edge and rectangular envelope lower edge of SmY

SmY	P	C	D
A / mm^2 of shape (SmW)	576	351	287
Ix/ mm^4 of shape (SmW)	13596	5144	3508
Iy/ mm^4 of shape (SmW)	68649	23714	14474
Iz / mm^4 of shape (SmW)	82245	28859	17982
A / mm^2 of rectangular envelope	922.75	528.4	401.87
Ix/ mm^4 of rectangular envelope	35273	11685	6679
Iy/ mm^4 of rectangular envelope	142737	46337	27120
Iz / mm^4 of rectangular envelope	178010	58023	33799
Breadth of rectangular envelope / mm	43	32	28
Height of rectangular envelope / mm	21	16	14
u (x axis)	43	32	28
v (y axis)	21	16	14
ln uv	6.83	6.28	6.00
ln uv^3	12.96	11.87	11.32
q	0.53	0.53	0.53
ψ_A	0.62	0.66	0.71
ψ_I^q	0.61	0.65	0.71
λ_{IA} (ψ_I^q / ψ_A)	0.97	0.98	0.99

Table 41 Scaled performance index for *adaxial* upper edge and rectangular envelope lower edge of SmZ

SmZ	P	C	D
A / mm^2 of shape (SmW)	592	366	349
Ix/ mm^4 of shape (SmW)	14860	5544	5252
Iy/ mm^4 of shape (SmW)	74315	26795	21732
Iz / mm^4 of shape (SmW)	89175	32339	26985
A / mm^2 of rectangular envelope	969.88	572.5	499.95
Ix/ mm^4 of rectangular envelope	39361	13592	10575
Iy/ mm^4 of rectangular envelope	156112	54888	40763
Iz / mm^4 of rectangular envelope	195473	68481	51338
Breadth of rectangular envelope / mm	44	34	31
Height of rectangular envelope / mm	22	17	16
u (x axis)	44	34	31
v (y axis)	22	17	16
ln uv	6.88	6.35	6.22
ln uv^3	13.06	12.01	11.76
q	0.53	0.53	0.53
ψ_A	0.61	0.64	0.70
ψ_I^q	0.60	0.62	0.69
λ_{IA} (ψ_I^q / ψ_A)	0.98	0.97	0.99

Figure 89 shows that the relative performance in bending mass-efficiency using the two different envelope methods follow the same trend, although their values are different.

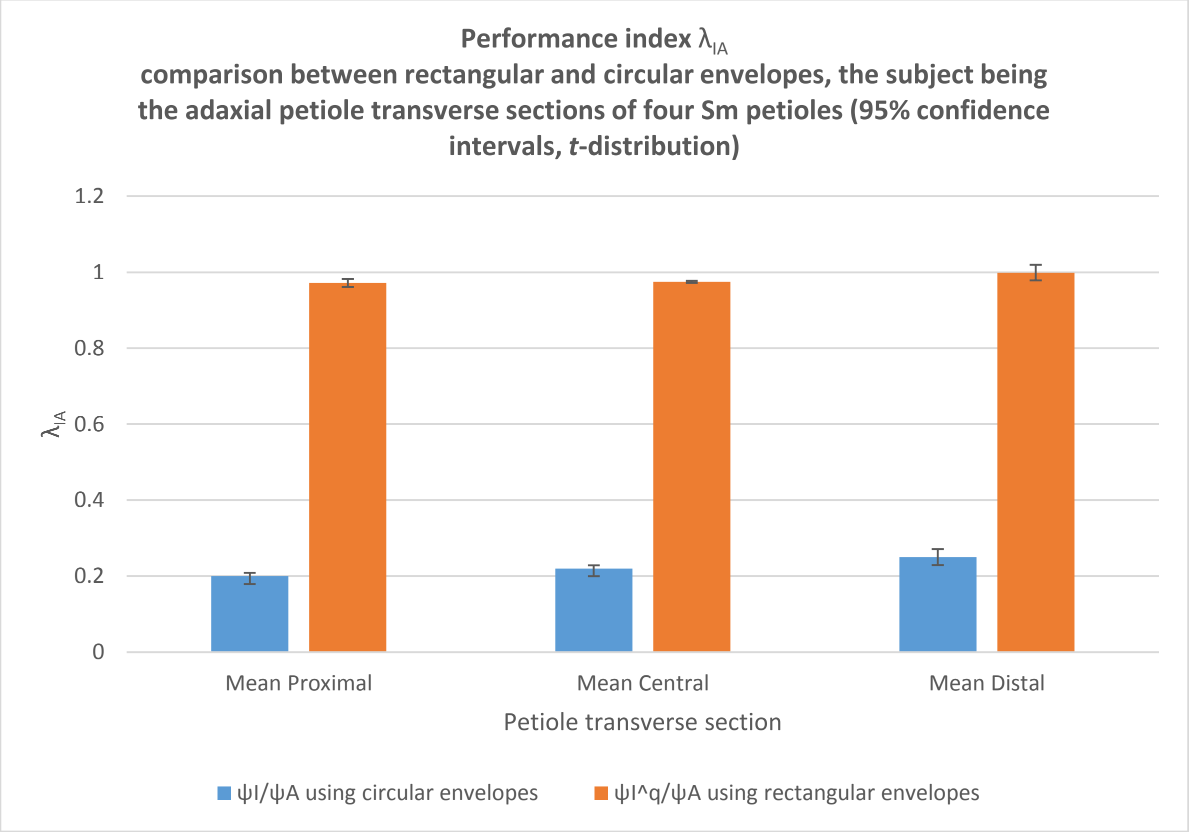

Figure 89 Comparison of λ_{IA} between circular and rectangular envelopes, using SEM with the subject being the *Sabal minor* palm *petiole* upper edge and rectangular and circular envelope lower edge (n=4)

4.3.8 Shape abstraction results using SEM

4.3.8.1 Adaxial Curve Families for 1.5λ and ±0.5λ

Shape transformer charts were created for waveform families designed in Rhinoceros® NURBS modelling for Windows. The shapes of the curves were initially based on three types of upper edges found on palm *petiole* transverse sections (Figure 91). Figure 90 shows an example of the 0.5λ families both with central peak and central trough (profiles LmC and LvP respectively) and the 1.5λ family from the PkC profile represented in Rhino. Two additional upper edge forms, 1.0λ and 2.0λ (*Bm* central trough and *Ke* central peak) were identified later in the research, the *shape transformer* plots for which are shown in Figure 91 and Figure 92.

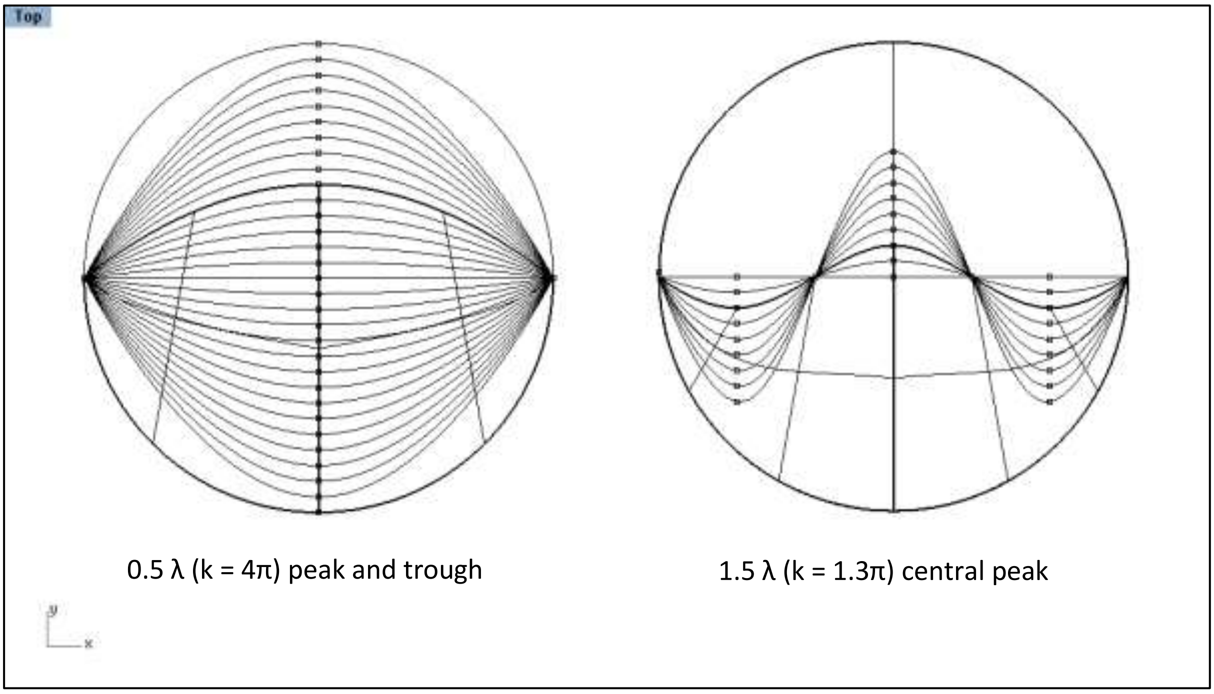

Figure 90 ±0.5 and 1.5 λ waveform examples as represented in Rhino

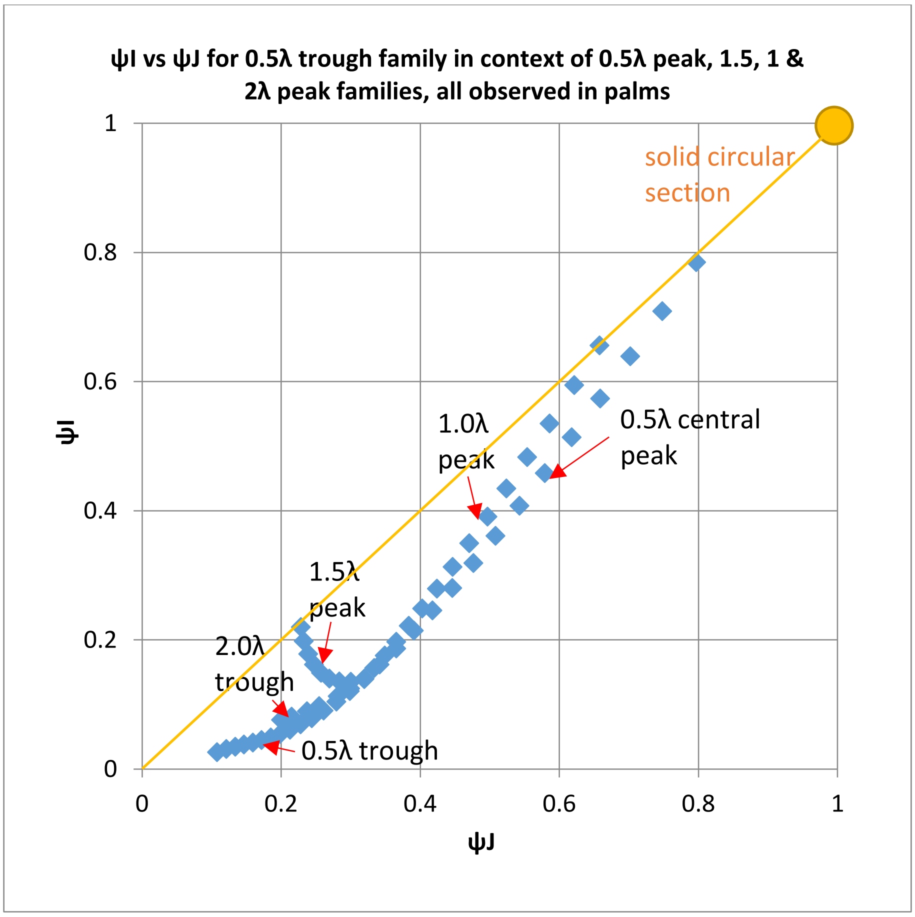

Figure 91 ψI vs ψJ for 0.5λ trough family in context of 0.5λ peak, 1.5, 1 & 2λ peak families

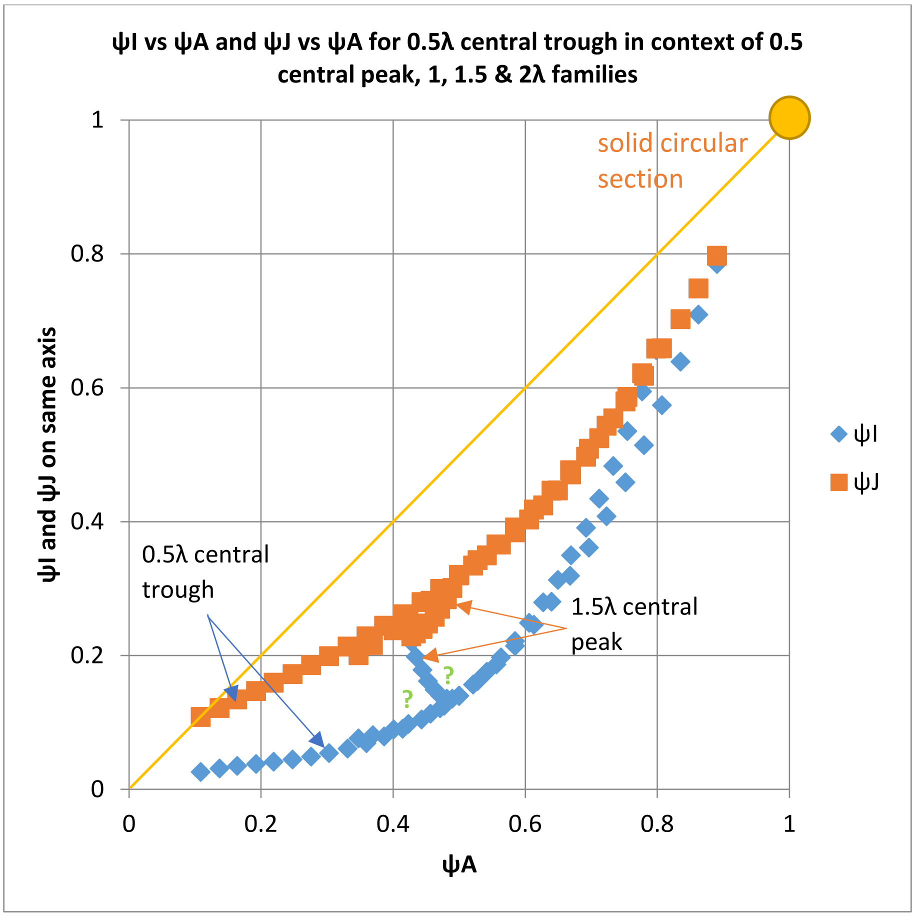

Figure 92 ψI vs ψA and ψJ vs ψA for 0.5λ central trough in context of 0.5 central peak, 1, 1.5 & 2λ families

Because of the anomalous orientation of the 1.5λ central peak data in Figure 92, it was thought that the area where the two green question marks needed investigating. Shape abstraction was used to produce ψ_I vs ψ_A charts of new families not seen in *petioles* in Figure 93, Figure 94 and Figure 95. Each waveform family has a distinct ψ_I/ψ_A gradient in Figure 93. However, notable alignment of the ψ_{JT}/ψ_A data for all the waveform families (Figure 94) shows that the mass-efficiency of the shape resistance to bending is dependent on λ and amplitude. However, λ and amplitude had very little effect on the resistance to torsion shape *efficiency*.

The ψ_I vs ψ_{JT} chart in Figure 95 shows that as λ increases, the curve rotates anticlockwise about the co-ordinates for a semi-circle. The amplitude of the waveforms increases from this point.

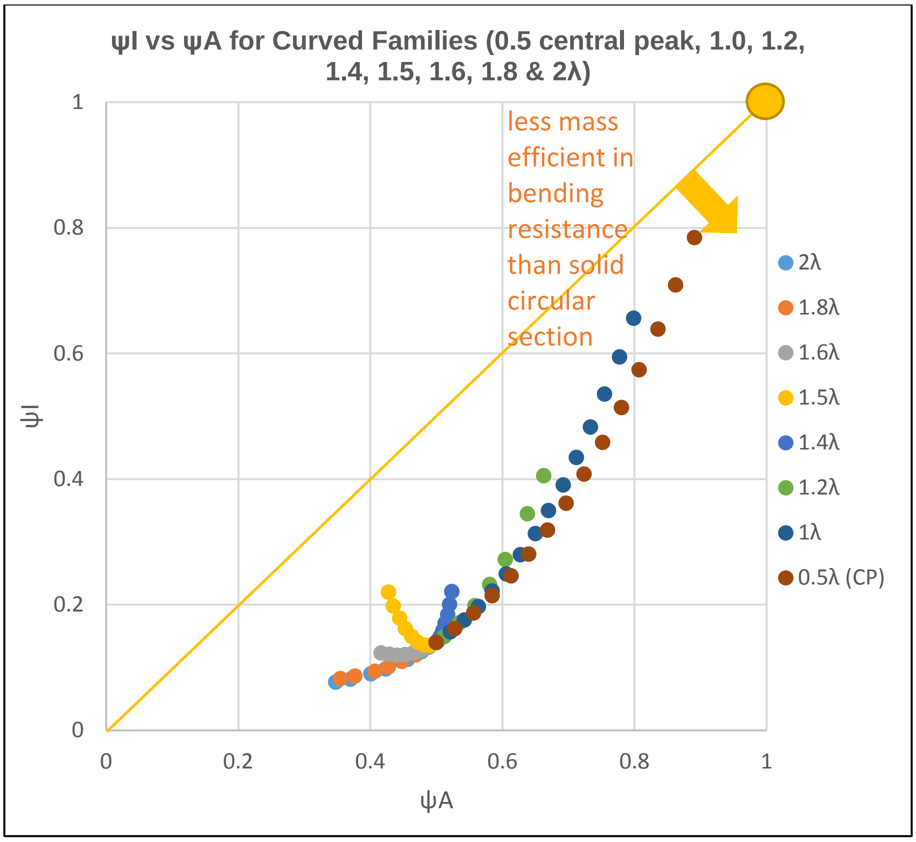

Figure 93 ψI vs ψA for Curved Families (central peak for 0.5, 1.0, 1.2, 1.4, 1.5, 1.6, 1.8 & 2λ)

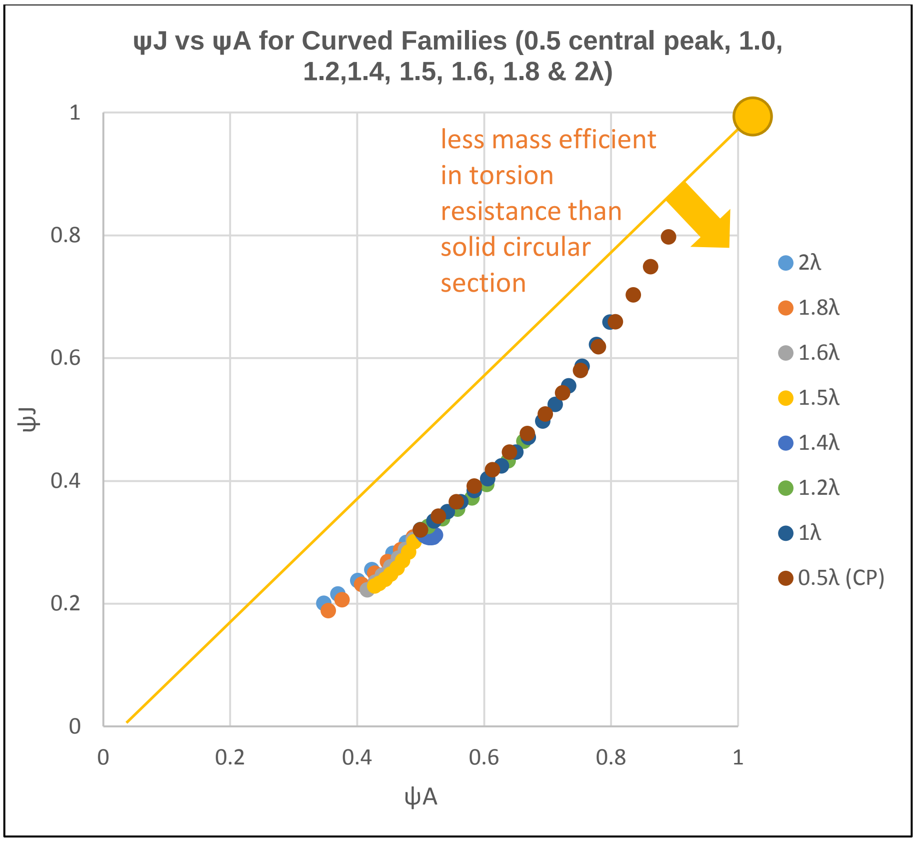

Figure 94 ψ_{JT} vs ψ_A for central peak 0.5, 1.0, 1.2, 1.4, 1.5, 1.6, 1.8 & 2λ families

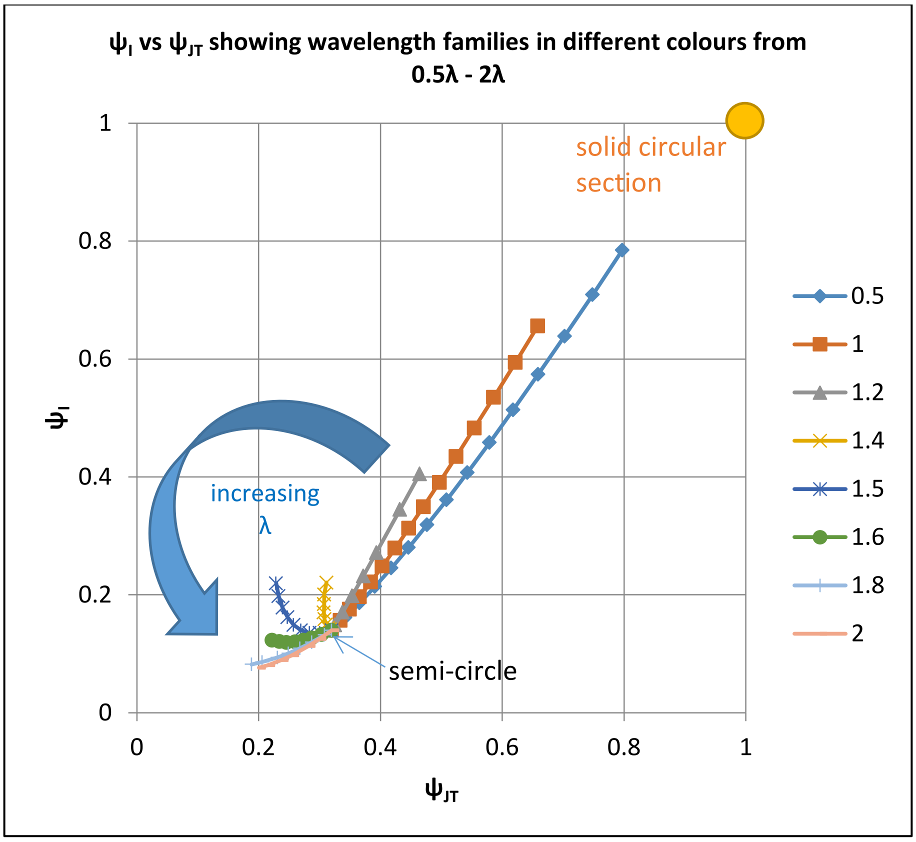

Figure 95 ψ$_I$ vs ψ$_{JT}$ showing from 0.5λ - 2λ waveform families

4.3.8.2 Performance Charts for shape abstraction

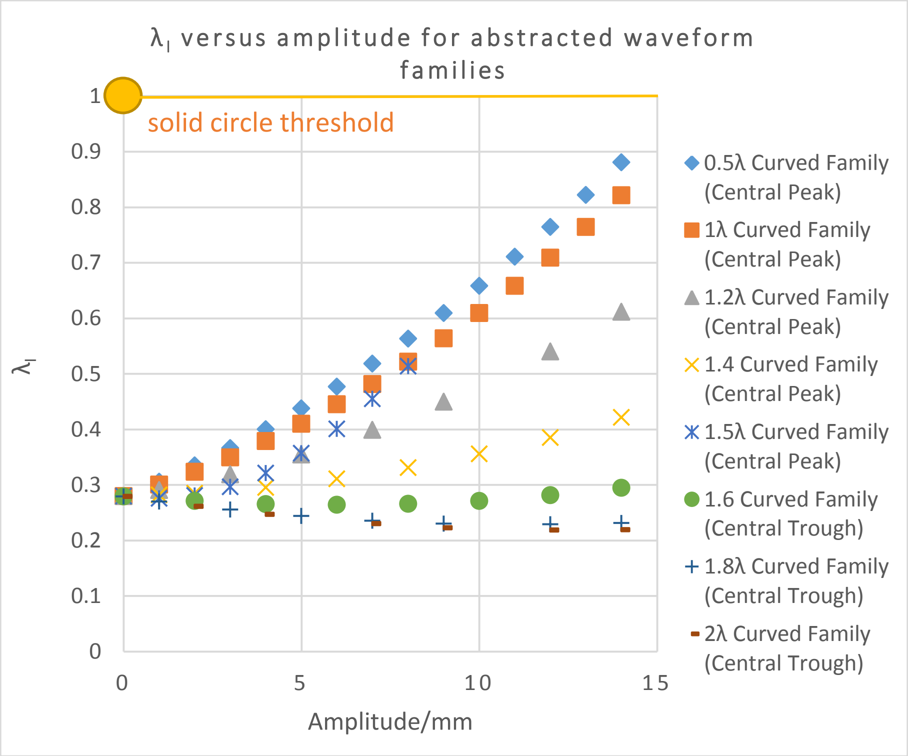

Figure 96 λ$_I$ versus amplitude for abstracted waveform families

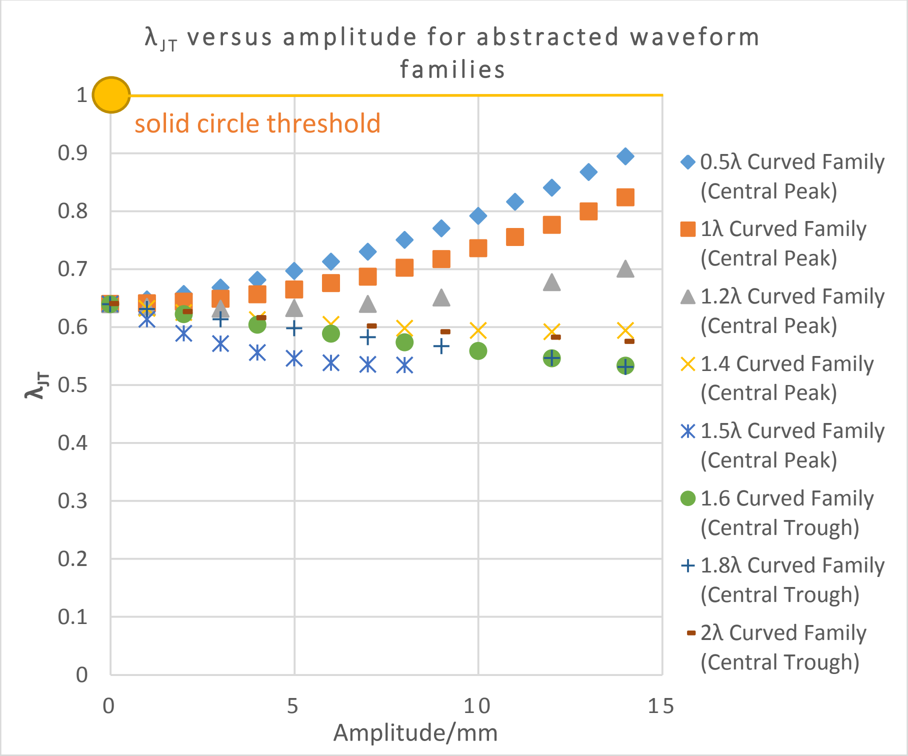

Figure 97 λ_{JT} versus amplitude for abstracted waveform families

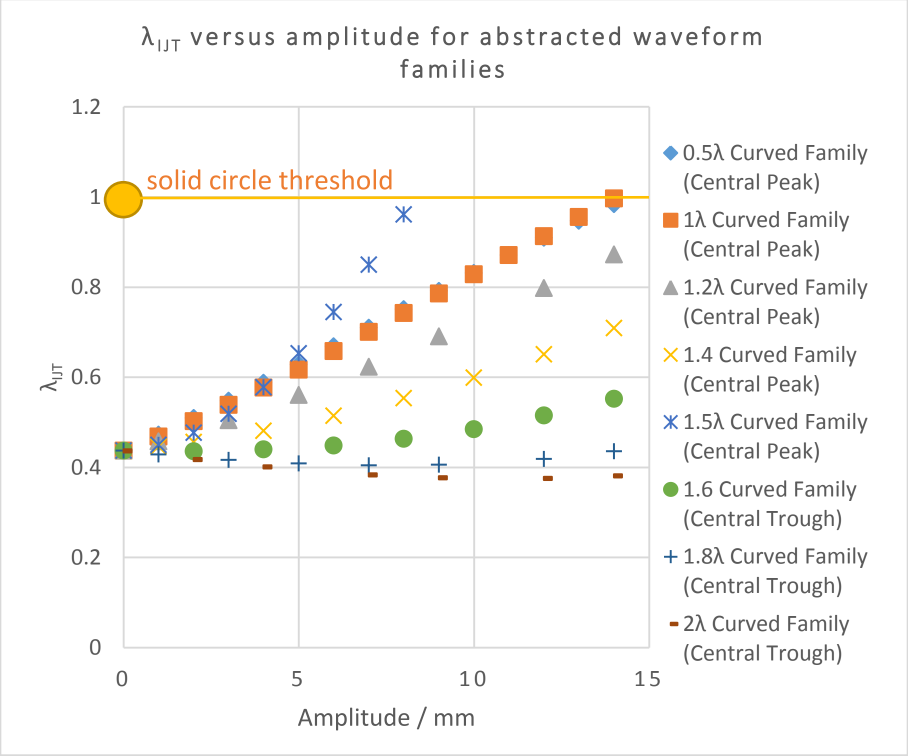

Figure 98 λ_{IJT} versus amplitude for abstracted waveforms families

5 Discussion

5.1 Internal structure - vascular bundle mapping

5.1.1 Area of vascular bundle transverse sections

A fresh *petiole* from the *T. fortunei* palm was cut into six equidistant lengths and the two sections at the extremities (P1 and P6), were looked at to determine the *VB* size and distribution. The size distribution of the *VBs* was observed along the longitudinal axis and transverse sections of the *petiole*.

It was found that the *VBs* were larger at the stem end than the distal end and that the larger *VBs* were located in the centre of the *petiole*, the smaller ones being located towards the periphery. The comparative difference in size between the inner and outer *VBs* increased towards the stem.

As smaller *VBs* have a higher Young's modulus, *E*, than that of larger *VBs* (Zhai, et al., 2011) it can be deduced, based on the area of the VBs alone (excluding their placement within the petiole), that the *E* of the *T. fortunei petiole* tested increased towards the leaf blade. Likewise, using the same reasoning, *E* would also increase towards the outer edges of the *petiole*, this transverse gradient being more accentuated, the nearer the section was to the palm stem.

The relevant hypothesis in this section is: 'The size, orientation and distribution of *VBs* within the *parenchyma* matrix may contribute to the mechanical efficiency of the *petiole*.' Two *VB* area gradients existed in the *T. fortunei* palm tested and according to (Ruggeberg, et al., 2008), gradients indicate an efficient use of energy required to make the materials. Material gradients imply structural efficiency. Palms have been in existence for over 120 million years and have adapted successfully to different environments over this time, so even though it is said by Niklas (Niklas, 1992) that it is easier for a plant to change its geometry than its constituent materials, in the time frame of evolution, they have been able to form efficient graded structures. Efficient use of material in the composition of the *petiole* means that energy is used to extend the life of the palm and ensure it is overbuilt adequately enough to withstand external forces and self- weight.

The author's results contributed to the knowledge two fold. Firstly, the author's work on resistance to torsion versus the *shape factor*s of the *T. fortunei petiole* (Windsor-Collins, et al., 2008) has contributed to the paper by Zhai (Zhai, et al., 2011) in terms of gaining insight into the mechanical behaviour of *T. fortunei* palm *petioles*. This was taken from the resistance to torsion versus the *shape transformer* data of *Tf petioles*. Secondly, it is known that the ratio of the transverse sectional area occupied by fibres in the *VBs* of *T. fortunei petioles* to the transverse sectional area of a fibre bundle dramatically increases with a decrease in bundle diameter (Zhai, et al., 2011) which implies that smaller *VBs* have a higher E. What the author's results show in addition to this, is that the area of the *T. fortunei VBs* decreased towards the leaf blade and the inner *VBs* decreased in cross sectional area to a lesser extent than the inner *VBs*. The difference in area of the outer and inner *VBs* decreased towards the leaf blade. It is inferred therefore that the *petiole* is more elastic on the inside and more elastic towards the stem. The most marked difference in elasticity between the inner and outer layers is nearest the stem, so from a material placement perspective, the *petiole* is like a tube, becoming more tube-like towards the stem.

The *VB* areas in the *T. fortunei petiole* leaf sheath in Zhai et al (Zhai, et al., 2011) correspond well with those observed in the *T. fortunei petiole* in this research (Table 10). Furthermore, the internal *VBs* nearest the stem corresponded to the same size as those in the middle layer of leaf sheath in the Zhai et al paper and the external *VBs* nearest the palm stem correspond to the outer layer of the leaf sheath in the paper by Zhai et al. It may be that these are continuous.

The findings are important for manufacturers of graded structures, in particular those producing reinforced structures. The cost of producing graded structures needs to be offset against the increased efficiency of the structure. Graded structures can be manufactured using rapid prototyping machines for which this may be applied.

Every *VB* was measured in terms of major and minor axis length by increasing the scale by 500% and so the error in area was very small. It was possible to distinguish between the area of the inner and outer *VBs* by 1/1000th of a mm^2.

In terms of what could be improved, a better insight into how the gradient changes along the length of the *petiole* would have been beneficial if more complete sections were available. However, Rich (Rich, 1987) said that the chemical composition of the cell walls is more likely to change under environmental forces than cell and tissue structure. Increasing the number of sections per *petiole* was not therefore considered a priority.

The palm *petiole* of the *T. fortunei* palm not only displays decreased *VB* area, increasing elasticity, towards the leaf blade but it must be taken into consideration that the number of *VBs* increases towards the leaf blade. Manufacturing this kind of reinforcement which bifurcates is not beyond possibility, but will increase manufacturing and installation costs.

5.1.2 Orientation of vascular bundles

A fresh *petiole* from the *T. fortunei* palm was cut into six equidistant sections along the length of the *petiole*. The two outermost sections, P1 and P6 at the stem and leaf blade ends of the *petiole* were looked at under high magnification on the computer to analyse the orientation of the *VBs*.

It was found that *VBs* were either circular or eccentric ellipses in transverse section. The outer *VBs* nearest the leaf blade were circular in transverse section and so had no orientation. However, the inner ones in the same section, ranged from circular to eccentrically elliptical, with the major axis in line with the nearest of the two outermost lateral extents of the *petiole*. In the section nearest the stem, both the inner and outer *VBs* were eccentrically elliptical with their major axis orientated towards the centroid of the transverse section.

The author infers from the work of Nogata and Takahashi (Nogata & Takahashi, 1995) that the orientation of the principal axis of the eccentric ellipse shaped *VBs*, is aligned with the predominant stress experienced by the *VB*. Also, the distribution of the *VBs* affects the flexural rigidity (Gibson, et al., 1995) which is the geometric flexibility in this reference as opposed to just E.

This implies that the stress experienced by the peripheral *VBs* nearest to the leaf blade was equal in all directions. The internal *VBs* in this section indicated that the predominant stress was in line with the outermost lateral extremes of the *petiole*. The proximal section nearest the stem shows the predominant stress, throughout the *petiole* to be aligned with the centroid of the *petiole* transverse section.

The outer *VBs* nearest the leaf blade do not indicate any predominant stress perhaps because most strain occurs when twisting and this occurs in both directions. To prevent fracture, the circular shape is optimum. The inner *VBs* nearest the leaf blade have lateral predominant stress used to return the leaf blade back to its rest position after twisting. The *VBs* nearest the stem show the predominant stress aligned with the centroid, which will have the effect of returning the *petiole* back to its rest position after bending or twisting.

The residual stress in *VBs* is tensile in the axial dimension and so has to be in the transverse direction also. With reference to the structure of nacre, Jackson et al says that interfaces are where the strain energy is absorbed when under tensile stress and that the more hierarchal levels there are, the more interfaces there are (Jackson, et al., 1988). He also says that strain energy can be absorbed at one hierarchical level to protect another hierarchical level from damage under that strain. A consequence of the residual stress in palm *VBs* being tensile is that damage to the surrounding *parenchyma* is prevented.

Again, the relevant hypothesis in this section is: 'The size, orientation and distribution of *VBs* within the *parenchyma* matrix may contribute to the mechanical efficiency of the *petiole*'. The distribution of the two shapes of *VBs*, circular and the eccentric ellipse, determines the direction of the internal dominant stresses. This should be used to model the internal structure of the *petiole* using FEA as the *VB* shapes are a result of all the internal and external forces and inherent 'design' of the *petiole*. In trees nature avoids notch stresses (Mattheck & Tessari, 2003) so the lines of stress evidenced in the orientation of the *VBs* indicate that they are serving a purpose other than the transmission of fluids and basic all round strength. Ruggeberg et al (Ruggeberg, et al., 2008) says that gradient distributions in *VBs* in the stem of the Mexican fan palm indicate an efficient use of energy required to make materials. The fact that the *VB* orientations change axially and transversely, indicates that the structure of the *petiole* is efficient to some extent, however, it will have built in reserves of strength to counteract anomalous loading and so will be 'over-built'.

The findings are important to the manufacturers of reinforced structures, in the extrusion of different shapes of reinforcement. To date, the author only knows of circular section reinforcements or circular bars with a ribbed surface or with nodes on the surface. It must be borne in mind that the *petiole* is a structure composed of many sub-structures and materials and so testing must be carried out with careful controls.

In terms of what could be improved, again more data between the extreme ends of the *petiole* would enable the tracking of the orientation gradient along the longitudinal axis of the *petioles*. Errors were not significant in this test as it only had to be decided if 1) the *VBs* were eccentrically elliptical or not and 2), which direction they were orientated with reference to a non-precise reference point.

5.1.3 Vascular bundle areal distribution

The vertical distribution of *VBs* changed along the longitudinal axis of the *T. fortunei petiole* (Table 12, Table 13 and Figure 52). At position P4, two thirds along the length of the *petiole* towards the leaf blade, the number of *vascular bundle* cross sections per unit area above line xx (the horizontal line that bisects the vertical line) was 3% more than below it. However, re-processing the data from the Windsor-Collins et al (Windsor-Collins, et al., 2006) paper it was found that at the end of the *petiole* nearest the leaf blade at position P6, the number of *VB* cross sections per unit area was 18% greater below line xx than above it. The total number of *VB* cross sections seen within the transverse section of the *petiole* increased towards the leaf blade as shown in Figure 57.

The findings in Figure 52 and Figure 57 show that the *VB* distribution is highly variable along its length, a sign of an efficient system. The increasing number of *VB* cross sections per unit area in the transverse sections of the *petiole* towards the leaf blade increases rigidity. More specifically, the distribution of the *VBs* will determine the type of rigidity that the *petiole* shows towards the leaf blade; torsion or bending.

The *VB* variation has to be variable to counteract the constant and variable forces imposed on the different parts of the *petiole*. The axiom of uniform stress is identified as a basic design rule for biological load carriers and Mattheck and Tessari (Mattheck & Tessari, 2003) show this to be true by developing three new computer programs using finite element analysis, namely CAO, SKO and CAIO. They compared force flow diagrams with fibre distribution and found that they could mimic trees. It follows that smooth transitions in *petiole* strength are evident in the smooth changes seen in transverse section *VB* counts as shown in Figure 57.

Figure 57 shows that there are two regions along the *petiole* length that show a significant change in the number of *VBs* in the transverse sections. These are between P1 and P2 nearest the stem and between P5 and P6 nearest the leaf blade. According to Jackson et al in their work on the mechanical design of nacre (Jackson, et al., 1988), higher numbers of hierarchal levels correspond to more interfaces and higher absorption of strain energy. The largest bending moment along the length of the *petiole* is located at the stem end, the load resulting from self-weight of the *petiole* and leaf blade together with external forces acting on them. Each branching in the *VBs* represents a hierarchal level and as such, much strain energy (resulting from this large bending moment) is absorbed between P1 and P2. At the leaf blade end of the *petiole*, all the stresses from blade movement and its self-weight are passed through to the *petiole*, via the part of the *petiole* that is smallest in cross section area and has the highest number of *VBs*. The small cross section area at P5, reduces the likelihood of fracture during twisting and bending in the outer parts of the *petiole* as the shear stresses, which are greatest at the *petiole*/air interface are less on the surface of a small diameter cylinder than on larger diameter one. The largest number of *VBs* nearest the blade end at P5 means that much strain energy is absorbed at this point where the most *VBs* branch. By reducing the torque through increasing the number of hierarchal levels, the efficiency of the system is improved.

The paper by Windsor-Collins et al (Windsor-Collins, et al., 2006) says that the increasing spatial density of the vascular bundles towards the leaf blade should allow the *petiole* to twist about greater angles before any kind of overall fracture. To add to this, a greater number of *VBs* at P6 means that there are fewer critical buckling loads and the load on each member is less. The higher the hierarchy, the more direct the load path is making it structurally efficient and reducing bending moments (Burgess & Pasini, 2004). The percentage increase in *VBs* from P1 to P2 may compensate for the high bending moment at the proximal end of the *petiole*. It may be that the percentage increase in *VBs* between P5 and P6 decreases the critical buckling load and reduces the load on each member reducing the strain energy near to the blade.

It is very likely that *VBs* in the *T. fortunei petiole* branch distally as with animal and dicotyledenous plant vascular systems. Constructal branching is commonly found in plants in terms of vascular systems (Bejan & Lorente, 2006). With reference to the *T. fortunei petiole,* the branches in the *VBs* (which provide mechanical support), allow the water and nutrients to flow between the stem and the furthest most parts of the leaf blade (the leaf blade being the source for the nutrients and the sink for the water through *transpiration*). Therefore, the *VBs* are optimised for two functions; strength and fluid transfer and a question for further research would be which of these is optimised more.

The results give an insight into how the internal structure gradients operate efficiently. Learning and applying techniques from this to new structures, will reduce material and energy waste. Structures to which these concepts can be applied are cars, aeroplanes, bicycles, architecture, sports equipment and wind turbine blades which employ branched, fibre reinforced, lightweight materials.

In terms of what could be improved, the *petioles* were extremely hard to cut and so some of the sections were not complete. For the *VB* count, what was produced, served its purpose. However, only the distal half of the *petiole* was studied for vertical *VB* distribution. More complete sections nearer to the interface with the stem are required to obtain a full evaluation of the *petiole*. A sharper tool would be beneficial to section the *petiole* and lasers should be considered. However, this would need to be balanced against cost.

A graticule was used to count *VBs* and partial ones were counted as one half. This technique was effective and is standard practice when counting large numbers of objects. The limitations of this study are that only one *petiole* from the *T. fortunei* palm was tested. It cannot be assumed that all palm *petioles* or indeed all *petioles* from the *T. fortunei* palm produce the same results. This is because structure varies between palm species and upon the age and environment of the palm.

5.2 Material properties and bi-layered model

5.2.1 Variation in Young’s modulus within the petiole

Six *petioles* from the fresh *T. fortunei* palm were cut into three equal segments, P, C and D and flexural tests performed on each to obtain the bulk Young’s modulus, $\bar{E}$, along the longitudinal axis of the *petiole*.

It was found that the $\bar{E}$ between the *petioles* of the same segments, P, C and D were significantly different from each other (Figure 58) as the CIs of the standard error as a percentage of the sample means were 23%, 11% and 15% for segments P, C and D respectively. However, segment D was significantly less than the central segment C. The values of $\bar{E}$ were similar to that of green coconut timber (Ashby, et al., 1995) and ranged between 2.25 and 8.49GPa.

The results show that with 95% confidence, the middle section of the *petiole* was on average 40% stiffer than the distal part of the *petiole* nearest the leaf blade. Stiffness here is not geometric stiffness, EI, but $\bar{E}$ alone. It can be said with 95% confidence that the central section of the *petiole* was on average, 33% stiffer than the section nearest the palm stem although the confidence intervals do overlap (Table 15).

It is proposed that the reason for the large confidence intervals, is that the *petioles* are of different age. According to Rich (Rich, 1987), the stiffness of palms increases with age so perhaps as all the *petioles* are different ages, they will display different values for $\bar{E}$. As a result, when averaged, they produced a large confidence interval. The reason for $\bar{E}$ being similar to that of green coconut palm timber is that *T. fortunei* is also an arborescent palm and the tests were carried out correctly.

The relevant hypothesis in this section is: ‘The independent *petiole* configurations are well suited to the function of the *petiole* as a whole. There may be a strong correlation between the properties and the transverse-section shapes of palm *petioles*’. The confidence intervals for the values of $\bar{E}$ obtained from the bending tests showed that there was no significant difference in $\bar{E}$ between the two ends of the *petiole*, but that it is higher mid-way along the length of the *petiole*. The reason for this may be that most of the *petiole* movement, is a result of high bending moments (at the stem) or high twisting moments (near to the leaf blade). These occur at the ends of the *petiole* requiring these locations to be elastic for self-righting purposes. The material of the middle section however may be stiffer (less elastic) allowing it to extend for the leaf blade to intersect the sunlight. The values for $\bar{E}$ correlate with the *shape transformers* in that the central section C had the highest ψ_l

with a value of 0.27 (Table 25 and Figure 68) compared to the ψ_l values of 0.22 and 0.21 for both the proximal and distal sections, P and D.

The findings are significant to say that generalisations should not be made on *petiole* material from the same palm or even from the same species of palm (unless they were the same age). The findings were used in conjunction with *petiole* shape profiles to determine the E of the inner and outer layers of the *T. fortunei petiole* in the bi-layered model.

As wood exhibits a higher modulus of elasticity and much higher proportional limit when tested rapidly than when tested slowly (Young & Budynas, 2002), it is important to understand that the flexural tests were performed over a short period of time (static bending tests). The standard impact test on a beam indicates a fibre stress at the proportional limit approximately twice as great as that found by the standard static bending test (Young & Budynas, 2002). Therefore, the $\bar{E}$ produced in this research should only be discussed in relation to short term loading from wind and rain, rather than that derived from self-weight load which is continuous.

One of the assumptions when using the Euler-Bernoulli beam formula is that the beam should be homogenous and of constant transverse cross section shape and size. However, the *petiole* segments were tapered and the material was anisotropic and inhomogeneous, and so errors were introduced using this formula. The small deflections of the beam were assumed to be subjected to vertical loads only, but in reality, the *petiole* represents a shaft as well as a beam as it is subjected to torsional forces as well as flexural ones as a result of it being not truly symmetrical about the bending plane.

The limitations of the results are that $\bar{E}$ should not be assumed to be constant across all *petioles* of the same *T. fortunei* palm. Therefore, any further tests incorporating these results should be carried out on the same samples.

5.2.2 Rigidity modulus variation along length of petiole

Two fresh *petioles* were cut from the *T. fortunei* palm and cut into three equidistant segments, P, C and D and tested in a torsion rig. Torsion readings were taken with increasing twist, decreasing twist and repeated tests to obtain the rigidity modulus, G of the material in each section.

Material from both *petioles* showed a decrease in the average G towards the leaf blade (Figure 59) from 2.4 GPa down to 1.0 GPa (average for both *petioles*). The material in the central and distal sections showed significantly different values for G between *petioles* (95% probability) whereas the

G of the two proximal sections did not. This means that the material in the *petiole* becomes easier to twist the closer it is to the leaf blade. However, the resistance to torsion according to shape showed the ψ_J *shape transformers* for the P and D sections to have the same ψ_J which was slightly less than the central section which had a value of 0.31 (Table 26 and Figure 71).

The relevant hypothesis in this section is: 'The independent *petiole* configurations are well suited to the function of the *petiole* as a whole. There may be a strong correlation between the properties and the transverse-section shapes of palm *petioles*'. The distal end of the *petiole* must remain intact while the leaf blade twists, so the material has to allow more torsion to occur at the distil end compared to the central and proximal parts of the *petiole*.

The G values for fresh *petiole* material from *T. fortunei* overlapped with those for fresh woods quoted by Vogel and had a maximum of 2683 MPa which was 2.8 times as resistant to torsion as fresh bamboo which was 915 MPa; the wood with the highest value for G tested by Vogel (Vogel, 1995). Only the distal section of Test 6 had a lower G (873 MPa) than that of fresh bamboo.

These results are useful in that they help form a picture of how the individual components of the *petiole* work together. The torsion tests provide values for G which takes into account the material properties and internal structure of the *VBs* and *parenchyma* because it assumes that the material is homogeneous.

In terms of what could be improved, the twisting should have been carried out in both directions to allow for small anomalies in shape.

The palm *petiole* wood samples tested were anisotropic and non-circular in cross section so applying the torque equation for circular shafts (equation (41) produced a G that was different to that to that of a homogeneous, isotropic shaft of circular transverse section as the *petiole* warped when twisted, even though warping restraints were in place at either end of the shaft (Figure 26). The inhomogeneous and anisotropic nature of the *petioles* meant that it was not possible to take a bulk cylindrical sample from them.

It is difficult to say how much of an effect the non-circular shape and anisotropy of the *petiole* has on the value of G in these tests, so caution should be exercised in using them.

5.2.3 Poisson's ratio and anisotropy within the *T. fortunei* petiole

Table 15 and Table 16 show the values for bulk E and G obtained from bending and torsions tests on two, fresh *T. fortunei petioles*. They were used to calculate the Poisson's ratio for each of the three segments P, C and D using equation (42).

It was found that only one of the six segments was within the normal range for Poisson's ratio, this being the P segment of Test 6 (Table 17) with a value of 0.11. The Poisson's ratio values for the *T. fortunei petiole* material ranged from 0.11 to 2.44. The Poisson's ratio of the P segment of Test 6 in Figure 60 *appears* valid as it is within the margin of error showing 95% confidence that the result is between 0.11 and 0.12. However, it must be treated with caution. The reason being, that although the same method was used to determine the Poisson's ratio for all segments of that *petiole*, none of the other values for Poisson's ratio are less than the maximum for isotropic materials. This is to be expected as a result of the anisotropic and heterogeneous nature of the *petiole*.

The formula used to determine Poisson's ratio (equation (42), assumed that the palm *petiole* material was homogeneous and isotropic. Wood however, is heterogeneous and anisotropic and has three principal axes with respect to grain and growth rings (Green, 1999). So normally, for practical wood purposes, they are only published as ratios: G_{LR}/E_L, G_{LT}/E_L and G_{RT}/E_L, the longitudinal axis represented by the subscript L, the tangential axis T and the radial axis, R (Green, 1999).

For reference to other people's work which demonstrate the same problem with anisotropy, Vogel (Vogel, 1995) provides bulk E and G values for various woods, a subset of which is shown in Table 18 and Figure 61. The resulting Poisson's ratio derived by the author of this thesis using these values is between 3.25 and 8.15. No individual margins of error are presented in this paper by Vogel, hence they are not shown on Figure 61. It is standard practice therefore not to present Poisson's ratio for woods as a consequence of their anisotropy.

Although these findings are not useful in themselves, they highlight the influence of anisotropy and inhomogeneity in Poisson's ratio calculations using bulk E and G values.

In addition to the anisotropy influencing the Poisson's ratio results, the formula used to calculate G, for the torsion of a shaft used applies to circular transverse sections only. It may be that segments C and D segments were less circular than Segment A. This adds to the unreliability of the Poisson's ratio values produced in Table 17.

The relevant hypothesis in this section is: 'The independent *petiole* configurations are well suited to the function of the *petiole* as a whole. There may be a strong correlation between the properties and the transverse-section shapes of palm *petioles*'. However, the results from this thesis show that there are many mechanisms that work together to make the *petiole* function as it does. The Poisson's ratio calculated in the way that it has done in this thesis is derived from bulk parameters rather than the vectorised values required for such an analysis.

5.2.4 Bi-layered model

By dividing the *petiole* into two regions, a thin outer layer made of epidermis and hypodermis, and an inner region, different Young's moduli, E, were obtained for both regions and likely values for the thickness, t, of the outer layer.

It is not known if the outer layer of palm *petioles* is lignified or not and by estimating the thickness of the outer layer visually, likely values of E of the outer layer were obtained and the question of whether the outer layer of the palm *petiole* was lignified or not, was answered.

These results suggest that the outer layer was not lignified. They also show E_2 to be 7.5 GPa, E_1t to be 7899×10^{-10} N/mm and t to be <0.2 mm.

These results mean that first, it is possible to work out the E values of two layers within the *petiole* by flexurally testing the *petiole* as a whole. Secondly, there must be another reason other than lignification for palm *petioles* to be so hard (as this is still a question asked by botanists).

As the degree of lignification of the outer layer of the palm *petiole* is uncertain (Cutler, 2005), the following tests were carried out; one where the outer layer was modelled on 100% lignin and the other where the outer layer contained lignified cells as with the palm stem outer layer from the journal paper by Gibson, 'The hierarchical structure and mechanics of plant materials' (Gibson, 2012).

If the material of the outer layer constituted solid lignin and E_1 was 3100 GPa, which is the value for periodate lignin at moisture content of 12% (Cousins, 1976), the resulting thickness of the outer layer would be 0.25 x 10-13 mm, derived as follows:

Instance where $E_1 = 3100$ GPa:

$E_1t = 7899 \times 10^{-10}$ N/mm

$E_1 = 31 \times 10^{5}$ N/mm^2

$\underline{t = 0.25 \times 10^{-13} \text{ mm}}$

If the outer layer constituted lignified cells rather than solid lignin and *E* varied between 0.01 GPa and 30 GPa as in palm stems (Gibson, 2012), the resulting thickness of the outer layer would vary between 7.9 x 10^{-8} mm and 2.6 x 10^{-11} mm, derived as follows:

Instance where E_1 = 0.01 GPa:

E_1t = 0.0000007899 N/mm

E_1 = 10 N/mm2

<u>t = 7.9 x 10^{-8} mm</u>

Instance where E_1 = 30 GPa:

E_1t = 0.0000007899 N/mm

E_1 = 30 kN/mm2

<u>t = 2.6 x 10^{-11} mm</u>

These values for t do not reflect the likely thickness of the outer layer as seen in Figure 21 which ranges from about .2 to .45 mm.

The results of this bi-layered model, in answer to Professor Cutler's question as to whether the outer layers of palm *petioles* are lignified (Cutler, 2005) and by personal communication in 2015 (Cutler, 2016), suggest that they are not. Although Figure 7c shows a *petiole VB* from the palm *Washingtonia robusta* not to be lignified through staining (and the stem *VBs* to be heavily lignified), further work should verify the results by phloroglucinol testing of the outer layer of the *T. fortunei* palm *petiole*, which stains lignin red. The leaf sheath (an extension of the *petiole* which surrounds the stem) of *T. fortunei* in the paper by Zhai et al (Zhai, et al., 2011) is shown to be lignified. The old leaf sheath supports the newer leaf sheaths once it has died and it should not be assumed that the *petiole* is also lignified. Assuming the outer layer of the *petiole* is not lignified, means that the cell walls are made of thick cellulose which is an alternative strengthening material (Cutler, 2016). This ties in with what Barros et al says (Barros, et al., 2015), that lignin, once deposited, cannot be removed, as for the *petiole* to change with age, requires change of cell structure, which is allowed by the absence of lignin.

The relevant hypothesis in this section is: ‘It may be possible to estimate material properties of the individual layers of a palm *petiole* by using its shape and its bulk material properties’. From the material properties, transverse section shape and estimation of outer layer thickness at two regions along the *petiole* length, it was possible to determine the Young’s modulus of the two layers within the transverse sections.

5.2.5 Comparison of $\bar{E}$ from the bending tests to E from VB area in *T. fortunei*

The Young’s modulus deduced from the flexural tests resulted in the central petiole section of the *Tf* petiole being the stiffest with the highest value of $\bar{E}$, although the 95% confidence intervals of the proximal section did overlap with those of the central and distal segments (Figure 58). The Young’s modulus values from the bending tests were bulk values and hence symbolised as $\bar{E}$ as opposed to E.

Absolute values of Young’s modulus could not be determined using the *VB* area method as the area of the *VB* is only proportional to the Young’s modulus. However, relative stiffness was determined. The relative stiffness of the *Tf* petiole was measured as E as opposed to $\bar{E}$ as it was possible to observe differences in *VB* cross sectional area transversely and longitudinally along the petiole. Observations (only available for the proximal and distal sections, not the central section) showed a decrease in area (increase in E) towards the periphery of the petiole and towards the leaf blade (Figure 49). The difference in area was shown to be highest at the stem end making it more tube like towards the stem.

Direct comparisons could not be made between the Young’s modulus data from the bending tests and that of the *VB* area observations because bulk values are different to specific relative values of stiffness in heterogeneous and anisotropic materials. However, we can say that as the petiole became more tube like, towards the stem, it became stiffer by way of the placement of the *VBs* as opposed to just their area alone. The relative E resulting from the area of a *VB* is just part of the contribution to the bulk $\bar{E}$ of the petiole within a segment – the placement of the *VBs* is a very important contributor to the overall stiffness.

5.3 Petiole shape - circular envelopes and SEM

A disadvantage of taking samples from palms grown in a glass house is that they are not subject to the *forced convection* they may otherwise be exposed to and so their *petioles* may have a different shape and material content. However, it is a good control sample set as it is known what environment the sampled palms were subjected to.

5.3.1 Shape profiler verification

It was found that the linear measurements using the shape profilers were 0.67% and 11.24% more than the standard widths of the 30mm and 8 mm gauge blocks respectively (Table 22). The area of the circular cylinder measured by the shape profilers was 3.02% less than the area when measured using Vernier callipers (Table 23).

The larger the size of the object being measured, the less the effect of the width of the profiler fingers had on the shape measurement accuracy. Figure 99 shows how the shape, a circle in this example, was digitised. The thickness of the pencil line did not result in a systematic error requiring correction as the inside edge of the line was digitised in Adobe Illustrator imaging software eliminating any error.

For circular cylinder area measurement as shown in Figure 99 the measurement error is the same as the linear measurement in the x axis, but will be considerably less in the y axis in line with the longitudinal axis of each profiler finger. This is because the fingers can extend and retract smoothly in the y direction whereas the resolution in the x axis depends on the finger width. It follows that small objects, of the same order of size as the profiler finger width, and having edges with high y/x gradients according to Figure 99, incur the most measurement error.

These results show how accurate the results can be in terms of measurement error to gauge what kind of shapes the profilers can be used for. For the purposes of this research, the profiles are such irregular shapes that it is not possible to say exactly what the measurement error is. However, the measurement error for calculating the area of a circle of diameter 42 mm is 3.02 %.

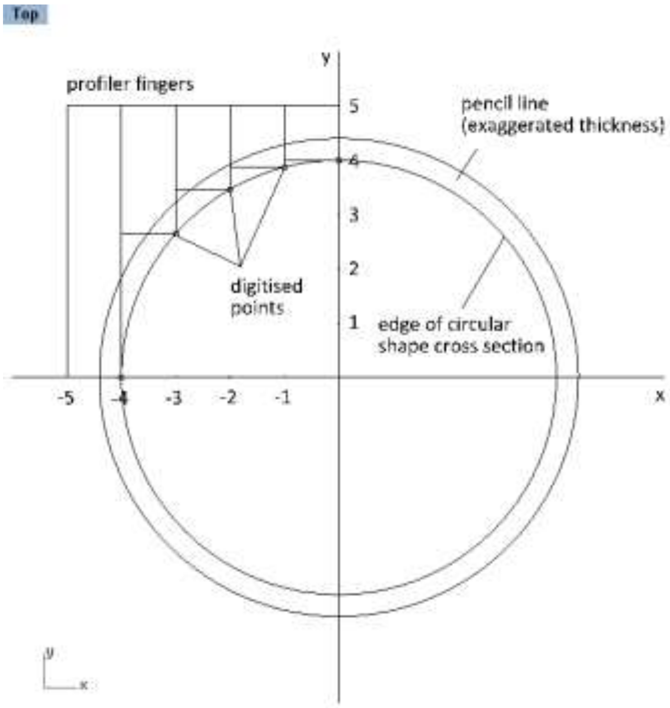

Figure 99 Position of profiler fingers relative to outer edge of circular shape edge and pencil line

The smaller the width of the profiler fingers is, the lower the measurement error would theoretically be, but the consequence of having narrower fingers is that they flex more when pushed onto the *petiole*. It is possible to obtain profilers that have very little resistance to movement, but the compromise is that during the transcribing process, the pencil disturbs the profiler finger positions inline and laterally.

5.3.2 Circular envelope

A 2D circular transverse section (which lies in the x, y plane) of a shaft (which exists in x, y, z space) remains in the x, y plane when shear stress is applied to the section resulting from torque being applied to the shaft. However, a non-circular 2D transverse section of a shaft does not remain in plane when shear stress is applied as a result of shear strain causing distortion of the 2D transverse section. Compared to a circular section where each point on the perimeter of the circle is the same distance to the centroid of the circle (Figure 39), the distance of the points on the edge of a non-circular section to the centroid are not the same. As a result, when shear stress is applied to a non-circular 2D transverse section, unequal shear forces result which cause the non-circular shape to move in the z axis and out of the x, y plane. This is because unequal shortening of the axial filaments occurs during twisting of a non-circular section shaft (Ryder, 1955).

When comparing the resistance to torsion of shapes, errors are incurred in the polar second moment of area using the rectangular envelope method as the torsional constant, J_T, is approximated, the extent of which depends on the aspect ratio of the rectangle. A circular envelope, just as the circular transverse section of the shaft mentioned above, does not move out of plane under shear stress. This is a result of its radial symmetry and the fact that it does not approximate to J_T as does the rectangular envelope. The approximation of J_T in rectangles incurs an error of up to 4% (Young & Budynas, 2002). It is possible to calculate the J_T of a rectangle exactly by using the Saint-Venant semi-inverse method, whereby the warping function of the surface is integrated over the surface area (Mirjalili & Pasini, 2007), but this is not carried out due to its time consuming process.

A paper by (Bouwman, et al., 2004) on which *shape factor*s best describe granules, shows that many types of *shape factor*s exist from aspect ratio *shape factor*s to mass *shape factor*s. In the light of this, the new *shape transformers* described in this thesis using circular envelopes are symbolised differently to that of the rectangular envelopes as follows where '*circ*' corresponds to the circular envelope:

$\psi_{Acirc} = A/A_{circ}$

$\psi_{Icirc} = I/I_{circ}$

$\psi_{Jcirc} = J_T/J_{circ}$

This is helpful when the *shape transformer* e.g. Ψ_{Jcirc} is written without its definition i.e. J_T/J_{circ} as it shows immediately that a more accurate torsion transformer is being used.

The relevant hypothesis in this section is: 'Using circular envelopes in *shape transformer* analysis provides more accurate torsion performance indices'. The circular envelope for *shape transformer* analysis reduces the effects of the warping factor. However, this is not eliminated as although the circular envelope does not move out of plane when torsion is applied, the non-circular shape does.

Circular envelopes are useful in the design of elliptical section engineering applications whereas the rectangular envelope is most useful for rectangular shape analysis as the section that the profiles are being compared to is the envelope section in the efficiency charts. Replacing the torsional constant J_T with the polar second moment of area J results in the removal of an approximation to J of up to 4% (Young & Budynas, 2002) as the warping factor is zero for circular envelopes. However, as the aspect ratio of the circular envelope is always unity, scaling of the shape envelope in one-dimension relative to the other dimension is not possible unlike the rectangular envelope method where the 'space envelope' is a design variable.

Advantages of circular envelopes

1) By being able to replace the torsional constant J_T by the polar second moment of area J when using circular envelopes, there is no need to simplify the formula for J_T thereby negating the error of up to 4%. When using rectangular envelopes, the efficiency limits in torsion are dependent on the scaling of the envelope, governed by the angle α of the diagonal to the horizontal edge of the rectangle. This is a result of the fact that Ψ_{JT} is a function of the angle α as opposed to Ψ_I which is not. In most cases such as hollow rectangles, the performance increases when the envelope tends to be square (i.e. $\alpha = 45°$), but for practical values of α, the increase in performance is less than 5%. “Hence, at the conceptual stage of design, Ψ_{JT} (and thus, efficiency parameter) could be assumed constant.” (Singh, et al., 2011). The angle, α varies with the aspect ratio of the envelope, and because the aspect ratio of the circular envelopes is always one, the efficiency parameter does not have to be assumed to be constant, it is constant.
2) The envelope and shape do not have to be scaled when rectangular envelopes are replaced by circular envelopes for the *shape transformers*: Ψ_A , Ψ_I and Ψ_{JT}.
3) Considerably reduces the computational effort required, reducing costs.

5.3.3 Shape transformers and SEM

One *petiole* from each of four palms was sampled to produce *shape transformers* for P, C and D sections along the longitudinal axis of the *petiole*. The *shape transformer* ratios were Ψ_I/Ψ_A , Ψ_{JT}/Ψ_A and Ψ_I/Ψ_{JT} which measured the shape efficiency of bending resistance to mass, torsional resistance to mass and twist-to-bend ratio respectively. As there are a lot of data and observations, the three *shape transformer* ratios will be treated in three different sub-sections.

All of these findings are significant in the quest to create more mass-efficient multi-objective structures. In particular, the analysis shows how shapes that are not symmetrical about the horizontal axis work by investigating the upper and lower parts of the shape independently as illustrated in Figure 100.

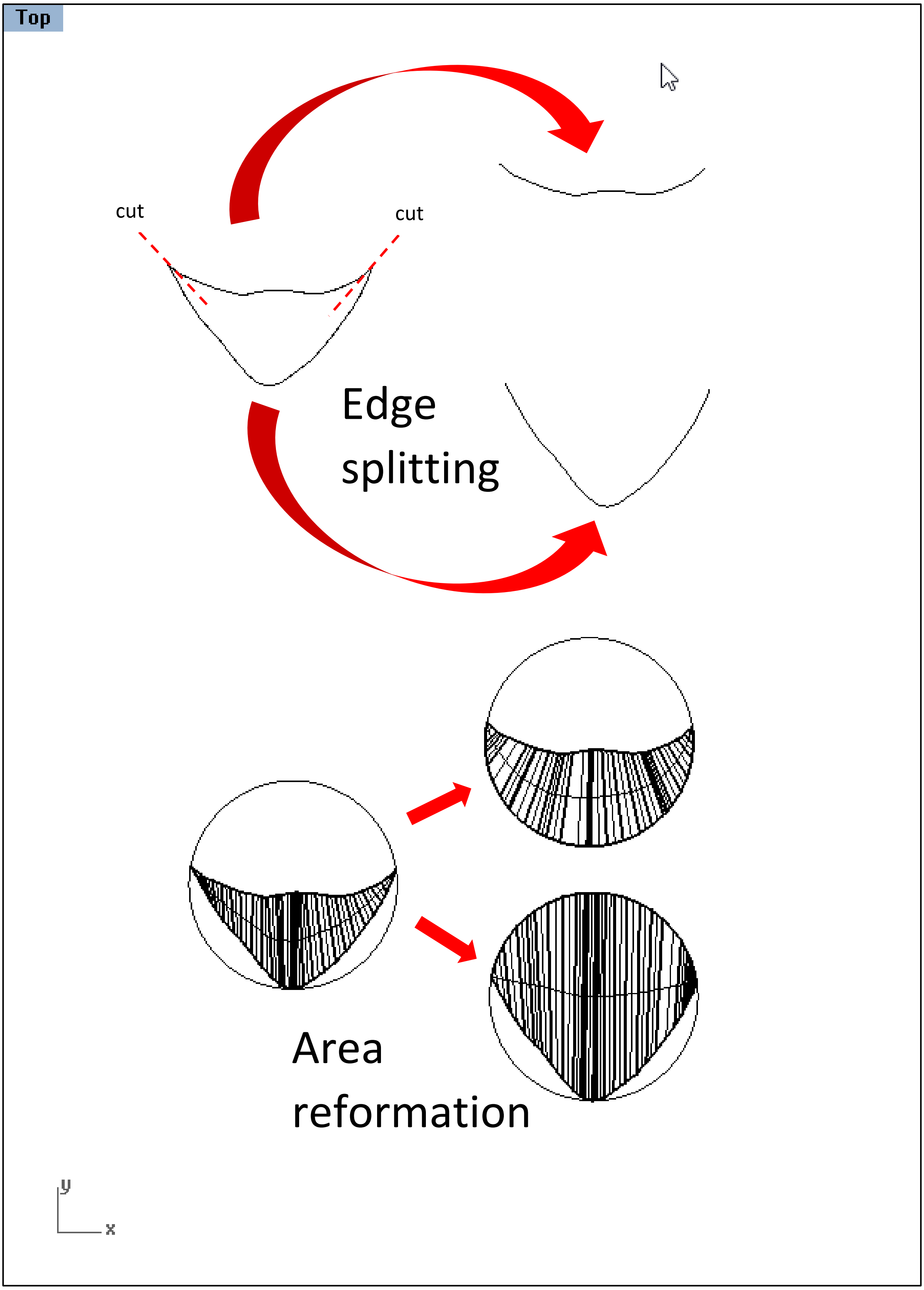

Figure 100 Schematic showing mechanism of Shape Edge Mapping (SEM)

The findings show clear trends in the *shape transformer* data and the extent of these trends is significant in terms of alignment to a quadratic curve. A quadratic curve was chosen as the trend line because it best describes the shape of most of the data trends. The quadratic curve was used consistently for all *shape transformer* data, for comparison of results.

The relevant hypothesis in this section is: 'The independent *petiole* configurations are well suited to the function of the *petiole* as a whole. There may be a strong correlation between the properties and the transverse-section shapes of palm *petioles*'. The *shape transformer* SEM data more so than the *shape transformer* data of the whole *petiole* shapes, show that there is a clear correlation between the shape and function of each part of the *petiole*, not just its general location along the longitudinal axis of the *petiole*, but more specifically, the edge location as can be seen in the SEM data.

The conventional method for producing shape efficiency charts using rectangular envelopes was employed to analyse the shape of palm *petioles*. These were mass-efficiency charts for shape flexural stiffness and shape resistance to torsion. Shape flexural stiffness versus shape torsional stiffness was also plotted. Published early work (Pasini & Mirjalili, 2006) shows *shape transformers* of *petiole* transverse-sections using rectangular envelopes of different aspect ratios plotted on the same efficiency selection chart. However, the aspect ratio of the envelope has to be the same as the other profiles being analysed otherwise the results are meaningless as a true comparison of section shape is not being made. The method shown in the paper by Pasini and Mirjalili (Pasini & Mirjalili, 2006) was repeated by Windsor-Collins et al (Windsor-Collins, et al., 2007a) for comparison to palm *petioles*, but however, neither papers applied envelope scaling as they should have done. Later work (Pasini, 2007) however shows that the rectangular envelopes were scaled to normalise them. A new method developed in this research uses circular envelopes which solves the problem of comparing shapes of varying envelope aspect ratios also on the same shape performance chart and uses the polar second moment of area J, in the torsion *shape transformer* rather than the torsional constant J_T (a function of warping). Recent published work incorrectly shows *shape transformers* derived for torsion using J rather than J_T and also without scale transformers for bending analysis. Employing circular envelopes in *shape transformer* analysis has enabled the Ψ_{JT} *shape transformer* data to be more accurate than when using rectangular envelopes as the circular envelope remains in plane when subject to torsion.

Compared to a solid circle, palm *petiole* transverse sectional shapes have a low twist-to-bend ratio as a result of shape. It is widely thought that palm *petioles* cope with wind spillage through torsion compared to bending which still may be the case, but it is now confirmed that this observation does not result from the shape of the palm *petiole*, but rather it's material and internal shape and structure. However, according to Windsor-Collins et al (Windsor-Collins, et al., 2007b), *palmate* leaves tend to spill the wind at the terminal or distal ends of their leaves. Often these leaf margins are split and have flexible ends which become aligned with the wind perhaps stabilising the leaf.

Although the form of 2D transverse-sections of natural section shapes may appear simple, they are multifunctional and this research used SEM to filter out the contributing factors for two of the functions; bending resistance efficiency and torsion efficiency, both with respect to mass. Data in the *shape transformer* efficiency charts for whole *petiole* shapes in Figure 68, Figure 71 and Figure 74, which are not filtered with SEM, appear scattered. As a result, data trends are not visible and consequently it is not possible to extend the trends to other family members not observed in nature. However, by employing circular envelopes and simultaneously isolating parts of the shape of similar form using SEM this was achieved.

SEM makes testing and adding variables to an original model simple and possible as can be seen in Figure 69, Figure 73 and Figure 75 where aligned *shape transformer* data can be extracted from scattered data.

By isolating the edges of the profiles in the SEM analysis, the data can be utilised as they are less scattered or in many examples very well aligned. Biomimetic analysis has now been provided with this combination of two techniques to extract precise information from natural structures which by definition are curved in form. Weaver (Weaver & Ashby, 1997) compared shapes with that of a circle of the same area, as opposed to a circular envelope, but this does not enable the user to identify shape family trends (shapes with small parameter changes) as the ratio of the area of the shape and the circle is always unity.

A limitation of SEM is that a shape with an extreme re-entrance feature such that it coincides with the circular arc, will effectively be two shapes, invalidating the analysis. Re-entrance features must therefore not coincide with the circular arc within the circumscribing envelope. The maximum dimension of the convex shape of the re-entrance feature, h, must be less than the radius, r, of the circumscribing envelope, A, in illustrated in Figure 101 and equation (60):

$$\frac{h}{r} < 1 \tag{60}$$

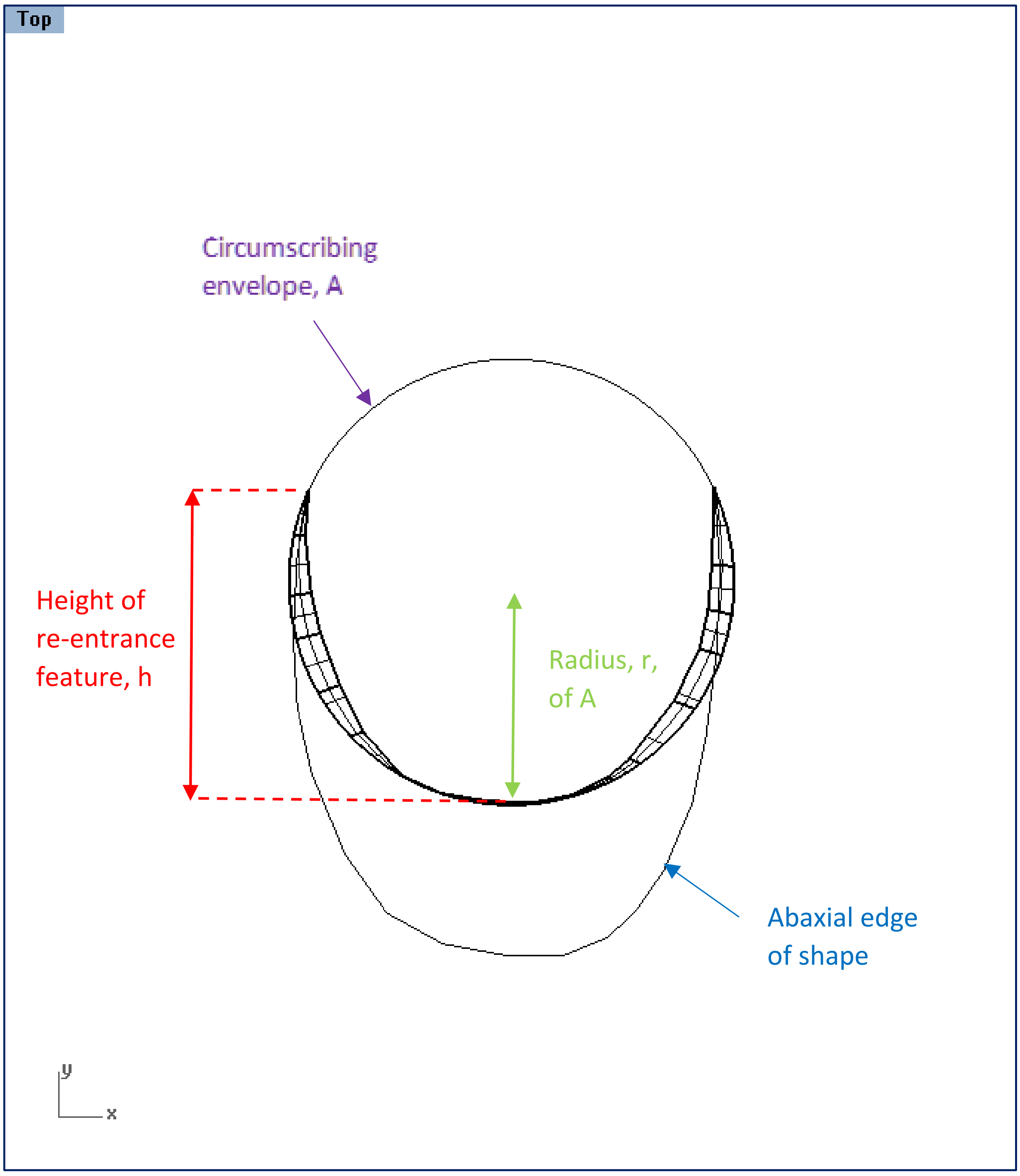

Figure 101 Re-entrance feature schematic where h must be less than r for use in SEM

The new SEM technique using circular envelopes has enabled the user to isolate the upper and lower edges of the *petioles* and detect trends as illustrated in Figure 44. Aligned SEM data from 2D sections of natural form are produced. Further detailed analysis of shape edges extracted from but not observed in the tested 2D shapes but that are classed in the same family using the SEM technique.

5.3.3.1 Mass-efficiency in bending ψ_I/ψ_A

Compared to the *adaxial* and whole *petiole* sections (Figure 69 and Figure 68), the *abaxial petiole* $\psi_{\mathrm{I}}:\psi_{\mathrm{A}}$ data shown in Figure 70 (where only the lower edge is the shape of the *petiole*) are grouped very closely. This means that the *abaxial petiole* shapes for each section and on all four palm *petioles* perform alike in their shape bending resistance and mass efficiency. It can be concluded that whatever the habitat of the palms tested, the ψ_{I} and the ψ_{A} of the *abaxial petiole* edge is similar. This may be because for each section along the *petiole*, the self-weight of the leaf blade and *petiole* is continuously present therefore requiring continuous bending resistance to counterbalance the self-weight. Only shape is being considered here - it would be expected for the size to be related to the self-weight of the blade and *petiole*. In tree branches for example the square of the diameter of tree branches is proportional to the load as a result of self-weight (Burgess & Pasini, 2004).

The relevant hypothesis here is, 'The independent *petiole* configurations are well suited to the function of the whole *petiole*. There may be a strong correlation between the properties and the transverse-section shapes of palm *petioles*'. These results clearly show that all the lower edges of the *petioles* have a similar ψ_{I} and ψ_{A}. However, looking at all the *petiole* profiles tested in Figure 66, the *abaxial* shapes look quite different. SEM has successfully extracted the contribution of each edge to the whole *petiole* in this example reinforcing the hypothesis that independent *petiole* configuration, in this case the *abaxial* edge, is well suited to the function of the whole *petiole*.

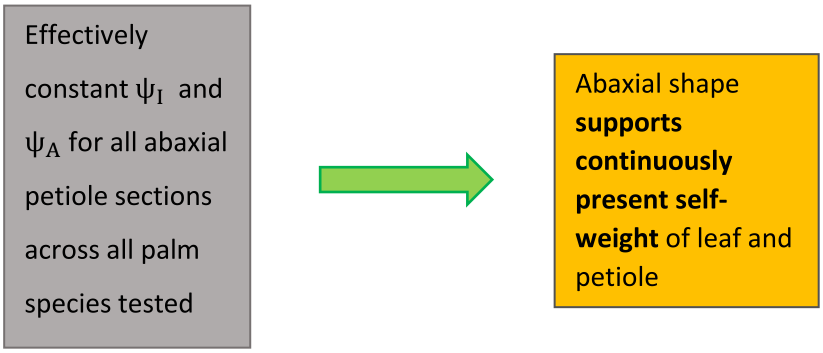

Figure 102 Inference of constant $\psi_{\mathrm{I}}:\psi_{\mathrm{A}}$ in *abaxial petiole* shapes

Looking at the *adaxial* (upper half) of the *petiole* shape, the $\psi_{\mathrm{I}}:\psi_{\mathrm{A}}$ plot in Figure 69 shows how the data for individual palm species, much more so than the *petiole abaxial* data, are separated from each other. Not only this but their P, C and D profiles are separated also and they all follow a quadratic trend-line with an R^2 value of 0.9984. This is despite the fact that the *petiole* shapes observed in Figure 66 again show a wide variety of upper edge shapes, from convex to concave and those with ridges in the centre. The trend line is a line of constant $\psi_{\mathrm{I}}:\psi_{\mathrm{A}}$ ratio, so all the *adaxial* *petiole* edges have the same mass-efficiency in shape bending resistance. However, their position along the trend line corresponds to their habitat. *Pk* and *Lv adaxial petioles*, at one end of the trend line furthest from the solid circle, have the most concave upper edges hence their low values for ψ_I and ψ_A. The natural environments that these two palms are subjected to are tropical storms for *Pk* and high winds and heavy rainfall for *Lv* (Table 24) so they need to flex easily to prevent breakage. *Ke* is the adjacent palm along the trend line and this resides in the sheltered forest understorey, so it does not need to bend as much. Lastly *Tf*, which is closest to the solid circle on the trend line, has the highest shape resistance to bending and its natural habitat is in the mountainous regions of China under heavy snow cover. It therefore needs to counteract the snow load through shape bending resistance shown by high ψ_I and ψ_A values.

This reinforces the hypothesis that independent *petiole* configuration, in this case the *adaxial* edge, is well suited to the function of the whole *petiole*. Although $\psi_I : \psi_A$ varies from species to species, the fact that there is a clear trend line across species indicates a high level of organisation to perform a specific function. The role of the *adaxial* edge, varies significantly between species, it is suggested because of different environmental conditions in the place where they have evolved (as three of the four palms tested were grown inside glass houses). As environmental conditions vary depending upon palm habitat, different palm species resist bending depending on their location, be it position exposed to high winds or under heavy snow cover.

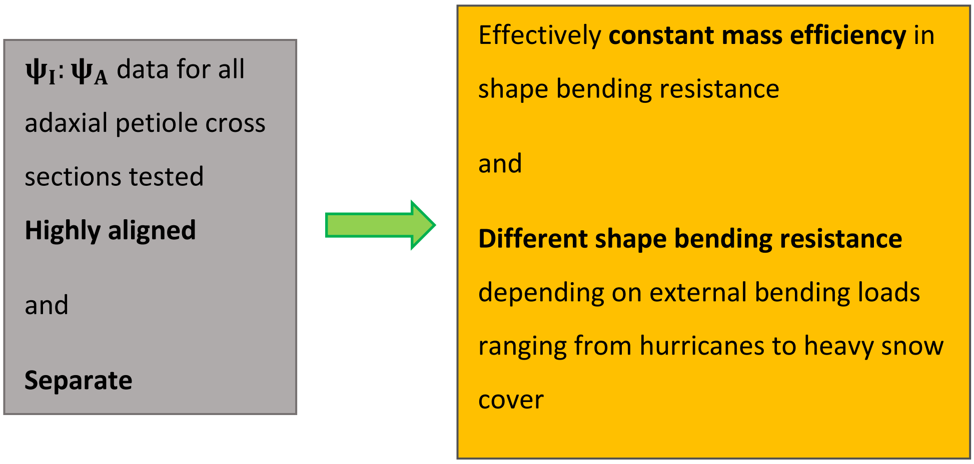

Figure 103 Inference of constant ψ_I:ψ_A but species specific ψ_I in *adaxial petiole* shapes

The *abaxial petiole* $\psi_I : \psi_A$ data is scattered with an R^2 value of 0.6881and contrasts with the highly aligned *adaxial petiole* data with an R^2 value of 0.9984. The *abaxial* edge may be able to change shape relatively easily in response to changes in loading through bending resulting from blade growth, the search for light and the associated increased weight, these changes causing the scatter in the data points.

Regarding the position of the data with respect to a solid circle in Figure 69 the *adaxial petiole* has about half the $\psi_I : \psi_A$ as a solid circle. However, not only is the *abaxial petiole* $\psi_I : \psi_A$ data close to that of a solid circle, but the actual ψ_I and ψ_A values are close to a solid circle (Figure 70), meaning that the lower part of the shapes are similar to a solid circle. The lower *abaxial* part of the *petiole* is under compression resulting from gravity and the mass of the *petiole* and the leaf blade. It therefore requires solid mass rather than lightweight structure to compensate for self-weight. This accounts for the likeness of the lower *petiole* edge to the circumscribed circle.

5.3.3.2 Mass-efficiency in torsion ψ_{JT}/ψ_A

Compared to the *adaxial* and whole *petiole* sections (Figure 72 and Figure 71), the *abaxial petiole* $\psi_J : \psi_A$ data shown in Figure 73 (where only the lower edge is the shape of the *petiole*) are grouped the closest. The *abaxial petiole* shapes for each section and on all four palm *petioles* perform alike in their shape torsional resistance to mass-efficiency ratio. It can be concluded that whatever the habitat of the palms tested, the $\psi_J : \psi_A$ of the *abaxial petiole* edge is constant.

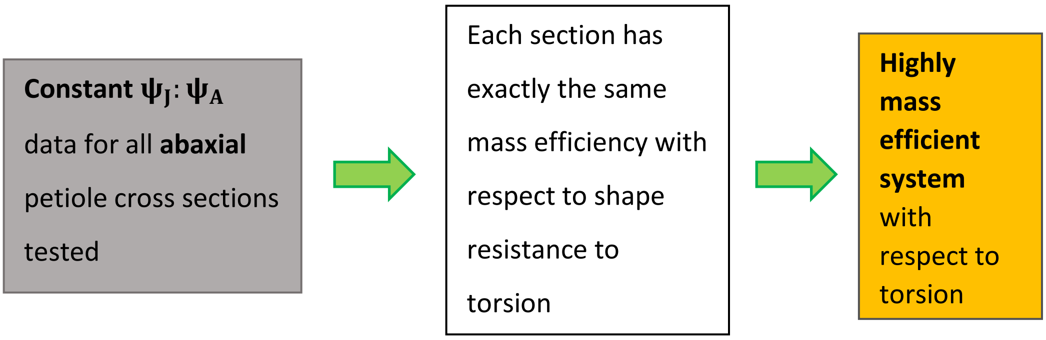

Figure 104 Inference of constant ψ_J:ψ_A in *abaxial petiole* shapes

The relevant hypothesis here is, ‘The independent *petiole* configurations are well suited to the function of the whole *petiole*. There may be a strong correlation between the properties and the transverse-section shapes of palm *petioles*’. These results clearly show that all the lower edges of the *petioles* have the same bending resistance to mass-efficiency ratio. However, looking at all the *petiole* profiles tested in Figure 66, the *abaxial* shapes look quite different. SEM has successfully extracted the contribution of each edge to the whole *petiole* in this example reinforcing the hypothesis that independent *petiole* configuration, in this case the *abaxial* edge, is well suited to the function of the whole *petiole*. Although the *abaxial petiole* shapes have the same $\psi_J : \psi_A$ ratio, their absolute ψ_J and ψ_A values are different, the shape resistance to torsion is lowest for *Tf* and jointly the highest for *Lv* and *Pk*. Contrary to this the shape resistance to torsion for the *adaxial petiole* shape is highest for *Tf* and lowest for *Lv* and *Pk* (joint), implying that the edges work together in an organised way (Figure 105).

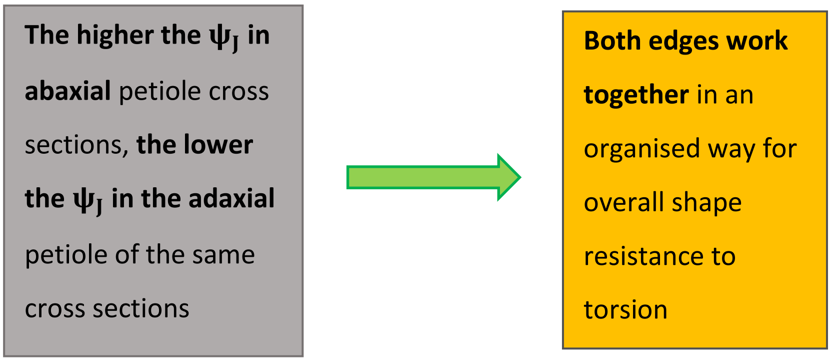

The higher the ψ_J in abaxial petiole cross sections, **the lower the ψ_J in the adaxial** petiole of the same cross sections

Both edges work together in an organised way for overall shape resistance to torsion

Figure 105 Relative contributions of *petiole* edges to overall resistance to torsion

Looking at the *adaxial* (upper half) of the *petiole* shape, the $\psi_J : \psi_A$ plot in Figure 72 shows how the data for individual palm species, are separated from each other more so than for the *petiole abaxial* data. Not only this but their P, C and D profiles are separated and they all follow a quadratic trend-line with an R^2 value of 0.9981. This is despite the fact that the *petiole* shapes observed in Figure 66 again show a wide variety of upper edge shapes, from convex to concave and those with ridges in the centre. The trend line is a line of constant $\psi_J : \psi_A$ ratio, so all the *adaxial petiole* edges have the same mass-efficiency in shape torsion resistance. However, their position along the trend line corresponds to their habitat. *Pk* and *Lv adaxial petioles*, at one end of the trend line furthest from the solid circle, have the most concave upper edges hence their low values for ψ_J and ψ_A. The natural environments that these two palms are subjected to are tropical storms for *Pk* and high winds and heavy rainfall for *Lv* (Table 24) so both species need to twist a lot to prevent breakage. *Ke* is the adjacent palm along the trend line and this resides in the sheltered forest understorey, so it does not need to twist as much. Lastly *Tf*, which is closest to the solid circle on the trend line, has the highest shape resistance to torsion and its natural habitat is in the mountainous regions of China under heavy snow cover. It therefore needs to counteract the torsion moment produced by the snow on both sides of the turning axis of the leaf blade, any imbalance causing torsion. This is shown by high ψ_J and ψ_A values.

Again this reinforces the hypothesis that independent *petiole* configuration, in this case the *adaxial* edge, is well suited to the function of the whole *petiole*. Although the extent of $\psi_J : \psi_A$ varies from species to species, the fact that there is a clear trend line across species indicates a high level of organisation to perform a specific function.

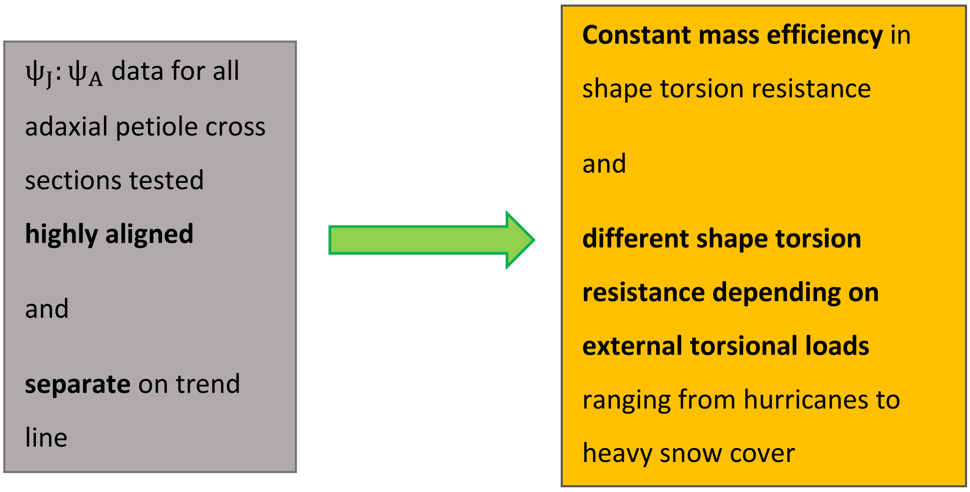

Figure 106 Inference of constant ψJ:ψA but species specific ψJ in *adaxial petiole* shapes

Regarding the position of the data with respect to a solid circle in Figure 72 and Figure 73, the *adaxial petiole* has about three quarters the $\psi_J : \psi_A$ as a solid circle which is unity i.e. three quarters of the mass-efficiency in shape resistance to torsion. However, not only is the *abaxial petiole* $\psi_J : \psi_A$ data close to that of a solid circle, but the actual ψ_J and ψ_A values are close to a solid circle, meaning that the lower edges are similar to a solid circle. The hollow circular cylinder is the most mass-efficient shape to resist torsion and the solid circle and the lower *abaxial* part of the *petiole* has a similar shape. It is therefore very effective at resisting torsion. This accounts for the likeness of the lower *petiole* edge to the circumscribed circle.

5.3.3.3 Shape twist-to-bend ratio ψ_I/ψ_{JT}

With regard to the grouping of the $\psi_I : \psi_J$ (twist to bend) shape data, the whole *petiole* sections (Figure 74) and the *adaxial petiole* edge sections (Figure 75) are spread out and distinguishable between species. However, the *abaxial* edge *petiole* twist-to-bend ratio data (Figure 76) are more grouped and the data for each species overlap.

The *abaxial petiole* shapes for each section and on all four palm *petioles* perform alike in their twist-to-bend ratio. It can be concluded that whatever the habitat of the palms tested, the $\psi_I : \psi_J$ of the *abaxial petiole* edge is similar. Relative to a circle, the *abaxial petiole* shapes twist more than bend, inferring that their way of counteracting external forces is by spillage through turning as opposed to bending (Figure 104).

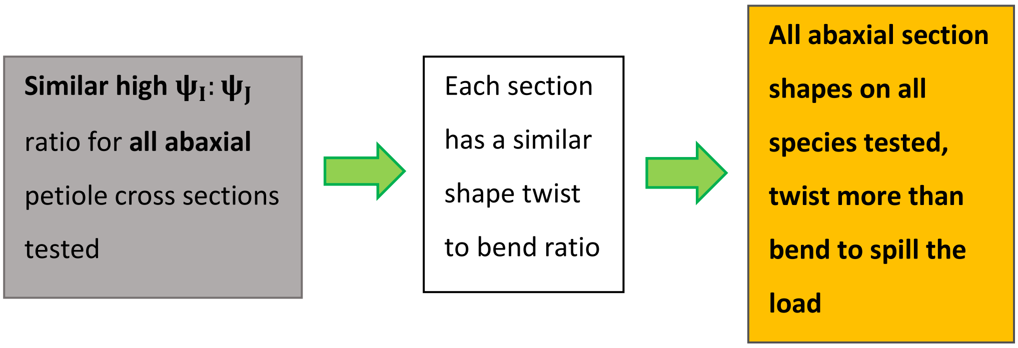

Figure 107 Inference of constant $\psi_I:\psi_J$ in *abaxial petiole* shapes

The relevant hypothesis here is, 'The independent *petiole* configurations are well suited to the function of the whole *petiole*. There may be a strong correlation between the properties and the transverse-section shapes of palm *petioles*'. These results clearly show that all the lower edges of the *petioles* have a similar twist-to-bend ratio. However, looking at all the *petiole* profiles tested in Figure 66, the *abaxial* shapes look quite different. SEM has successfully extracted the contribution of each edge to the whole *petiole* in this example reinforcing the hypothesis that independent *petiole* configuration, in this case the *abaxial* edge, is well suited to the function of the whole *petiole*. Looking at the *adaxial* (upper half) of the *petiole* shape, the $\psi_I : \psi_J$ plot in Figure 75 shows how the data for individual palm species, are separated from each other more so than for the *petiole abaxial* data. Not only this but their P, C and D profiles are separated and they all follow a quadratic trend-line with an R^2 value of 0.9993. This is despite the fact that the *petiole* shapes observed in Figure 66 again show a wide variety of upper edge shapes, from convex to concave and those with ridges in the centre. The trend line is a line of constant $\psi_I : \psi_J$ ratio, so all the *adaxial petiole* edges have the same twist-to-bend ratio. However, their position along the trend line corresponds to their habitat. *Pk* and *Lv adaxial petioles*, at one end of the trend line furthest from the solid circle, have the most concave upper edges hence their low values for ψ_I and ψ_J. The natural environments that these two palms are subjected to are tropical storms for *Pk* and high winds and heavy rainfall for *Lv* (Table 24) so both species need to twist and bend a lot to prevent breakage. *Ke* is the adjacent palm along the trend line and this resides in the sheltered forest understorey, so it does not need to twist and bend as much. Lastly *Tf*, which is closest to the solid circle on the trend line, has the highest shape resistance to torsion and bending and its natural habitat is in the mountainous regions of China under heavy snow cover. It therefore needs to counteract the torsion moment produced by the snow on both sides of the turning axis of the leaf blade, any imbalance causing torsion as well as counteracting the weight of the snow by resisting bending. This is shown by high ψ_I and ψ_J values.

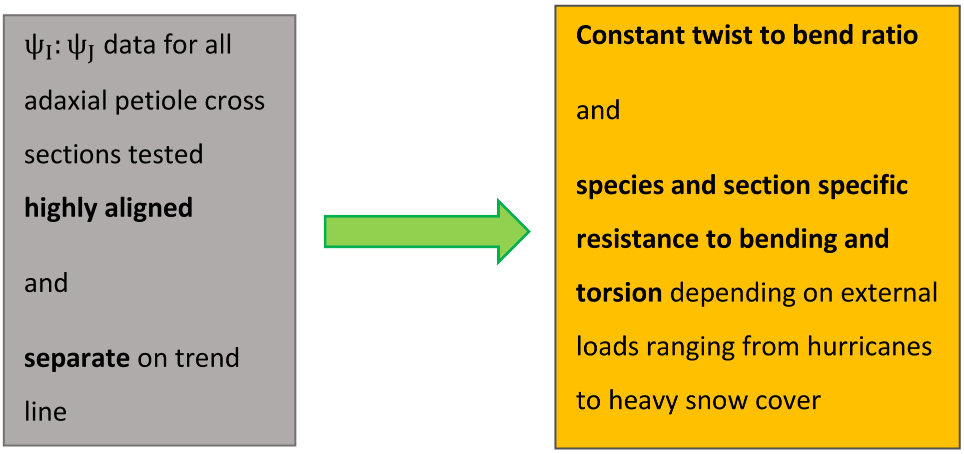

Figure 108 Inference of constant ψI:ψJ but species specific ψI and ψJ for *adaxial petiole* shapes

Again this reinforces the hypothesis that independent *petiole* configuration, in this case the *adaxial* edge, is well suited to the function of the whole *petiole*. Although the extent of $\psi_I : \psi_J$ varies from species to species, the fact that there is a clear trend line across species indicates a high level of organisation to perform a specific function.

Regarding the position of the data with respect to a solid circle in Figure 75 and Figure 76, the *adaxial petiole* has about two thirds of the $\psi_I : \psi_J$ as a solid circle i.e. two thirds of the twist-to-bend ratio. The *abaxial petiole* $\psi_I : \psi_J$ data is higher than that of a solid circle which is unity, and the actual ψ_I and ψ_J values are close to a solid circle, meaning that the lower edges are similar to a solid circle.

The hollow circular cylinder is the most mass-efficient shape to resist torsion and the fact that the comparison is with a solid circle as opposed to a hollow one, increases the resistance to bending of the reference circle. The lower *abaxial* part of the *petiole* has a similar shape to a solid circle. It is therefore very effective at resisting torsion and bending. This accounts for the likeness of the lower *petiole* edge to the circumscribed circle.

5.3.3.4 SEM verification using regular shapes

SEM analysis was carried out on a circle, equilateral triangle, square and hexagon for verification of the SEM method (Figure 46), designed in this research.

The *shape transformers* ψ_A, ψ_I and ψ_J for the circle were all unity (Figure 86 and Table 37) as expected being bound by a circular envelope. For the equilateral triangle, square and hexagon, $\psi_I$and ψ_J were identical and had values of 0.2, 0.4 and 0.7 respectively as the polar second moment of area was twice that of the second moment of area for each shape, as with the circular envelope. Differences in values between ψ_I and ψ_J were evident for both the *adaxial* and *abaxial* edges, the difference decreasing from the equilateral triangle (which showed the most difference), to the square and finally to the hexagon which showed the smallest difference. This corresponds to the increasing proportion of the envelope being occupied by the shape.

The performance indices λ_{IA}, λ_{JA} and λ_{IJ} for the circle were all unity (Figure 87 and Table 37) again as expected being bound by a circular envelope and values for ψ_A, ψ_I and ψ_J also of unity. For the equilateral triangle, square and hexagon, $\lambda_{IA}$and λ_{JA} for the whole shapes were identical for each shape and had values of 0.5, 0.7 and 0.8 respectively. This is because their ψ_I and ψ_J were also the same for each shape resulting from their polar second moment of areas being twice that of their second moment of areas. λ_{IJ} was the same for all of the whole shapes also as a result of the ψ_I and ψ_J being the same for each shape. Differences in values between $\lambda_{IA}$and λ_{JA} were evident for both the *adaxial* and *abaxial* edges, the difference decreasing from the equilateral triangle (which showed the most difference), to the square and finally to the hexagon which showed the smallest difference. Again, this corresponds to the increasing proportion of the envelope being occupied by the shape. The more the *abaxial* shape became like a circle, the higher the λ_{IA} and λ_{JA} as the circle is the most efficient solid cross section shape to resist torsion.

All of the above observations verify that that SEM produces the stated expected results.

5.3.3.5 Comparison of rectangular and circular envelopes using SEM

The upper edges of the *Sm petiole* sections, P, C and D for four *petioles* were tested in SEM, first with a rectangular envelope lower edge and then with a circular arc lower edge for the purposes of comparison.

It was found that λ_{IA} for both envelopes show the same trend along the *petiole* length (Figure 89), bending resistance performance increasing towards the leaf blade end although their values are different. This is because the *I* and *J* of a circular envelope are different to the *I* and *J* of a rectangular envelope, hence the difference in *shape transformer* values and ultimately the performance index.

5.3.4 Performance indices

Performance indices were calculated for each whole *petiole* section and each *petiole* SEM section (*petiole adaxial* edge and *petiole abaxial* edge). They represent the gradients of the *shape transformer* charts and therefore show the ratios between the *shape transformers*; the relative shape efficiencies. They do not however, show the absolute efficiencies of the *shape transformers*. A performance index of 1.0 is represented by a solid circle and shapes can be greater or less than this. As areas to be discussed for *shape transformers* and performance indices overlap, only areas not discussed in the *shape transformer* section will be discussed in this performance index section.

5.3.4.1 Performance index λ_{IA} bending resistance mass efficiency

It was found that λ_{IA} for the *abaxial petiole* with a value of 0.9 (Table 30 and Figure 79), was very close to that of the solid circle with a value of 1.0, but that λ_{IA} for the *adaxial petiole* (Table 29 and Figure 78), was much less with a value of 0.3 about a third of the solid circle. The function of the *adaxial petiole* is therefore not to optimise λ_{IA}. However, the lower edge is three times as efficient in bending resistance as the upper edge.

All of the palm species showed significantly different values of λ_{IA} between species (Table 28 and Figure 77). The palm *Ke* showed the greatest change along its length. None of the three palm species showed the same variation in λ_{IA} along its length. Futuyama (Futuyma, 1986) says that ‘Often evolution is equated to ‘progress’ from ‘lower’ to ‘higher’ forms of life, but palms have stayed simple in form and have been on Earth for a relatively long time'. When SEM analysis is performed on palm *petioles*, then parts of the *petiole* do appear simple in terms of optimising one function as with the *abaxial petiole* shape in bending resistance. However, when combined, appear more complex as in the whole *petiole* shapes which goes against what Futuyama says in terms of palms being simple.

5.3.4.2 Performance index λ_{JA} torsional resistance mass efficiency

Observing the whole *petiole* sections, two of the species tested (*Ke* and *Pk*), showed a general increase in λ_{JA} along the longitudinal axis of their *petioles* towards the leaf blade (Table 31 and Figure 80) whereas *Lv* and *Tf* showed a general decrease in the torsion performance index distally. Table 24 shows that the *petioles* are from different parts of the world and from three very different environments (high winds, forest understory and heavy snow cover) and they show different values for λ_{JA} in their whole transverse sections (Figure 80).

It was found that the λ_{JA} of the *abaxial petiole* with a value of 0.88 was close to that of the solid circle with a value of 1.0 (Table 33 and Figure 82). The performance index, λ_{JA}, for the *adaxial petioles* with a value of 0.65 was about three quarters of those of the *abaxial petioles* meaning that the function of the *adaxial petiole* was not as optimised for λ_{JA} as much as the *abaxial petiole* (Table 32 and Figure 81).

Convergent evolution over the long history of palms whereby distantly related palms independently evolve the same way after adapting to similar environments does not in this example result in transverse sections of palms being very similar. Table 24 shows that *Pk* and *Lv* both survive high winds yet their torsion performance indices for their whole *petiole* shapes are distinctly different (Figure 80).

5.3.4.3 Performance index λ_{IJ} twist-to-bend efficiency

For the *abaxial petiole* it was found that λ_{IJ}, was greater than that of the solid circle (Table 36 and Figure 85) meaning that they had a higher twist-to-bend ratio than the solid circle. These shapes have evolved to allow twisting without breakages to the *petiole*, whilst still keeping the leaf blade upright to intersect the sunlight for survival. The λ_{IJ} of 0.4 for the *adaxial petiole* (Table 35 and Figure 84), was about a third of that for the *abaxial petioles* (1.05).

All of the palm species showed significantly different values of λ_{IJ} for the whole *petiole* apart from *Pk* and *Lv* (Table 34 and Figure 83). Therefore, *convergent evolution* over the long history of palms in this example results in transverse sections of the *Pk* and *Lv* palms being very similar despite evolving in different parts of the world; Hawaii and Mauritius respectively, both locations being subjected to high winds and rainfall.

5.3.5 Comparison of material properties and shape in *T. fortunei*

The results of the material tests on the *T. fortunei* palm *petiole* were compared to the corresponding *shape transformer* results.

Young's modulus, $\bar{E}$ correlated positively with the shape bending stiffness performance index λ_{IA}, in that they both showed higher stiffness in the central section (Figure 58 and Figure 68). It was found that the rigidity modulus, G (Figure 59) which decreased towards the leaf blade, correlated with λ_{JTA} which also decreased towards the leaf blade (Figure 71). Shape is therefore an important indicator of how bending and torsion resistance varies along the *petiole*.

The findings show that the 95% confidence intervals for bulk values of E and G are wide (Figure 58 and Figure 59). Engineers in the preliminary stages of modelling design, when extracting ideas from nature, should likewise give their independent stiffness variables a wide tolerance.

The relevant hypothesis here is 'The independent *petiole* configurations are well suited to the function of the *petiole* as a whole. There may be a strong correlation between the properties and the transverse-section shapes of palm *petioles*'. The combined results of the material tests and *shape transformers* of the *T. fortunei* show that there is a strong correlation between material properties and the contribution of transverse shape to stiffness of palm *petioles*. However, only one palm *petiole* was tested as the other palm *petioles* were endangered species and/or protected specimens.

5.3.6 Shape abstraction using SEM

Most notably, the *shape transformer* chart for ψ_I vs ψ_{JT} (Figure 95) showed that with increasing amplitude in the 1.5λ family (as seen in the *Pk* distal section with tropical storm habitat), ψ_I increased and ψ_{JT} decreased. This meant that as the mass-efficiency in bending resistance increased with increased amplitude of the upper edge while the mass-efficiency in torsion decreased proportionally with respect to a solid circle which is useful for sections that need to increase their twist-to-bend ratio. This is evident in Figure 97 which shows how the performance index of the 1.5λ family is the optimum shape for twist-to-bend ratio efficiency of all the shapes tested. A trade-off exists in that mass is more efficiently used in bending but less efficiently used in torsion although the same mass is being used. To approximately formulate, equation (61) holds true for the 1.5λ upper form and the circular arc (in this case a semi-circular) lower shaped edge.

$$\psi_I = \frac{1}{\Psi_{JT}} \tag{61}$$

It is notable that the ψ_{JT}/ψ_A data for all the waveform families closely align to a quadratic curve (Figure 94) which shows that amplitude has no effect on the resistance to torsion shape mass-efficiency with respect to a solid circle.

Other waveform families however perform more efficiently than the 1.5λ family in that increasing ψ_I is accompanied by increasing ψ_A and ψ_J as with the 1.4λ, 1.2λ, 1.0λ and 0.5λ central peak families (Figure 93 and Figure 95). In fact, the performance charts in Figure 96 and Figure 97 show that the 0.5λ central peak family, as can be seen in *Lm* C and D sections, performs best (is most mass efficient) at all amplitudes in shape resistance to bending and torsion.

In periods of high forced convection, moving mass from the troughs to the peaks of the 1.5λ transverse section shape, would enable the *petiole* to become more resistant to bending and less resistant to torsion. The function is therefore allowed to change without any extra energy being invested in material; the material is simply taken away from the trough and added to the peak by adaptive growth, with zero net material gain by changing shape.

Five different waveforms were observed on the upper surface of seven species of palm so it cannot be said that *convergent evolution* over the long history of palms results in transverse sections of palms being very similar.

These shape abstraction findings using SEM are significant not only in that SEM has been successfully applied, but that the 1.5λ waveform family has the highest twist-to-bend ratio performance, a benefit to manufacturers of similar structures to reduce cost of materials. The findings also show that different families, each with their own properties and different mass efficiencies work together on the same palm *petiole*.

5.4 Recommendations for further research

1) The complex structure of biological materials is the main contributor to their exceptional functionality. No method has yet been devised to extract the biomimetic information from

plants – to date biologists have simply seen an interesting phenomenon in an organism and discovered how it works (Vincent, 2008). Usually, the biological principle is only applied to one ‘biomimetic device’, but is not extrapolated to other designs. The waveform *shape transformer* analysis in this research however, attempts to do this; an abstraction from palm *petioles*.

2) Analyse hollow sections as a further contribution to SEM. *shape transformers* of hollow sections can be obtained if the inner edge follows the same ‘*n*’ as the Lame curves for geometric shapes. In other words, the hollow shape has to be the same shape as the outer shape, currently the case when rectangular envelopes are used for shape analysis of natural section shapes.

3) The boundaries of natural structures are very important in terms of ‘wettability’, adhesion, tribology (the study of interacting moving surfaces) and corrosion in their physical applications (Bain & Whitesides, 1989). With the application of circular envelopes and SEM at much smaller scales than what has been covered in this research, insight into the physical effects of elements of shape may be made. In some plants, e.g. succulents, the epidermis and the layers of cells underneath are thickened. *Palmate* leaves often are quite tough to tear, and this initial research, using the bi-layered model, leads to the conclusion that is not a result of lignified cells.

4) Cross correlate *palmate* palm taxonomic groupings with mechanical performance groups derived from the outer shape of their *petioles*. The mechanical performance resulting from *petiole* shape has been shown in this research to be very species specific.

5) No experimental measurement of palm *petiole* strain distribution has been published apart from that of Chazdon (Chazdon, 1985). Topology optimisation via Bi-directional Evolutionary Structure Optimisation (BESO) whereby finite elements of a model are added or subtracted depending on relative stress levels should be compared with SEM developed in this research using palm *petiole* sections and other 2D natural shapes for the structures. *Petiole* transverse-sectional shapes could then be tested using BESO to check if the *petiole* shape is optimum. The families of shapes in the efficiency performance charts could then be tested, in particular, those not seen in palms, but from the same ‘shape family’.

6) The arrangement of the *VBs* at the periphery of the palm stem are more parallel to the stem axis compared to the helically arranged *VBs* in the centre (Zimmermann & Tomlinson, 1972).

A similar *VB* arrangement may be found within the palm *petiole*, an area for further research.

7) The leaf sheath of the *T. fortunei* is a convenient structure to obtain single strands of *VBs* as when the leaf blade senesces, or is removed, the fibres of the sheath remain while the *parenchyma* disappears. Three layers of fibres constitute the leaf sheath as shown in Figure 8. The fibre bundles in the middle layer had a larger diameter (418.0 µm) than the inner and outer layers (202.1 and 342.5 µm respectively), meaning that the middle layer has the lowest Young's modulus and tensile strength (Zhai, et al., 2011). However, the confidence intervals for the size of the *VBs* in the middle and outer layers mean that the data are indistinguishable, so it can only be said that the inner layer had *VBs* of smaller diameter and therefore greater tensile strength and Young's modulus. The bundles within the three layers should be traced to specific areas within the *petiole*, to indicate which bundles have the highest tensile strength and elastic modulus. Possibly, the inner layer of the *T. fortunei* leaf sheath follows through to the outer layer of the *petiole*, an area for further research.

8) Electrical impulses produced by the stem under stress can only do so within live cells as confirmed by Nogata and Takahashi in their paper named 'Intelligent functionally graded material: bamboo' (Nogata & Takahashi, 1995), so an examination into growth areas within the *VB* versus the relative contracted compressed woody cells also within the *VB* and resulting stress strain map requires further examination to understand better how the *petiole* can change its structure.

9) The *hastula* (Figure 37), a structure located at the interface between the *petiole* and the leaf blade, of the *palmate* palm, may act as a warping restraint, resisting its ability to twist, as its main flange is orientated normal to the *petiole* axis, an area for further research. Currently it is not known what the purpose of the *hastula* is (Dransfield, 2003). Such a warping restraint causes longitudinal stresses to occur within the shaft, which otherwise would not occur making it stiffer to rotate.

10) Develop idea of using circular envelopes in *shape transformers* for comparison with additional relevant shapes for cantilevers supported at one end only. In nature, the two most common simple geometric structures to be found are the hollow cylinder and the solid cylinder, the former being more mass-efficient [in torsion] as the mass is further away from the neutral axis, where the stress is highest (Burgess, 2005), so comparing the efficiency of non-proportionally scaled shapes with circles and annular rings would be the logical way forward.

11) Develop 3D *shape transformers* to allow mapping of the *shape transformers* along the longitudinal axis of the structure as properties and mass efficiencies of shapes vary along the *petiole*. This will aid design engineers when attempting to learn from natural forms.

12) The 1.5λ upper edge waveform in living cantilevers may be the most mass-efficient way of increasing bending resistance and reducing the resistance to torsion as they are in the palm *petioles* tested in this research. These preliminary findings could be applied to technical design for efficient manufacture of high twist-to-bend structures, reducing the cost of manufacture.

13) According to Tomlinson, palm *petioles* adapt to stress by changing certain aspects of their shape (Tomlinson, 2004). Whether it is possible to identify the palm species by these shapes is a matter for further research and is discussed further in section 2.11 'Differentiating *petioles* by shape'.

14) Plant species classification via *petiole* shape. In the paper by Kamel and Loutfy (Kamel & Loutfy, 2001), they find that they can discriminate between species of Lauraceae plants (Laurels), but not between distantly related taxa by looking at their *petiole* shape. However, they were not looking at shape alone, but a mixture of shape and size together. It is now possible to separate shape from size and not only that, but analyse the shapes of the upper and lower edges of *petioles*. It has been found with palm *petioles* in this research that the species can be differentiated by shape alone and so shape analysis using circular envelopes and SEM should be applied to other *petioles* for taxonomic grouping.

15) The *hastula* on the *palmate* palm may act as a warping restraint, resisting its ability of the *petiole* to twist, as its main flange is orientated normal to the *petiole* axis. Currently it is not known what the purpose of the *hastula* is (Dransfield, 2003).

6 Conclusions

Arborescent *palmate* palms can endure sustained wind loading, impact from heavy precipitation and significant self-weight forces from their own leaf blades. The purpose of this research was to understand how palms can withstand such forces and survive. The subject of this investigation is the structure that joins the leaf blade to the palm stem which for convenience, is referred to as the '*petiole*'. The research entails the observation of *petiole* internal structure, *petiole* material testing and the measurement and analysis of external *petiole* shape. The palms studied originate from three very different environments: high winds with heavy precipitation, low energy forest understorey environment and lastly, heavy snow fall.

There are four main contributions to knowledge in this thesis, each of which relate to the four hypotheses as below:

The first hypothesis, 'The size, orientation and distribution of *VBs* within the *parenchyma* matrix may contribute to the mechanical efficiency of the *petiole*'. This hypothesis was found to be proven in this research. In terms of *VB* size and knowing that smaller *VBs* have a higher Young's modulus, the *Tf* palm *petiole* tested is more elastic internally and more elastic towards the stem. The largest elasticity gradient between the inner and outer layers of the *petiole* is at the stem end, making the *petiole* more like a tube towards the stem. The orientation of the longest axes of the *VB* cross sections is linked directly to the direction of predominant stress. The circularity of the outer *VBs* nearest the leaf blade indicate that there is no predominant stress as twisting occurs in both directions, cancelling the stress out. The circular shape of the *VBs* at the blade end is also optimum for least fracture during twisting. All the *VBs* nearest to the stem, point towards the centroid of the section whereas the lateral orientation of the inner *VBs* at the leaf blade position causes the leaf blade to return to its original position after twisting. The largest number of *VBs* counted are in the transverse section nearest the leaf blade. Increasing the number of *VBs* in a *petiole* section reduces the load on each *VB* which in turn, decreases critical buckling loads, making the load path more efficient and reducing bending moments. The biggest change in the number of *VBs* per unit distance along the longitudinal axis of the *petiole* is found to be located at the stem and also at the leaf blade: the former to counteract the high bending moment; the latter to reduce the buckling load, thus decreasing the strain energy nearest to the blade.

The second hypothesis is that 'It may be possible to estimate material properties of the individual layers of a palm *petiole* by using its shape and its bulk material properties'. This hypothesis was found to be proven in this research. Initially, Young's modulus, $\bar{E}$, is determined for the material in the proximal, central and distal segments of the *Tf* palm *petiole*. Each segment is treated as a homogeneous, isotropic beam for the purpose of estimating $\bar{E}$. It is found that the values of $\bar{E}$ for the proximal and distal segments are the same. The central segment has a higher value of $\bar{E}$ meaning that the *petiole* is therefore less elastic in the middle section. The highest bending moment along the length of the *petiole*, is at the proximal end nearest the stem. The highest twisting moment along the length of the *petiole* is nearest the leaf blade at the distal end. The segments at each end of the *petiole* need to be more elastic for self-righting purposes and will therefore have a lower value of $\bar{E}$. The higher value of $\bar{E}$ in the central segment and the resulting higher bending stiffness, allows the central segment to extend away from the stem, allowing the leaf blade to receive more *insolation* for growth. To estimate the individual E of the two *Tf petiole* layers, as well as the thickness of the outer layer, a bi-layered model is designed specifically for this research. The values of E for the inner and outer layers are estimated using: simultaneous equations, the bulk $\bar{E}$ values of two adjacent sections of the *Tf petiole* (with constant outer layer thickness) and the values of the second moment of area of the two segments. The model is then used to determine the degree of lignification of the outer layer, which was not previously known. The model suggests that the outer layer of the *Tf petiole* is not lignified.

The third hypothesis is that 'Using circular envelopes in *shape transformer* analysis provides more accurate torsion performance indices'. This hypothesis was found to be proven in this research. A novel circular envelope design is used in an adapted *shape transformer* technique. This technique separates shape from size and then normalises shape. The benefits of this are first, to considerably reduce the computational effort required to process the *shape transformers* by eliminating the need for scaling and second, to eliminate the error of up to 4%, caused by estimating the torsional constant for the conventional rectangular envelope method. The scaling required for rectangular envelopes is eliminated when using circular envelopes. This is because, unlike rectangular envelopes, in which envelopes are scaled in proportion to their different aspect ratios, the aspect ratio of the circular envelope is always unity. Elimination of the error of the torsional constant value which results from its approximation, is achieved by replacing the torsional constant (a warping factor) with the polar second moment of area for the circular envelope. To date, *shape transformer* data for natural section shapes have been observed as scattered data points on mass-efficiency charts. These mechanical shape property values are effectively bulk properties with too high a variance for input into engineering models. In contrast, the novel Shape Edge Mapping (SEM) technique developed for this research, provides an accurate, filtering method to break down the complex data of natural forms. The result is to expose the mechanical properties of shape in natural forms for use in preliminary stages of bio-engineering design.

The fourth hypothesis is that ‘The independent *petiole* configurations are well suited to the function of the *petiole* as a whole. There may be a strong correlation between the properties and the transverse-section shapes of palm *petioles*.’ This hypothesis was found to be proven in this research. Palm *petioles* from three distinct environments were investigated by observing the SEM *shape transformers* for bending and torsion. Without SEM, the data are too scattered to reveal any useful data trends owing to the composite nature of the *petiole* shapes. SEM separates the *petiole* transverse section shapes into upper edges and lower edges at the points where the lateral extents of the *petiole* are greatest. Each edge is subsequently re-formed by SEM into a 2D shape. This is achieved by combining the *petiole* edge with a second edge, formed from the arc of the circle circumscribing the *petiole* edge. The SEM plots reveal the following:

- Bending resistance of the *abaxial petiole* SEM sections is constant as the sections support the self-weight of the leaf and *petiole*, the weight of which is constant.
- The *adaxial petiole* SEM sections show constant mass-efficiency in bending resistance, inferring a highly mass-efficient system. Additionally, the shape bending resistance correlates positively with the three distinct native environments of the *petioles* under examination, namely: snow loaded leaf blade, low energy forest understory and very high *forced convection* and precipitation.
- The mass-efficiency in resistance to torsion for the *abaxial petiole* SEM sections are shown to be constant, inferring a highly mass-efficient system.
- It was revealed that when shape torsion resistance is high in the *abaxial petiole* SEM section, resistance is low in the *adaxial petiole* SEM section and visa-versa. Thus, there is an inverse relationship from which can be inferred, that the upper and lower edges of the *petiole* work together in an organised way, for overall shape-resistance to torsion.
- The *adaxial petiole* SEM sections show constant mass-efficiency in torsion resistance, inferring a highly mass-efficient system. Additionally, the shape torsion resistance correlates positively with the three distinct native environments of the *petioles* under examination, namely: snow loaded leaf blade, low energy forest understory and very high *forced convection* and precipitation.
- Although the twist-to-bend ratios are found to be constant in both *abaxial petiole* SEM sections and the *adaxial petiole* SEM sections, the *abaxial petiole* SEM sections are shown to twist more than bend and the *adaxial petiole* SEM section shapes to bend more than twist. Also, the *abaxial petiole* SEM sections have far higher shape bending and torsion resistance

values than the *adaxial petiole* SEM sections, thus implying that the shapes of the two edges are each highly adapted to their physical roles.

The *shape transformer* SEM results for the palm species examined, reveal specific common shape characteristics resulting in for example, high resistance to bending of the *abaxial* shape of the *petiole* nearest the leaf blade and a constant mass-efficiency in resistance to bending and torsion for both the *abaxial* and *adaxial* SEM sections. In addition to common shape characteristics, the *petiole* SEM shapes also reveal a wide range of mass-efficiency in torsion and bending resistance across the palm species tested and also along the longitudinal axes of the *petioles* tested.

The novel SEM technique used here to understand shapes abstracted from palm *petioles* can extend to far broader use in the analysis of the contribution to mechanical function of forms derived from, but not observable in, nature. SEM is used for shape abstraction of the ridges and troughs on the upper surfaces of palm *petioles* which are likened to waveform shapes. The results reveal however, that the *adaxial* shape of the distal section of the palm species *P. kaalae*, had the highest twist-to-bend ratio as opposed to any abstracted shape. It also reveals that the central and distal sections of *L. morrisii* were the most mass-efficient in shape resistance to bending and torsion, again as opposed to an abstracted shape. For manufacturers of structures with complex specific bending and torsion properties, these findings may increase mass-efficiency with potential consequent cost savings.

The six objectives set out in 'Aims and Objectives', of section 1.5 of this thesis, are below (italicised) followed by comments on the extent to which each objective has been achieved.

1. *Map the 2D and 3D distribution of vascular bundles in the T. fortunei palm petiole and relate to the stiffness of the petiole.* The distribution of the *VBs* in the *Tf petiole* in terms of areal density, was calculated for six 2D transverse profiles spread equidistantly along the longitudinal axis of the *petiole* creating a 3D image. The relative stiffness E was mapped according to the size of the *VBs* and contrasted with the bulk $\bar{E}$ values from the flexural tests. It was concluded that the individual stiffness of the *VBs* was modified considerably by the placement of the *VBs* within the *petiole*.
2. *Relate the external profile of the T. fortunei palm petiole to its flexural and torsional stiffness through shape transformers and physical bending and torsion tests.* The flexural and torsional stiffness of the *Tf petiole* according to shape was determined by using modified *shape transformers* to which circular envelopes were integral. These correlated positively with the bulk Young's modulus and rigidity modulus results obtained from the flexural and torsional tests. It concludes that shape is an important indicator of bending and torsion resistance performance.

3. *Design an effective and inexpensive method to obtain shape profiles of living natural structures with a measurement error of less than 1%.* Shape profilers were used to provide a novel, economic, non-destructive method of measuring the external shape and size of palm *petioles*. However, the measurement error varied depending on the shape being measured as a result of the finger width of the profilers. It was possible to reduce the measurement error to 0.67% for a linear measurement of a 30 mm gauge block, but as the *petiole* profiles are such irregular shapes it was not possible to determine a single value for the measurement error. The measurement error for calculating the area of a circle of diameter 42 mm was 3.02 %.
4. Develop a *shape transformer* to reduce inaccuracies in the conventional *shape transformer* model. *Shape transformers* for torsion were made more accurate by changing the shape of envelope from rectangular to circular. The torsional constant (a warping factor) for the rectangular envelope was approximated using formulae with an error of up to 4% whereas the polar second moment of area of the circular envelope can be worked out exactly, eliminating the error from the envelope.
5. *Design a method to break down 2D shapes to smaller components to identify significant contributors of shape to bending and torsion stiffness.* Shape Edge Mapping (SEM) was designed in this research to filter the shape transformer data to produce more accurate input to engineering models. The upper and lower edges of the *petiole* transverse sections were isolated and their individual contribution to torsion and bending was achieved.
6. *Map the contribution of shape within the petioles of different species of palmate and costapalmate palms.* Four palms from three different environments were analysed for bending and torsion resistance according to shape. The three environments amounted to three different types of loading namely: high *forced convection* and precipitation, low energy forest understory and heavy snow loading. The results revealed a positive correlation and showed how the palm *petiole* reacts and survives in these different kinds of environment.

7 References

Abad, E. M., Khanoki, S. A. & Pasini, D., 2012. Fatigue design of lattice materials via computational mechanics: Application to lattices with smooth transitions in cell geometry. *International Journal of Fatigue,* Volume 47, pp. 126-136.

Abbey, D. G., 1998. Hurricane-resistant landscapes. *City Trees, The Journal of The Society of Municipal Arborists,* 4(6).

Ashby, M. F., 1991. Materials and shape. *Acta Metallurgica et Materialia,* 39(6), pp. 1025-39.

Ashby, M. F., 1999. *Material selection in mechanical design.* 2nd ed. Oxford: Pergamon Press.

Ashby, M. F., 2005. *Materials selection in mechanical design.* Oxford: Elsvier Butterworth-Heinemann.

Ashby, M. F., Gibson, L. J., Wegst, U. & Olive, R., 1995. The mechanical properties of natural materials. I. Material property charts. *Proc. R. Soc.,* Volume 450, p. 123–140.

Bain, C. D. & Whitesides, G. M., 1989. modelling organic surfaces with self assembled monolayers. *Angewandte Chemie International,* 28(4), pp. 506-512.

Barros, J., Serk, H., Granlund, I. & Pesquet, E., 2015. The cell biology of lignification in higher plants. *Annals of Botany,* Volume 115, pp. 1053-1074.

Barthlott, W. & Koch, K., 2011. Biomimetic materials. *Beilstein Journal of Nanotechnology,* Volume 2, pp. 135-136.

Birmingham, R. W., 1994. *PhD Thesis.* Newcastle: University of Newcastle.

Bouwman, A. M. et al., 2004. Which shape factor(s) best describe granules?. *Powder Technology,* 146(1-2), pp. 66-72.

Burgess, S. C., 1999. *Shape factors and material indices for dimensionally constrained structures Part 2: shafts.* London, SAGE on behalf of the Institution of Mechanical Engineers, pp. 381-388.

Burgess, S. C., 1999. *Shape factors and material indices for dimensionally constrained structures. Part 1: beams.* London, SAGE on behalf of the Institution of Mechanical Engineers.

Burgess, S. C., 2005. [Interview] (15 November 2005).

Burgess, S. C. & Pasini, D., 2004. Analysis of the structural efficiency of trees. *Journal of Engineering Design,* 15(2), pp. 177-193.

Burman, M., 1998. *Fatigue crack initiation and propagation in sandwich structures.* Stockholm: Department of Aeronautics, Royal Institute of Technology.

Chazdon, R. L., 1985. The costs of leaf support in understory palms: economy versus safety. *American Society of Naturalists,* 127(1), pp. 9-30.

Cousins, W. J., 1976. Elastic modulus of lignin as related to moisture content. *Wood science and technology,* Volume 10, pp. 9-17.

Cox, H. L., 1965. *The design of structures of least weight.* 1st ed. Oxford: Pergamon Press.

Cutler, D. F., 2005. Design in plants. In: M. W. Collins, M. A. Atherton & J. A. Bryant, eds. *Nature and Design.* Southampton: WIT Press, pp. 95-124.

Cutler, P. D., 2016. [Interview] (15 July 2016).

Dransfield, J., 2003. *Personal communication.* London: s.n.

Dransfield, J. & Baker, W., 2015. *wiki/Sabal_palmetto.* [Online]
Available at: http://www.palmpedia.net
[Accessed 7 02 2016].

Ennos, A. R., 1993. The mechanics of the flower stem of the sedge Carex acutiformis. *Annals of Botany,* Volume 72, pp. 123-127.

Ennos, A. R., Spatz, H. C. & Speck, T., 2000. The functional morphology of the petioles of the banana, Musa textilis. *Journal of Experimental Botany,* 51(353), pp. 2085-2093.

Ennos, R., 2001. *Trees.* 1 ed. London: The Natural History Museum.

Ennos, R., 2013. *Examiner's report* [Interview] (5 December 2013).

Fahn, A., 1990. *Plant Anatomy.* 4 ed. New York: Pergamon Press.

Fisher, J. B., Saunders, R. W. & Edmonson, N., 1987. The flowering and fruiting of Corypha umbraculifera. *Principes,* Volume 31, pp. 68-77.

Futuyma, D. J., 1986. *Evolutionary Biology.* 2 ed. Oxford: Blackwell Scientific Publications.

Ganeriwala, S. N., 1990. Relationship between morphology and mechanical properties of tobacco leaf lamina. *Journal of material science,* Volume 25, pp. 2199-2206.

Gibbons, M., 2003. *A pocket guide to palms.* New Jersey: Chartwell Books Inc..

Gibson, L. J., 2012. The hierarchical structure and mechanics of plant materials. *Journal of the Royal Society Interface,* Volume 9, pp. 2749-2766.

Gibson, L. J. et al., 1995. *The mechanical properties of natural materials. II. Microstructures for mechanical efficiency.* London, The Royal Society, p. 141–162.

Green, D. W. J. a. K. D., 1999. Mechanical Properties of Wood. In: *Wood Handbook - Wood as an Engineering Material.* Madison, WI: Gen. Tech. Rep. FPL-GTR-113, p. 463.

Halle, F., 1977. The longest leaf in palms?. *Principes,* 21(18).

Harder, D. L., Hurd, C. L. & Speck, T., 2006. Comparison of mechanical properties of four large, wave-exposed seaweeds. *American Journal of Botany,* Volume 93, pp. 1426-1432.

Harley, M. M., 2006. A summary of fossil records for Arecaceae. *Botanical Journal of the Linnean Society,* 151(1), pp. 39-67.

Hesse, L. et al., 2016. *Magnetic resonance imaging reveals functional anatomy and biomechanics of a living dragon tree,* s.l.: s.n.

Hunt, D. G., 2004. *Wood as an engineering material.* Southampton, WIT Press, p. 176.

Isnard, S. & Rowe, N. P., 2008. The climbing habit in palms: Biomimetics of the cirrus and flagellum. *American Journal of Botany,* 95(12), pp. 1538-1547.

Jackson, A. P., Vincent, J. F. & Turner, R. M., 1988. The mechanical design of nacre. *Proceedings of the Royal Society of London,* 234(1277), pp. 415-440.

Kamel, E. A. & Loutfy, M. H., 2001. The significance of cuticular features, petiole anatomy and SDS-PAGE in the taxonomy of the Lauraceae. *Pakistan journal of biologocal sciences,* 4(9), pp. 1094-1100.

Mattheck, C. & Tessari, I., 2003. *Uniform stress - a design rule for biological load carriers.* Karlsruhe, Germany, Forschungszentrum Karlsruhe.

Mauseth, J. D., 2012. *Botany: An introduction to plant biology.* 5th ed. Sudbury: Jones and Bartlett Publishers.

Mirjalili, V. & Pasini, D., 2007. *Shape efficiency maps for optimum shape selection in torsion stiffness design.* Anaheim, ACTA Press.

Niklas, K. J., 1992. *Plant biomechanics: an engineering approach to plant form and function.* 1 ed. Chicago: University of Chicago Press.

Nik, M. A., Fayazbakhsh, K., Pasini, D. & Lessard, L., 2012. Surrogate-based multi-objective optimisation of a composite laminate with curvilinear fibres. *Composite Structures,* 94(8), pp. 2306-2313.

Nogata, F. & Takahashi, H., 1995. Intelligent functionally graded material: bamboo. *Composites Engineering,* 5(7), pp. 743-751.

Parkhouse, J. G., 1984. *Structuring: a process of material distribution.* London, Elsevier.

Pasini, D., 2007. Shape transformers for material and shape selection of lightweight beams. *Journal of Materials and Design,* 28(7), pp. 2071-2079.

Pasini, D., 2008. On the biological shape of the Polygonaceae Rheum rubarbarum petiole. *International Journal of Design & Nature and Ecodynamics,* 3(1), pp. 1-26.

Pasini, D. & Burgess, S. C., 2002. *Optimal structural features in trees and their application in engineering.* Udine, WITPress, pp. 3-15.

Pasini, D., Burgess, S. C. & Smith, D. J., 2001. *Performance indices for arbitrarily scaled rectangular cross-sections in bending stiffness design.* London, Institute of Mechanical Engineers.

Pasini, D. & Mirjalili, V., 2006. *The optimised shape of a leaf petiole.* Southampton, WITPress, pp. 35-45.

Pasini, D., Smith, D. J. & Burgess, S. C., 2003. Selection of arbitrarily scaled cross-sections in bending siffness design. *Journal of Materials Design and Applications,* Volume 217, pp. 113-125.

Pasini, D., Smith, D. J. & Burgess, S. C., 2003. *Structural efficiency maps for beams subjected to bending.* London, Intitution of mechanical engineers.

Rich, P. M., 1987. Mechanical structure of the stem of arborescent palms. *Botanical Gazette,* 148(1), pp. 42-50.

Ruggeberg, M., Speck, T. & Burgert, I., 2008. Structure-function relationships of different vascular bundle types in the stem of the Mexican fan palm (Washingtonia robusta). *New Phytologist,* Volume 182, pp. 443-450.

Ryder, G. H., 1955. *Strength of Materials.* 1 ed. London: Cleaver-Hume Press.

Ryder, G. H., 1955. *Strength of Materials.* 1 ed. London: Cleaver-Hume Press.

Shanley, F. R., 1943. Aircraft structural research. *Aircraft Engineering,* 15(7), pp. 200-206.

Shanley, F. R., 1960. *Weight-strength analysis of aircraft structures.* 2nd ed. New York: Dover.

Singh, J., Mirjalili, V. & Pasini, D., 2011. Integrated shape and material selection for single and multi-purpose criteria. *Materials and Design,* 32(5), pp. 2909-2922.

Spatz, H. -C., KOHLER, L. & NIKLAS, K. J., 1999. Mechanical behaviour of plant tissues: composite materials or structures?. *The Journal of Experimental Biology,* Volume 202, pp. 3269-3272.

Thomas, J. P. & Qidwai, M. A., 2004. Mechanical design and performance of composite multifunctional materials. *Acta Materialia,* Volume 52, pp. 2155-2164.

Tomlinson, P. B., 1990. *The structural biology of palms.* 1 ed. Oxford: Oxford University Press.

Tomlinson, P. B., 2004. [Interview] (24 February 2004).

Tomlinson, P. B., 2006. The uniqueness of palms. *Botanical Journal of the Linnean Society,* 151(1), pp. 5-14.

Tomlinson, P. B. & Hugget, B. A., 2012. Cell longevity and sustained primary growth in palm stems. *American Journal of Botany,* 99(12), pp. 1891-1902.

Trtik, P., Dual , J., Muench , B. & Holzer , L., 2007. 3D imaging of microstructure of spruce wood. *Journal of Structural Biology,* Volume 159, pp. 46-55.

Vincent, J., 2008. Biomimetic materials. *Journal of Materials Research,* 23(12), pp. 3140-3147.

Vogel, S., 1992. Twist-to-bend ratios and cross-sectional shapes of petioles and stems. *Journal of Experimental Botany,* 43(256), pp. 1527-1532.

Vogel, S., 1995. Twist-to-bend ratios of woody structures. *Journal of Experimental Botany,* 46(289), pp. 981-985.

Weaver, P. M. & Ashby, M. F., 1996. The optimal selection of material and section-shape. *Journal of Engineering Design,* 7(2), pp. 129-150.

Weaver, P. M. & Ashby, M. F., 1997. Material limits for shape efficiency. *Progress In Materials Science,* 41(12), pp. 61-128.

Wegst, U. G., 2011. Bending efficiency through property gradients in bamboo, palm, and wood-based composites. *Journal of the Mechanical Behaviour of Biomedical Materials,* Volume 4, pp. 744-755.

Windsor-Collins, A. G., Atherton, M. A., Collins, M. W. & Cutler, D. F., 2006. Structural and torsional properties of the Trachycarpus fortunei palm petiole. In: C. A. Brebbia, ed. *Design & Nature III: Comparing design in nature with science and engineering.* Southampton: WIT Press, pp. 185 - 194.

Windsor-Collins, A. G., Atherton, M. A., Collins, M. W. & Cutler, D. F., 2007a. Section properties of palm petioles, Part 1: The influence of shape on the flexural and torsional properties of selected palm petioles. *International Journal of Design & Nature and Ecodynamics,* 2(4), pp. 328-355.

Windsor-Collins, A. G., Atherton, M. A., Collins, M. W. & Cutler, D. F., 2008. Section properties of palm petioles, Part 2: The relationship of palm histology with the torsional rigidity of the palm Trachycarpus fortunei. *International Journal of Design & Nature and Ecodynamics,* 3(3), pp. 190-202.

Windsor-Collins, A. G., Cutler, D. F., Atherton, M. A. & Collins, M. W., 2007b. The palm - a model for success?. In: J. A. Bryant, M. A. Atherton & M. W. Collins, eds. *Design and Information in Biology - from Molecules to Systems.* Southampton: WIT Press, pp. 303-324.

Winter, D. F., 1993. On the stem curve of a tall palm in a strong wind. *Society for Industrial and Applied Mathematics Review,* 35(4), pp. 567-579.

Young, W. & Budynas, R. G., 2002. *Roark's formulas for stress and strain.* 7 ed. New York: McGraw-Hill.

Zhai, S. et al., 2011. Tensile strength of windmill palm (Trachycarpus fortunei) fiber bundles and its structural implications. *Journal of Material Science,* Volume 47, pp. 949-959.

Zimmermann, M. H. & Tomlinson, P. B., 1972. The vascular system of monocotyledonous stems. *Botanical Gazette,* 133(2), pp. 141-155.

8 Appendices

8.1 Petiole field forms

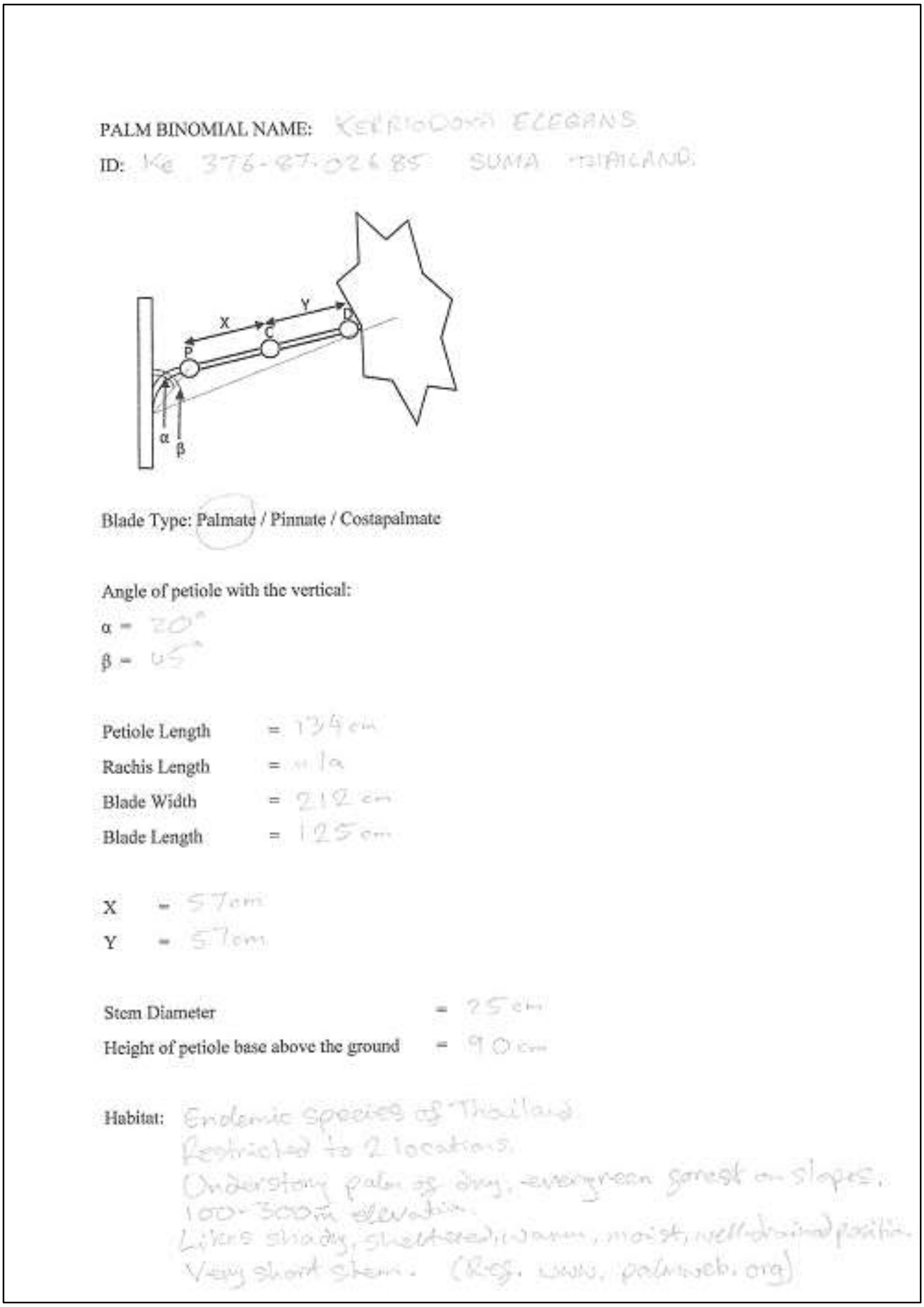

PALM BINOMIAL NAME: KERRIODOXA ELEGANS
ID: Ke 376-87-02685 SUMA THAILAND

Blade Type: [✓ Palmate] / Pinnate / Costapalmate

Angle of petiole with the vertical:
α = 20°
β = 05°

Petiole Length = 134 cm
Rachis Length = n/a
Blade Width = 212 cm
Blade Length = 125 cm

X = 57cm
Y = 57cm

Stem Diameter = 25 cm
Height of petiole base above the ground = 90 cm

Habitat: Endemic species of Thailand.
Restricted to 2 locations.
Understory palm of dry, evergreen forest on slopes,
100-300m elevation.
Likes shady, sheltered, warm, moist, well-drained position.
Very short stem. (Ref. www.palmweb.org)

Figure 109 *Kerriodoxa elegans* palm *petiole* field form

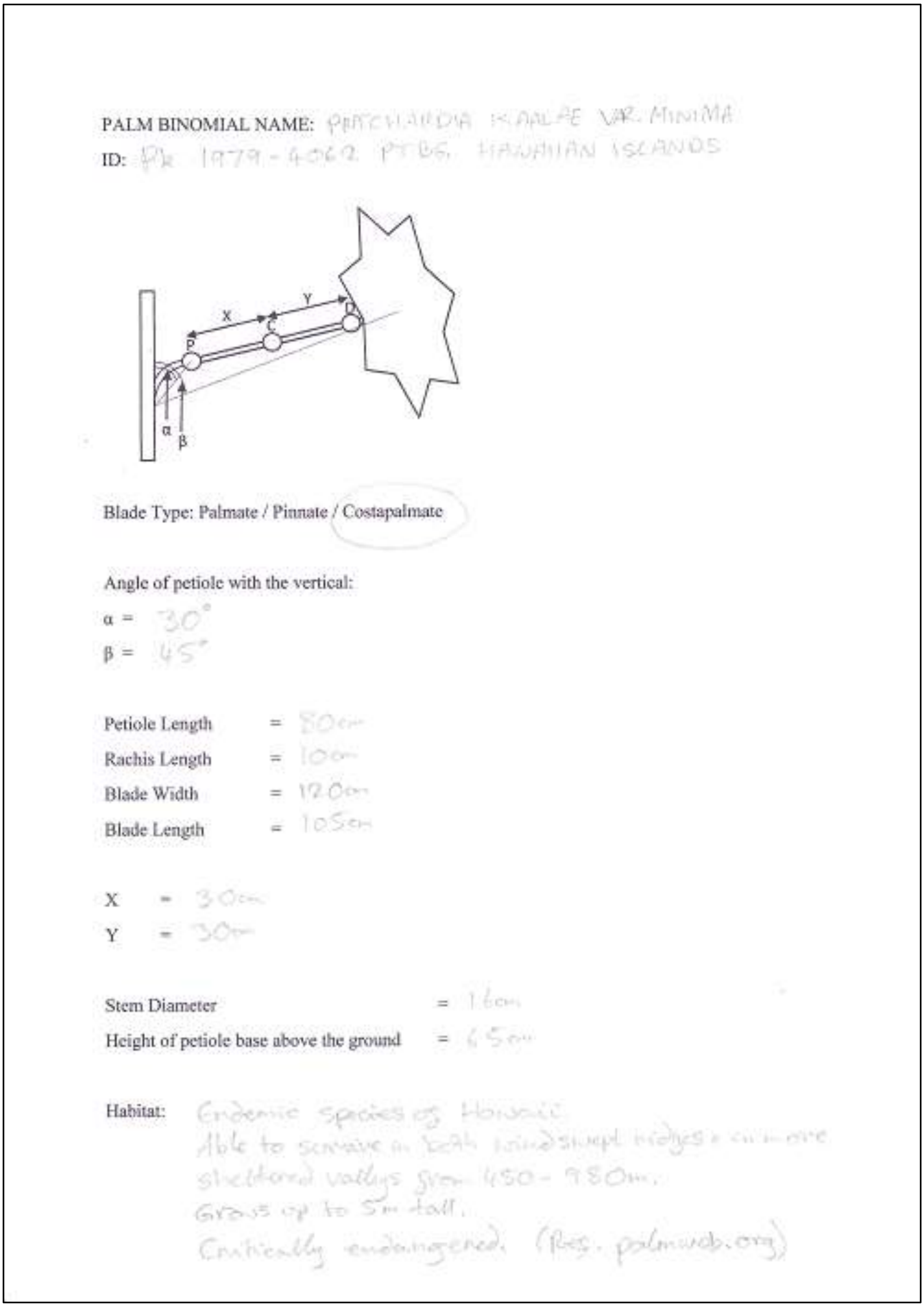

PALM BINOMIAL NAME: PRITCHARDIA KAALAE VAR. MINIMA
ID: Pk 1979-4062 PTBG. HAWAIIAN ISLANDS

Blade Type: Palmate / Pinnate / [✓ Costapalmate]

Angle of petiole with the vertical:
α = 30°
β = 45°

Petiole Length = 80cm
Rachis Length = 10cm
Blade Width = 120cm
Blade Length = 105cm

X = 30cm
Y = 30cm

Stem Diameter = 16cm
Height of petiole base above the ground = 65cm

Habitat: Endemic species of Hawaii
Able to survive in both windswept ridges & in more
sheltered vallys from 450-980m.
Grows up to 5m tall.
Critically endangered. (Res. palmweb.org)

Figure 110 *Pritchardia kaalae* palm *petiole* field form

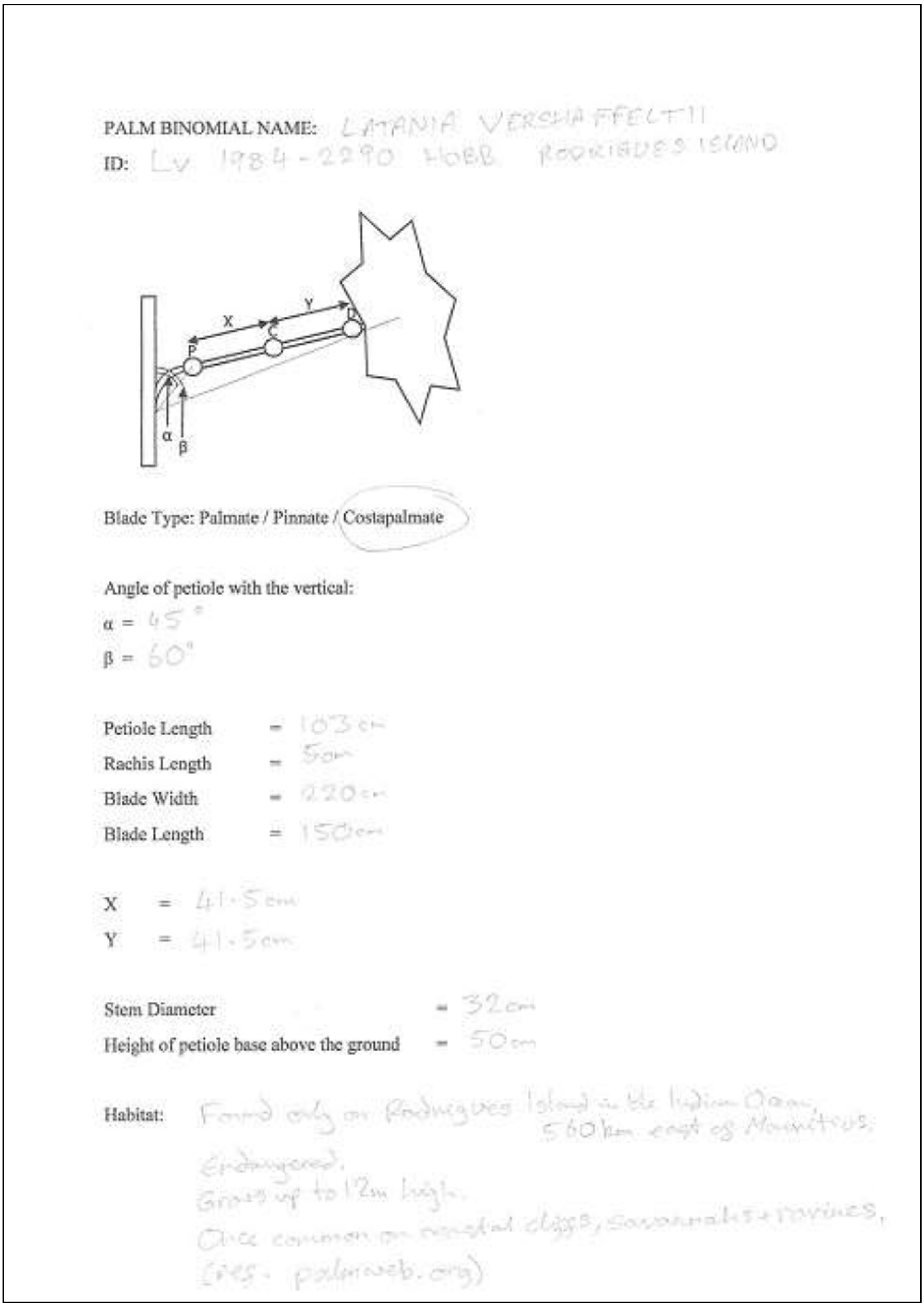

PALM BINOMIAL NAME: LATANIA VERSHAFFELTII
ID: LV 1984-2290 HOBB RODRIGUES ISLAND

Blade Type: Palmate / Pinnate / [✓ Costapalmate]

Angle of petiole with the vertical:
α = 45°
β = 60°

Petiole Length = 103 cm
Rachis Length = 5cm
Blade Width = 220 cm
Blade Length = 150 cm

X = 41.5 cm
Y = 41.5 cm

Stem Diameter = 32 cm
Height of petiole base above the ground = 50 cm

Habitat: Found only on Rodrigues Island in the Indian Ocean, 560 km east of Mauritius.
Endangered.
Grows up to 12m high.
Once common on coastal cliffs, savannahs + ravines,
(PES - palmweb.org)

Figure 111 *Latania vershaffeltii* palm *petiole* field form

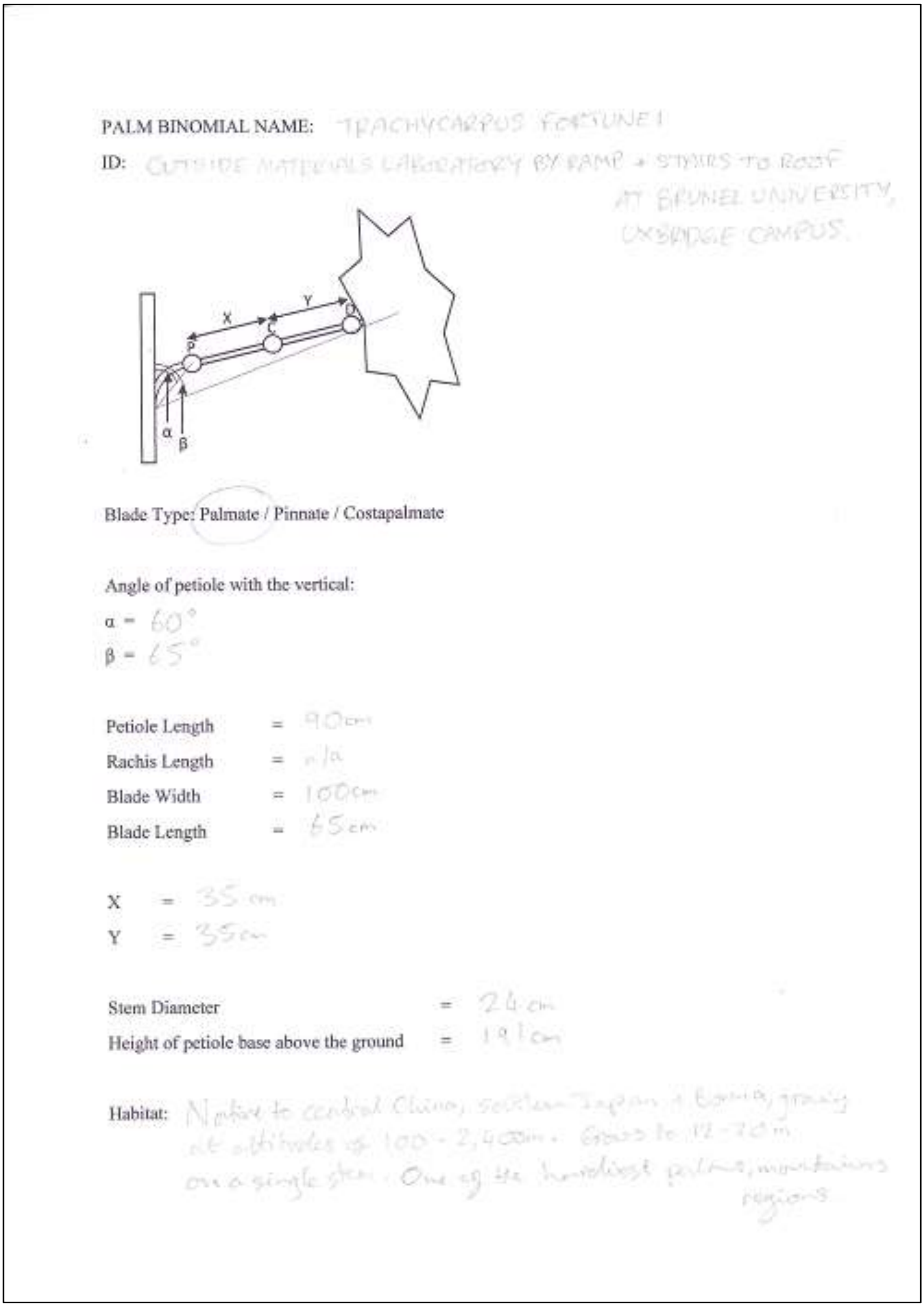

PALM BINOMIAL NAME: TRACHYCARPUS FORTUNEI

ID: OUTSIDE MATERIALS LABORATORY BY RAMP + STAIRS TO ROOF AT BRUNEL UNIVERSITY, UXBRIDGE CAMPUS.

Blade Type: [✓ Palmate] / Pinnate / Costapalmate

Angle of petiole with the vertical:

α = 60°

β = 65°

Petiole Length = 90cm

Rachis Length = n/a

Blade Width = 100cm

Blade Length = 65cm

X = 35 cm

Y = 35cm

Stem Diameter = 24 cm

Height of petiole base above the ground = 191 cm

Habitat: Native to central China, southern Japan & Burma, growing at altitudes of 100 - 2,400m. Grows to 12-20m on a single stem. One of the hardiest palms, mountains regions

Figure 112 *Trachycarpus fortunei* palm *petiole* field form

8.2 Raw petiole profiles

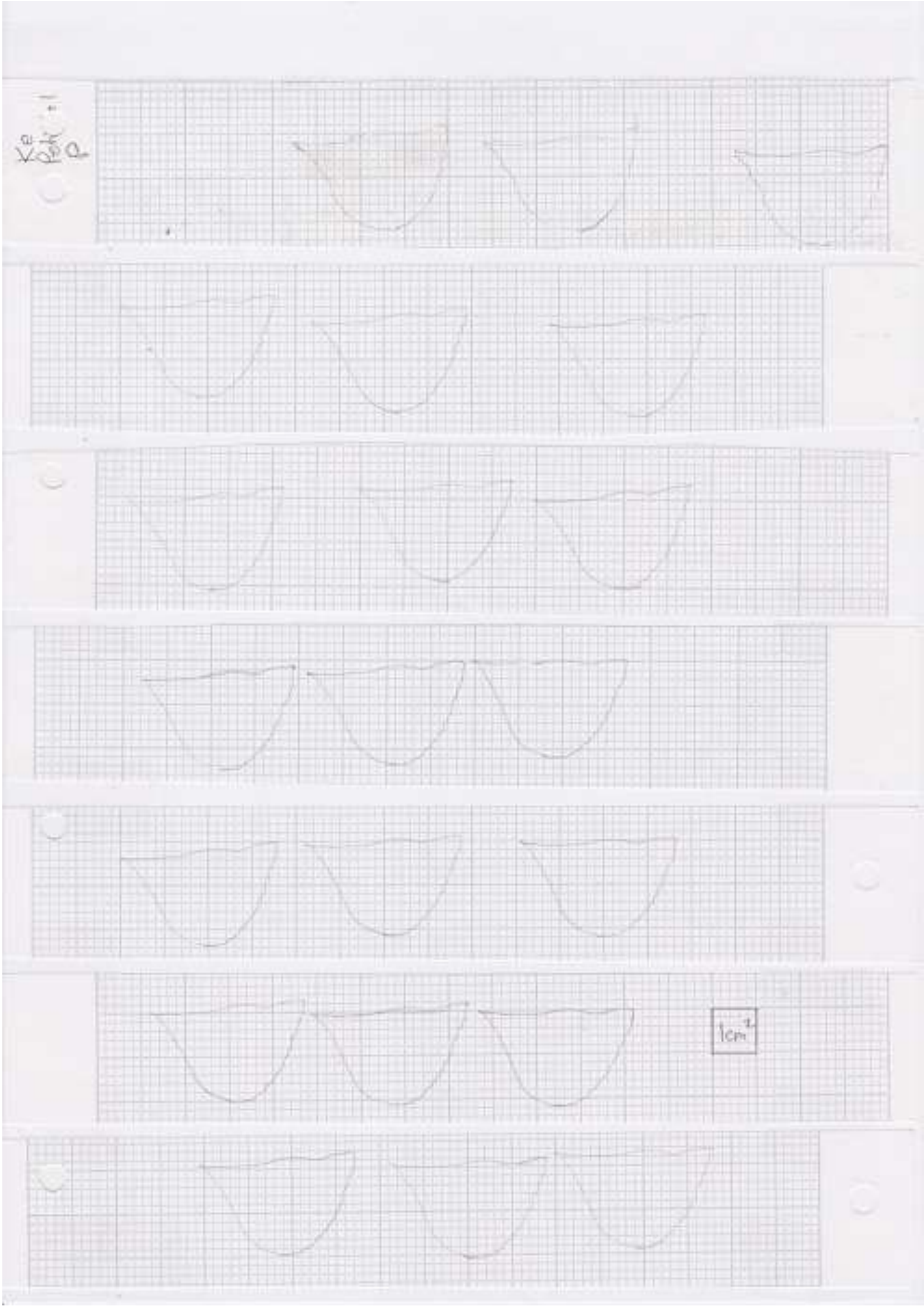

Figure 113 Raw profiles KeP – one *petiole* (part 1 of 2)

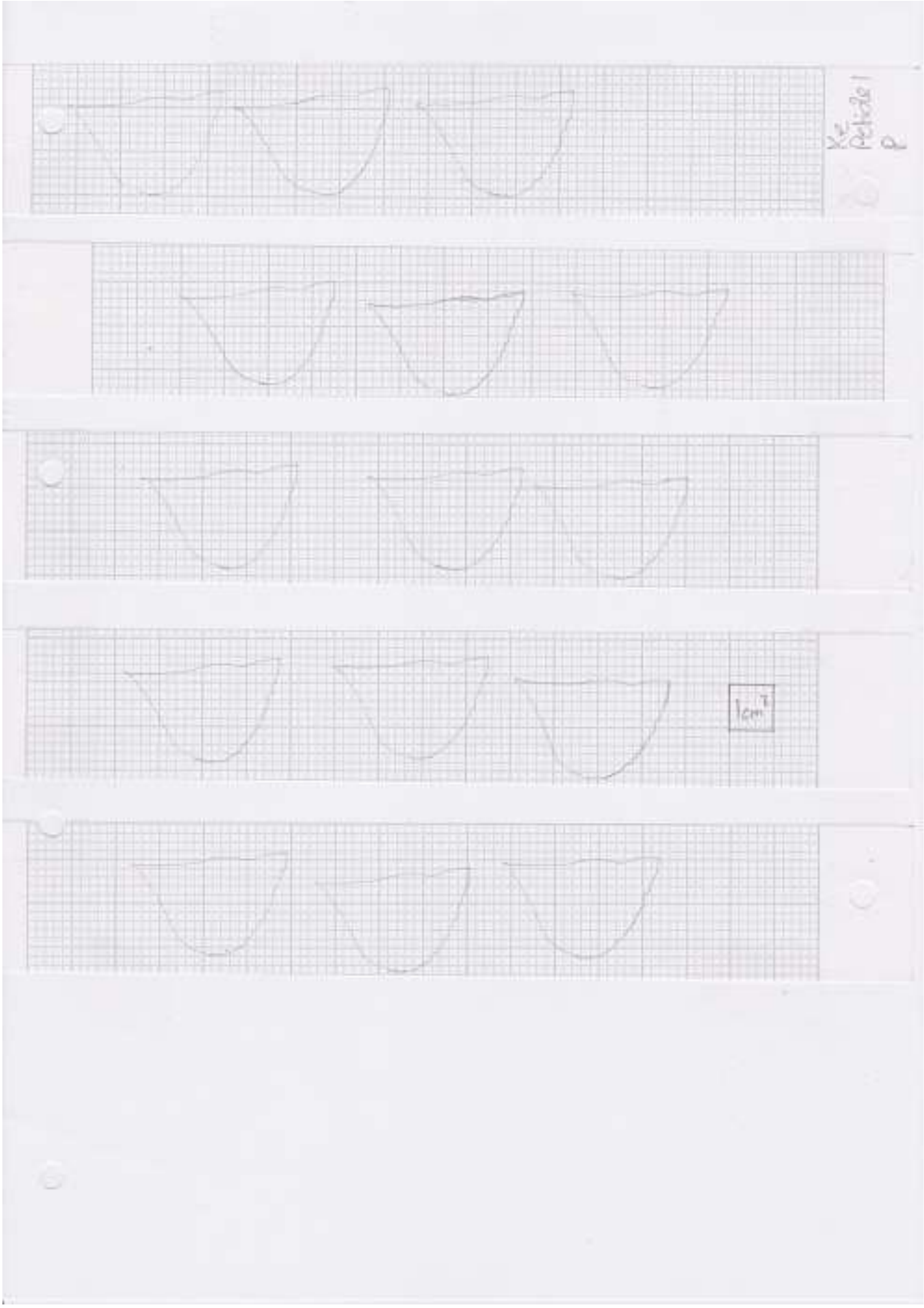

Figure 114 Raw profiles KeP – one *petiole* (part 2 of 2)

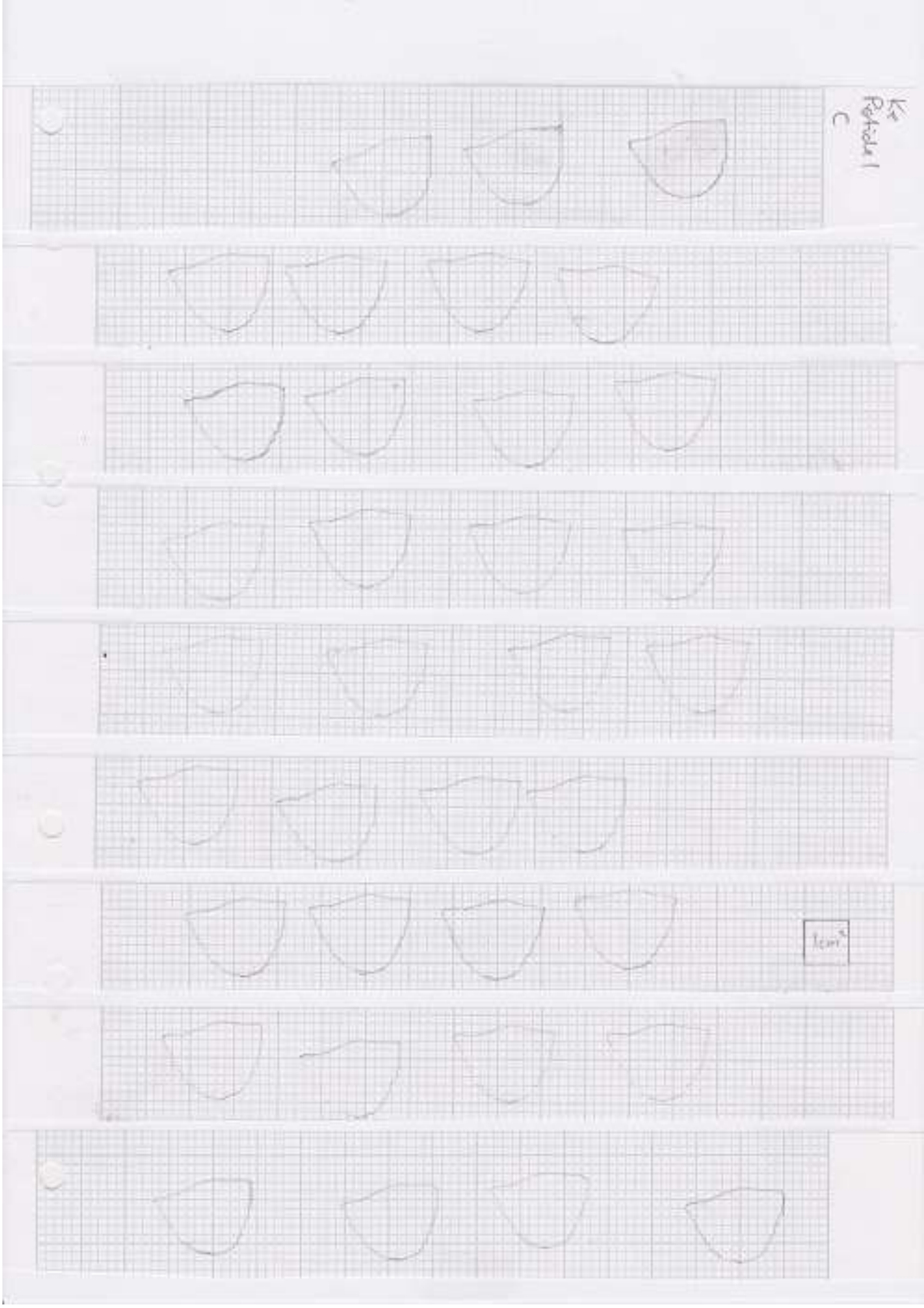

Figure 115 Raw profiles KeC – one *petiole*

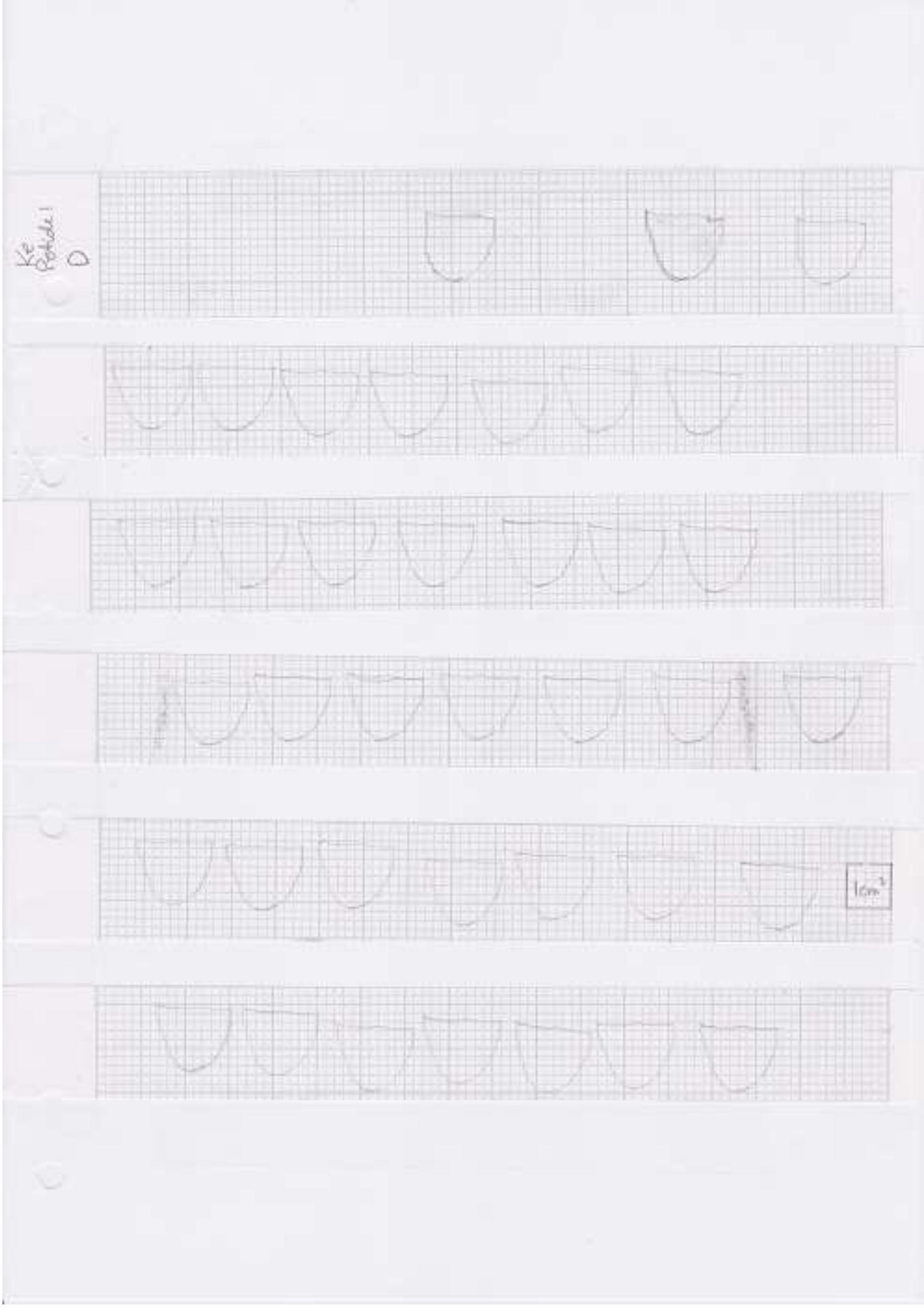

Figure 116 Raw profiles KeD – one *petiole*

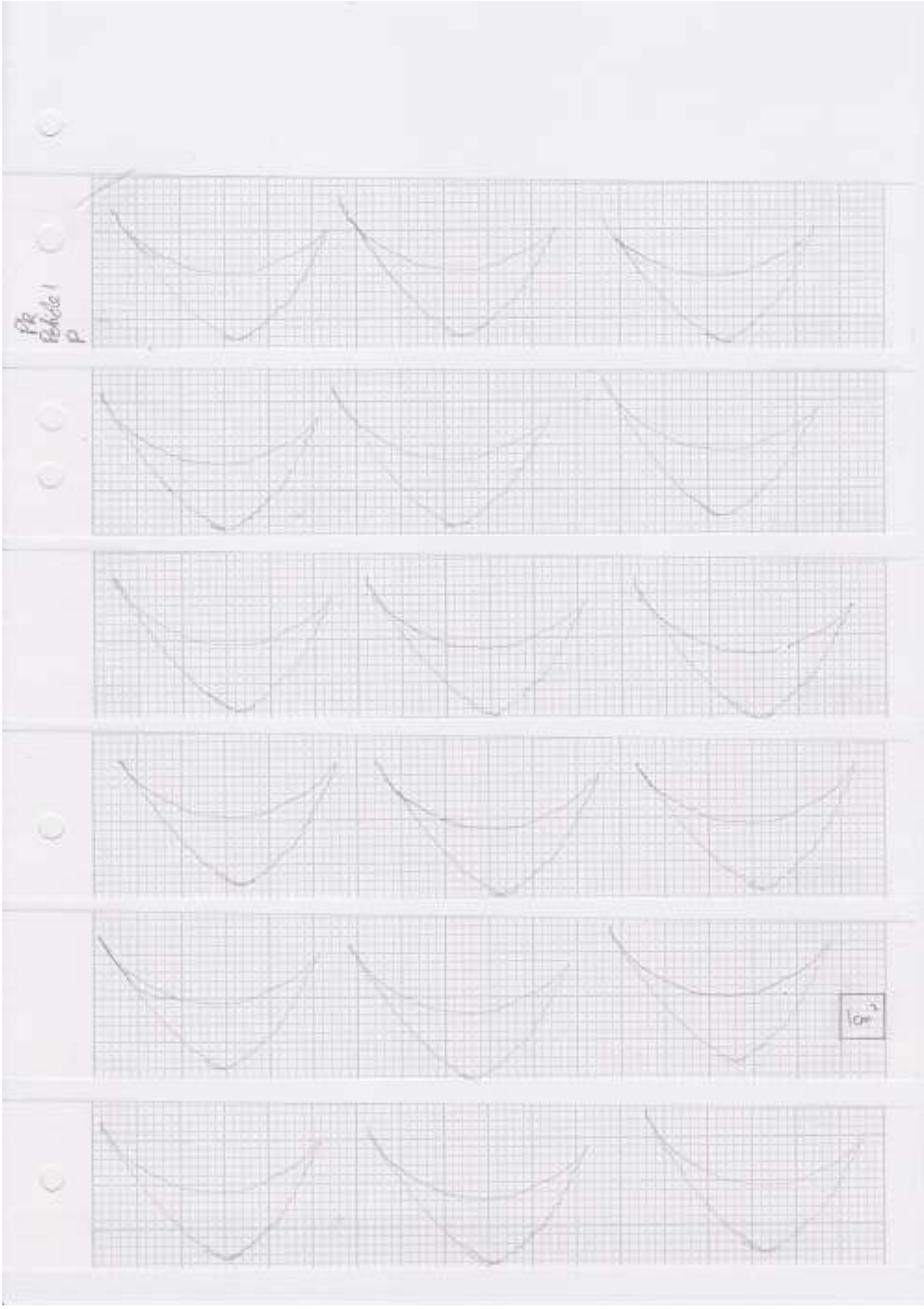

Figure 117 Raw profiles PkP – one *petiole* (part 1 of 2)

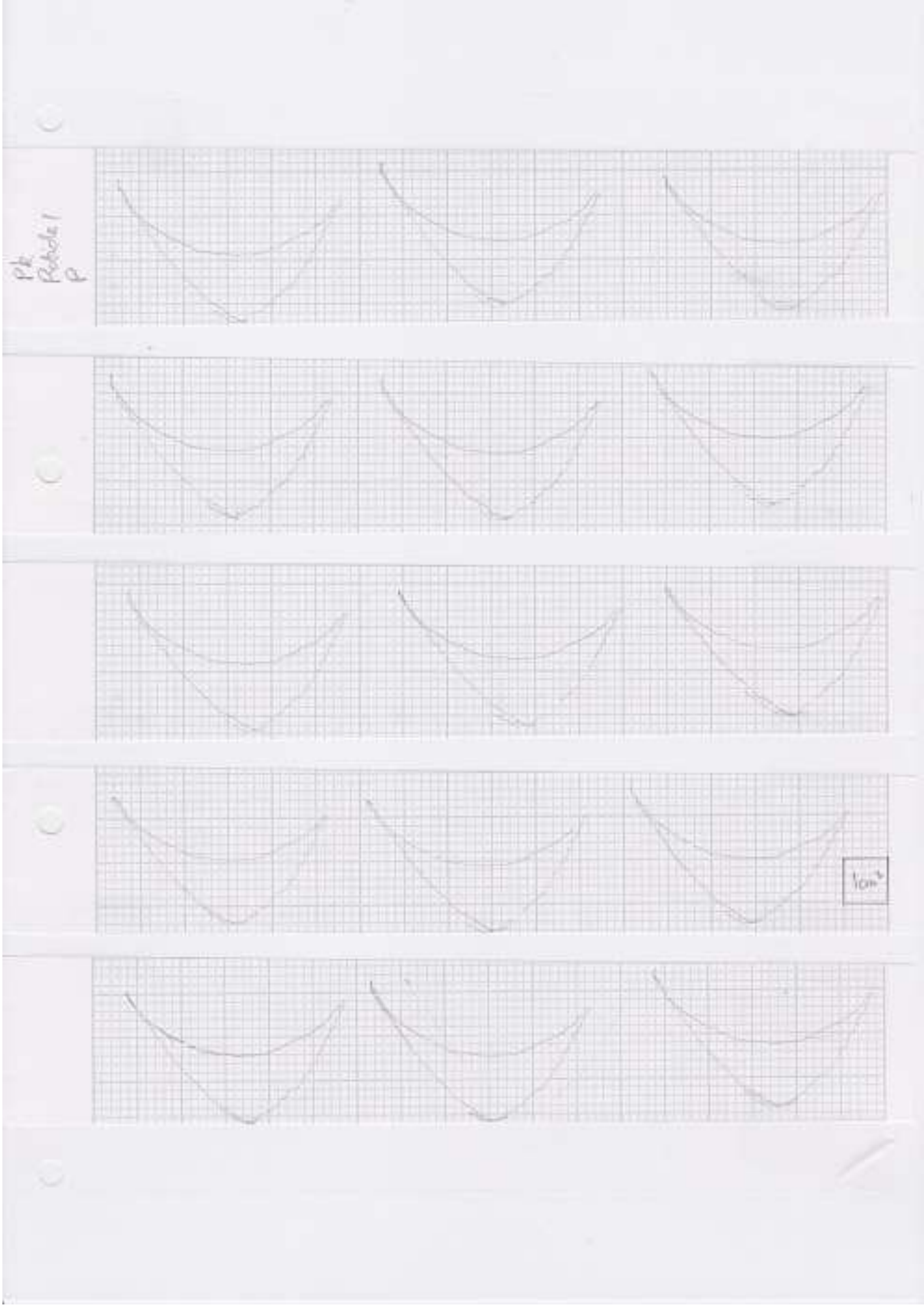

Figure 118 Raw profiles PkP – one *petiole* (part 2 of 2)

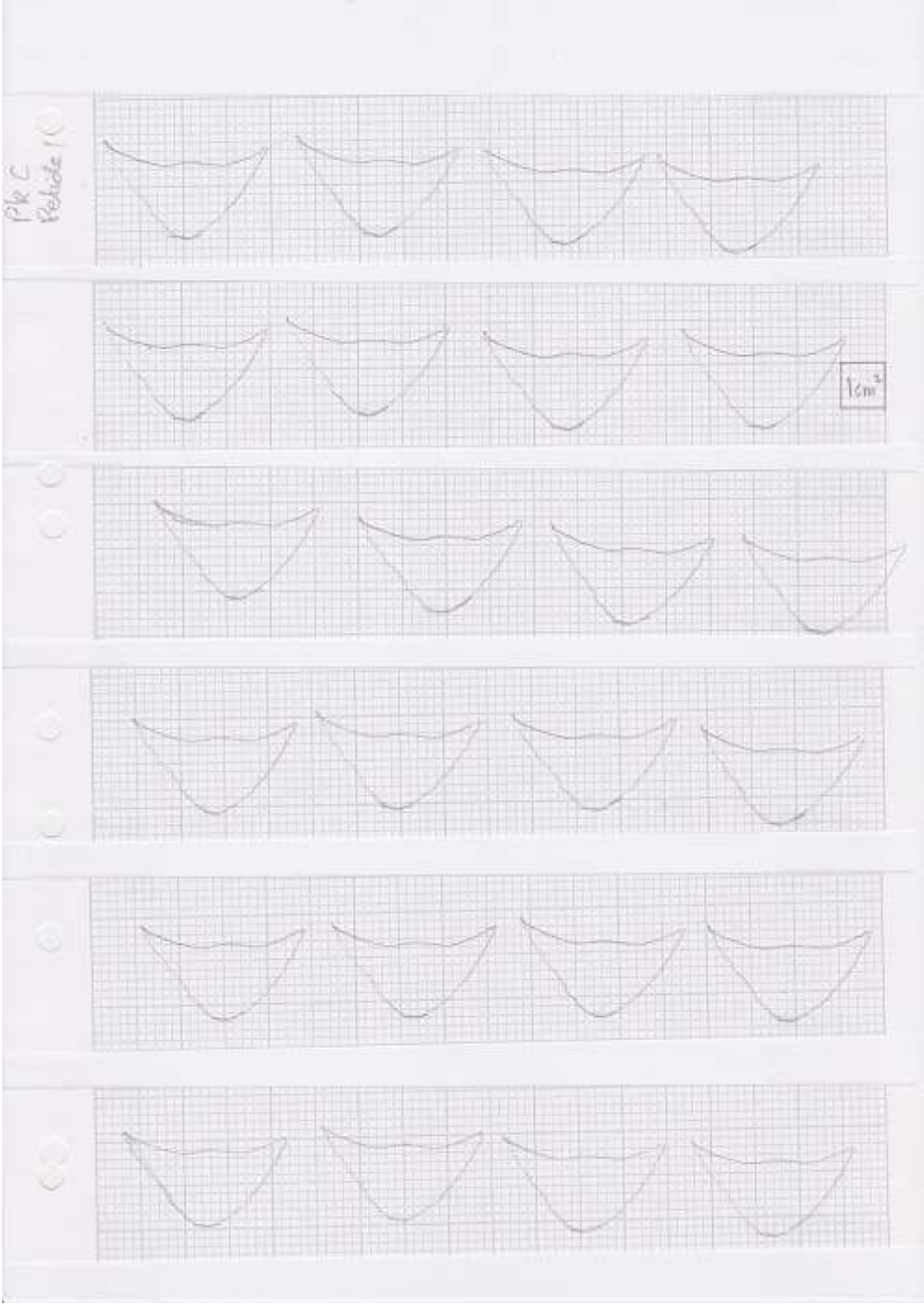

Figure 119 Raw profiles PkC – one *petiole* (part 1 of 2)

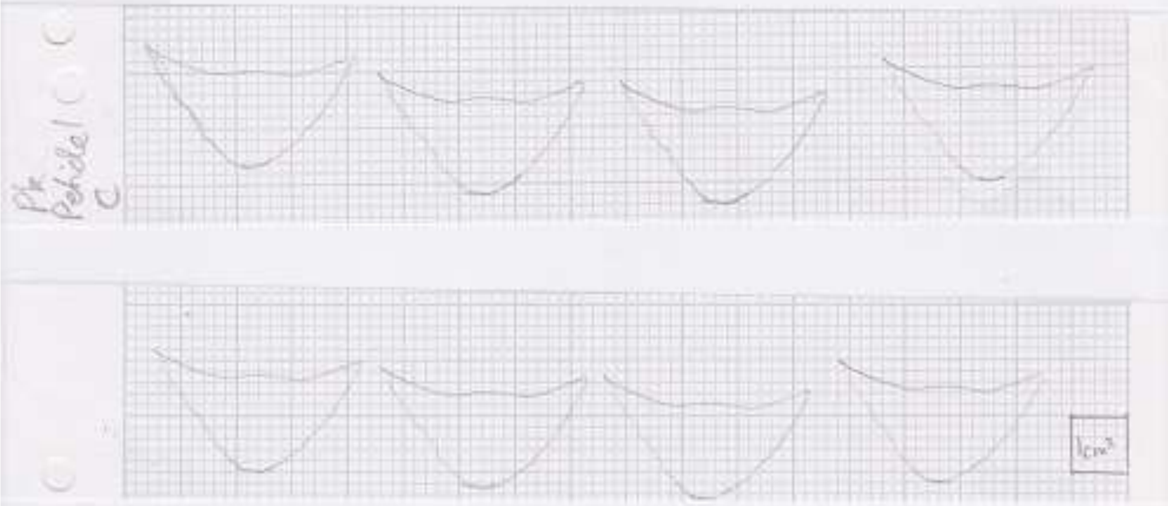

Figure 120 Raw profiles PkC – one *petiole* (part 2 of 2)

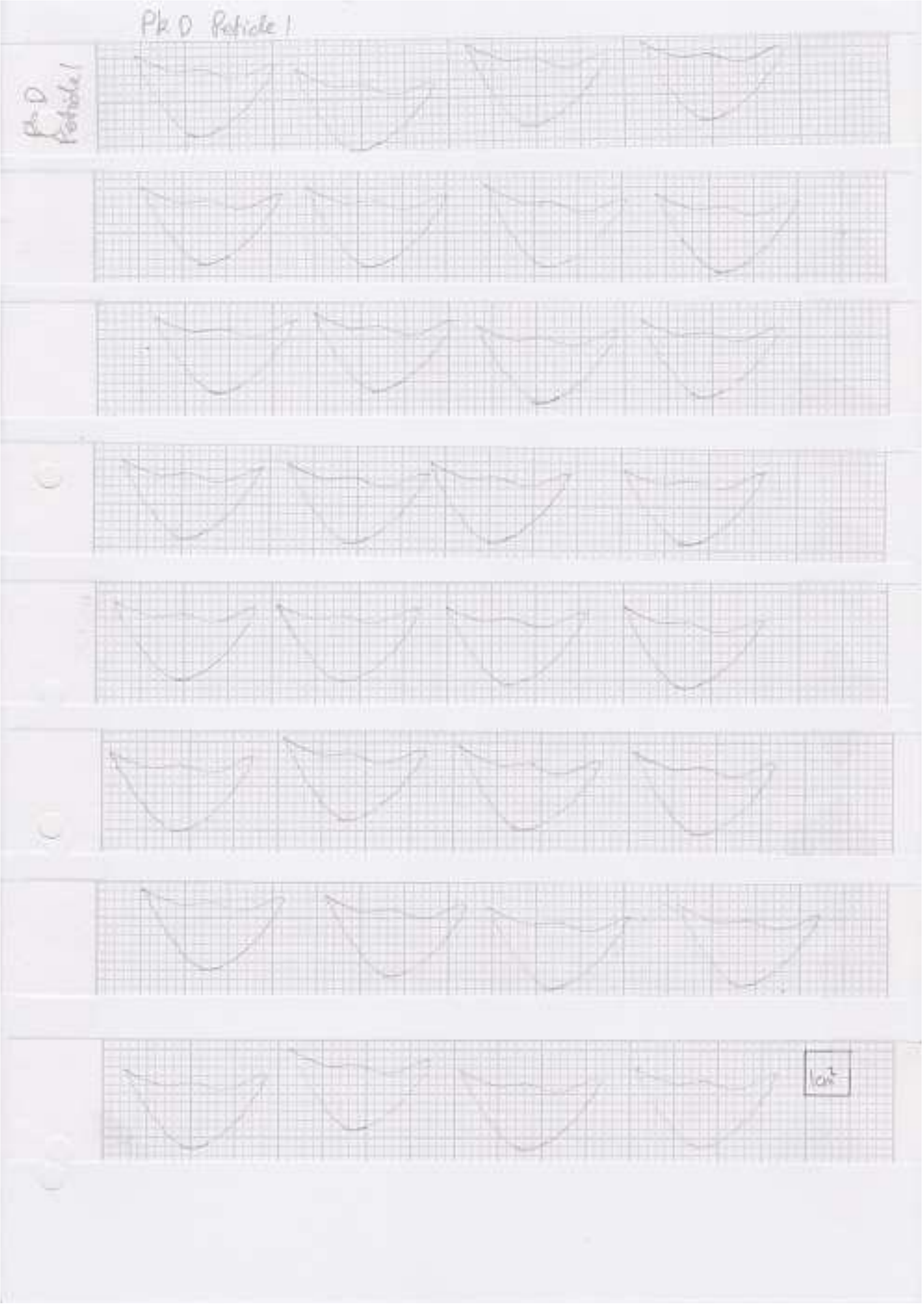

Figure 121 Raw profiles PkD – one *petiole*

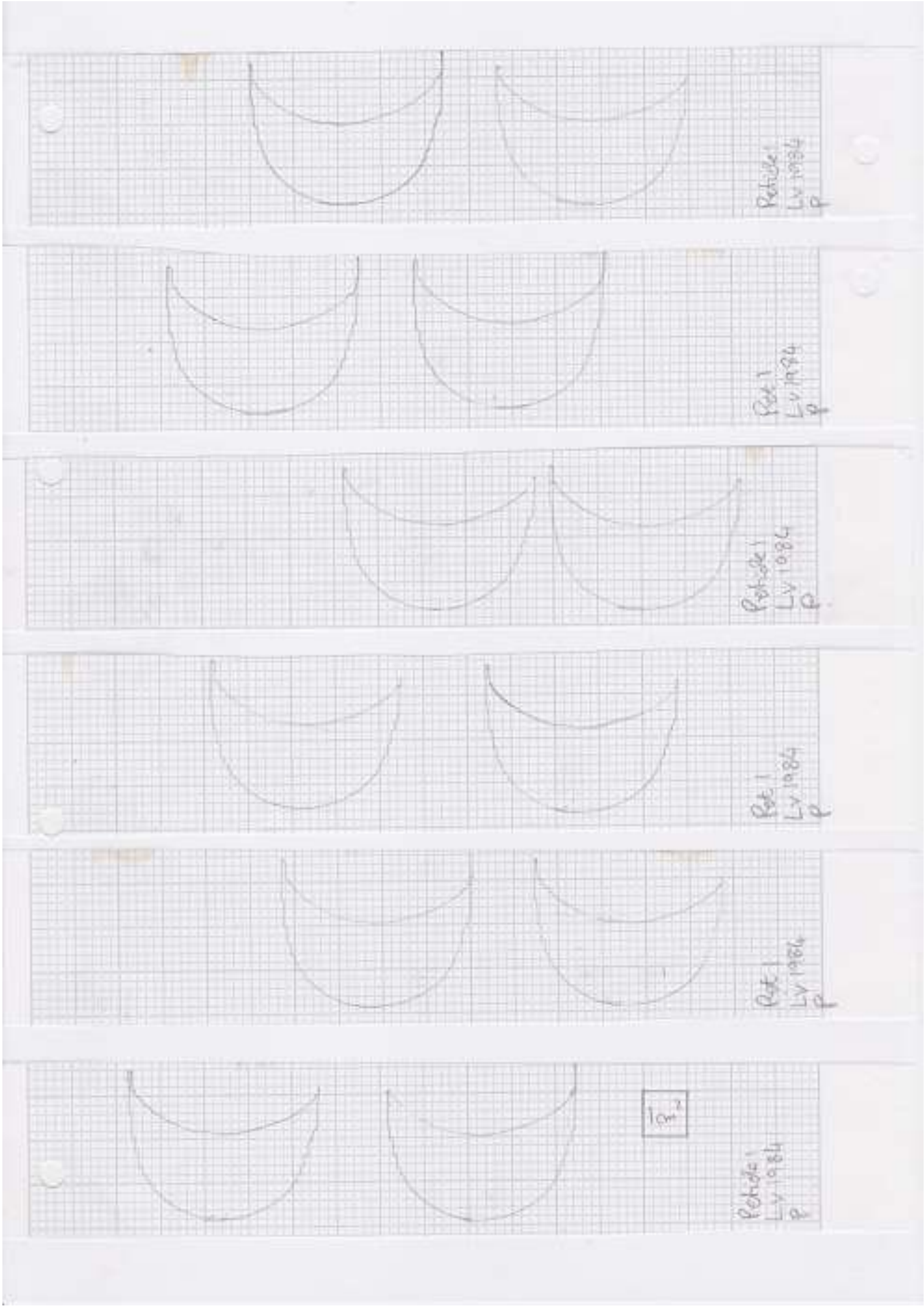

Figure 122 Raw profiles LvP – one *petiole* (part 1 of 3)

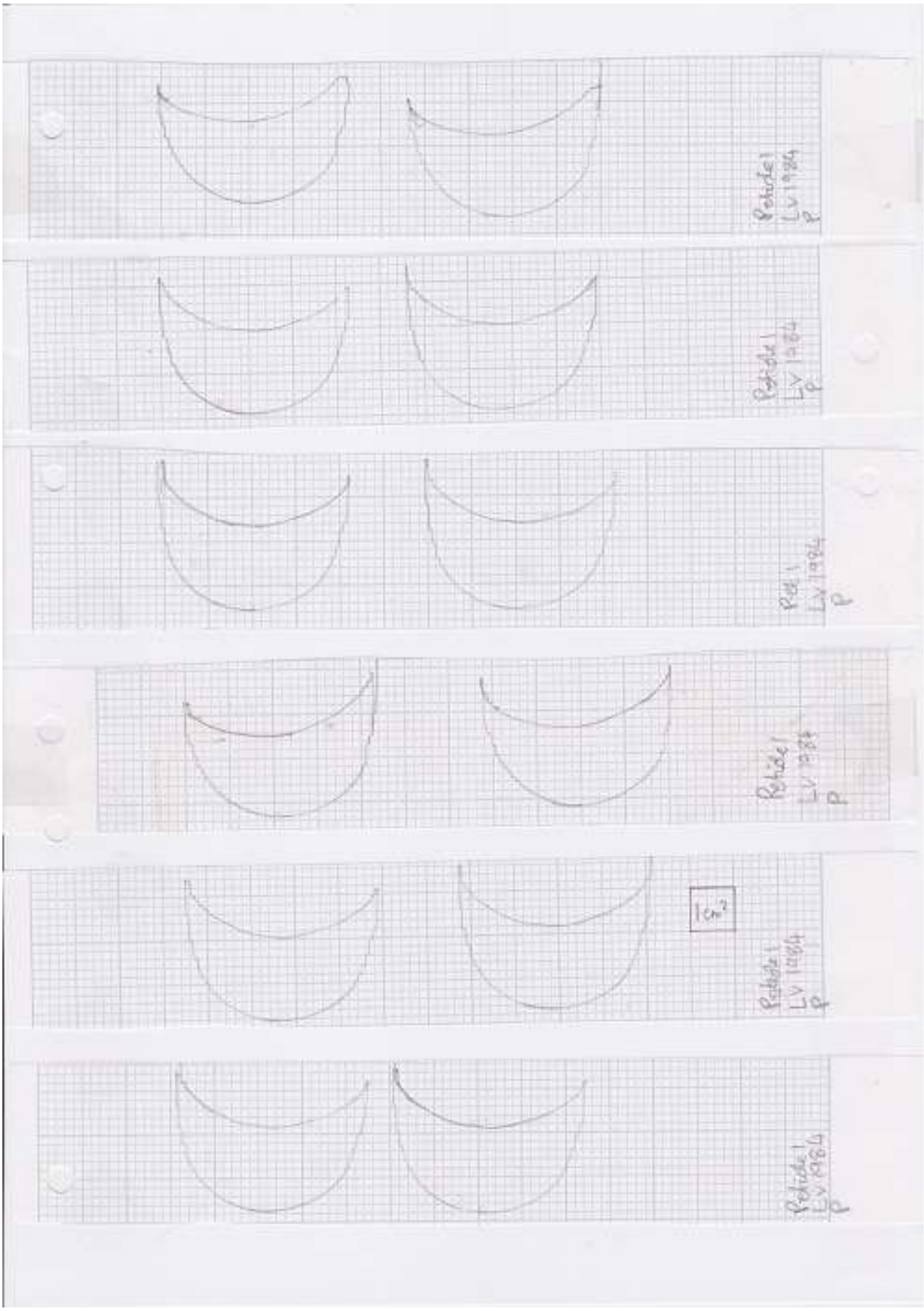

Figure 123 Raw profiles LvP – one *petiole* (part 2 of 3)

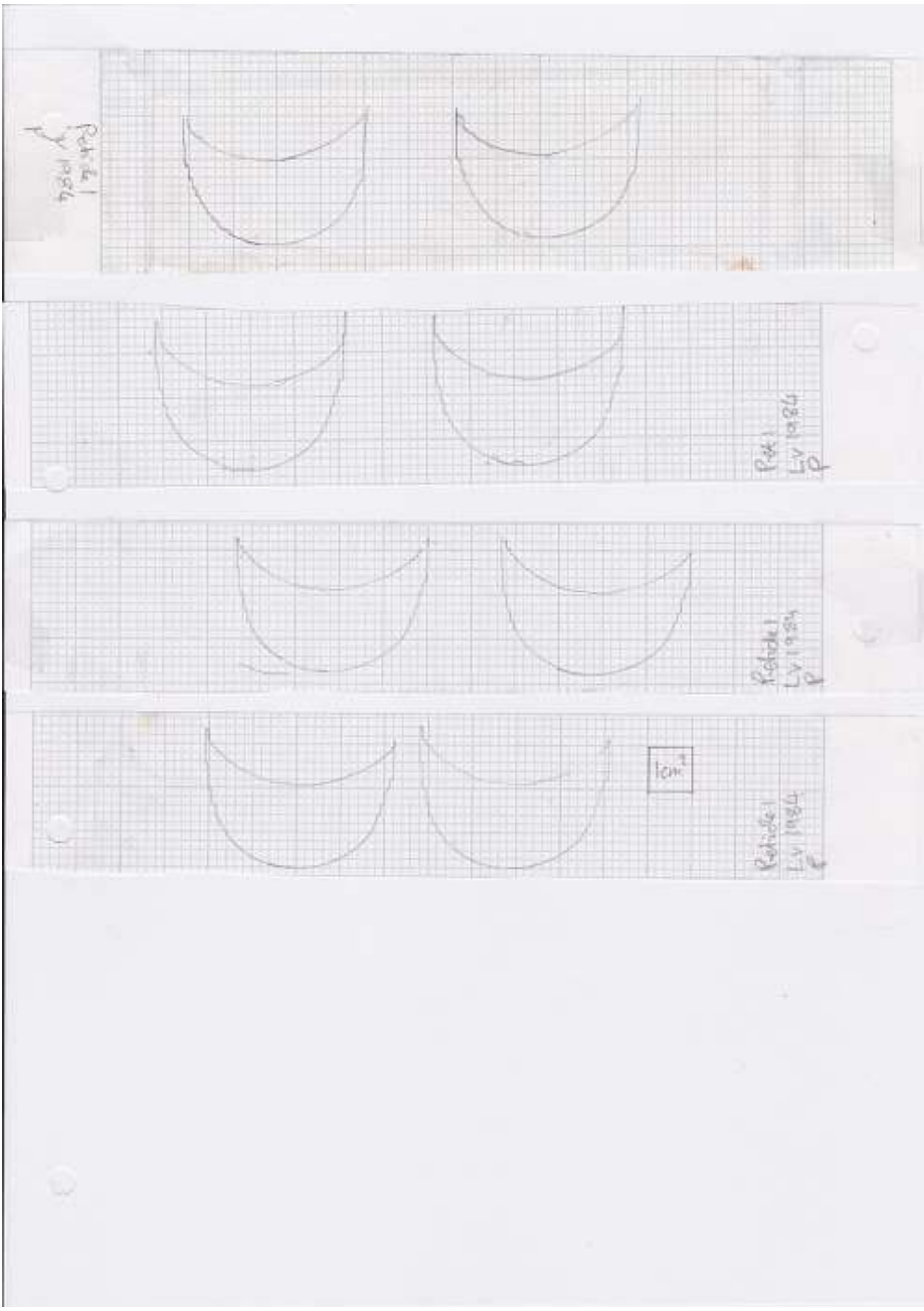

Figure 124 Raw profiles LvP – one *petiole* (part 3 of 3)

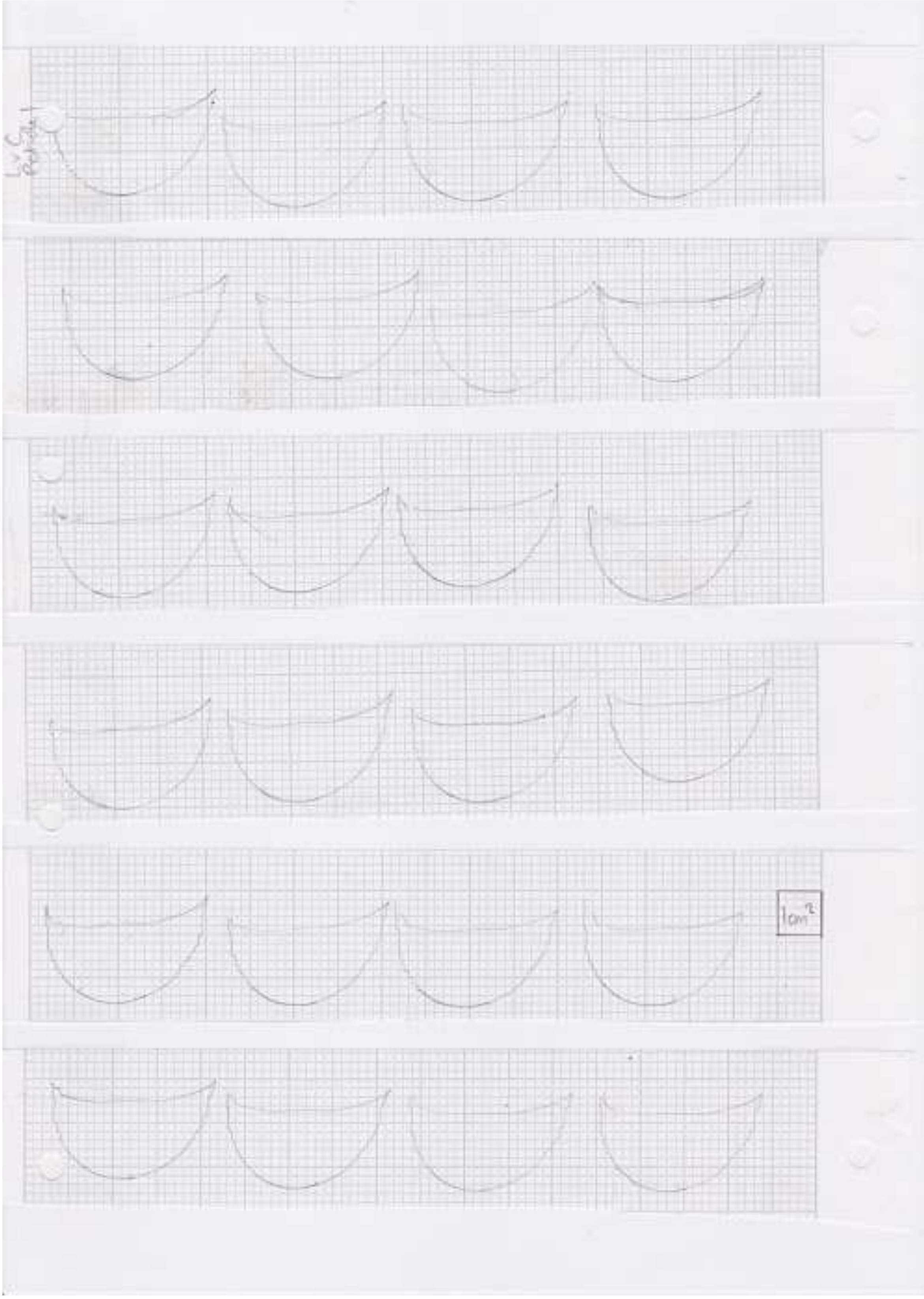

Figure 125 Raw profiles LvC – one *petiole* (part 1 of 2)

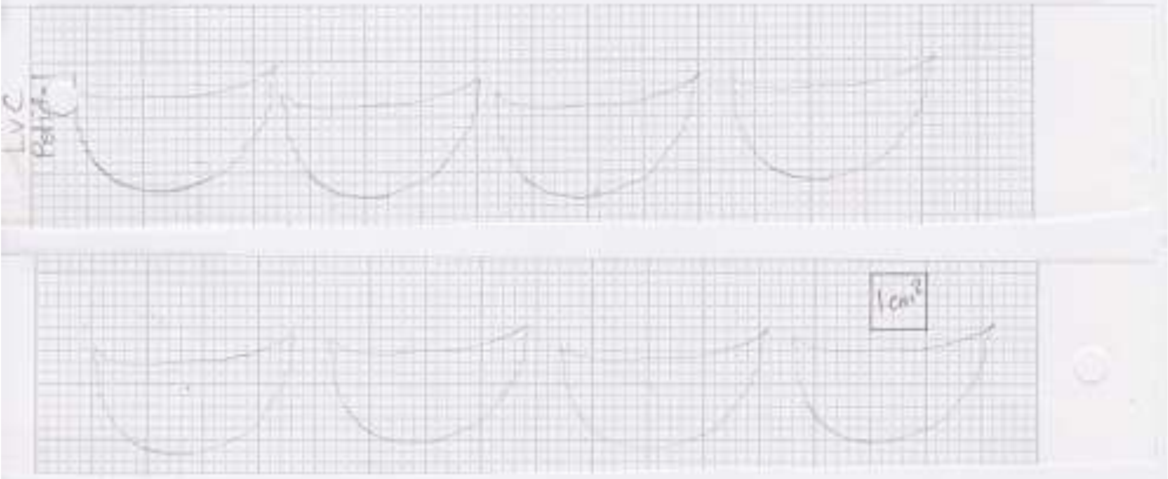

Figure 126 Raw profiles LvC – one *petiole* (part 2 of 2)

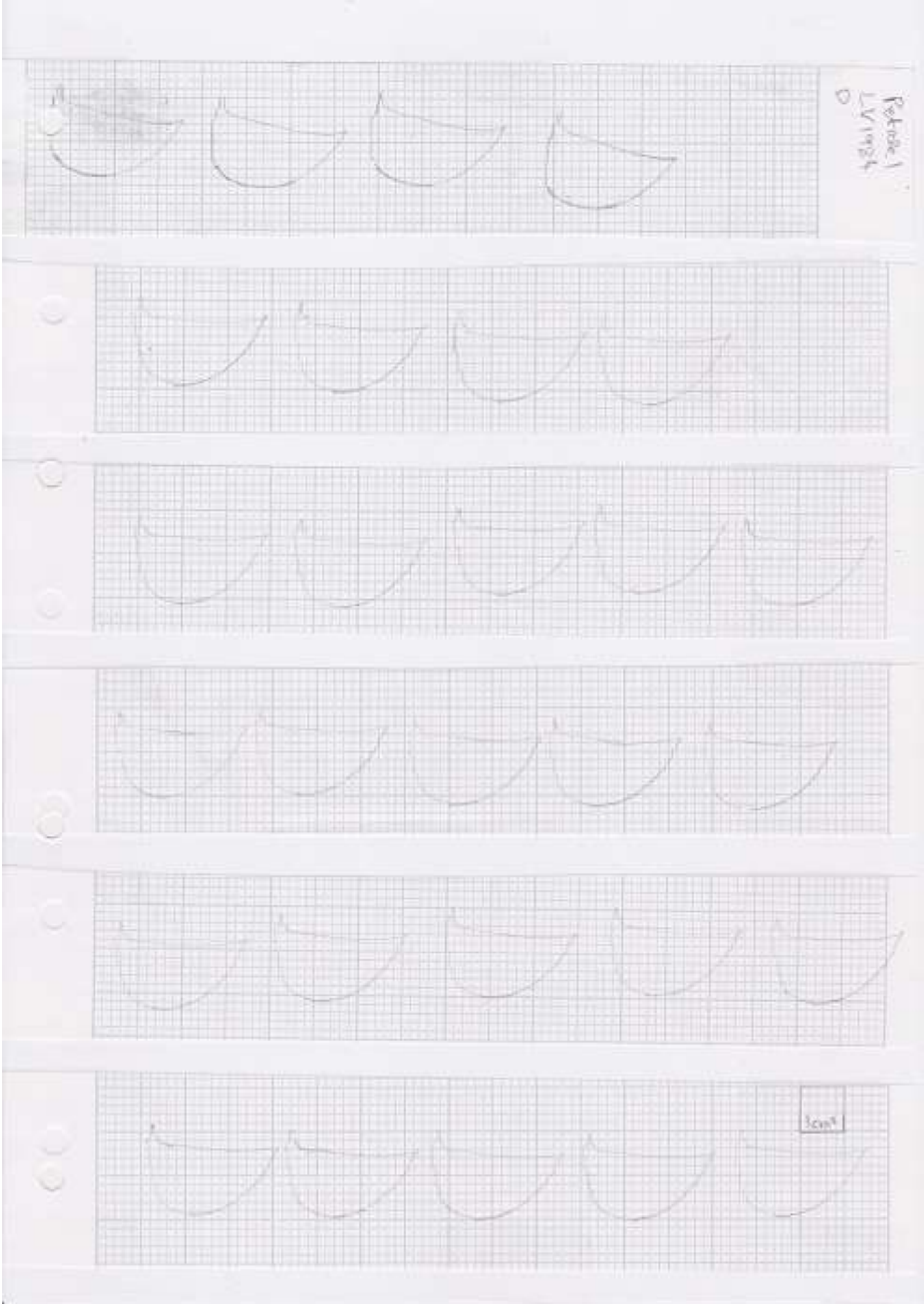

Figure 127 Raw profiles LvD – one *petiole* (part 1 of 2)

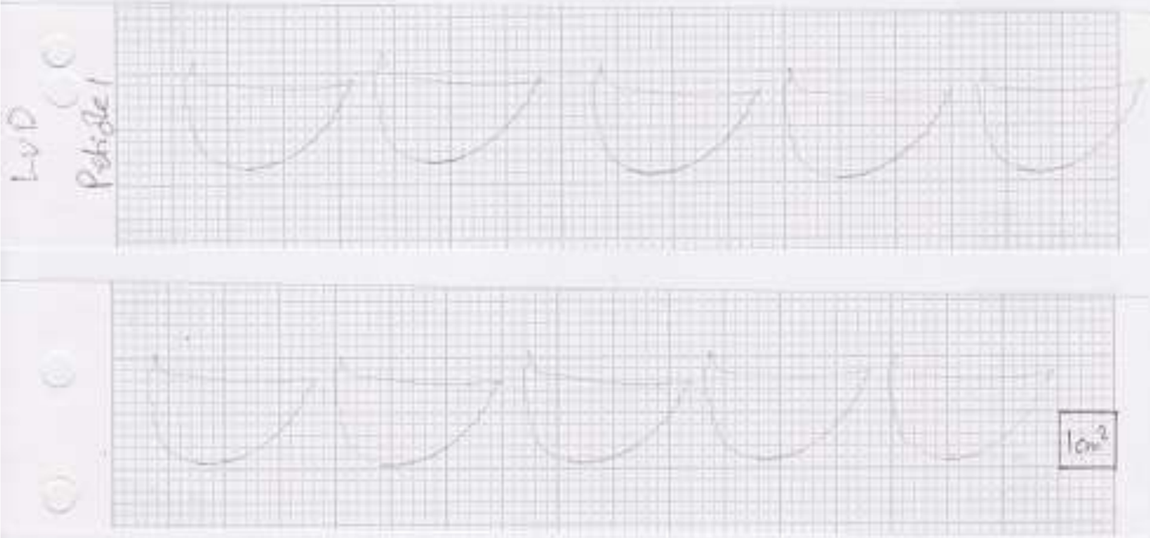

Figure 128 Raw profiles LvD – one *petiole* (part 2 of 2)

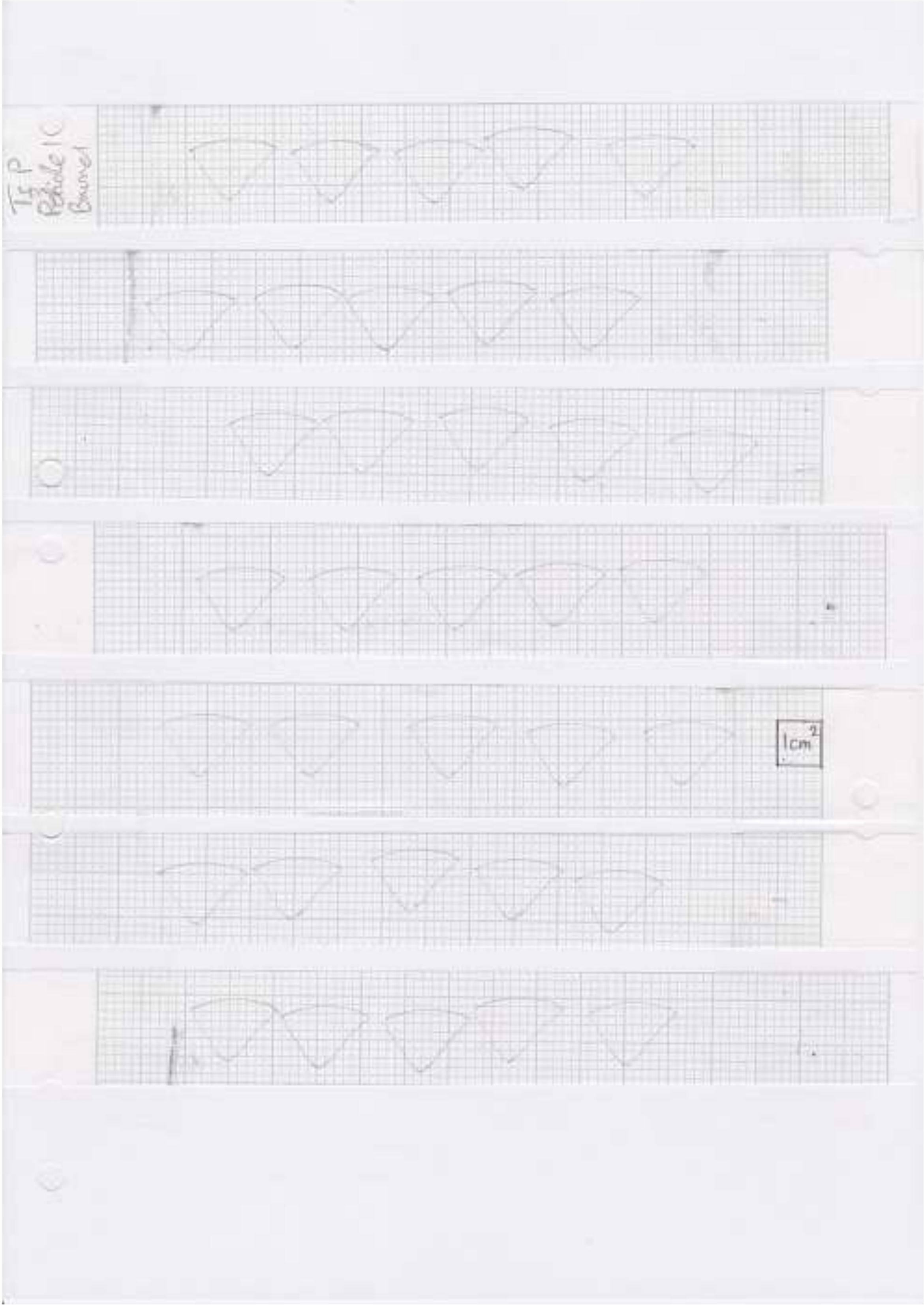

Figure 129 Raw profiles TfP – one *petiole*

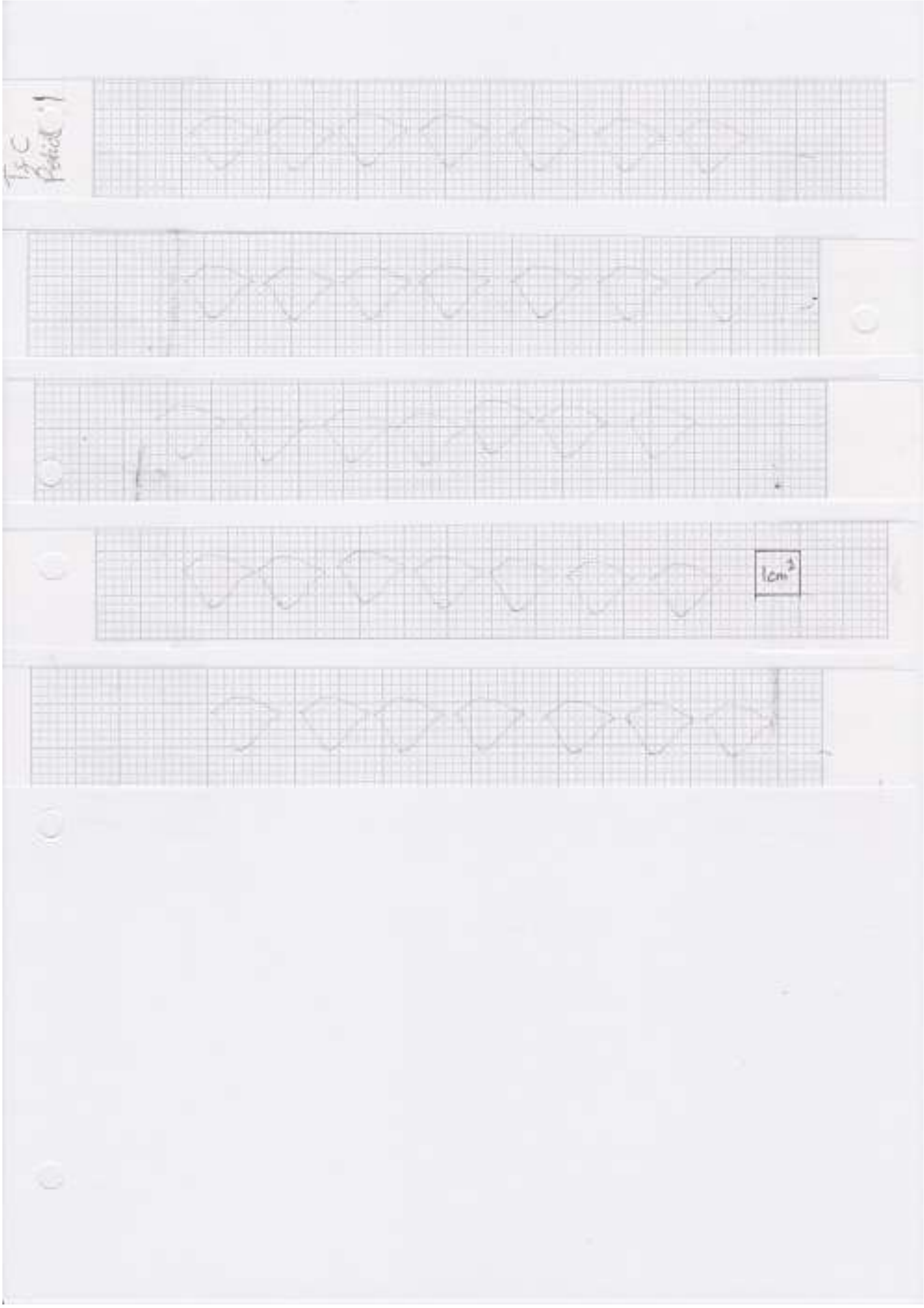

Figure 130 Raw profiles TfC – one *petiole*

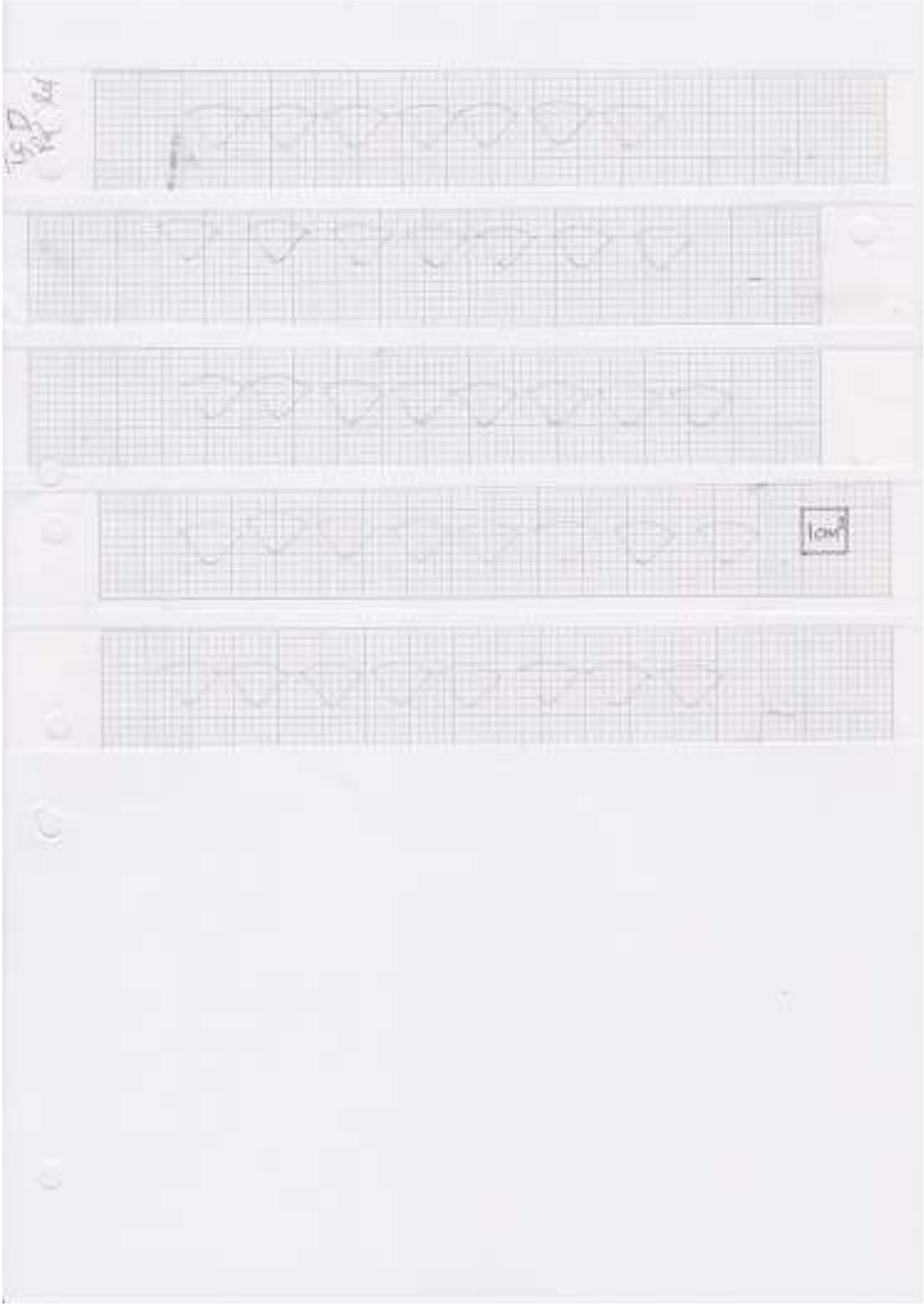

Figure 131 Raw profiles TfD – one *petiole*

8.3 Digitised petiole profiles in Adobe Illustrator

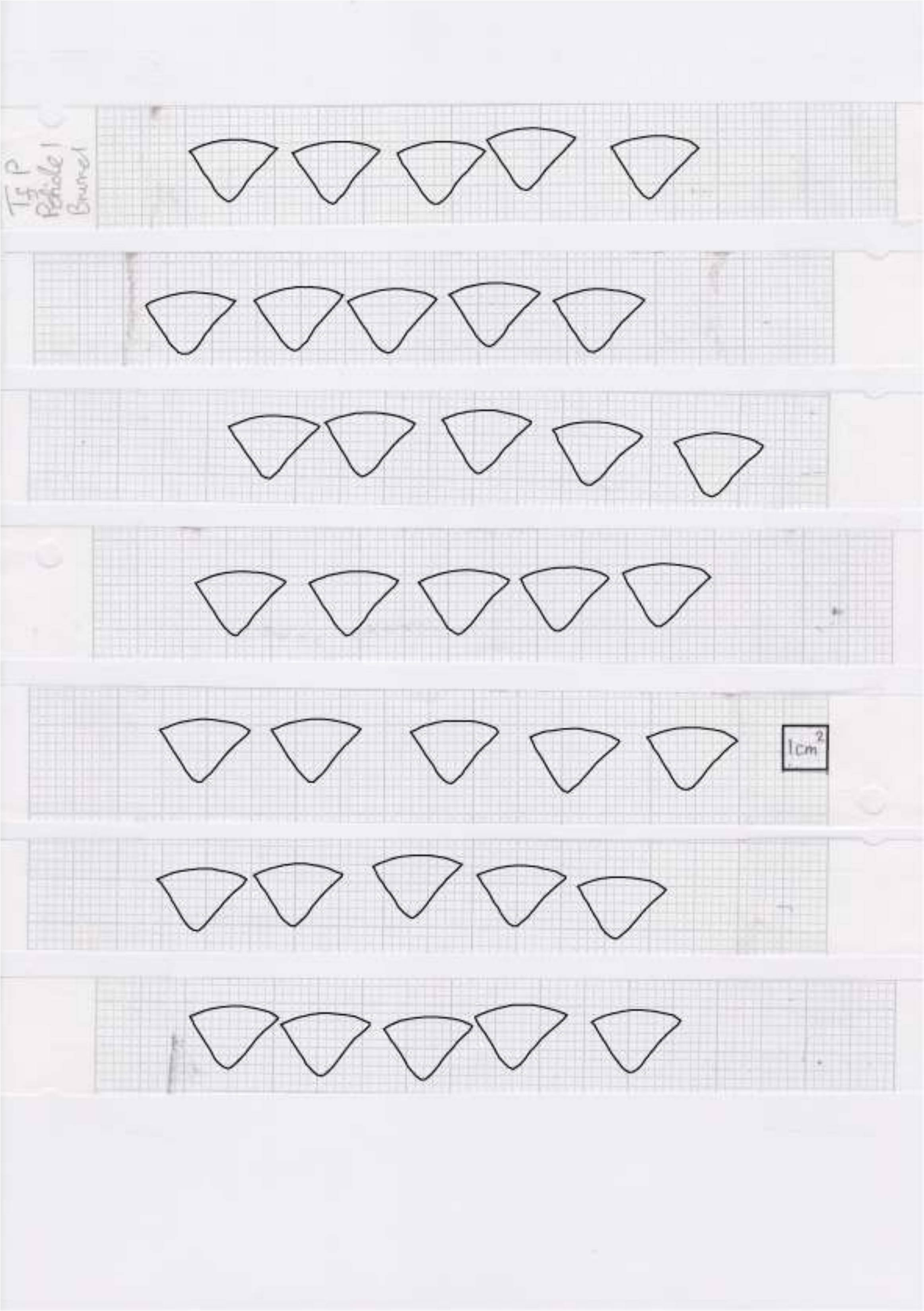

Figure 132 Digitised profiles of *Tf* P in Adobe Illustrator

8.4 Rhinoceros® NURBS modelling for Windows® petiole profiles

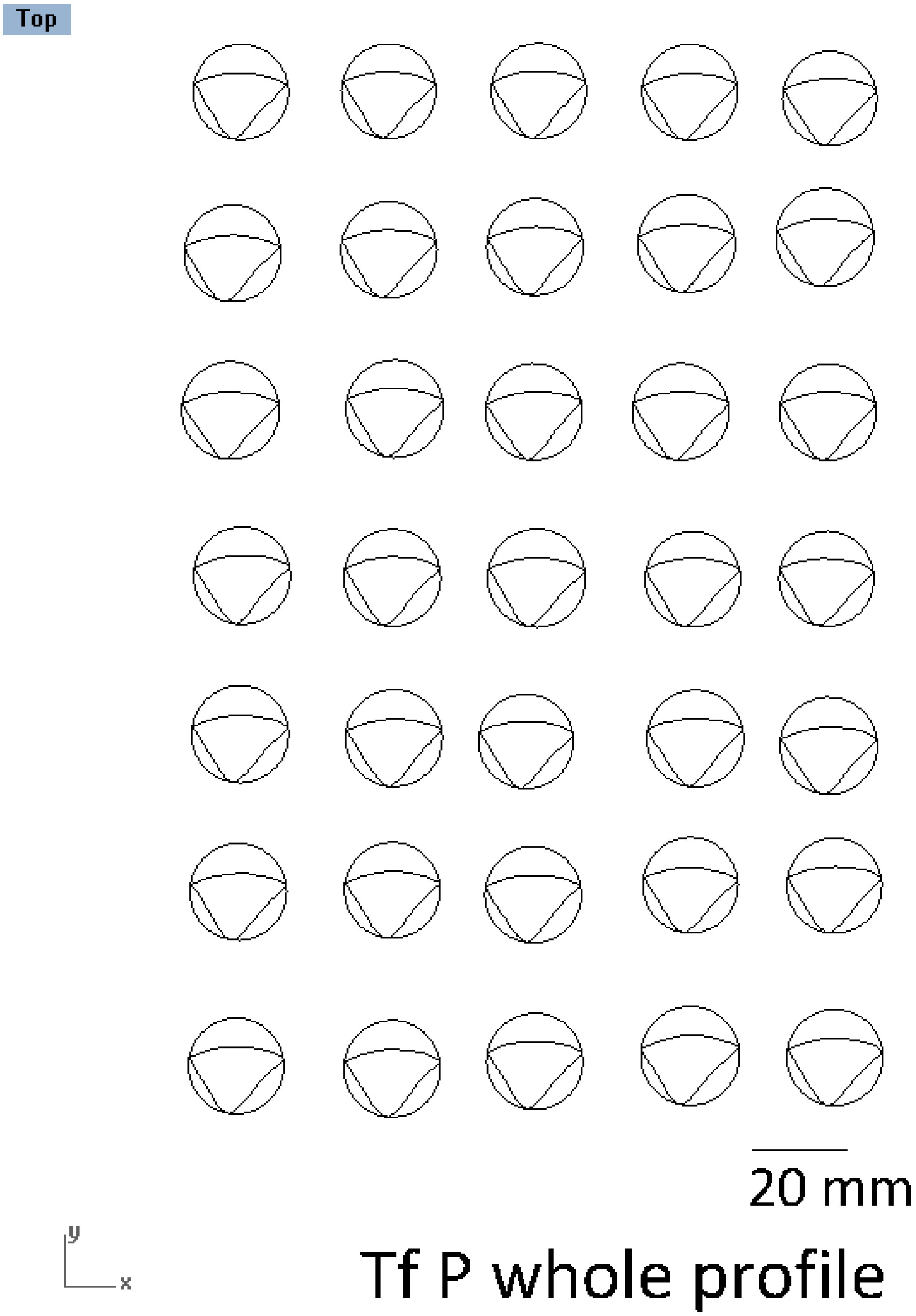

Figure 133 Whole profile of *Tf* P circumscribed in Rhino

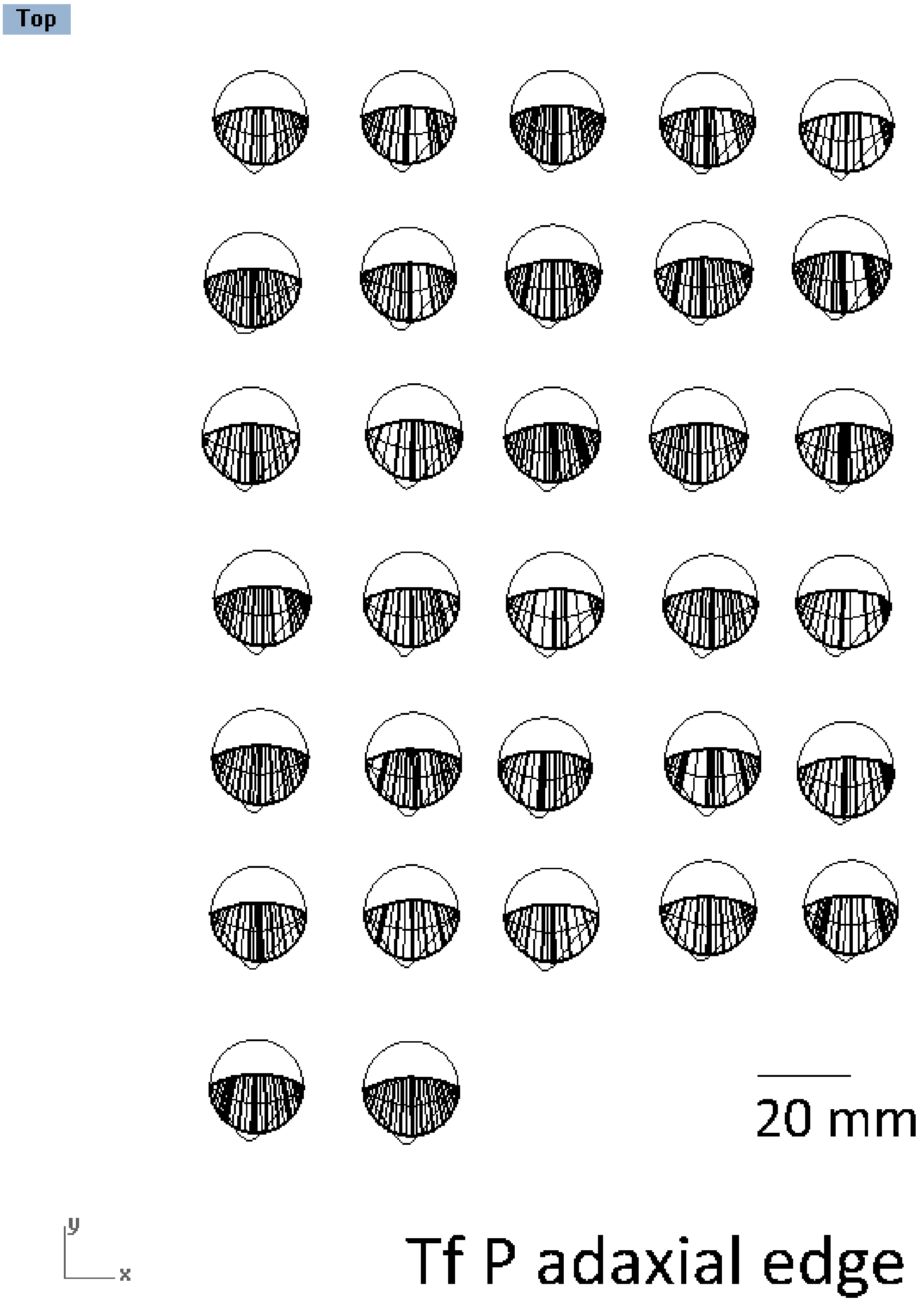

Figure 134 *Adaxial* edge of *Tf* P circumscribed in Rhino

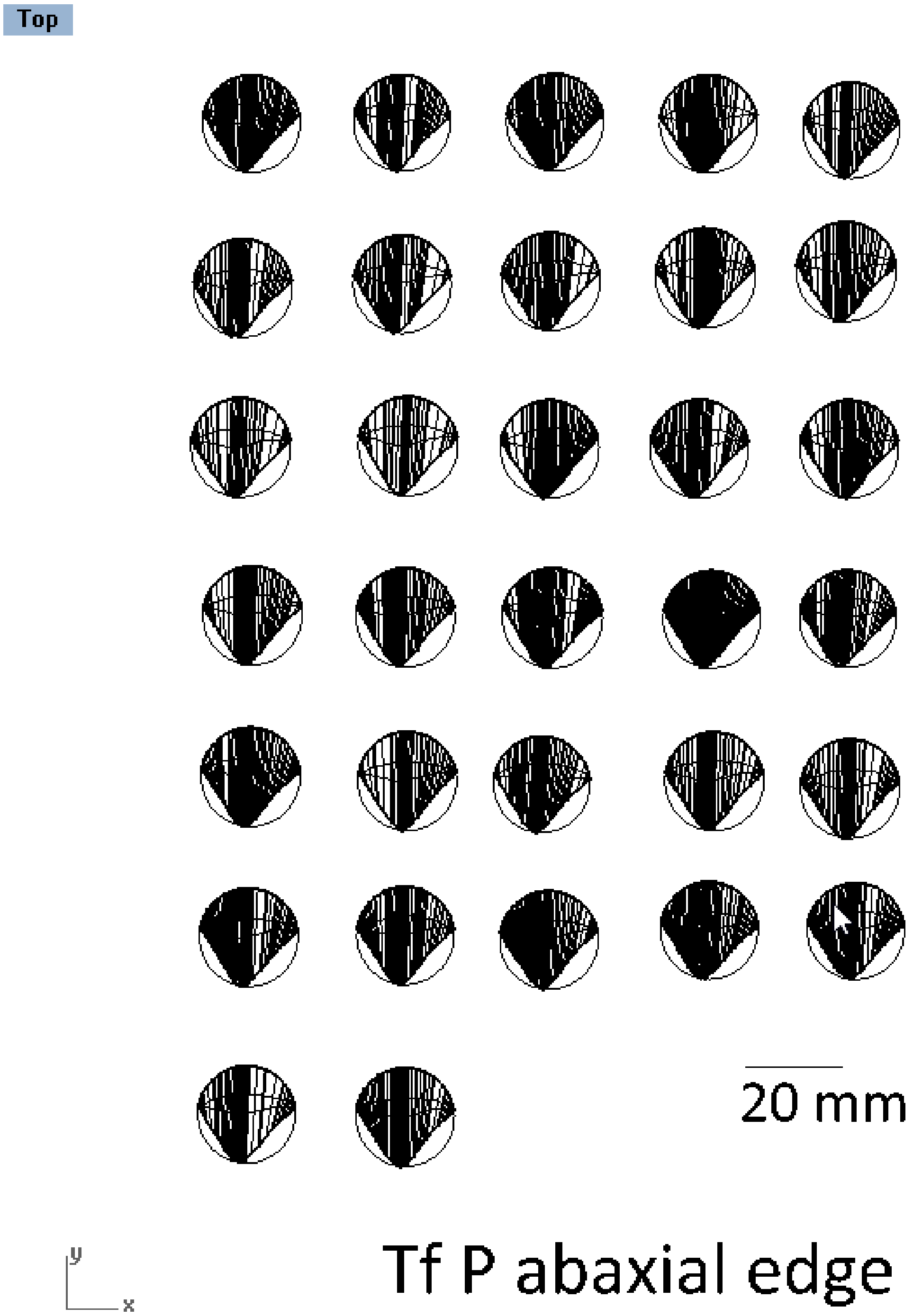

Figure 135 *Abaxial* edge of *Tf* P circumscribed in Rhino